UNIVERSITAT POLITÈCNICA DE VALÈNCIA

Instituto Universitario Mixto de Tecnología Química

(UPV-CSIC)

Controlling the nature of metal species in zeolites: implications in Catalysis

PhD Thesis

Presented by:

Adrián Martínez Gómez-Aldaraví

Supervisors:

Dr. Manuel Moliner Marín

Dra. Mª Cristina Martínez Sánchez

Valencia, June 2025

Dr. MANUEL MOLINER MARÍN, tenured researcher at Instituto Universitario Mixto de Tecnología Química (UPV-CSIC) and Dr. Mª CRISTINA MARTÍNEZ SÁNCHEZ**,** tenured researcher at Instituto Universitario Mixto de Tecnología Química (UPV-CSIC),

CERTIFY that the present doctoral thesis, entitled:

"Controlling the nature of metal species in zeolites: implications in catalysis"

has been developed by ADRIÁN MARTÍNEZ GÓMEZ-ALDARAVÍ under their supervision at the Instituto Universitario Mixto de Tecnología Química (UPV-CSIC).

Valencia, June 2025

Dr. Manuel Moliner Marín

Dr. Mª Cristina Martínez Sánchez

“Después de la perfección no hay nada por encima. No hay espacio para la creación, lo que significa que tampoco lo hay para la sabiduría o el talento. Para científicos como nosotros, la perfección es "desesperante". Incluso cuando algo creado sea superior a todo lo demás existente, seguirá estando muy lejos de la perfección. Los científicos estamos condenados a luchar constantemente contra esta paradoja, y más aún, debemos poder ser capaces de encontrar el placer en ello.”

“Beyond perfection, nothing greater remains. It leaves no space for creation and thus, none for wisdom or for talent. For scientists like us, perfection is a tormenting ideal. Even when something created surpasses everything else existent, it still remains far away from being perfect. We are condemned to wrestle with this paradox, again and again, and even more, we must learn to find pleasure in it.”

Mayuri Kurotsuchi (Bleach, ep 200, Tite Kubo)

Agradecimientos/Acknowlegdements

Me gustaría agradecer formalmente al Ministerio de Ciencia, Innovación y Universidades del gobierno de España por la financiación de la beca PRE2019-088361 (cód. proyecto SEV-2016-0683-19-1) que me ha permitido la realización de la presente tesis doctoral en el Instituto de Tecnología Química (UPV-CSIC), así como la participación en diferentes congresos y realizar mi estancia en la Universidad de Tokio.

Quiero agradecer a mis directores de tesis, el Dr. Manuel Moliner y la Dra. Mª Cristina Martínez Sánchez por brindarme la oportunidad de hacer la tesis doctoral bajo su supervisión y por todo lo aprendido de ellos en estos años. Desde el rigor, la necesidad de ser metódico y el valor para atreverse a tener ideas que he aprendido de Manolo, hasta el tesón para no rendirse nunca por muy mal que pinte la situación y que la ciencia no es sólo hacer experimentos, sino disfrutar con las personas en el camino, expropiación masiva de caramelos incluida, de Cristina. Del mismo modo me gustaría agradecer al Dr. Pedro Serna por su inestimable tutela y ayuda, no solo en la consecución de estos capítulos, sino en el desarrollo de habilidades transversales que seguro serán útiles allá donde vaya.

Quiero agradecer a mis compañeras de laboratorio Isabel, Eli y Fanny por todos estos años compartidos y por enseñarme cómo se debe de trabajar en un laboratorio y en las trincheras de batalla del mundo académico, así como a Marcela, Benjamín y Christos. Sois el futuro chavales, dad lo mejor de vosotros.

Me gustaría hacer especial mención al equipo de caracterización por la magnífica labor que hacen siempre, especialmente a; Maribel y a Amparo por su cariño siempre a la hora de tratar todas mis muestras a pesar de que sé que a veces arrasaba como un tornado por ahí, a mis superheroínas Fany y Chusa por haberme dejado todos estos años ser el niño mimado de Combi y haberme ayudado siempre, incluso con las mayores locuras con las que he aparecido por ahí (mesa de cirugía con la bolsa de N_2 a punto de explotar incluida), a Alejandro por haberme dejado consejos sobre RMN y por esas conversaciones sobre cómo levantar el país. A Rosa y a José Miguel por haberme enseñado lo que debía saber de espectroscopía de infrarrojos y por haberse dejado marear en más de una ocasión para sacar adelante mis locuras. Quiero agradecer también a Ximo, Merche y a Ali por todo el cariño estos años en el servicio de microscopía, por haberme dejado ser un poco parte de su vida a través de todas aquellas conversaciones en las, a veces eternas sesiones de microscopía electrónica.

En estos agradecimientos por supuestísimo que tenéis sitio los muchachos de taller por todos los marronazos de los que nos salváis de continuo. Especial mención, no sólo por su trabajo sino por luego darme los mejores ratos del mundo en las comidas a Oscar, por su inquebrantable paciencia, sentido del humor y entereza ante aquellas situaciones que eran el preludio de catástrofe, a Rafa por haber sido piedra angular con todo el tema informático y por todos aquellos momentos de anécdotas épicas y a Álvaro, mi actor favorito de UPA Dance, por haber sufrido conmigo los calvarios de los reactores, por estar desde primera hora de la mañana listo para ponernos al día de todo el *goship* del mundo y/o escrudiñar los últimos capítulos de anime entre tuercas, tornillos y cables, además de ser el que resistía siempre

conmigo al huracán moreno de Málaga (mi queridísima Lidia), que también tiene su sitio aquí. Muchas gracias por toda la ayuda estos años no sólo en el apartado de compras sino por todo el apoyo y todos los buenos ratos riendo que hemos pasado juntos.

Quiero agradecer a toda la gente con las que he compartido trinchera tantos años, mis niños bonitos del Palomar (Marcos, Elena, Iván, Eva) por su continuo apoyo desde el principio, las chicas de nanomedicina (Eva y Carla) por haberme dejado seguir con la mala tendencia de ser el niño mimado de Combi, a toda la gente increíble de Síntesis (José Valero, Alberto, Xisco, Marta, Manu, Bea, Raquel, Tomás, y sobre todo a Amparo) por vuestro cariño y haberme dejado usar vuestro laboratorio para más de una salvajada mía, a Andresito y a Marwan, mis insurgentes de pilas, por todas las risas entre cervezas. Quiero hacer especial mención a la sede de becaries P2 (Lore, Sofía, mi eterno Calamardo, Bego) por su amistad todos estos años entre cromas rotos, memes repartidos por los laboratorios de reacción, risas y suspiros cuando se veía el drama de que algo no saliera. Gracias a Bea Moreno por su incombustible alegría y su actitud ante todos los problemas que ambos hemos ido encontrando por el camino y por brindarme su valiosa amistad dentro y fuera del ITQ. Gracias toda la gente de R1 por haberme enseñado y ayudado todos estos años, especialmente a Javi Ceuta, que se ha ganado el cielo conmigo, por todo lo aprendido juntos, por su apoyo y por los momentos tan épicos en R1, a Carlos y Raúl por esas productivas conversaciones entre horas y horas de pastillear, a Eva Briz, a Esther y a Aroa, por habernos aguantado tantos años a los 4 jinetes del apocalipsis con tan buen humor, tanto cariño y tan buen rollo.

Quiero agradecerles a mis tres mosqueteros (Agus, Plá y Jose) y al pequeño D'Artagnan (Ferrán), que siempre va con ellos por todo lo vivido estos años. Hay muchos méritos de los que puedo presumir en esta tesis, pero de que se hubieran cruzado nuestros caminos está entre los que más. Gracias por haberme permitido vivir esta aventura, desde todos los momentos de hacernos la puñeta hasta las mañanas enteras riendo porque no estamos bien ninguno de los 5, pasando por todas las situaciones inverosímiles que hemos vivido en congresos, en el día a día y cuando nos hemos juntado fuera y esos momentos de animarnos café en mano cuando la vida se nos complicaba de más.

Quiero agradecer también, a toda la gente maravillosa que empezó conmigo, mi vieja guardia. A Edi por su extraordinaria forma de ser, de animar siempre, de seguir siendo dos Gryffindors para los que el tiempo no ha pasado cuando se han reencontrado. A la Nuri, por su amistad, dentro y fuera, por esas horas de resintonizar la CNN de las anécdotas de la actualidad sensacionalista, por presentarme a la gente cuando era un pollo perdido en su primer día, por haberme mantenido en tu vida. A Ximo, por su longeva amistad y todos esos momentos comiendo en el Coffe entre risas, anécdotas increíbles y, a veces, Calamardo autoinvitándose a comer con nosotros. Así mismo gracias por ser el que dio lugar a la aparición del pre-doc de la bata negra en el ITQ.

This paragraph is written in English so the wonderful people I met during my stay at the University of Tokyo can read it. First, I want to thank Professors Toru Wakihara and Tatsuya Okubo for allowing me to join their laboratory, where I met incredible people and learned so much about the fascinating mysteries that zeolites still hold.

I would like to express my deepest thanks to Zhou, Boqing, Yu, and Yo for their warm welcome and for showing me such beautiful places in Tokyo. I'm also deeply grateful to Elango and Fujinouva for their kindness when I first arrived, for always supporting me since the beginning, and for the countless conversations and the exchanges of Spanish, Italian, and Japanese lessons.

I want to thank all the students I met there for your eagerness to help and learn together, and for those spontaneous Takoyaki sessions and Nintendo Switch tournaments that helped to make the long waiting nights in the lab so much brighter.

I especially want to thank Elena Brozzy, my partner in crime during those months, for the affection, the support, and the beautiful friendship you shared with me during those three months. Thank you for exploring so many incredible places with me, often on a whim, with barely anything planned, jumping onto buses that could have taken us who-knows-where, or ending up speechless while singing at karaoke. Thank you for the friendships I carry with me. Friendships we try to keep alive to this day, despite the distance.

Finally, I want to thank Luis for all his help from the moment I landed in Japan, and above all, Raqueru-sensei, for looking after me during my stay and for encouraging to do my best, for the beautiful conversations we had about science and life, for showing me Japan's hidden treasures and for showing me why are you so beloved between the Japanese students. I came back home with the memory of one of the people I've come to admire the most, not only academically, and I will never be able to thank her enough for having made it possible for me to live one of the most meaningful chapters, not only of my PhD, but of my life.

A mi sista Alexa por el incondicional apoyo y lealtad todos estos años, por todas esas meriendas compartiendo los infortunios del día a día en la llorería, las risas y los recuerdos sobre un buen café, los rámenes, las videollamadas y las sesiones de obligarnos mutuamente a ir a escribir a la biblioteca. Has sido un pilar fundamental todos estos años, especialmente éste último. Muchas gracias por haber estado al pie del cañón tirando de mí. Me faltan años para devolverte todo lo que has hecho.

A Víctor y a Aitor, mis dos hermanos de otra sangre, a María Eugenia y a Sapi, por brindarme vuestro apoyo incondicional y vuestra amistad desde que tengo memoria, pero tan determinante en esta última etapa, haciendo que, me encuentre donde me encuentre, no pueda olvidar nunca donde está mi casa. Gracias a este mérito estoy un paso más cerca de ser el hermano que os merecéis. Por toda una vida siguiendo juntos con lo que venga a vuestro lado.

A Eva y a Aída, las que durante todo este tiempo han acabado convirtiéndose en mis hermanas mayores de "combinasión combinasión", me faltarían páginas en toda esta tesis para reflejar lo mucho que os debo por todo y lo que os quiero. Fuisteis las primeras en apostar por mí cuando llegué y en enseñarme prácticamente todo lo que sé, aun cuando fue más que evidente, que os venía fatal que os pasasen la patata caliente del novato de Alicante. Infinitas gracias por todos estos años de risas, de lloros cuando las cosas no salían, por las tardes de música haciendo experimentos, por aquellos momentos ¿pero que ha pachado? cuando nos entraban en el e-mail correos, que darían lugar a días de risas interminables, o cuando nos pillaban trabajando los viernes por la tarde al ritmo de la radio las visitas inesperadas de última hora.

Por todos esos momentos de salseo, de fraternidad y de enseñarme lo increíblemente orgánico y satisfactorio que es todo cuando un grupo de trabajo se vuelve un equipo. Espero haber sido el aprendiz Jedi que unas maestras y amigas como vosotras se merecen (aunque tenga claro que me pueden catalogar más de Lord Sith). Os quiero chicas.

A continuación, quiero agradecer a mi familia el papel tan relevante que han tenido para que yo pueda estar aquí el día de hoy. A mi hermana Andrea, por haber sido siempre mi apoyo y mi lacaya/confidente desde siempre, estos últimos años la vida me ha enseñado a valorar el increíble tesoro que tengo mejor que nunca y estoy increíblemente orgulloso de quién eres y de lo que has conseguido, aunque sea yo el mayor todavía eres tú quien me enseña las cosas. A mi abuela Sagrario, que siempre ha sido el ejemplo de tesón y fe para las causas indefendibles, el símbolo de la unión de la familia y del amor y cariño en pequeños gestos. Aunque este año nos hayan separado, estés allá donde estés, espero haber sido un nieto a tu altura. Has sido, eres y siempre serás eterna.

A Marina, la que es mi mayor respaldo, la científica que más admiro y respeto, académica y humanamente hablando, mi definición de hogar, que ha sido la mayor responsable de que esto haya sido posible gracias a su continuo apoyo, su infinito amor y hasta sus reprimendas de cómo se espera de un doctor que se hagan las cosas. Por permitirme cada día aprender un poco más de la vida y de la ciencia contigo, por haberme impulsado tanto y por haber empujado tanto de mí en esta etapa, especialmente cuando no me podía aguantar ni yo mismo. Por seguir pinchándome para que busque la excelencia, pero manteniendo la esencia propia, por haber sido mi pepito grillo cuando estaba desubicado y por nunca dejarme olvidar lo bonito de querer ser curioso y

fascinarme hasta por la mayor tontería del mundo. Te quiero 3000 en todos los universos.

Y finalmente, gracias a ti Adrián. Por esa pasión (y que muchísimas veces ha traído más problemas que soluciones) que tienes cuando algo te fascina, por haber sido capaz de llegar hasta aquí después de, literalmente, una auténtica Odisea de más de 5 años con todas las innumerables cosas que han pasado y que dejarían atónito a cualquiera. Por ser tan increíblemente terco, que has ignorado todas las señales del universo que constantemente sugerían que igual era buena idea dejarlo y nunca te has rendido y, por enseñarme una vez más que, cuando más débil te percibías, más fuerte has resultado ser. Lo has hecho estupendamente, y te has ganado todas y cada una de las cosas y de las experiencias por las que dar gracias en este capítulo de tu historia. Has aguantado como un jabato, y me siento increíblemente orgulloso de ti, de lo que has conseguido y de lo que no has renunciado para poder llegar a conseguirlo.

RESUMEN

Las zeolitas son sólidos microporosos, ampliamente utilizados como catalizadores heterogéneos debido su elevada estabilidad hidrotermal, su elevada área específica, su selectividad por control de forma y sus propiedades físico-químicas ajustables. La optimización de dichas propiedades permite la consolidación de los catalizadores zeolíticos como alternativas sostenibles y eficientes para mejorar numerosos procesos de interés industrial y medioambiental.

En la presente tesis doctoral se aplicaran diversas metodologías de síntesis directa y post-sintéticas que permitan un control de las propiedades finales de la zeolita, desde la escala microscópica hasta la escala molecular y atómica, permitiendo el diseño racional de zeolitas con propiedades físico-químicas y texturales controladas, que repercutirán directamente en la distribución de los centros activos, en el control del tamaño de partícula de zeolita y en su comportamiento catalítico final frente a reacciones de interés.

La primera parte de este trabajo (**Capítulo 4**) se centra en la síntesis de zeolitas de poro medio de estructura tipo MFI con centros activos de Pt con estabilidad mejorada y mayor resistencia a la desactivación del catalizador por sinterizado de los centros metálicos. Para ello, se han incluido en la síntesis cationes alcalinos que maximicen la dispersión de los nanoclusters y una segunda especie metálica que actúe como especie aleante, dando lugar a clústeres de la aleación bimetálica que presenten mejor comportamiento catalítico. Los materiales, una vez sintetizados con la proporción atómica adecuada de centros metálicos, catión alcalino y especie aleante, han

resultado ser catalizadores eficientes y estables para la reacción de deshidrogenación no-oxidativa de propano, reacción de elevado interés industrial que requiere condiciones muy severas de temperatura en ambiente redox.

La segunda parte de la tesis doctoral (**Capítulo 5**) se centra en (i) la síntesis de zeolitas de poro medio tipo MFI con propiedades difusivas controladas gracias al control del tamaño final de cristal de la zeolita, con centros metálicos de Pt introducidos por encapsulación directa para la mejora de la actividad catalítica para la conversión de moléculas voluminosas de interés como el fenilacetileno y, (ii) en el desarrollo de coberturas homogéneas hidrófobas con estructura cristalina tipo MFI empleando la novedosa metodología de la síntesis hidrotermal ultrarrápida, con el fin de mejorar la estabilización de los centros activos metálicos ante fenómenos de arrastre/lixiviado o sinterizado.

Finalmente, la última parte (**Capítulo 6**) plantea la combinación de estrategias basadas en la optimización de la composición del gel de síntesis, de la metodología de incorporación de los centros activos y del control sobre el tamaño final de partícula de zeolita para el desarrollo de zeolitas de poro medio (tipo MFI) y poro grande (tipo BEA) con centros ácidos Brønsted y centros metálicos de Ni que ejerzan de catalizadores multifuncionales eficientes para la reacción de oligomerización de etileno, de elevado interés industrial. Para ello, mediante el uso de agentes directores de estructura orgánicos específicos se ha ejercido un control sobre el tamaño de cristal final de los materiales y mediante el procedimiento de incorporación de los centros Ni se ha controlado el estado final de los centros activos, modulando la actividad catalítica de los materiales.

RESUM

Les zeolites són sòlids microporosos, àmpliament utilitzats com a catalitzadors heterogenis degut a la seua elevada estabilitat hidrotermal, la seua elevada àrea específica, la seua selectivitat per control de forma i les seues propietats fisicoquímiques ajustables. L'optimització d'aquestes propietats permet la consolidació dels catalitzadors zeolítics com a alternatives sostenibles i eficients per a millorar nombrosos processos d'interés industrial i mediambiental.

En la present tesi doctoral s'aplicaren diverses metodologies de síntesi directa i post-sintètiques que permeten un control de les propietats finals de la zeolita, des de l'escala microscòpica fins a l'escala molecular i atòmica, permetent produir de manera racional zeolites amb propietats fisicoquímiques i texturals controlades, repercutint directament en la distribució dels centres actius, en el control de la grandària de partícula de zeolita i en el seu comportament catalític final enfront de reaccions d'interés.

La primera part d'aquest treball (**Capítol 4**) es centra en la síntesi de zeolites de porus mitjà d'estructura tipus MFI amb centres actius de Pt amb estabilitat millorada i major resistència a la desactivació del catalitzador per sinteritzat dels centres metàl·lics. Per això, s'han inclòs en la síntesi cations alcalins que maximitzen la dispersió dels nanoclústers i una segona espècie metàl·lica que actue com a espècie aliant, donant lloc a clústers de l'aliatge bimetàl·lic que presenten millor comportament catalític. Els materials, una vegada sintetitzats amb la proporció atòmica adequada de centres metàl·lics, catió alcalí i espècie aliant, han resultat ser catalitzadors eficients i estables per a

la reacció de deshidrogenació no-oxidativa de propà, reacció de molt elevat interés industrial que requereix condicions molt de temperatura en ambients redox.

La segona part de la tesi doctoral (**Capítol 5**) es centra en (i) la síntesi de zeolites de por mitjà tipus MFI amb propietats difusives controlades gràcies al control sobre la grandària final de partícula de zeolites, i amb centres metàl·lics de Pt introduïts per encapsulació directa per a la millora de l'activitat catalítica per a la conversió de molècules voluminoses d'interés com el fenilacetilé i, (ii) en el desenvolupament de cobertures homogènies hidròfobes amb estructura cristal·lina tipus MFI emprant la nova metodologia de la síntesi hidrotermal ultraràpida per a la millora de l'estabilització dels centres actius metàl·lics davant fenòmens d'arrossegament/lixiviat o sinteritzat.

Finalment, la última part (**Capítol 6**) planteja la combinació d'estratègies basades en l´optimització de la composició del gel de síntesi, de la metodologia d'incorporació dels centres actius i del control sobre la grandària final de partícula de zeolita per al desenvolupament de zeolites de porus mitjà (tipus MFI) i porus gran (tipus BEA) amb centres àcids Brønsted i centres metàl·lics de Ni que exercisquen de catalitzadors multifuncionals eficients per a la reacció de oligomerització d'etilé, d'un elevat interés industrial. Per a això, mitjançant l'ús d'agents directors d'estructura orgànics específics es va exercir un control sobre la grandària de cristall final dels materials, i mitjançant el procediment d'incorporació dels centres Ni es va controlar l'estat final dels centres actius, modulant l'activitat catalítica dels materials.

SUMMARY

Zeolites are microporous solids extensively employed as heterogeneous catalysts due to their remarkable hydrothermal stability, high specific surface area, shape-selectivity, and tunable physicochemical properties. The optimization of these features has established zeolitic catalysts as sustainable and efficient alternatives to carry out numerous industrial and environmentally relevant processes.

This doctoral dissertation explores a range of direct and post-synthetic methodologies aimed at tailoring the properties of zeolites (from the microscopic to the molecular and atomic scale), thereby enabling the rational design of zeolitic materials with controlled physicochemical and textural attributes. These modifications have a direct impact on the spatial distribution of active sites, the control of crystal size, and the overall catalytic performance in reactions of interest.

The first part of this study (**Chapter 4**) pursued the synthesis of medium-pore MFI-type zeolites incorporating platinum active centres with enhanced stability and resistance to catalyst deactivation through metal sintering. To achieve this, alkali cations were introduced into the synthesis medium to promote metal species dispersion, along with a secondary metal that allows forming bimetallic alloys with superior catalytic properties. The resulting materials, synthesised with optimised atomic ratios of metal species, alkali cations, and alloying agents, demonstrated excellent performance and stability in the non-oxidative dehydrogenation of propane, a reaction of

significant industrial relevance carried out under harsh thermal conditions and redox atmosphere.

The second part of this thesis (**Chapter 5**) encompasses (i) the synthesis of MFI-type zeolites with tailored diffusive properties through crystal size control, incorporating Pt nanoparticles via direct encapsulation to enhance catalytic performance in reactions involving bulky substrates like phenylacetylene, and (ii) the development of homogeneous hydrophobic crystalline coatings with MFI structure using an innovative ultrafast hydrothermal synthesis technique. This strategy aims to improve the retention and stabilisation of active metal centres against leaching and sintering processes.

The final section (**Chapter 6**) proposes a combined approach that integrates synthesis gel composition tuning, active site incorporation methodology, and particle size control to prepare medium-pore (MFI-type) and large-pore (BEA-type) zeolites possessing Brønsted acid sites and nickel active centres. These multifunctional catalysts exhibited high efficiency in the ethylene oligomerisation reaction, a process of major industrial significance. Through the use of tailored organic structure-directing agents and precise control over Ni incorporation pathways, both the final crystal size and the chemical state of the active centres were optimised, effectively modulating the catalytic behaviour of the materials.

Table of Contents

CHAPTER 1:
INTRODUCTION

1.1. FROM GREEN CHEMISTRY TO SUSTAINABLE CHEMISTRY

Chemistry has been an integral part of human progress and development since its earliest days. From the creation of cave pigments in prehistoric times or the first alcoholic fermentations of hops in Mesopotamia to produce beer, to the materials employed in construction, transportation, and textiles used nowadays[1]. Chemistry is linked to every aspect of human activity, and human activity leaves an imprint on the environment.

By the 19th century, concerns regarding environmental pollution began to emerge as a consequence of the rapid expansion of industrial activities, particularly those involving the transformation of raw materials into commodities and energy. The environmental impact of these processes became increasingly evident, with scientists such as the Swedish chemist Svante Arrhenius identifying a rise in global temperatures due to the accumulation of carbon dioxide ("carbonic acid" in accordance with the convention at that time) in the atmosphere, phenomenon currently recognized as global warming[2].

This problem has become the result of decades of pollutant emissions into the environment from human activities, particularly during the two industrial revolutions, which led to an exponential increase in harmful emissions, being gas pollutants the most extended contaminants.

Residual products of industry, transportation, and various daily activities involving chemical transformations are considered as major pollutants. The last decades of 20th century underwent a significant growth in atmospheric gas emissions due to the increasing energy demands of global economic

sectors, as seen in **Figure 1.1**, where the main focus continues being fossil fuels employed in industrial activities. This escalation led to the identification of climate change, an undesired phenomenon progressively raising the planet's temperature, altering climatology, and putting at risk entire ecosystems. Nowadays, climate change stands as the most critical environmental challenge[3].

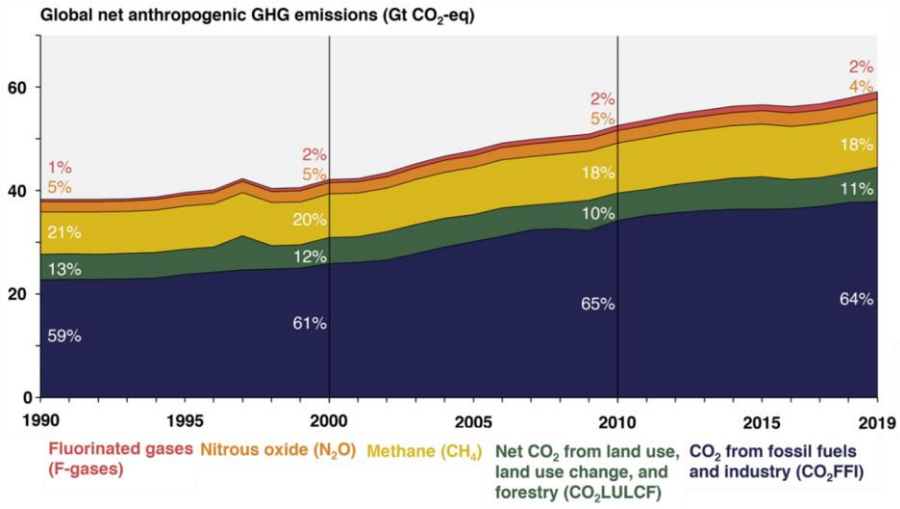

Figure 1.1. Global greenhouse gas emissions expressed as gigatonnes of CO_2 equivalent between 1990 and 2020. Data obtained from the US Environmental Protection Agency[4].

In this respect, numerous industrial sectors have neglected the environmental consequences of their activities and products for decades. However, growing environmental awareness and the enforcement of environmental regulations imposed by most governments to the companies forced the development of alternative production methods maintaining the synthesis of chemical products while minimizing their environmental impact and waste generation.

Consequently, the chemical industry is often perceived as a major contributor to environmental pollution and a serious big hazard, despite its crucial role in improving quality of life through advancements in food and water treatment, pharmaceutical development, and the creation of innovative materials used across almost all industries[5-8]. In light to these concerns, interdisciplinary collaboration between chemistry and fields such as biology, ecology, toxicology, risk management, and economics has led to the emergence of a new way of thinking known as ***Green Chemistry***.

According to the International Union of Pure and Applied Chemistry (IUPAC), Green Chemistry is defined as "the way of thinking applied to chemistry that aims to design chemical processes and products that eliminate the use or generation of substances harmful to humans, the environment and the rest of the biosphere"[9,10]. Green Chemistry relied on 12 principles (see **Figure 1.2**) that outline specific guidelines for producing and utilizing chemical products in an environmentally sustainable manner, minimizing pollution and optimizing the use of raw materials.

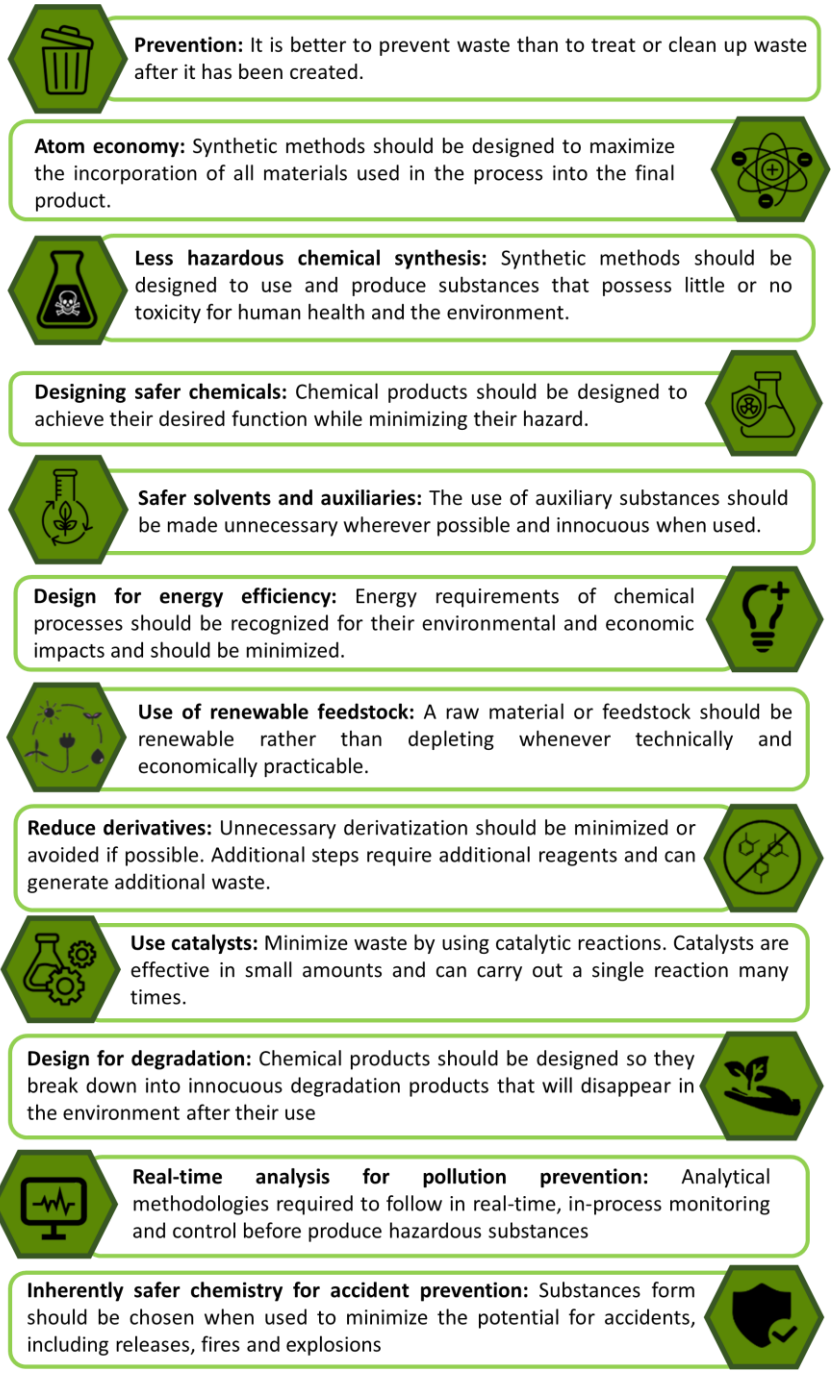

Figure 1.2. Scheme of the 12 principles of green chemistry published by Anastas P *et al*[11].

Although these principles establish clear guidelines to enhance process efficiency, ensuring safety, and minimizing environmental impact, they are inherently aligned with a linear economy model (take-make-use-dispose)[12]. As a result, they are insufficient on their own to achieve a truly sustainable, long-term framework capable of integrating multiple principles simultaneously. For instance, a product may be biodegradable yet derived from non-renewable sources, or, conversely, it may be produced from renewable materials but require excessive energy consumption or generate numerous by-products that necessitate additional treatment, thereby increasing its overall environmental footprint.

Within this framework, ensuring long-term sustainability should be both the objective and the guiding principle, leading to the emergence of the concept of ***Sustainable Chemistry***. This term, introduced by the Organization for Economic Co-operation and Development (OECD) in the 1990s, is defined as "a scientific concept that seeks to improve the efficiency with which natural resources are used to meet human needs for chemical products and services"[13]. Sustainable Chemistry focuses on the design and how to produce and use chemical products and processes in an efficient, safe, and environmentally responsible way. It aims to maximize resource efficiency by conserving energy and non-renewable resources while minimizing hazardous risks and pollution and also reducing waste throughout a product's life cycle efficient design. Additionally, it drives innovation across all sectors, fostering the development of new chemicals, production methods, and product stewardship practices that enhance performance and value while ensuring the protection of human health and the environment. Sustainable Chemistry implies Green Chemistry, but a Green Chemistry process may not be

sustainable[14]. The continuous improvement philosophy, combined with the comprehensive integration of key Green Chemistry principles alongside technical, economic, and social considerations, is essential for achieving a sustainable transition (see **Figure 1.3**).

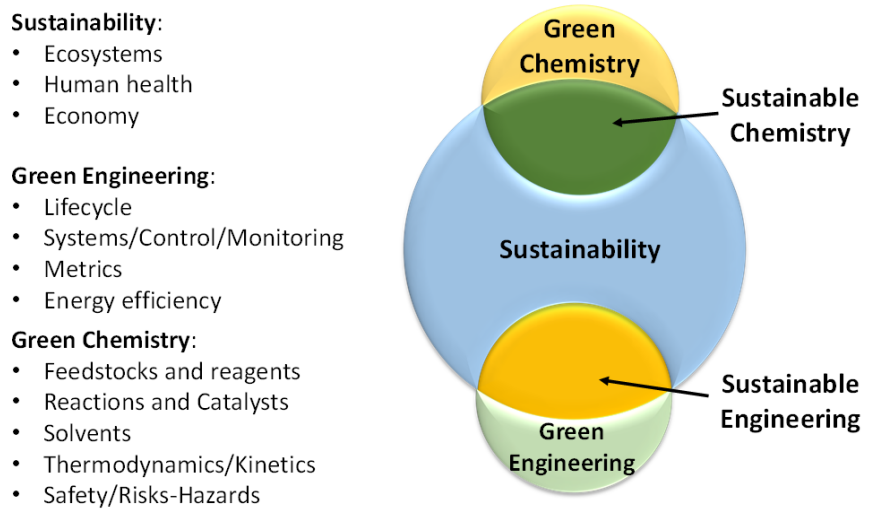

Figure 1.3. Scope of Sustainability, Green Engineering and Green Chemistry, Sustainable Engineering and Chemistry arise from expanding the objectives of Green Chemistry and Engineering to incorporate additional factors beyond technical considerations. Adapted from Martel-Parrish *et al*[15].

1.2. HETEROGENOUS CATALYSIS

Among the various strategies outlined in the 12 principles of Green Chemistry, the use of catalysts has been particularly impactful in steering chemical processes toward greater sustainability. Catalysts offer several advantages, including: (**i**) lowering activation energy, thereby reducing the overall energy input required for the reaction, (**ii**) eliminating the need for stoichiometric amounts of reagents, and (**iii**) enhancing selectivity, which

minimizes the formation of undesired by-products and consequently reduces the need for additional separation steps that consume solvents and energy[16].

Homogeneous catalysts, which are in the same physical phase as the reagents, are widely employed in the pharmaceutical and agro-food industries, as well as in certain fine chemical processes[17], because they offer complete theoretical accessibility to active sites and exhibit outstanding performance in terms of chemoselectivity, regioselectivity, and enantioselectivity[18]. However, being in the same physical state as the reactant medium implies additional operations required to separate the catalyst from the medium, increasing the need for auxiliary substances and energy to apply these unitary operations. In terms of developing more sustainable chemical processes, chemical industries (*i.e.* polymer production, biorefineries, petrochemical…) are focusing on the use of *heterogeneous catalysts*, which are in the different physical phase (generally in solid state) than the reagents. Indeed, the possibility of separating the catalyst from the final products for its recyclability makes heterogenous catalysis more cost-competitive and environmentally attractive.

Nowadays, heterogeneous catalysis is responsible for approximately 80% of industrial chemical transformations, consuming almost 25% of the electric power destined to industries[19,20]. Consequently, enhancement in catalyst efficiency leads to substantial reductions in energy demand. Heterogeneous catalysis operates through surface reactions, where the reactant species undergo adsorption onto the catalyst's active surface as the initial step of the chemical reaction. **Table 1.1** provides a summary of the most prominent industrial processes that utilize heterogeneous catalysts, highlighting those with the highest production volumes.

Table 1.1. Most common industrial processes employing heterogenous catalyst. References obtained from G. Palmissano *et al*[20].

Process	*Catalyst*	*Reactants*	*Target Products*
Ammonia synthesis	Fe_3O_4	N_2, H_2	NH_3
Nitric Acid production	Pt or Ru	NH_3, O_2	HNO_3
Sulfuric Acid production	V_2O_5	S, O_2, H_2O	H_2SO_4
Methanol production	Cu-based, ZnO/Cr_2O_3	CO, H_2	CH_3OH
Olefin hydrogenation	Ni	Alkenes	Alkanes
Olefin metathesis	Re, Mo, Re_2O_7, WO_3	Alkenes	Alkenes with a different structure
Catalytic Cracking	Zeolite Y	High-molecular weight hydrocarbons from petroleum crude oils	Aromatics, shorter chain linear/branched alkane and alkenes
Catalytic steam reforming	Ni supported on Al_2O_3 - MgO	CH_4, H_2O	CO, H_2
Catalytic reforming	Pt and/or Re on Al_2O_3	Naphtha's distilled from crude oil	High-octane liquid products
Ethylene oxide production	Ag on Al_2O_3	C_2H_2, O_2	C_2H_4O
Fischer-Tropsch	Fe, Co or Ru	CO, H_2	Mixture Gasoline/Diesel-range molecules
α-Olefins polymerization	Ziegler-Natta catalyst	α-Olefins	Polymers of α-Olefins
Hydrodesulfuration/ Hydrodenitrogenation	Co/MoS_2 or Ni/WS_2	Crude oil or products of cracking	Crude oil/ products of cracking free of sulfur-/nitrogen-containing components

As presented in **Table 1.1**, heterogeneous catalysts can exhibit different chemical structures, each of them is suitable for a different type of chemical reaction and presents specific advantages and/or limitations that determine their suitability for a given application.

In this context, the concept of shape selectivity gained significant prominence from the 1960s, particularly in the petrochemical industry and petroleum refining processes for the production of refined fuels[21]. The shape-selectivity property is characteristic of crystalline microporous materials, where the specific spatial arrangement of atoms in the framework creates molecular-scale channels. These channels allow the diffusion of chemical species only if they satisfy certain steric constraints. Depending on the stage at which this size-controlled selectivity occurs, it can be classified as **(i)** reactant selectivity (where molecules are excluded to enter the channel system by size), **(ii)** product selectivity (where transformed molecules can exit by size), or **(iii)** reaction intermediate selectivity (where the reaction is guided by the available space for intermediate species to be formed)[22]. Among the crystalline materials that can be used as potential heterogenous catalysts, **zeolites** stand out due to their excellent properties and high thermal stability. Their application in industrial chemical processes has gained significant prominence in recent decades.

1.3. ZEOLITES: A MORE SUSTAINABLE HETEROGENOUS CATALYST

Zeolites have become the most employed crystalline inorganic microporous-type materials nowadays. Their structures are formed by a tridimensional framework of TO_4 tetrahedron (with T= Si, Al, P, Ge, B, Ga, among other species), interconnected by the oxygen atoms, which form a system of channels and cavities of molecular dimensions. Unlike other dense phases, which also belong to the tectosilicate family group like quartz (22 T atoms/1000 $Å^3$), zeolites have lower framework density (usually bellow 19 T atoms/1000 $Å^3$), implying the formation of larger micropores volumes.

From the structural point of view, zeolites can be defined as silicates in which some Si atoms have been substituted by Al atoms, resulting in a net negative charge excess. To achieve a good balance of the electrostatic forces (in pure silica zeolites the net charge is neutral), cationic species can be hosted in cavities and/or channels of the zeolitic framework, preferentially in extra-framework positions.

The cationic species can be organic or inorganic, and they can be exchanged by other more convenient cationic species, provided by the fact that zeolites have the capability of exchange ionic species with the surrounding environment or, if those cations present catalytic activity, they will give catalytic properties to the material. In addition, high Si/Al ratio zeolites can stabilize the framework net charge with protons after removing the organic cationic species by thermal treatment.

The empiric formula of a zeolite can be described as:

$$M_{x/n}^{n+} Al_x Si_{1-x} O_2 \cdot z\ H_2O$$

Where z represents those water molecules (neutral charge) hosted in the zeolitic system. M^{n+} refers to the cationic specie, organic or inorganic (alkaline or alkaline-earth cations are generally used) and is responsible for providing the positive charges to counterbalance the negative charges introduced by the aluminium atoms.

The tridimensional structure presents some electrostatic limitations between adjacent atoms, so limiting the presence of consecutive negative charged tetrahedra. This phenomenon was described by Lowenstein[23] and stablishes the chemical imposition of, at least, one Si tetrahedra for each Al tetrahedra (Si/Al $\in$ 1 - ∞) to avoid very strong electrostatic rejection between the negative charged tetrahedral atoms.

Nowadays, the Structure Commission of the International Zeolite Association (IZA) has accepted 256 different zeolitic structures. The possibility to incorporate different type of heteroatoms (Al, B, Ga, Ge, Ti, Sn, Zr) provides different linking angles to the tetrahedral units (primary building units), all ranging between 127^o and 180^o. The primary building units assemble with different linking angles from different intermediate units, named secondary building units (SBU)[24], finally resulting in more complex units, named composite unit buildings (CBU). The continuous adhesion of the SBUs results in the final zeolite structure conformation[25] (see **Figure 1.4**). Although many of the structures have at least one common SBU, the combination of SBUs and CBUs assemblies defines each type of crystalline framework, presenting then specific channel system and pore distribution. The versatility of

crystalline structures plays a key role to modulate the diffusion of the molecules and to selectively filter them by size, acting as molecular sieves and becoming as relevant and interesting materials for the industry.

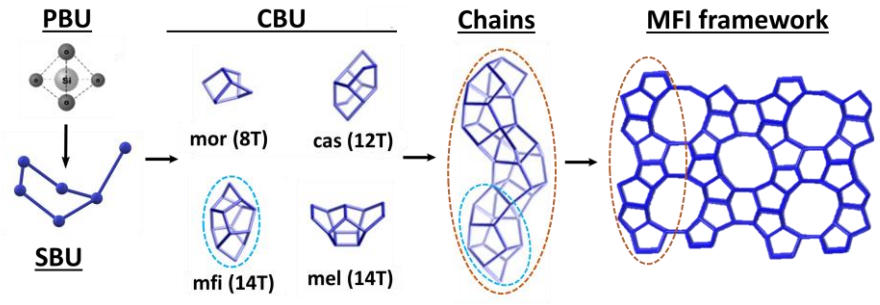

Figure 1.4. Construction of MFI zeolite from simple building units into the final zeolite framework. Extracted from IZA Database[26].

The most widely used criteria to classify zeolites are by **(i)** the pore size, **(ii)** the dimensionality (channel spatial arrangement) or **(iii)** the type of channel system.

The **pore diameter** is one of the most relevant properties studied in the zeolitic materials, which will determine their behaviour as molecular sieve by discriminating the molecules entering inside the channel system according to their size and shape. The definition of pore ring refers to those TO_4 tetrahedrons surrounding the free diameter of the zeolite channel.

Regarding the pore size, zeolites can be classified as small pore, medium pore, large pore or extra-large pore zeolites (see **Figure 1.5**).

- Small pore zeolites: zeolites with a pore size between 3.5Å-4Å and 8 TO_4 units per ring. Some examples are the zeolite A (LTA)[27], ABW[28] and chabazite (CHA)[29]

- Medium pore zeolites: zeolites possessing between 9-11 TO_4 units per ring, and pore diameter between 5-5.5Å. Some examples are ZSM-5 (MFI)[30] and ZSM-11 (MEL)[31].
- Large pore zeolites: zeolites possessing 12 TO_4 units per ring, and pore diameter between 6.5 Å -7 Å. Some examples are BEA[32] and ISV[34].
- Extra-large pore zeolites: zeolites possessing more than 12 TO_4 units per ring, and pore diameters above 7 Å. Some examples of extra-large pore zeolites are UTD-1 (DON)[34], CIT-5 (CFI)[35] and EMM-23 (EWT)[36] zeolites.

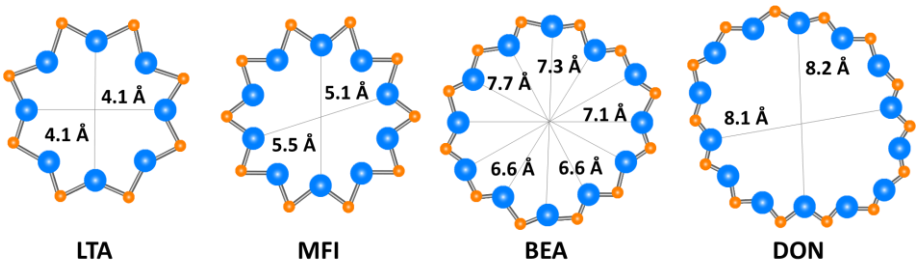

Figure 1.5. Pore diameters of zeolite A (LTA, small pore), ZSM-5 (MFI, medium pore), Beta (BEA, large pore) and UTD-1 (DON, extra-large pore).

Another commonly extended criterion to classify the different zeolites is according to the **spatial arrangement** (see **Figure 1.6**) of their porous system[37]. Regarding this criterion, the zeolites can be classified as:

- Monodirectional zeolites: zeolites presenting only one channel system. Examples of zeolites belonging to this family are EU-1 (EUO)[38] and ZSM-12 (MTW)[39]

- Bidirectional zeolites: zeolites containing two different channel system. An example of zeolites that belong to this group is mordenite (MOR)[40]
- Tridirectional zeolites: zeolites presenting channel systems in the three-dimensional directions. Different examples of zeolites commonly employed that belong to this group are faujasite (FAU)[41] or beta (BEA)[42]

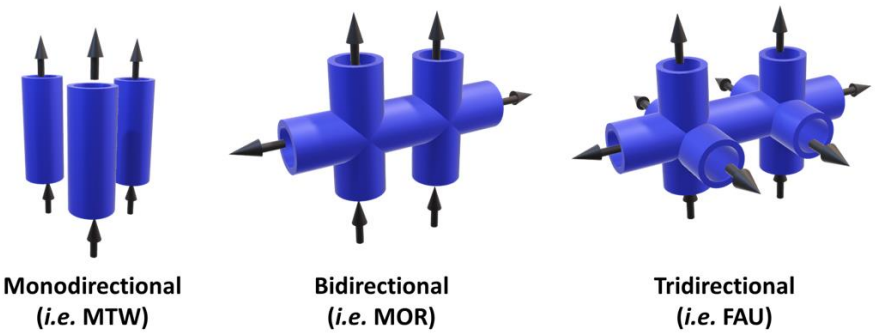

Figure 1.6. Zeolite classification according to spatial arrangement of the porous systems.

It is worth highlighting that the channel systems in the zeolites can be independent (non-connected) among them (MWW)[43], totally interconnected among them (BEC)[44] or the channel system can be linked by cavities (such as LTA or AFX)[45,46].

1.3.1. Zeolite properties

The physicochemical properties of zeolites are intrinsically given by their chemical composition and crystalline structure. Below is an overview of the key properties that facilitate their use for a wide range of applications.

- **Acid-base properties.** In the zeolitic framework, the isomorphic substitution of trivalent atoms in lattice positions originally occupied by silicon atoms results in an excess of negative charge. To maintain the electrostatic charge balance, extra-framework cations are required as charge-counterbalance species. These cations can be easily exchanged by ammonium (NH_4^+) ions, resulting in ammonium zeolites. Upon undergoing thermal treatments, the ammonium ions decompose, leaving behind protons in the extra-framework sites, and giving Brønsted acidity to the zeolite[47]. Indeed, high-silica zeolites can be stabilized in the synthesis processes without any additional counter-balance inorganic cations, and the zeolite in its protonic form (acid form) can be obtained directly in the post-synthetic calcination of the residual organic matter after synthesis. The acid strength is determined by the chemical environment surrounding the trivalent atoms to which they are attached, as well as by the nature of the substituent species. In general, acidity increases with a higher degree of silicon atom substitution within the zeolitic framework[48]. Another form of acidity can be Lewis acidity, which may arise from: **(i)** the presence of aluminium oxyhydroxide species in extra-framework positions on the zeolite surface, typically resulting from the dealumination process induced by thermal or acid treatment; or **(ii)** the incorporation of heteroatoms with void electronic d orbitals into the zeolitic framework, becoming them electron acceptors (*i.e.*, Ti, Sn, Zn, Zr, Mo). Additionally, zeolites can also exhibit Lewis basicity, which can be classified into two types: global Lewis basicity, which considers the overall structure of the zeolite (including exchangeable cations), and local Lewis basicity,

which focuses on the oxygen atoms in the framework. **Figure 1.7** illustrates the spatial distribution of Brønsted acid sites (BAS) and Lewis acid sites (LAS)[49,50].

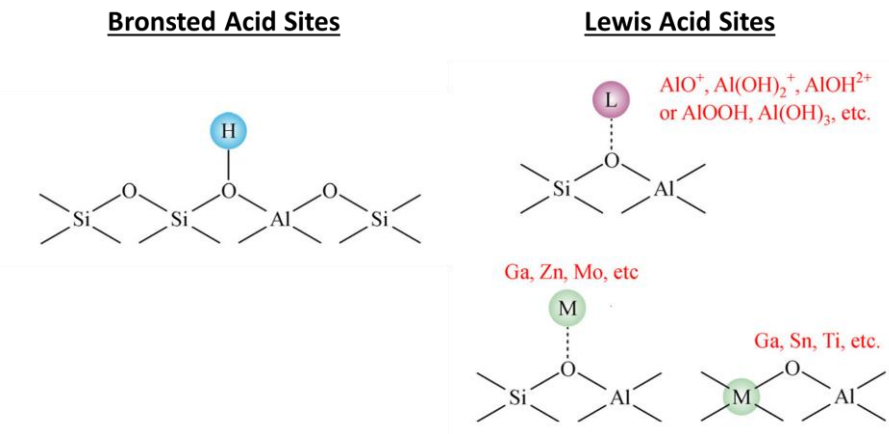

Figure 1.7. Brønsted acid sites (BAS) and Lewis acid sites (LAS) on zeolites. Scheme obtained from Deng *et al*[51].

- **Cation exchange capacity.** This property is directly associated with the presence of charge-counterbalance cations located in the zeolite framework. The high mobility of these cations facilitates their substitution by others of similar nature, with the exchange capacity increasing proportionally to the negative charge that must be neutralized within the structure. Consequently, zeolites with a high aluminium content (low Si/Al ratio) exhibit a greater cation exchange capacity, as they contain a higher number of compensating cations compared to zeolites with a higher Si/Al ratio[52].
- **Adsorption capacity.** The primary advantage of zeolites lies in their selectivity over size and shape, attributed to the controlled dimensions of their cavities and channels. This characteristic enables selective adsorption of molecules smaller than the pore size while

excluding larger species. Additionally, the channel network provides a substantial accessible surface area for adsorbate molecules, resulting in materials with a higher specific surface area than most heterogeneous catalysts. This surface area can be further enhanced through mesoporosity generation, either during synthesis or via post-synthetic modifications. The adsorption capacity of zeolites is also influenced by their chemical composition, atomic distribution, and specific crystalline structure, as well as by their hydrophilic or hydrophobic nature and affinity for target species. Notably, an increase in the Si/Al ratio enhances the hydrophobicity of the zeolite, which also increases when lowering the defects density within the zeolite framework[53].

- **Metal hosting capacity:** Zeolites possess the capability to stabilize metal species within their porous framework, serving as a confinement medium that enhances resistance to metal sintering and extends catalytic durability and reusability in redox reactions. These metal species can be incorporated as counter-balance cations occupying exchangeable positions, induced by isomorphic substitution[54] done by post-synthetic treatments, or as nanoparticles of varying sizes hosted within the porous network. When introduced during direct synthesis, the zeolite framework crystallizes around these metal species, effectively encapsulating them within the structure[55].

1.3.2. Zeolite synthesis, main mechanism and synthesis parameters

The common procedure to obtain zeolites is the hydrothermal synthesis[56]. In this synthesis procedure, different element precursors (usually in aqueous solution) are provided to the synthesis gel until reaching a suitable pH (generally needs to be highly alkaline) that can dissolve the Si species and maintain the other species in the desired phase. Right after obtaining a homogeneous media, the temperatures are risen usually between 100-200^{o}C, temperatures at which the water present in the synthesis media boils, providing enough autogenous pressure to favour the crystallization process.

The common synthesis gel contains an aqueous mixture of Si and Al precursors (or other desired heteroatom precursors) that must be incorporated into the final crystalline structure, with alkaline inorganic species and/or cationic organic species that can provide at the same time the positive counterbalance charges and the required alkaline pH.

The measurable crystallization process of a zeolite under isothermal conditions follows a sigmoidal pattern-type evolution of crystallinity increase over time, as illustrated in **Figure 1.8**. Initially, an induction period occurs, during which the nuclei of the zeolite's crystalline phase begin to form (nucleation step).

This is followed by a phase of crystal growth (crystal growth step) where the degree of crystallinity increases exponentially. At longer times, a decline in the crystallization rate is observed due to the depletion of remanent soluble species necessary for further crystal growth, thereby limiting the resulting rate of crystallinity increase of the solid.

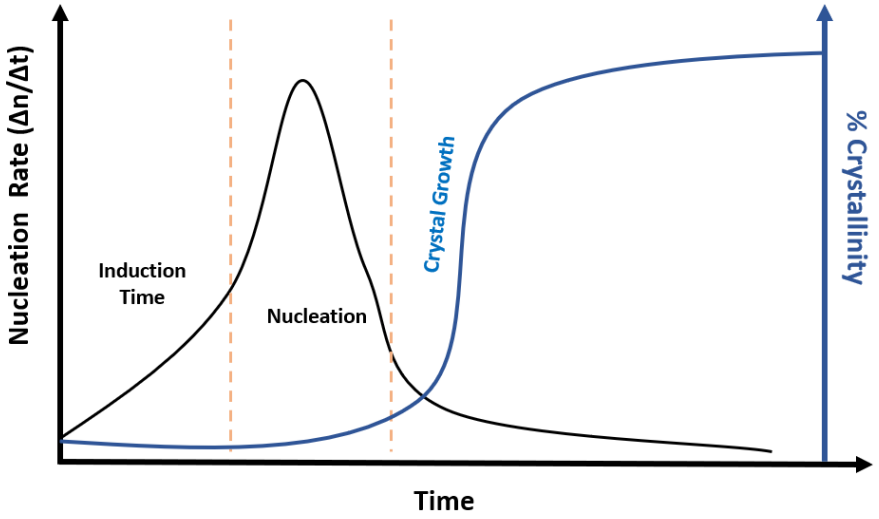

Figure 1.8. Crystallization curve of a zeolite under isothermal conditions expressed as % crystallinity of the final solid powder (blue) and nuclei formation rate (black). Model extracted and adapted from Cundy *et al*[56].

- Nucleation step:

Despite the measurable progression of zeolite crystallinity, as illustrated in **Figure 1.8**, the elucidation of the mechanisms underlying zeolite nucleation remains one of the most challenging topics nowadays in the field of zeolite synthesis, highlighting their complexity.

Classical Nucleation Theory (CNT) describes the formation of solid nuclei from a liquid or gaseous phase containing dissolved monomeric precursor species once a critical Gibbs free energy threshold is surpassed[57,58]. At this point, nucleation occurs, leading to the formation of a new phase with a lower, thermodynamically more favourable, free energy[59].

However, the limitations of the classical model resulted in the development of alternative nucleation models, collectively known as non-classical nucleation theories, which suggest that nucleus formation involves phases that are denser and more ordered than simple monomers. Among these mechanisms, two-stage nucleation crystallization (TSN, comprising an initial formation phase followed by nucleation)[60], the presence of pre-crystallized nuclei (PCN)[61], spinodal decomposition (SD, where two coexisting phases are enriched in specific chemical species while being depleted in others, where diffusion limitation is the barrier to form new phases the diffusion limitations)[62], and arrested spinodal decomposition (where a kinetically stable sol-gel precursor undergoes prior to phase separation through spinodal decomposition)[63] are proposed.

Although non-classical models offer a more precise representation by considering factors such as species diffusion and growth on pre-formed ordered nuclei, they still fail to accurately encompass the complexity of all the sub-processes involved in the nucleation mechanism pathway.

This limitation has led to the development of more current models, which claim that nucleation is the combination of multiple interrelated chemical equilibrium processes occurring simultaneously, as illustrated in **Figure 1.9.**

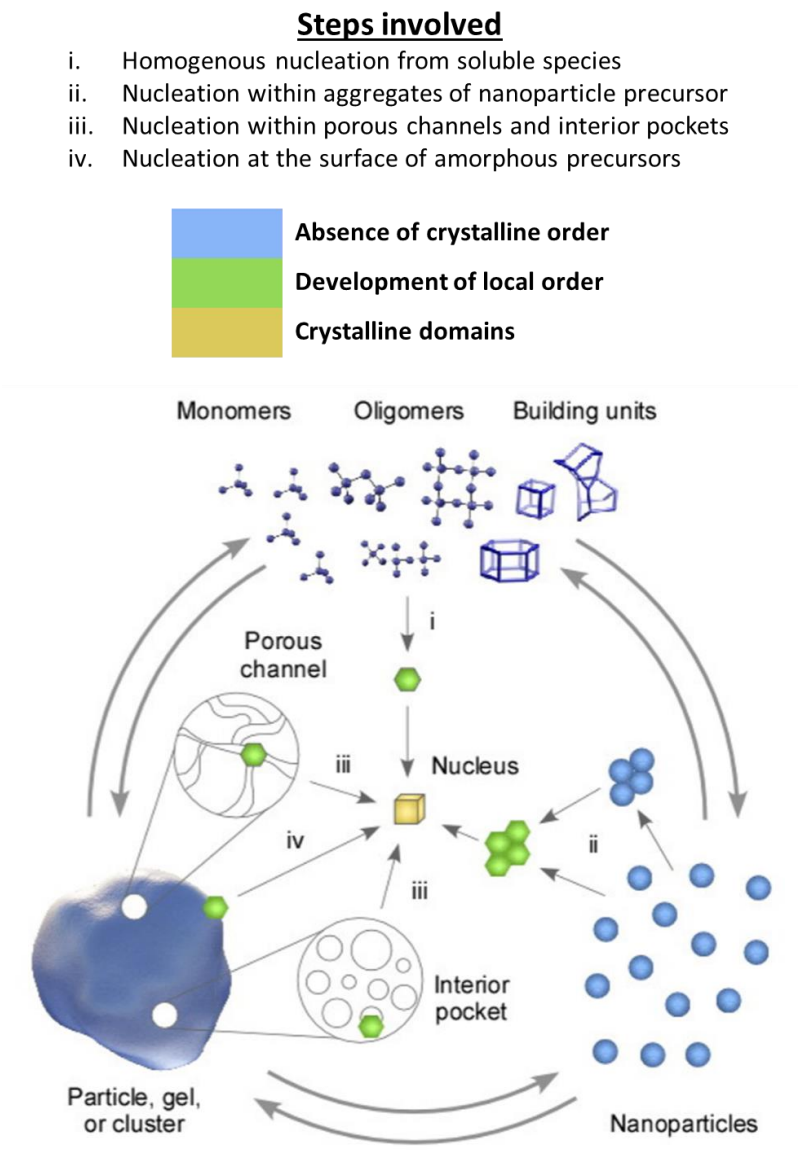

Figure 1.9. Hypothetical pathways of zeolite nucleation. Mechanisms can involve the assembly or evolution of diverse soluble species (monomers, oligomers, and building units) and amorphous precursors (particles, gels, clusters, and nanoparticles). Scheme obtained and adapted from Rimer *et al*[64].

- Crystal Growth step:

As mentioned above, crystal growth is the second stage conventionally attributed to the zeolite crystallization process. According to classical crystal growth theory, this process occurs through the addition of monomeric precursor species onto the surface of crystals already formed[59]. This incorporation takes place either directly from the dissolution medium or via surface molecular diffusion mechanisms[64,65]. However, as with nucleation mechanism models, the classical models also totally disregarded parallel crystallisation processes and did not take into account either the different nature of the precursor species or the sol-gel zones supersaturated by the presence of the different components involved in the synthesis gel. Thus, new models have been developed to take into account this added complexity.

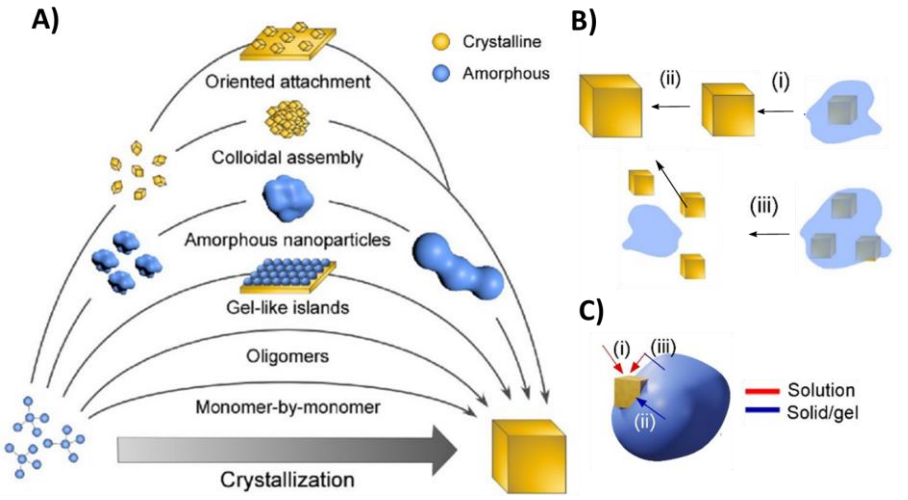

Figure 1.10. A) Schematic representation of various zeolite crystal growth pathways reported in the literature, classified as particle-attachment crystallization (PAC) mechanisms[66-68]. **B)** A model representing the transformation of amorphous particles into zeolite crystals through the transformation from a gel phase (i) and solution phase (ii)[69,70] to a crystal, and (iii) the autocatalytic release of nuclei from amorphous precursors[71]. **C)** Potential crystallization pathways of zeolite crystals in the amorphous precursor medium, where species incorporation can occur through (i) the dissolution medium (red), (ii) solid particle modifications (blue), or (iii) local dissolution and reprecipitation mechanisms[72]. The diagram was adapted from Rimer *et al*[64].

There are numerous factors that can directly influence the formation of the final crystalline structure and tailor the physicochemical properties of the resulting zeolitic material. Those parameters are discussed below.

Structure-Directing Agent (SDA): These are species that influence the type and composition of the obtained zeolite crystalline structures[73]. Through electrostatic interactions, the SDA can balance the electronegative charge of the zeolitic lattice, allowing the bonding of the silicates and aluminates during synthesis, and thereby guiding the crystallization process to the formation of

a given structure[74]. SDAs can be either inorganic, such as alkali and alkaline earth metal cations, allowing to obtain low Si/Al ratio zeolites (between 1-5)[75], or organic (OSDAs), primarily comprising amines or quaternary ammonium salts. Additionally, other organic species, including phosphazenes[76], tetraalkylphosphoniums[77-79], crown ethers[80-82], and coordination complexes[83], are also employed for this purpose. The introduction of OSDAs significantly advanced zeolite synthesis by enabling the synthesis of higher Si/Al ratio materials[84]. This advancement facilitated the production of high silica content and pure silica zeolites with diverse topologies, exhibiting superior hydrothermal stability compared to their aluminium-rich counterparts and avoiding the generation of impurity phases that are prone to take place in inorganic SDA guided synthesis[85]. Unlike inorganic ions, the atomic mobility within OSDAs imparts flexibility to these molecules, enabling them to adopt multiple spatial conformations, which in turn facilitates the formation of a diverse range of zeolitic structures[86].

Organic molecules used in zeolite synthesis can be classified according to different criteria, being their role in the crystallization process the most employed one. Based on this classification, they can be categorized as: **(i)** pore-filling agents, which stabilize the thermodynamics of crystallization by occupying the pores without directing the formation of a specific structure[87-89], **(ii)** structure-directing agents that influence crystallization by promoting organic-inorganic interactions through Van der Waals and Coulombic forces, thereby favouring thermodynamic stability towards some phase selectivity[90-92], and **(iii)** templating agents, where a direct structural correlation exists between the OSDAs size and spatial configuration and the resulting zeolite pore structure[93].

Although the introduction of OSDAs facilitated the synthesis of novel zeolitic structures with potential applications in industry, these molecules possess noticeable drawbacks, as toxicity and, in some cases, flammability. Additionally, OSDAs with complex molecular structures are costly to produce, often requiring additional synthesis, purification, and concentration steps, thereby increasing both their environmental impact and energy consumption. Furthermore, their removal from porous channel system typically requires high-temperature combustion, leading to the emission of greenhouse gases such as CO_2 and NO_x. To mitigate these issues, alternative approaches are being explored, such as:

- Employing low-toxicity templates like polyquaternium-6, a common shampoo ingredient, which facilitate the synthesis of EMT-rich faujasites[94], or guanidine derived molecules to produce ALPO-5 (AFI type aluminophosphate)[95].
- Employing low-cost template approaches, where a minor amount of the OSDA is used to guide the nucleation product and a larger amount of less selective molecule is added as pore filler while the crystal continues growing, presenting several cost-saving benefits. Some structures obtained by this strategy are SSZ-13 (CHA type)[96], SSZ-33 (CON type) or SSZ-35 (STF type)[97]. A newer alternative based on this approach is charge density mismatch (CMD) that combines alkaline or alkaline earth cations to cooperate with OSDAs[98].
- Employing recyclable OSDAs, based on strategies focused on OSDA recovery through various extraction techniques[99,100]. This approach relies on designing OSDAs composed of at least two components that, through covalent or non-covalent interactions, can withstand

the extreme conditions of hydrothermal synthesis while remaining intact and can be selectively reversed after zeolite crystallization, enabling OSDA recovery and reuse[100].

New trends of hydrothermal syntheses are based on avoiding the use of OSDAs, relying instead on rational design approaches that involve precise adjustments of the molar ratios in synthesis gels, the introduction of nuclei to seed the final phase in solution, or the direct addition of zeolite crystals. This methodology has been proven effective in synthesizing some of the most widely used zeolites, including ZSM-5[101,102], BEA[103-105], FER[106], and ECR-1[107,108] due to the selective effect provided by the seeds that ensures the crystallization towards a specific crystalline phase. Other newer trends rely on the use of bio-templates, such as, (**i**) the one reported by Valchev *et al*[109], where MFI type membranes with micropores and macropores were successfully developed by using eggshells as template molecule. For this purpose, the eggshell fibres are rearranged in the synthesis medium to form an interwoven network, giving rise to the scaffold that produces the macroporosity. Subsequently, crystallization occurs using seeding nuclei that adhere to the external surface of the fibres, where they crystallize, and after removing the remaining eggshell by thermal degradation, a micro-macroporous MFI zeolite lattice is obtained (see **Figure 1.11**). (**ii**) Another examples of biotemplate-assisted zeolite synthesis is the use of natural polymers such as chitosan or low-lignin cellulose fibres to give LTA and FAU zeolites[110-113].

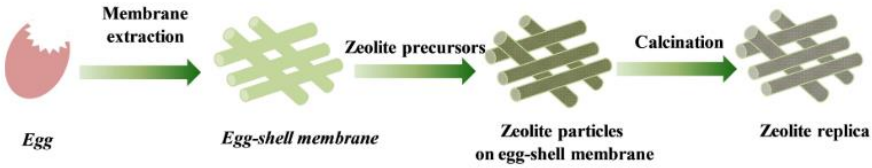

Figure 1.11. Egg-shell directed synthesis of micro-macroporous MFI type membrane. Obtained from Srivasta *et al*[114].

Framework atom precursors: A diverse range of inorganic and organic sources are employed in zeolite synthesis, each varying in chemical state and initial polymerization degree. These differences influence their reactivity, making them necessary to develop a carefully designed selection of the most suitable sources to achieve the targeted structure with tailored properties[56]. Among the most frequently utilized Si precursors, different allotropic variations are used, such as silicon alkoxides (*i.e.* tetramethylorthosilicate, TMOS or tetraethylortosilicate, TEOS), silicon halides ($SiCl_4$), as well as colloidal silica (LUDOX®) and amorphous fumed silica (Aerosil®). The incorporation of other heteroatoms into the zeolite framework is achieved by introducing precursors of these heteroatoms into the synthesis gel. These precursors can vary in nature and include other metal alkoxides (*i.e.,* $Ti(C_2H_5O)_4$), inorganic acids and salts (*i.e.*, HBO_3, H_3PO_4, $CuSO_4$), halides (*i.e.*, $SnCl_4$), or oxides (*i.e.*, $Al(OH)_3$). If the intended incorporation involves metallic species to be encapsulated within the zeolite matrix, the metallic precursor is typically combined with a complexing agent (most commonly nitrogen-containing molecules such as ethylenediamine or tetraethylenepentamine)[115]. This prevents the precipitation of the metallic species in the alkaline environment of the synthesis gel. During the crystallization process, the zeolite framework forms around the organometallic complex molecules. Upon subsequent calcination, the

organic matter is removed, leaving the metallic species uniformly dispersed within the zeolite structure, where they remain confined and stabilized within the pores and/or cavities[116].

An alternative approach to provide the inorganic species required for the formation of the targeted zeolite framework involves utilizing a pre-existing zeolitic structure. Under the highly alkaline conditions of the synthesis gel, the initial zeolite structure dissolves, releasing secondary structural units that are in common with the target zeolite. Simultaneously, tetravalent and trivalent elements are provided from the original zeolite, enabling efficient and selective synthesis pathways for specific zeolitic materials[117-119].

To ensure a uniform distribution of all species within the synthesis gel, they are dissolved in a solvent, typically water in the case of hydrothermal synthesis. However, alternative solvents can also be employed[120], not only to work at different vapor pressure but also to alter polarity, as seen in solvothermal synthesis using organics solvents, such as ethanol (EtOH).

Currently, the need to make zeolite synthesis more sustainable and environmentally friendly has led to the implementation of various strategies focused on optimizing precursor utilization and minimizing solvent usage in the synthesis process. The high cost and, in many cases, the potential hazards associated with these precursors represent significant challenges for the industrial-scale production of zeolites. Common commercial silicon and aluminium precursors (*i.e.*, TEOS, fumed silica, $NaAlO_2$, aluminium silicate mixtures….) are not environmentally sustainable, as their production involves multiple treatment, purification, and concentration steps, which contribute to increase waste generation[114].

This industrial disadvantage has heightened interest in employing natural sources as providers of silicon and/or aluminium, such as sands, earth minerals, clays, ashes, certain plant-based materials, or biological templates. Additionally, there is even more attention growing toward synthesizing zeolites from industrial waste (*i.e.* coal ash, biomass residues, and sugarcane bagasse ash). Among natural sources, laminated silicates (similar chemical structure than zeolites) are particularly abundant in the Earth's crust. Several studies have demonstrated the successful synthesis of 13X and Y zeolites using bentonite as a precursor[121,122].

Similarly, ZSM-5 has been obtained by adding tetrapropylammonium (TPA) to kaolinite feedstock[123], followed by crystallization. However, replacing TPA with NaOH results in the formation of LTA zeolite[124]. Furthermore, the use of dealuminated metakaolin in combination with TPA has enabled the synthesis of ZSM-5 with an increased Si/Al ratio[125]. On the other hand, it has been reported that using natural clay (attapulgite), BEA and MOR type structures, also widely used in the industry, can be synthesised[126].

Another viable source of Si or Al precursors are industrial wastes, which hold significant potential for scaling up zeolite synthesis at an industrial level although nowadays the process must overcome the feedstock limitations. Among these, there are noteworthy examples such as: **(i)** combustion ashes generated in power plants, where the burning of materials for energy production results in a solid residue. The composition of these ashes, rich in Si and Al, makes them suitable precursors for synthesizing zeolites with a medium-to-low Si/Al ratio[127,128], **(ii)** biomass residues such as those obtained from the rice agri-food industry, whose husks have 20% amorphous silica (90% recovered from the ashes if the husks are previously calcined) and have

allowed synthesis processes of MFI, Beta, NaY zeolites[129-133] or the cupola slag obtained from the iron manufacturing industry, which allowed to synthetize high-siliceous MFI zeolites[134].

Mineralizing agent / pH synthesis: A mineralizing agent is a chemical species that is able to increase the solubility of the precursor species involved in the synthesis gel by solvolysis and polycondensation reactions that promote the breaking and reassembly of Si-O-Si bonds during the zeolite crystallization process[135]. These chemical species exhibit nucleophilic properties, being the hydroxide ions (OH^-) and fluoride ions (F^-) the most employed ones. Their presence influences the nature of the final synthesis gel, modulating the basic pH (only OH^- ions) or neutral pH (stoichiometric balance between F^- and OH^-). Traditionally, hydrothermal synthesis relied exclusively on OH^- anions as the mineralizing agent. However, this approach presented several limitations that adversely affected the synthesis process, including the Hofmann degradation of OSDAs at high pH and temperatures[136] and an increased formation of structural defects in high-silica zeolites due to the absence of compensating cations to stabilize the final structure. To overcome these challenges, the combined use of OH^- and F^- anions was introduced, facilitating the incorporation of OSDAs that are unstable under high pH and enhancing the solubility of inorganic precursors through the formation of TF_6^{n-} complexes, where T represents the heteroatoms forming the tetrahedral units of the primary building blocks. Additionally, literature reported the role of F^- in stabilizing small secondary building units, such as double four-membered rings (D4R), enabling the synthesis of zeolites with low or without aluminium content[137,138,139,140]. The incorporation of F^- anions reduce structural defects and results in the formation of larger zeolite crystals

compared to those synthesized under basic pH conditions[141]. This modification enhances the hydrophobic nature of the resulting zeolites, thereby influencing their physicochemical properties[142].

Framework heteroatom directing effect: As previously introduced, silicon atoms within the crystal lattice can be substituted by heteroatoms of different valence (see **Table 1.2**). This substitution can occur through direct synthesis, wherein the heteroatom precursor is introduced into the synthesis gel and incorporated during the crystallization process, or via post-synthetic methods, in which silicon atoms are replaced by new species while preserving the original structure[24].

Analysing the coordination environment within the lattice, the spatial distribution in the crystal structure, and the bond distances provide valuable insights into the resulting physicochemical properties of the synthesized zeolites.

Table 1.2. Examples of heteroatoms employed for the isomorphic Si substitution in zeolites.

Substituent species	***Atom***
Pentavalent	P, V, As
Tetravalent	Ti, Ge, Sn, Zr
Trivalent	Al, B, Ga, Fe, Cr,
Divalent	Zn, Be, Mg

Beyond their impact on the final physicochemical properties, heteroatoms can influence the stability of specific secondary building units due to variations in bond lengths and angles. This effect can guide the crystallization of zeolitic structures containing these units[143] or promote the positioning of other atoms in crystallographic sites that would otherwise be inaccessible in the absence of such heteroatoms[144].

Among the various heteroatoms considered, aluminium is the primary element incorporated into the zeolitic catalysts that have been examined in this doctoral thesis. As a trivalent species, it forms AlO_4^- tetrahedra within the zeolites crystalline framework, introducing a negative charge that can be balanced by protons after calcination procedures, thereby generating Brønsted acid sites. Its distribution within the structure is governed by electrostatic interactions, with cations present in the medium, either organic (OSDAs) or inorganic (alkaline or alkaline earth metals), serving as charge-compensating species. When using an SDA, the AlO_4^- tetrahedra are positioned near the positive charge of the organic cation, and building, such as SiO_4 tetrahedral units, the zeolite cavities walls. Unlike other heteroatoms that exhibit more varied bond lengths and angles compared to the Si-O-Si bond (127-180°), the Al-O-Si bond angle is more similar (125-179°), resulting in a less pronounced structure-directing effect. This allows to obtain a greater variety of zeolitic structures that can host Al atoms in their composition.

Crystallization temperature: The synthesis temperature is a crucial factor in the crystallization process of any crystalline solid, as it directly influences both the kinetics and thermodynamics of the crystallization step, ultimately determining the resulting crystalline phase formed[145]. To achieve the desired crystalline phase, an energy barrier must be surpassed to initialize the crystallization steps[146], so more ordered species can be formed (such as precursor clusters, sol-gel regions, and pre-nucleated species), leading to the formation of the crystalline nuclei[147]. This thermodynamic pathway is also influenced by the reactivity of the initial precursor species. Moreover, both the synthesis temperature and the heating rate of the gel are key parameters

that not only dictate the final stable phase but also significantly impact the morphological characteristics of the resulting microporous solid particles.

Crystallization time: The maintenance of the synthesis gel under the adequate temperature conditions for carrying out the hydrothermal synthesis is another crucial parameter in zeolite formation. Once the required energy barrier to facilitate crystallization thermodynamics has been surpassed, the subsequent processes become kinetically controlled, being generally faster as the temperature is increased[148]. If the residence time is too short, complete crystallization may not be achieved, whereas long periods may lead to the formation of very large crystals or even the appearance of thermodynamically more stable phases (*i.e.*, dense phases)[149]. A more detailed discussion on the combined impact of synthesis temperature and crystallization time on the final morphological properties of crystalline zeolites is presented in **Chapter 5**.

1.4. APPLICATION OF ZEOLITES IN SUSTAINABLE CHEMISTRY PROCESSES.

As it has been already discussed, zeolites can exhibit a large variety of topologies depending on their chemical composition and the synthesis parameters. This structural versatility enables controlling the diffusion of molecules through their porous system of channels and cavities, making them interesting molecular shape-selective materials. Additionally, their chemical composition can be tailored to introduce acidic properties (Brønsted or Lewis) or incorporate metallic species, further enhancing their functional versatility. These attractive features have established zeolites as outstanding materials for advancing numerous industrial applications in a

more sustainable manner. Some of the most significant applications are outlined below.

Cationic exchangers: The remarkable mobility of compensating cations within the zeolitic structure enables their exchange with other cations of similar nature, making zeolites highly effective as cation exchangers in pollutant removal application. This property has been particularly valuable in softening domestic and industrial water by replacing Ca^{2+} and Mg^{2+} ions with softer cations (Na^{+} or K^{+})[150]. Additionally, zeolites have been employed for the removal of heavy metals (*i.e.*, Pb, Cd, Hg, Cr, Zn) from water[151], the sequestration of radioactive species[152], and the elimination of organic contaminants by modifying their surface through anchoring surfactant species[153,154].

Adsorbent: The high surface area of zeolites, along with their ability to discriminate molecules due to their shape, the complexity of their channel and cavity systems, and their polarity, make them highly effective in separation and purification processes for both liquid and gas streams. These materials are particularly efficient in distinguishing molecules based on, **(i)** size and interactions with the zeolitic adsorbent (thermodynamic separation) **(ii)** differences in diffusion rates of the components (kinetic separation) within the fluid stream[155]. Among the processes that enhance the sustainability of zeolites adsorption capacity, the separation of simple gases, which are either by-products of combustion processes (such as CO_2, NO_x, and H_2O)[156] or products from other chemical processes in refineries (including CH_4, H_2, and light paraffins/olefins), can be highlighted. Additionally, the high adsorption capacity of zeolites has been effectively utilized for removing atmospheric pollutants such as CO, NH_3, NO_x, H_2S, and SO_2 [157-160].

Thermal Energy Storage: Thermal energy storage systems based on water adsorption in zeolites represent an emerging technology that harnesses the heat exchanged during adsorption/desorption processes. Various zeolites with different topologies (SAPO-34, FAU, LTA)[161] have been investigated for this innovative application, capitalizing their highly hydrophilic nature, that enables significant higher energy densities than conventional thermal storage systems (10–50 kWh/m³). Among different described materials, AlPO-34 allows achieving an energy density of 240 kWh/m³ and can provide thermal support in a temperature range between 40–140°C[162], whereas the module developed by ZAE Bayer, which utilizes a water adsorption system with zeolite X to supply heating for a school[163], allows achieving an energy density of 124 kWh/m³ without suffering energetic yield loss or zeolite degradation after several recycles[164]. The operational scheme of this system is illustrated in **Figure 1.12**.

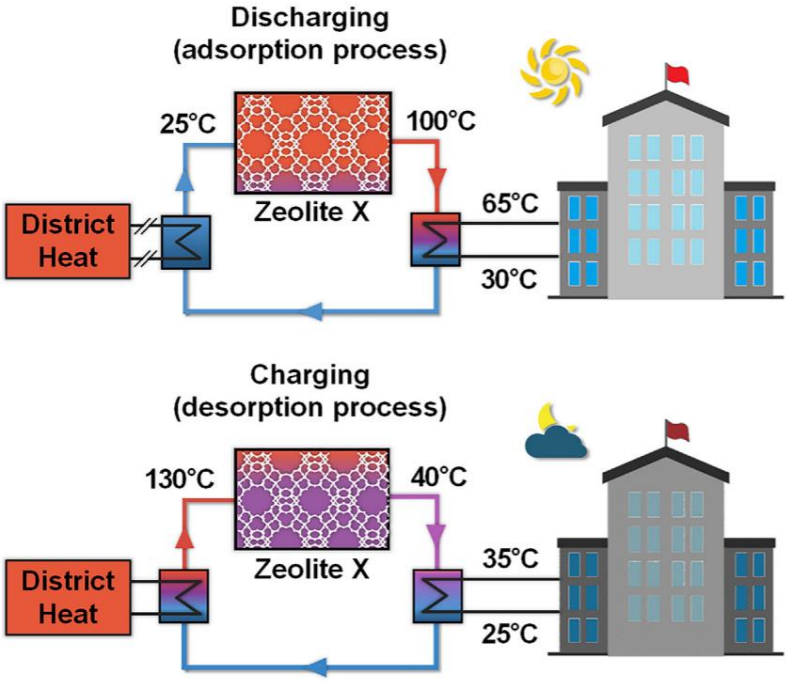

Figure 1.12. Sustainable Energy Storage System for School Heating based on Zeolite/Water adsorption phenomena. Scheme adapted from Hauer *et al*[163].

Catalyst: The high surface area, high hydrothermal stability, high adsorption capacity, the diffusive properties determined by the diverse topologies and morphologies of zeolites, along with their selective control over reactants and products in addition to the ability to tailor their physico-chemical properties through the incorporation of active sites (by direct synthesis or via post-synthetic modifications), explain their exceptional versatility as heterogeneous catalysts[165]. Although zeolites have traditionally been employed in catalytic cracking, paraffin hydroisomerization, and various petrochemical processes[166,167], their application has now been expanded to other efficient and sustainable chemical pathways that leverage their exceptional properties. The following sections outline some of the most

significant advancements, categorized according to the type of catalysis involved.

- **Brønsted Acid Catalysis**:

Among the reactions catalysed by Brønsted acid sites, the direct conversion of methanol into olefins (MTO) or, depending on the desired product, into gasoline (MTG), aromatics (MTA), or propylene (MTP) has gained significant attention. This is primarily due to the potential use of methanol (produced by a wide variety of routes like from syngas treatment, bacterial fermentation, from biomass-derived feedstocks or CO_2 conversion)[168-170] as a feedstock for producing platform molecules (see **Figure 1.13**)[171]. This reaction is of high industrial relevance for several reasons: **(i)** it can be performed under ambient pressure using an acid zeolite, **(ii)** it generally achieves high conversion rates within relatively short reaction times[172], **(iii)** the combination of shape-selectivity and intrinsic acidity of the zeolite enables control over the product distribution (small-pore zeolites such as CHA favour the MTP process, whereas larger-pore structures like MFI and BEA promote hydrocarbon formation up to the aromatic-gasoline range)[173], and **(iv)** catalyst deactivation primarily occurs via pore blockage due to coke formation, allowing regeneration through calcination, which effectively restores catalytic activity. Additional examples of industrially relevant reactions catalysed by Brønsted acid zeolites are the oligomerization of olefins ($>C_3$ molecules) to obtain liquid fuels or, considering the use of biomass-derived feedstocks, transformation of furanic compounds (sugar derivatives) into high-value products, as for instance, aromatic hydrocarbons via Diels-Alder cycloaddition with ethylene under high-pressure conditions

[174]. Notably, the use of acid MFI and FAU zeolites has been reported to carry out this reaction in tandem in the presence of liquid ethanol instead of ethylene gas, simplifying the process while enhancing safety and sustainability because the required ethylene is formed as result of the ethanol dehydration *in situ*[175].

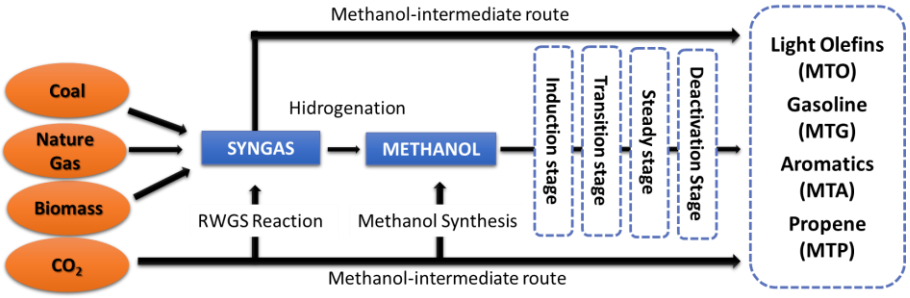

Figure 1.13. Reaction network scheme for the conversion of methanol obtained from different feedstocks to produce hydrocarbons[171].

- **Lewis Acid Catalysis:**

Notable examples include the production of terephthalic acid (key monomer in the plastics industry) using large-pore zeolites with Lewis acid sites to process biomass-derived precursors, such as 5-hydroxymethylfurfural[176]. Additionally, the transformation of tetroses (sugars) into α-hydroxy acid esters has been demonstrated with high selectivity towards methyl vinyl glycolate when employing Sn-MFI and Sn-Beta zeolites[177]. In contrast, the use of mesoporous structures such as Sn-MCM-41 or Sn-SBA-15, resulted in the formation of significantly larger molecular products[177]. Other catalytic applications of Lewis acid zeolites in industrially relevant reactions include the Baeyer-Villiger oxidation[178], which converts ketones into esters or lactones[179], and the Meerwein-Ponndorf-Verley reduction, where carbonyl compounds are selectively reduced to their corresponding alcohols[180-182].

- **Metal Supported Catalysis:**

The ability of zeolites to accommodate metallic active sites (whether noble or non-noble) while enhancing their stability against sintering and deactivation through spatial confinement is a significant advantage in heterogeneous redox catalysis. This property enables a range of catalytic applications, including **(i)** the selective reduction of NOx using Cu cations stabilized by the negative charges of framework Al (**see Figure 1.14**)[183-185], **(ii)** hydrogenation reactions of C1 compounds, being specially relevant the hydrogenation of CO_2, facilitated by Ni^0 centers[186,187] or noble metal sites such as Pd, Rh, or Ru[188], **(iii)** dehydrogenation reactions of paraffins catalysed by transition metals or noble metals, particularly the non-oxidative dehydrogenation of propane using pure silica MFI zeolites containing Pt nanoparticles[189] (this topic will be explored in detail in **Chapter 4)**, **(iv)** oxidation reactions, being one of the most noticeable example the oxidation of methane to produce methanol[190] using Cu-containing zeolites, formic acid by using Fe-containing zeolites[191] or CO_2 by using, Pd-containing zeolites[192,193]. In the specific case of zeolites with encapsulated noble metals, their application in the selective hydrogenation of more complex molecules is particularly noteworthy. For instance, Wang et al. utilized Pd@Silicalite-1 to selectively hydrogenate furfural molecules derived from biomass, producing furans with high selectivity[194]. Additionally, Pd containing zeolites are also employed for the semi-hydrogenation of molecules with multiple bonds, such as the conversion of phenylacetylene to styrene[195], a reaction that will be explored in detail in **Chapter 5**. Regarding bimetallic zeolitic catalysts, the use of zeolites incorporating different metal-metal active centres has been

explored for the non-oxidative dehydrogenation of propane, where alloy formation enhances catalytic performance, as demonstrated in PtIn@Silicalite-1 and PtSn@Silicalite-1 systems[189,196-202].

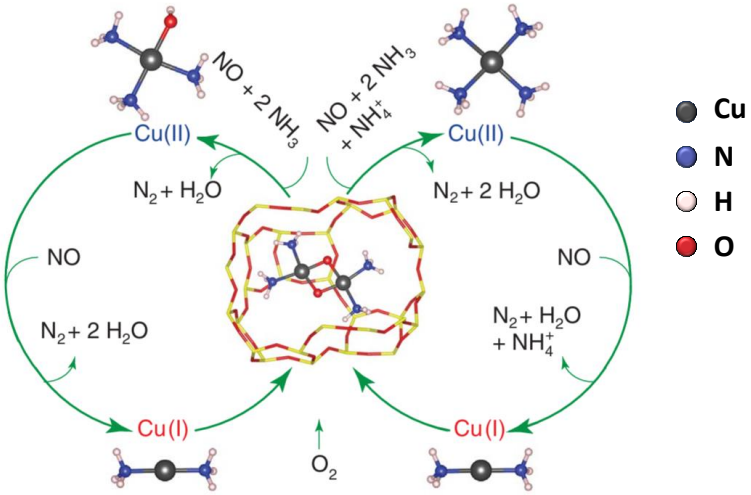

Figure 1.14. Proposed low-temperature SCR catalytic cycle carried out by a Cu-CHA. Reduction steps proceed on site-isolated Cu(II) ions residing near one (left-hand cycle) or two (right-hand cycle) framework Al centres with constrained diffusion of Cu(I) ions into single cages and oxidation by Cu(II) N_2 + H_2O Cu(II) N_2 + 2 H_2O O_2 (inner step). NH_4^+ is formed and consumed in the right-hand cycle to maintain stoichiometry and charge balance. Scheme adapted from Gounder *et al.*[185].

- **Multifunctional Catalysis:**

These processes involve the cooperative (cooperative catalysis) or successive (tandem catalysis) reaction between the reactant and various types of zeolite active zeolite centres, such as metal-metal, acid centres (Brønsted or Lewis) paired with metal centres, and Brønsted acid centres interacting with Lewis acid centres. Examples of multifunctional zeolites include Sn-Al-Beta, which combines both types of acidity to enable the cooperative catalysis of multi-

step biomass derivative conversions, such as the transformation of 1,3-dihydroxyacetone to ethyl lactate[203] or the conversion of glucose to methyl lactate using Sn-Al-FAU, as reported by Iglesias et al[204]. Other applications of multifunctional catalysts include Ag/Zr-BEA or ZnHf-MFI catalysts, which are used for the direct conversion of bioethanol to butadiene[205,206], a highly valuable platform molecule for various chemical processes. Additionally, one of the most industrially relevant reactions under stringent conditions is ethylene oligomerization, which requires multifunctional zeolites possessing Brønsted acid sites and Ni^{2+} metal cation centers[207-209] (see **Figure 1.15**). The complexity of these zeolitic catalysts is examined in **Chapter 6**.

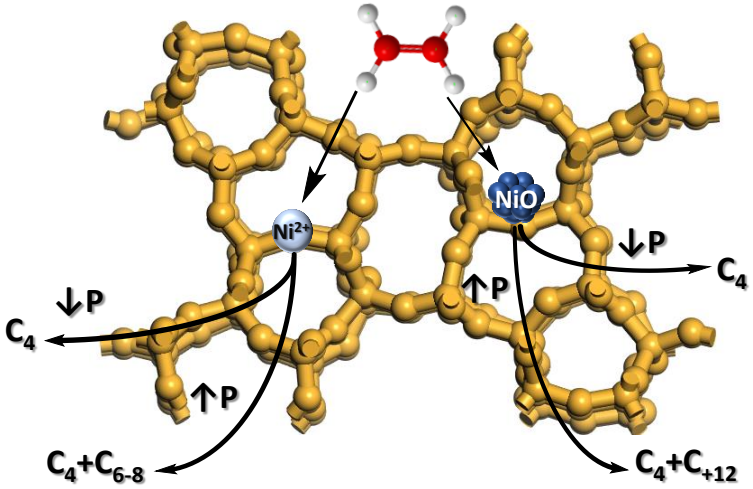

Figure 1.15. Bifunctional MFI-type catalyst with Bronsted Acid Centres and Nickel metallic centres for the ethylene oligomerization reaction[210].

This introduction has emphasised the properties, advantages, and diverse applications that highlights zeolites as a sustainable and promising alternative for various heterogeneous catalysis processes. However, despite their

potential, these materials may still encounter deactivation issues, require costly regeneration procedures, or entail significant economic and environmental issues during production. Therefore, a comprehensive understanding of the factors and strategies that maximize their benefits (particularly by enhancing their catalytic behaviour and stability in catalytic processes) is crucial. In the following chapters of this doctoral thesis, key aspects of their synthesis will be explored, focusing on strategies for the selective placement and stabilization of metallic active centres in zeolites, optimizing their catalytic performance, and applying these materials in reactions of current industrial relevance.

1.5. REFERENCES.

(1) Hudson, J. The History of Chemistry, 1st ed.; Chapman & Hall, 1992. https://doi.org/10.1007/978-1-4684-6441-2.

(2) Arrhenius, S. On the Influence of Carbonic Acid in the Air upon the Temperature of the Ground. In The future of Nature; Robin, L., Sörlin, S., Warde, P., Eds.; Yale University Press, 2013; pp 303–316. https://doi.org/10.2307/j.ctt5vm5bn.

(3) Mikhaylov, A.; Moiseev, N.; Aleshin, K.; Burkhardt, T. Global Climate Change and Greenhouse Effect. Entrep. Sustain. Issues 2020, 7 (4), 2897–2913. https://doi.org/10.9770/jesi.2020.7.4(21).

(4) United States Environmental Protection Agency (EPA). Global Greenhouse Gas Overview. Climate Change 2022 - Mitigation of Climate Change. https://doi.org/10.1017/9781009157926.004.

(5) Woodhouse, E. J.; Breyman, S. Green Chemistry as Social Movement? Sci. Technol. Hum. Val 2005, 30 (2), 199–222. https://doi.org/10.1177/0162243904271726.

(6) Ahmed, S. F.; Mofijur, M.; Nuzhat, S.; Chowdhury, A. T.; Rafa, N.; Uddin, M. A.; Inayat, A.; Mahlia, T. M. I.; Ong, H. C.; Chia, W. Y.; Show, P. L. Recent Developments in Physical, Biological, Chemical, and Hybrid Treatment Techniques for Removing Emerging Contaminants from Wastewater. J. Hazard. Mater. 2021, 416, 125912. https://doi.org/10.1016/J.JHAZMAT.2021.125912.

(7) Saikumar, A.; Singh, A.; Dobhal, A.; Arora, S.; Junaid, P. M.; Badwaik, L. S.; Kumar, S. A Review on the Impact of Physical, Chemical, and Novel Treatments on the Quality and Microbial Safety of Fruits and Vegetables. Syst. Microbiol. Biomanufacturing 2023, 4 (2), 575–597. https://doi.org/10.1007/S43393-023-00217-9.

(8) Allende, A.; Tomás-Barberán, F. A.; Gil, M. I. Minimal Processing for Healthy Traditional Foods. Trends. Food. Sci. Technol. 2006, 17 (9), 513–519. https://doi.org/10.1016/J.TIFS.2006.04.005.

(9) Linthorst, J. A. An Overview: Origins and Development of Green Chemistry. Found. Chem. 2010, 12 (1), 55–68. https://doi.org/10.1007/S10698-009-9079-4.

(10) Tundo, P.; Anastas, P.; Black, D. S. C.; Breen, J.; Collins, T.; Memoli, S.; Miyamoto, J.; Polyakoff, M.; Tumas, W. Synthetic Pathways and Processes in Green Chemistry. Introductory Overview. Pure Appl. Chem. 2000, 72 (7), 1207–1228. https://doi.org/10.1351/PAC200072071207.

(11) Anastas, P. T.; Warner, C. W. Green Chemistry: Theory an J Practice; Oxford University Press, 2000. https://doi.org/10.1093/oso/9780198506980.003.0001.

(12) Mutlu, H.; Barner, L. Getting the Terms Right: Green, Sustainable, or Circular Chemistry? Macromol. Chem. Phys. 2022, 223 (13), 1–7. https://doi.org/10.1002/macp.202200111.

(13) Organisation for Economic Co-operation and Development. Sustainable Chemistry: Evidence on Innovation from Patent Data. OECD Publishing: Paris February 28, 2011, pp 8–10. https://doi.org/10.1787/7a1b762c-en.

(14) Kümmerer, K. Sustainable Chemistry: A Future Guiding Principle. Angew. Chem. 2017, 129 (52), 16640–16641. https://doi.org/10.1002/ange.201709949.

(15) Marteel-Parrish, A. E.; Abraham, M. A. Green Chemistry and Engineering: A Pathway to Sustainability; John Wiley & Sons, 2013. https://doi.org/10.1002/9781118720011.

(16) Anastas, P. T.; Kirchhoff, M. M.; Williamson, T. C. Catalysis as a Foundational Pillar of Green Chemistry. Appl. Catal. A: Gen. 2001, 221, 3–13. https://doi.org/10.1016/S0926-860X(01)00793-1.

(17) Bender, T. A.; Dabrowski, J. A.; Gagné, M. R. Homogeneous Catalysis for the Production of Low-Volume, High-Value Chemicals from Biomass. Nat. Rev. Chem. 2018, 2 (5), 35–46. https://doi.org/10.1038/s41570-018-0005-y.

(18) Fassbach, T. A.; Ji, J. M.; Vorholt, A. J.; Leitner, W. Recycling of Homogeneous Catalysts–Basic Principles, Industrial Practice, and Guidelines

for Experiments and Evaluation. ACS Catal. 2024, 14 (9), 7289–7298. https://doi.org/10.1021/acscatal.4c01006.

(19) Friend, C. M.; Xu, B. Heterogeneous Catalysis: A Central Science for a Sustainable Future. Acc. Chem. Res. 2017, 50 (3), 517–521. https://doi.org/10.1021/acs.accounts.6b00510.

(20) Palmisano, G.; Al Jitan, S.; Garlisi, C. Heterogeneous Catalysis Fundamentals, Engineering, and Characterizations, 1st ed.; Elsevier, 2022. https://doi.org/10.1016/C2020-0-02936-1.

(21) Chen, N. Y. - Shape Selective Catalysis in Industrial Applications, 2nd ed.; Garwood, W. E., Dwyer, F. G., Eds.; CRC Press, 1996. https://doi.org/10.1201/9781003418207.

(22) Csicsery, S. M. The Future of Shape Selective Catalysis. Stud. Surf. Sci. Catal. 1995, 94 (C), 1–12. https://doi.org/10.1016/S0167-2991(06)81202-4.

(23) Lowenstein, W. The Distribution of Aluminium in the Tetra-Hedra of Silicates and Aluminates. Am Min 1954, 39 (1–2), 92–96.

(24) Corma, A.; Davis, M. E. Issues in the Synthesis of Crystalline Molecular Sieves: Towards the Crystallization of Low Framework-Density Structures. ChemPhysChem 2004, 5 (3), 304–313. https://doi.org/10.1002/CPHC.200300997.

(25) Baerlocher, C.; McCusker, L. B.; Olson, D. H. Atlas of Zeolite Framework Types, 6th ed.; Elsevier Science, 2007. https://doi.org/10.1016/B978-0-444-53064-6.X5186-X.

(26) Baerlocher, C.; McCusker, L. MFI: Framework Type. https://europe.iza-structure.org/IZA-SC/framework.php?ID=149 (accessed 2025-03-06).

(27) Breck, D. W.; Eversole, W. G.; Milton, R. M.; Reed, T. B.; Thomas, T. L. Physical and Inorganic Chemistry: Crystalline Zeolites. I. The Properties of a New Synthetic Zeolite, Type A. J. Am. Chem. Soc. 1956, 78 (23), 5963–5972. https://doi.org/10.1021/JA01604A001.

(28) Newsam, J. M. Synthesis and Structural Characterization of a Lithium Gallosllicate with the Zeolite ABW Framework. J. Phys. Chem 1988, 92, 445–452. https://doi.org/10.1021/j100313a041.

(29) Kington, G. L.; Laing, W. The Crystal Structure of Chabazite and Its Sorptive Properties. Trans. Faraday Soc. 1955, 51 (0), 287–298. https://doi.org/10.1039/TF9555100287.

(30) Olson, D. H.; Kokotailo, " G T; Lawton, S. L.; Meler, W. M. Crystal Structure and Structure-Related Properties of ZSM-5. J. Phys. Chem 1981, 85, 2238–2243. https://doi.org/10.1021/j150615a020.

(31) Kokotailo, G. T.; Chu, P.; Lawton, S. L.; Meier, W. M. Synthesis and Structure of Synthetic Zeolite ZSM-11. Nature 1978, 275 (5676), 119–120. https://doi.org/10.1038/275119a0.

(32) Higgins, J. B.; LaPierre, R. B.; Schlenker, J. L.; Rohrman, A. C.; Wood, J. D.; Kerr, G. T.; Rohrbaugh, W. J. The Framework Topology of Zeolite Beta. Zeolites 1988, 8 (6), 446–452. https://doi.org/10.1016/S0144-2449(88)80219-7.

(33) Villaescusa, L. A.; Díaz, I.; Barrett, P. A.; Nair, S.; Lloris-Cormano, J. M.; Martínez-Mañez, R.; Tsapatsis, M.; Liu, Z.; Terasaki, O.; Camblor, M. A. Pure Silica Large Pore Zeolite ITQ-7: Synthetic Strategies, Structure-Directing Effects, and Control and Nature of Structural Disorder. Chem. Mater. 2007, 19 (7), 1601–1612. https://doi.org/10.1021/cm0622248.

(34) Freyhardt, C. C.; Tsapatsis, M.; Lobo, R. F.; Balkus, K. J.; Davis, M. E. A High-Silica Zeolite with a 14-Tetrahedral-Atom Pore Opening. Nature 1996, 381 (6580), 295–298. https://doi.org/10.1038/381295a0.

(35) Wagner, P.; Yoshikawa, M.; Lovallo, M.; Tsuji, K.; Taspatsis, M.; Davis, M. E. CIT-5: A High-Silica Zeolite with 14-Ring Pores. Chem. Commun 1997, 9 (22), 46. https://doi.org/10.1039/A704774F.

(36) Willhammar, T.; Burton, A. W.; Yun, Y.; Sun, J.; Afeworki, M.; Strohmaier, K. G.; Vroman, H.; Zou, X. EMM-23: A Stable High-Silica Multidimensional Zeolite with Extra-Large Trilobe-Shaped Channels. J Am Chem Soc 2014, 136 (39), 13570–13573. https://doi.org/10.1021/ja507615b.

(37) McCusker, L. B.; Baerlocher, C. Chapter 3 Zeolite Structures. Stud. Surf. Sci. Catal. 2001, 137, 37–67. https://doi.org/10.1016/S0167-2991(01)80244-5.

(38) Liang, G.; Chen, J.; Dou, T.; Wu, Z.; Li, X.; Liu, Y. Full-Crystalline Monolithic EU-1 Zeolite: Sustainable Synthesis and Its Applications in the Hydroisomerization of Ethylbenzene with Meta-Xylene. Catal Sci Technol 2023, 13 (10), 3060–3068. https://doi.org/10.1039/d3cy00140g.

(39) LaPierre, R. B.; Rohrman, A. C.; Schlenker, J. L.; Wood, J. D.; Rubin, M. K.; Rohrbaugh, W. J. The Framework Topology of ZSM-12: A High-Silica

Zeolite. Zeolites 1985, 5 (6), 346–348. https://doi.org/10.1016/0144-2449(85)90121-6.

(40) Boronat, M.; Martínez-Sánchez, C.; Law, D.; Corma, A. Enzyme-like Specificity in Zeolites: A Unique Site Position in Mordenite for Selective Carbonylation of Methanol and Dimethyl Ether with CO. J. Am. Chem. Soc. 2008, 130 (48), 16316–16323. https://doi.org/10.1021/JA805607M.

(41) Martins, L.; Hölderich, W.; Cardoso, D. Methylammonium-FAU Zeolite: Investigation of the Basic Sites in Base Catalyzed Reactions and Its Performance. J Catal 2008, 258 (1), 14–24. https://doi.org/10.1016/j.jcat.2008.05.018.

(42) Higgins, J. B.; LaPierre, R. B.; Schlenker, J. L.; Rohrman, A. C.; Wood, J. D.; Kerr, G. T.; Rohrbaugh, W. J. The Framework Topology of Zeolite Beta. Zeolites 1988, 8 (6), 446–452. https://doi.org/10.1016/S0144-2449(88)80219-7.

(43) Leonowicz, M. E.; Lawton, J. A.; Lawton, S. L.; Rubin, M. K. MCM-22: A Molecular Sieve with Two Independent Multidimensional Channel Systems. Science (1979) 1994, 264 (5167), 1910–1913. https://doi.org/10.1126/SCIENCE.264.5167.1910.

(44) Liu, Z.; Ohsuna, T.; Terasaki, O.; Camblor, M. A.; Diaz-Cabañas, M. J.; Hiraga, K. The First Zeolite with Three-Dimensional Intersecting Straight-Channel System of 12-Membered Rings [12]. J. Am. Chem. Soc. 2001, 123 (22), 5370–5371. https://doi.org/10.1021/JA0107778.

(45) Corma, A.; Rey, F.; Rius, J.; Sabater, M. J.; Valencia, S. Supramolecular Self-Assembled Molecules as Organic Directing Agent for Synthesis of

Zeolites. Nature 2004, 431 (7006), 287–290. https://doi.org/10.1038/nature02909.

(46) Lobo, R. F.; Zones, S. I.; Medrud, R. C. Synthesis and Rietveld Refinement of the Small-Pore Zeolite SSZ-16. Chem. Mat. 1996, 8 (10), 2409–2411. https://doi.org/10.1021/CM960289C.

(47) Boronat, M.; Corma, A. Factors Controlling the Acidity of Zeolites. Catal. Lett. 2014, 145 (1), 162–172. https://doi.org/10.1007/S10562-014-1438-7.

(48) Yabushita, M.; Kobayashi, H.; Neya, A.; Nakaya, M.; Maki, S.; Matsubara, M.; Kanie, K.; Muramatsu, A. Precise Control of Density and Strength of Acid Sites of MFI-Type Zeolite Nanoparticles via Simultaneous Isomorphous Substitution by Al and Fe. CrystEngComm 2020, 22 (44), 7556–7564. https://doi.org/10.1039/D0CE01031F.

(49) Schoonheydt, R. A.; Geerlings, P.; Pidko, E. A.; Van Santen, R. A. The Framework Basicity of Zeolites. J. Mater. Chem. 2012, 22 (36), 18705–18717. https://doi.org/10.1039/C2JM31366A.

(50) Huang, M.; Kaliaguine, S.; Auroux, A. Lewis Basic and Lewis Acidic Sites in Zeolites. Stud. Surf. Sci. Catal. 1995, 97 (C), 311–318. https://doi.org/10.1016/S0167-2991(06)81903-8.

(51) Zhao, X.; Xu, J.; Deng, F. Solid-State NMR for Metal-Containing Zeolites: From Active Sites to Reaction Mechanism. Front Chem Sci Eng. 2020, 14 (2), 159–187. https://doi.org/10.1007/S11705-019-1885-1.

(52) Tatlier, M.; Atalay-Oral, C.; Bayrak, A.; Maraş, T.; Erdem, A. Impact of Ion Exchange on Zeolite Hydrophilicity/Hydrophobicity Monitored by Water

Capacity Using Thermal Analysis. Thermochim. Acta 2022, 713, 179240. https://doi.org/10.1016/J.TCA.2022.179240.

(53) Catuzo, G. L.; Santilli, C. V.; Martins, L. Hydrophobic-Hydrophilic Balance of ZSM-5 Zeolites on the Two-Phase Ketalization of Glycerol with Acetone. Catal. Today 2021, 381, 215–223. https://doi.org/10.1016/J.CATTOD.2020.07.008.

(54) Armor, J. N. Metal-Exchanged Zeolites as Catalysts. Micropor. Mesopor. Mater. 1998, 22 (1–3), 451–456. https://doi.org/10.1016/S1387-1811(98)00098-5.

(55) Farrusseng, D.; Tuel, A. Perspectives on Zeolite-Encapsulated Metal Nanoparticles and Their Applications in Catalysis. New J. Chem. 2016, 40 (5), 3933–3949. https://doi.org/10.1039/C5NJ02608C.

(56) Cundy, C. S.; Cox, P. A. The Hydrothermal Synthesis of Zeolites: History and Development from the Earliest Days to the Present Time. Chem. Rev. 2003, 103 (3), 663–701. https://doi.org/10.1021/CR020060I.

(57) Karthika, S.; Radhakrishnan, T. K.; Kalaichelvi, P. A Review of Classical and Nonclassical Nucleation Theories. Cryst. Growth Des. 2016, 16 (11), 6663–6681. https://doi.org/10.1021/ACS.CGD.6B00794.

(58) Willard, G. On the Equilibrium of Heterogeneous Substances. Am. J. Sci. 1878, s3-16 (96), 441–458. https://doi.org/10.2475/AJS.S3-16.96.441.

(59) Yoreo, J. J. De; Vekilov, P. G. Principles of Crystal Nucleation and Growth. Rev. Mineral. Geochem. 2003, 54 (1), 57–93. https://doi.org/10.2113/0540057.

(60) Vekilov, P. G. The Two-Step Mechanism of Nucleation of Crystals in Solution. Nanoscale 2010, 2 (11), 2346–2357. https://doi.org/10.1039/C0NR00628A.

(61) Smeets, P. J. M.; Finney, A. R.; Habraken, W. J. E. M.; Nudelman, F.; Friedrich, H.; Laven, J.; De Yoreo, J. J.; Rodger, P. M.; Sommerdijk, N. A. J. M. A Classical View on Nonclassical Nucleation. PNAS 2017, 114 (38), E7882–E7890. https://doi.org/10.1073/PNAS.1700342114.

(62) Binder, K.; Fratzl, P. Spinodal Decomposition. In Phase transformations in materials; Kostorz, G., Ed.; Wiley-VCH, 2001; pp 411–474. https://doi.org/10.1002/352760264X.

(63) Anderson, V. J.; Lekkerkerker, H. N. W. Insights into Phase Transition Kinetics from Colloid Science. Nature 2002, 416 (6883), 811–815. https://doi.org/10.1038/416811a.

(64) Mallette, A. J.; Shilpa, K.; Rimer, J. D. The Current Understanding of Mechanistic Pathways in Zeolite Crystallization. Chem. Rev. 2024, 124 (6), 3416–3493. https://doi.org/10.1021/acs.chemrev.3c00801.

(65) Markov I. Crystal Growth. In Crystal Growth for Beginners; Markov, I., Ed.; WordScientific, 2003; pp 181–332. https://doi.org/10.1107/S0108767304015065.

(66) Mirabello, G.; Ianiro, A.; Bomans, P. H. H.; Yoda, T.; Arakaki, A.; Friedrich, H.; de With, G.; Sommerdijk, N. A. J. M. Crystallization by Particle Attachment Is a Colloidal Assembly Process. Nat. Mater. 2019, 19 (4), 391–396. https://doi.org/10.1038/s41563-019-0511-4.

(67) Kumar, M.; Luo, H.; Román-Leshkov, Y.; Rimer, J. D. SSZ-13 Crystallization by Particle Attachment and Deterministic Pathways to Crystal Size Control. J. Am. Chem. Soc. 2015, 137 (40), 13007–13017. https://doi.org/10.1021/JACS.5B07477.

(68) Kumar, M.; Li, R.; Rimer, J. D. Assembly and Evolution of Amorphous Precursors in Zeolite L Crystallization. Chem. Mater. 2016, 28 (6), 1714–1727. https://doi.org/10.1021/ACS.CHEMMATER.5B04569.

(69) Li, Q.; Creaser, D.; Sterte, J. An Investigation of the Nucleation/Crystallization Kinetics of Nanosized Colloidal Faujasite Zeolites. Chem. Mater. 2002, 14 (3), 1319–1324. https://doi.org/10.1021/CM011242G.

(70) Mintova, S.; Fieres, B.; Bein, T. Crystal Growth of Nanosized LTA Zeolite from Precursor Colloids. Stud. Surf. Sci. Catal. 2002, 142, 223–229. https://doi.org/10.1016/S0167-2991(02)80032-5.

(71) Itani, L.; Liu, Y.; Zhang, W.; Bozhilov, K. N.; Delmotte, L.; Valtchev, V. Investigation of the Physicochemical Changes Preceding Zeolite Nucleation in a Sodium-Rich Aluminosilicate Gel. J. Am. Chem. Soc. 2009, 131 (29), 10127–10139. https://doi.org/10.1021/JA902088F.

(72) Jain, R.; Niu, Z.; Choudhary, M.; Bourji, H.; Palmer, J. C.; Rimer, J. D. In Situ Imaging of Faujasite Surface Growth Reveals Unique Pathways of Zeolite Crystallization. J. Am. Chem. Soc. 2023, 145 (2), 1155–1164. https://doi.org/10.1021/JACS.2C10839.

(73) Wang, Z.; Chu, W.; Zhao, Z.; Liu, Z.; Chen, H.; Xiao, D.; Gong, K.; Li, F.; Li, X.; Hou, G. The Role of Organic and Inorganic Structure-Directing Agents in

Selective Al Substitution of Zeolite. J. Phys. Chem. Lett. 2021, 12 (38), 9398–9406. https://doi.org/10.1021/ACS.JPCLETT.1C01448.

(74) Lee, H.; Zones, S. I.; Davis, M. E. Zeolite Synthesis Using Degradable Structure-Directing Agents and Pore-Filling Agents. J. Phys. Chem. B 2005, 109 (6), 2187–2191. https://doi.org/10.1021/JP048908P.

(75) Awala, H.; Gilson, J. P.; Retoux, R.; Boullay, P.; Goupil, J. M.; Valtchev, V.; Mintova, S. Template-Free Nanosized Faujasite-Type Zeolites. Nat. Mater. 2015, 14 (4), 447–451. https://doi.org/10.1038/nmat4173.

(76) Simancas, R.; Dari, D.; Velamazán, N.; Navarro, M. T.; Cantín, A.; Jordá, J. L.; Sastre, G.; Corma, A.; Rey, F. Modular Organic Structure-Directing Agents for the Synthesis of Zeolites. Science (1979) 2010, 330 (6008), 1219–1222. https://doi.org/10.1126/SCIENCE.1196240.

(77) Martinez-Ortigosa, J.; Millán, R.; Simancas, J.; Hernández-Rodríguez, M.; Vidal-Moya, J. A.; Jordá, J. L.; Martineau-Corcos, C.; Sarou-Kanian, V.; Boronat, M.; Blasco, T.; Rey, F. Crystalline Phase Transition in As-Synthesized Pure Silica Zeolite RTH Containing Tetra-Alkyl Phosphonium as Organic Structure Directing Agent. J. Mater. Chem. A 2024, 12 (2), 876–891. https://doi.org/10.1039/D3TA06071C.

(78) Yamasaki, Y.; Tsunoji, N.; Takamitsu, Y.; Sadakane, M.; Sano, T. Synthesis of Phosphorus-Modified Small-Pore Zeolites Utilizing Tetraalkyl Phosphonium Cations as Both Structure-Directing and Phosphorous Modification Agents. Micropor. Mesopor. Mater. 2016, 223, 129–139. https://doi.org/10.1016/J.MICROMESO.2015.10.038.

(79) Onishi, M.; Tsunoji, N.; Sadakane, M.; Sano, T. Synthesis of Phosphorus-Modified AFX Zeolite by the Hydrothermal Conversion of Tetraalkylphosphonium Hydroxide-Impregnated FAU Zeolite. BCSJ 2021, 94 (1), 1–7. https://doi.org/10.1246/BCSJ.20200224.

(80) Nearchou, A.; Castaing, R.; Raithby, P. R.; Sartbaeva, A. Zeolites Fit for a Crown: Studying Organic-Framework Host-Guest Interactions through Thermogravimetric Techniques. Micropor. Mesopor. Mater. 2020, 308, 110479. https://doi.org/10.1016/J.MICROMESO.2020.110479.

(81) Chatelard, C.; Dodin, M.; Martinez-Franco, R.; Tuel, A. Synthesis of NaY Zeolites with Exceptionally High SiO2/Al2O3 Ratios via a Dissolution-Recrystallization Process. Micropor. Mesopor. Mater. 2023, 357, 112614. https://doi.org/10.1016/J.MICROMESO.2023.112614.

(82) Ke, Q.; Sun, T.; Cheng, H.; Chen, H.; Liu, X.; Wei, X.; ang, S.; Sun, D.; heng, D.; Liu, X.; Wei, X.; ang, D. W.; Ke, Q. Targeted Synthesis of Ultrastable High-Silica RHO Zeolite Through Alkali Metal–Crown Ether Interaction. Chem. Asian. J 2017, 12 (10), 1043–1047. https://doi.org/10.1002/ASIA.201700303.

(83) Watts, A. E.; Turrina, A.; Wright, P. A. Insights into the Chemistry of Organic Structure-Directing Agents in the Synthesis of Zeolitic Materials, 1st ed.; Gómez-Hortigüela, L., Ed.; Springer, 2017. https://doi.org/10.1007/978-3-319-74289-2.

(84) Barrer, R. M.; Denny, P. J. 201. Hydrothermal Chemistry of the Silicates. Part IX. Nitrogenous Aluminosilicates. J. Chem. Soc. 1961, 56 (0), 971–982. https://doi.org/10.1039/JR9610000971.

(85) Kerr, G. T. Chemistry of Crystalline Aluminosilicates. III. The Synthesis and Properties of Zeolite ZK-5. Inorg. Chem. 1966, 5 (9), 1539–1541. https://doi.org/10.1021/IC50043A016.

(86) Moliner, M.; Rey, F.; Corma, A. Towards the Rational Design of Efficient Organic Structure-Directing Agents for Zeolite Synthesis. Angew. Chem. Int. Ed. 2013, 52 (52), 13880–13889. https://doi.org/10.1002/ANIE.201304713.

(87) Wickleder, S.; Housecroft, C.; Pour, Z. A.; Sebakhy, K. O. A Review on the Effects of Organic Structure-Directing Agents on the Hydrothermal Synthesis and Physicochemical Properties of Zeolites. Chemistry 2022, 4 (2), 431–446. https://doi.org/10.3390/CHEMISTRY4020032.

(88) Araya, A.; Lowe, B. M. Effect of Organic Species on the Synthesis and Properties of ZSM-5. Zeolites 1986, 6 (2), 111–118. https://doi.org/10.1016/S0144-2449(86)80007-0.

(89) Wu, Q.; Zhu, L.; Chu, Y.; Liu, X.; Zhang, C.; Zhang, J.; Xu, H.; Xu, J.; Deng, F.; Feng, Z.; Meng, X.; Xiao, F. S. Sustainable Synthesis of Pure Silica Zeolites from a Combined Strategy of Zeolite Seeding and Alcohol Filling. Angew. Chem. Int. Ed. 2019, 58 (35), 12138–12142. https://doi.org/10.1002/ANIE.201906559.

(90) Luan, H.; Wu, Q.; Wu, J.; Meng, X.; Xiao, F.-S. Templates for the Synthesis of Zeolites. Chin. J. Chem. 2024, 43 (4), 100252. https://doi.org/10.1016/J.CJSC.2024.100252.

(91) Wakihara, T.; Okubo, T. Hydrothermal Synthesis and Characterization of Zeolites. Chem. Lett. 2005, 34 (3), 276–281. https://doi.org/10.1246/CL.2005.276.

(92) Vinaches, P.; Bernardo-Gusmão, K.; Pergher, S. B. C. An Introduction to Zeolite Synthesis Using Imidazolium-Based Cations as Organic Structure-Directing Agents. Molecules. MDPI AG August 1, 2017. https://doi.org/10.3390/molecules22081307.

(93) Lew, C. M.; Xie, D.; Schmidt, J. E.; Elomari, S.; Davis, T. M.; Zones, S. I. The Confluence of Organo-Cations, Inorganic Species, and Molecular Modeling on the Discovery of New Zeolite Structures and Compositions. In AI-Guided Design and Property Prediction for Zeolites and Nanoporous Materials; Sastre, G., Daeyaert, F., Eds.; John Wiley & Sons, 2023; pp 1–32. https://doi.org/10.1002/9781119819783.ch1.

(94) Liu, S.; Li, L.; Li, C.; Xiong, X.; Xiao, F. S. Synthesis of EMT-Rich Faujasite in the Presence of Organic Template of Low-Cost Polyquaternium-6. J. Porous Mater. 2008, 15 (3), 295–301. https://doi.org/10.1007/S10934-006-9078-Y.

(95) Wang, J.; Song, J.; Yin, C.; Ji, Y.; Zou, Y.; Xiao, F. S. Tetramethylguanidine-Templated Synthesis of Aluminophosphate-Based Microporous Crystals with AFI-Type Structure. Micropor. Mesopor. Mater. 2009, 117 (3), 561–569. https://doi.org/10.1016/J.MICROMESO.2008.07.040.

(96) Bello-Jurado, E.; Millet, I.; Van Tendeloo, L.; Schütze, F. W.; Vennestrøm, P. N. R.; Corma, A.; Moliner, M. Enhancing Nucleation to Synthesize Al-Rich CHA Zeolites under Ultra-Low OSDA Contents: Application

for Heavy-Duty NH3-SCR of NOx. Micropor. Mesopor. Mater. 2024, 371, 113071. https://doi.org/10.1016/J.MICROMESO.2024.113071.

(97) Zones, S. I. US8007763. US 8,007,763 B2, 2011.

(98) Lewis, G. J.; Miller, M. A.; Moscoso, J. G.; Wilson, B. A.; Knight, L. M.; Wilson, S. T. Experimental Charge Density Matching Approach to Zeolite Synthesis. Stud. Surf. Sci. Catal. 2004, 154, 364–372. https://doi.org/10.1016/S0167-2991(04)80824-3.

(99) Jones, C. W.; Tsuji, K.; Takewaki, T.; Beck, L. W.; Davis, M. E. Tailoring Molecular Sieve Properties during SDA Removal via Solvent Extraction. Micropor. Mesopor. Mater. 2001, 48 (1–3), 57–64. https://doi.org/10.1016/S1387-1811(01)00330-4.

(100) Lee, H.; Zones, S. I.; Davis, M. E. A Combustion-Free Methodology for Synthesizing Zeolites and Zeolite-like Materials. Nature 2003, 425 (6956), 385–388. https://doi.org/10.1038/nature01980.

(101) Chen, Y. H.; Zhang, Q.; Han, D. M.; Y, C. H. Fluoride- and OSDA-Free Synthesis of ZSM-5 with Controllable b-Axis Orientation: Insights into the Role of Medium Alkalinity and Seed Induction. Adv. Powder. Technol. 2024, 35 (11), 104698. https://doi.org/10.1016/J.APT.2024.104698.

(102) Nada, M. H.; Larsen, S. C. Insight into Seed-Assisted Template Free Synthesis of ZSM-5 Zeolites. Micropor. Mesopor. Mater. 2017, 239, 444–452. https://doi.org/10.1016/J.MICROMESO.2016.10.040.

(103) Sakai, M.; Fujimaki, N.; Kobayashi, G.; Yasuda, N.; Oshima, Y.; Seshimo, M.; Matsukata, M. Formation Process of *BEA-Type Zeolite Membrane under OSDA-Free Conditions and Its Separation Property.

Micropor. Mesopor. Mater. 2019, 284, 360–365. https://doi.org/10.1016/J.MICROMESO.2019.04.056.

(104) Pilar, R.; Moravkova, J.; Sadovska, G.; Sklenak, S.; Brabec, L.; Pastvova, J.; Sazama, P. Controlling the Competitive Growth of Zeolite Phases without Using an Organic Structure-Directing Agent. Synthesis of Al-Rich *BEA. Micropor. Mesopor. Mater. 2022, 333, 111726. https://doi.org/10.1016/J.MICROMESO.2022.111726.

(105) Sazama, P.; Wichterlová, B.; Sklenák, Š.; Parvulescu, V. I.; Candu, N.; Sádovská, G.; Dědeček, J.; Klein, P.; Pashkova, V.; Šťastný, P. Acid and Redox Activity of Template-Free Al-Rich H-BEA* and Fe-BEA* Zeolites. J. Catal. 2014, 318, 22–33. https://doi.org/10.1016/J.JCAT.2014.06.024.

(106) Zhang, H.; Guo, Q.; Ren, L.; Yang, C.; Zhu, L.; Meng, X.; Li, C.; Xiao, F. S. Organotemplate-Free Synthesis of High-Silica Ferrierite Zeolite Induced by CDO-Structure Zeolite Building Units. J. Mater. Chem. 2011, 21 (26), 9494–9497. https://doi.org/10.1039/c1jm11786f.

(107) Song, J.; Dai, L.; Ji, Y.; Xiao, F. S. Organic Template Free Synthesis of Aluminosilicate Zeolite ECR-1. Chem. Mater. 2006, 18 (12), 2775–2777. https://doi.org/10.1021/CM052593O.

(108) Ding, H.; Song, J. W.; Ren, L. M.; Xiao, F. S. Synthesis of Zeolite ECR-1 from Hydrothermal Phase Transition of Zeolite Y. Chem. J. Chin. Univ. 2009, 30 (2), 255–257.

(109) Valtchev, V.; Gao, F.; Tosheva, L. Porous Materials Viaegg-Constituents Templating. New J. Chem. 2008, 32 (8), 1331–1337. https://doi.org/10.1039/B804449J.

(110) Louis, B.; Gomes, E. S.; Losch, P.; Lutzweiler, G.; Coelho, T.; Faro, A.; Pinto, J. F.; Cardoso, C. S.; Silva, A. V.; Pereira, M. M. Biomass-Assisted Zeolite Syntheses as a Tool for Designing New Acid Catalysts. ChemCatChem 2017, 9 (12), 2065–2079. https://doi.org/10.1002/CCTC.201700062.

(111) Liu, S.; Cheng, Z.; Li, B.; Zeng, H.; Liang, W.; Luo, Y.; Bai, Y.; Gao, H.; Pan, X.; Shu, X. Recent Advances in Biomass-Assisted Synthesis of Hierarchical Porous Zeolite. Mater Today Sustain 2024, 27, 100917. https://doi.org/10.1016/J.MTSUST.2024.100917.

(112) Greer, H.; Wheatley, P. S.; Ashbrook, S. E.; Morris, R. E.; Zhou, W. Early Stage Reversed Crystal Growth of Zeolite A and Its Phase Transformation to Sodalite. J. Am. Chem. Soc. 2009, 131 (49), 17986–17992. https://doi.org/10.1021/JA907475Z.

(113) Vu, D.; Marquez, M.; Larsen, G. A Facile Method to Deposit Zeolites Y and L onto Cellulose Fibers. Micropor. Mesopor. Mater. 2002, 55 (1), 93–101. https://doi.org/10.1016/S1387-1811(02)00409-2.

(114) Rani, P.; Srivastava, R. Comprehensive Understanding of the Eco-Friendly Synthesis of Zeolites: Needs of 21st Century Sustainable Chemical Industries. Chem. Rec. 2020, 20 (9), 968–988. https://doi.org/10.1002/TCR.202000062.

(115) Balkus, K. J.; Gabrielov, A. G. Zeolite Encapsulated Metal Complexes. J. Inclusion Phenom. Mol. Recognit. Chem. 1995, 21 (1–4), 159–184. https://doi.org/10.1007/BF00709415.

(116) Ou, Z.; Li, Y.; Wu, W.; Bi, Y.; Xing, E.; Yu, T.; Chen, Q. Encapsulating Subnanometric Metal Clusters in Zeolites for Catalysis and Their Challenges.

J. Chem. Eng. 2022, 430, 132925. https://doi.org/10.1016/J.CEJ.2021.132925.

(117) Lv, W.; Sun, F.; Zhang, R.; Jiao, W.; Qin, Z.; Dong, M.; Fan, W.; Wang, J. Al-Rich Cu-SSZ-13 Zeolite Synthesized by Interconversion from Y: Crystallization Process Resolution and Application in the Selective Catalytic Reduction of NO with NH3. Micropor. Mesopor. Mater. 2024, 370, 113073. https://doi.org/10.1016/J.MICROMESO.2024.113073.

(118) Kweon, S.; An, H.; Son, Y. M.; Park, M. B.; Min, H. K. Hydrothermal Interconversion of FAU-Type Zeolite in the Presence of Sodium and Tetramethylammonium Ions. Micropor. Mesopor. Mater. 2021, 317, 111019. https://doi.org/10.1016/J.MICROMESO.2021.111019.

(119) Goel, S.; Zones, S. I.; Iglesia, E. Synthesis of Zeolites via Interzeolite Transformations without Organic Structure-Directing Agents. Chem. Mater. 2015, 27 (6), 2056–2066. https://doi.org/10.1021/CM504510F.

(120) Arumugam, M.; Wong, K. L.; Nadarajan, A.; Lai, S. Y.; Goh, C. K.; Triwahyono, S.; Taufiq-Yap, Y. H. Green Solvothermal Synthesis and Characterisation of Surface Organosilylated Hierarchical Nanozeolite ZSM-5. Micropor. Mesopor. Mater. 2022, 329, 111516. https://doi.org/10.1016/J.MICROMESO.2021.111516.

(121) Faghihian, H.; Godazandeha, N. Synthesis of Nano Crystalline Zeolite Y from Bentonite. J. Porous Mater. 2009, 16 (3), 331–335. https://doi.org/10.1007/S10934-008-9204-0.

(122) Chen, C.; Park, D. W.; Ahn, W. S. CO2 Capture Using Zeolite 13X Prepared from Bentonite. App. Surf. Sci. 2014, 292, 63–67. https://doi.org/10.1016/J.APSUSC.2013.11.064.

(123) Shimizu, S.; Kiyozumi, Y.; Maeda, K.; Mizukami, F.; Pál-Borbély, G.; Magdolna Mihályi, R.; Beyer, H. K. Transformation of Intercalated Layered Silicates to Zeolites in the Solid State. Adv. Mater. 1996, 8 (9), 759–762. https://doi.org/10.1002/ADMA.19960080913.

(124) Ríos, C. A.; Williams, C. D.; Fullen, M. A. Nucleation and Growth History of Zeolite LTA Synthesized from Kaolinite by Two Different Methods. App. Clay Sci. 2009, 42 (3–4), 446–454. https://doi.org/10.1016/J.CLAY.2008.05.006.

(125) Pan, F.; Lu, X.; Wang, Y.; Chen, S.; Wang, T.; Yan, Y. Organic Template-Free Synthesis of ZSM-5 Zeolite from Coal-Series Kaolinite. Mater. Lett. 2014, 115, 5–8. https://doi.org/10.1016/J.MATLET.2013.10.007.

(126) Li, X. Y.; Jiang, Y.; Liu, X. Q.; Shi, L. Y.; Zhang, D. Y.; Sun, L. B. Direct Synthesis of Zeolites from a Natural Clay, Attapulgite. ACS Sustainable Chem. Eng. 2017, 5 (7), 6124–6130. https://doi.org/10.1021/ACSSUSCHEMENG.7B01001.

(127) Yu, J.; Yang, Y.; Chen, W.; Xu, D.; Guo, H.; Li, K.; Liu, H. The Synthesis and Application of Zeolitic Material from Fly Ash by One-Pot Method at Low Temperature. Green Energy Environ. 2016, 1 (2), 166–171. https://doi.org/10.1016/J.GEE.2016.07.002.

(128) Dere Ozdemir, O.; Piskin, S. A Novel Synthesis Method of Zeolite X From Coal Fly Ash: Alkaline Fusion Followed by Ultrasonic-Assisted Synthesis

Method. Waste Biomass Valori 2019, 10 (1), 143–154. https://doi.org/10.1007/S12649-017-0050-7.

(129) Tan, W. C.; Yap, S. Y.; Matsumoto, A.; Othman, R.; Yeoh, F. Y. Synthesis and Characterization of Zeolites NaA and NaY from Rice Husk Ash. Adsorption 2011, 17 (5), 863–868. https://doi.org/10.1007/S10450-011-9350-6.

(130) Kordatos, K.; Gavela, S.; Ntziouni, A.; Pistiolas, K. N.; Kyritsi, A.; Kasselouri-Rigopoulou, V. Synthesis of Highly Siliceous ZSM-5 Zeolite Using Silica from Rice Husk Ash. Micropor. Mesopor. Mater. 2008, 115 (1–2), 189–196. https://doi.org/10.1016/J.MICROMESO.2007.12.032.

(131) Mohamed, M. M.; Zidan, F. I.; Thabet, M. Synthesis of ZSM-5 Zeolite from Rice Husk Ash: Characterization and Implications for Photocatalytic Degradation Catalysts. Micropor. Mesopor. Mater. 2008, 108 (1–3), 193–203. https://doi.org/10.1016/J.MICROMESO.2007.03.043.

(132) Petkowicz, D. I.; Rigo, R. T.; Radtke, C.; Pergher, S. B.; dos Santos, J. H. Z. Zeolite NaA from Brazilian Chrysotile and Rice Husk. Micropor. Mesopor. Mater. 2008, 116 (1–3), 548–554. https://doi.org/10.1016/J.MICROMESO.2008.05.014.

(133) Prasetyoko, D.; Ramli, Z.; Endud, S.; Hamdan, H.; Sulikowski, B. Conversion of Rice Husk Ash to Zeolite Beta. Waste Manag. 2006, 26 (10), 1173–1179. https://doi.org/10.1016/J.WASMAN.2005.09.009.

(134) Anuwattana, R.; Balkus, K. J.; Asavapisit, S.; Khummongkol, P. Conventional and Microwave Hydrothermal Synthesis of Zeolite ZSM-5 from the Cupola Slag. Micropor. Mesopor. Mater. 2008, 111 (1–3), 260–266. https://doi.org/10.1016/J.MICROMESO.2007.07.039.

(135) Kessler, H. Recent Advances in Zeolite Synthesis. Stud. Surf. Sci. Catal. 1989, 52 (C), 17–37. https://doi.org/10.1016/S0167-2991(08)60513-3.

(136) Burton, A. W.; Zones, S. I. Organic Molecules in Zeolite Synthesis: Their Preparation and Structure-Directing Effects. Stud. Surf. Sci. Catal. 2007, 168, 137–179. https://doi.org/10.1016/S0167-2991(07)80793-2.

(137) Díaz-Cabañas, M. J.; Barrett, P. A.; Camblor, M. A. Synthesis and Structure of Pure SiO2 Chabazite: The SiO2 Polymorph with the Lowest Framework Density. Chem. Comm. 1998, No. 17, 1881–1882. https://doi.org/10.1039/A804800B.

(138) Dusselier, M.; Davis, M. E. Small-Pore Zeolites: Synthesis and Catalysis. Chem. Rev. 2018, 118 (11), 5265–5329. https://doi.org/10.1021/ACS.CHEMREV.7B00738.

(139) Lu, P.; Mayoral, A.; Gómez-Hortigüela, L.; Zhang, Y.; Camblor, M. A. Synthesis of 3D Large-Pore Germanosilicate Zeolites Using Imidazolium-Based Long Dications. Chem. Mater. 2019, 31 (15), 5484–5493. https://doi.org/10.1021/ACS.CHEMMATER.9B00959.

(140) Cai, X.; Zhao, Y.; Zi, W.; Jiao, F.; Du, H. Synthesis and Characterization of A Stable Extra-Large-Pore Zeolite with 15×12×12 Member-Ring Channels. Chem. Eur. J. 2022, 28 (45), e202200934. https://doi.org/10.1002/CHEM.202200934.

(141) Louis, B.; Kiwi-Minsker, L. Synthesis of ZSM-5 Zeolite in Fluoride Media: An Innovative Approach to Tailor Both Crystal Size and Acidity. Micropor. Mesopor. Mater. 2004, 74 (1–3), 171–178. https://doi.org/10.1016/J.MICROMESO.2004.06.016.

(142) Wang, C.; Guo, H.; Leng, S.; Yu, J.; Feng, K.; Cao, L.; Huang, J. Regulation of Hydrophilicity/Hydrophobicity of Aluminosilicate Zeolites: A Review. Crit. Rev. Solid State Mater. Sci. 2021, 46 (4), 330–348. https://doi.org/10.1080/10408436.2020.1819198.

(143) Devos, J.; Shah, M. A.; Dusselier, M. On the Key Role of Aluminium and Other Heteroatoms during Interzeolite Conversion Synthesis. RSC Adv. 2021, 11 (42), 26188. https://doi.org/10.1039/D1RA02887A.

(144) Li, C.; Vidal-Moya, A.; Miguel, P. J.; Dedecek, J.; Boronat, M.; Corma, A. Selective Introduction of Acid Sites in Different Confined Positions in ZSM-5 and Its Catalytic Implications. ACS Catal. 2018, 8 (8), 7688–7697. https://doi.org/10.1021/ACSCATAL.8B02112.

(145) S. P. Zhsanov. Some Problems of Zeolite Crystallization. Adv. Chem. Am. Chem. Soc 1974, 101, 20–43. https://doi.org/10.1021/ba-1971-0101.ch002.

(146) Yang, S.; Navrotsky, A. An in Situ Calorimetric Study of Zeolite Crystallization Kinetics. Micropor. Mesopor. Mater. 2002, 52 (2), 93–103. https://doi.org/10.1016/S1387-1811(02)00276-7.

(147) Itani, L.; Bozhilov, K. N.; Clet, G.; Delmotte, L.; Valtchev, V. Factors That Control Zeolite L Crystal Size. Chem. Eur. J 2011, 17 (7), 2199–2210. https://doi.org/10.1002/CHEM.201002622.

(148) Uzcátegui, D.; González, G. Study of the Kinetics of Crystallization of Zeolite MEL. Catal.Today 2005, 107–108, 901–905. https://doi.org/10.1016/J.CATTOD.2005.07.041.

(149) Francis, R. J.; O'Hare, D. The Kinetics and Mechanisms of the Crystallisation of Microporous Materials. J. Chem. Soc., Dalton Trans. 1998, 0 (19), 3133–3148. https://doi.org/10.1039/A802330A.

(150) SenGupta, A. K. Ion Exchange in Environmental Processes: Fundamentals, Applications and Sustainable Technology, 1st ed.; Wiley, 2017; Vol. 1. https://doi.org/10.1002/9781119421252.

(151) Velarde, L.; Nabavi, M. S.; Escalera, E.; Antti, M. L.; Akhtar, F. Adsorption of Heavy Metals on Natural Zeolites: A Review. Chemosphere 2023, 328, 138508. https://doi.org/10.1016/J.CHEMOSPHERE.2023.138508.

(152) Jiménez-Reyes, M.; Almazán-Sánchez, P. T.; Solache-Ríos, M. Radioactive Waste Treatments by Using Zeolites. A Short Review. J. Environ. Radioact. 2021, 233, 106610. https://doi.org/10.1016/J.JENVRAD.2021.106610.

(153) Reeve, P. J.; Fallowfield, H. J. Natural and Surfactant Modified Zeolites: A Review of Their Applications for Water Remediation with a Focus on Surfactant Desorption and Toxicity towards Microorganisms. J. Environ. Manage. 2018, 205, 253–261. https://doi.org/10.1016/J.JENVMAN.2017.09.077.

(154) Hrenovic, J.; Rozic, M.; Sekovanic, L.; Anic-Vucinic, A. Interaction of Surfactant-Modified Zeolites and Phosphate Accumulating Bacteria. J. Hazard. Mater. 2008, 156 (1–3), 576–582. https://doi.org/10.1016/J.JHAZMAT.2007.12.060.

(155) Pérez-Botella, E.; Palomino, M.; Valencia, S.; Rey, F. Zeolites and Other Adsorbents. In Nanoporous Materials for Gas Storage; Kaneko K., Rodríguez-

Reinoso, F., Eds.; Springer Verlag, 2019; pp 173–208. https://doi.org/10.1007/978-981-13-3504-4_7.

(156) Pérez-Botella, E.; Valencia, S.; Rey, F. Zeolites in Adsorption Processes: State of the Art and Future Prospects. Chem. Rev. 2022, 122 (24), 17647–17695. https://doi.org/10.1021/acs.chemrev.2c00140.

(157) Kerry, F. G. Industrial Gas Handbook: Gas Separation and Purification, 1st ed.; CRC Press, 2007. https://doi.org/10.1201/9781420008265.

(158) Liu, Y.; Tao, H.; Yang, X.; Wu, X.; Li, J.; Zhang, C.; Yang, R. T.; Li, Z. Adsorptive Purification of NOx by HZSM-5 Zeolites: Effects of Si/Al Ratio, Temperature, Humidity, and Gas Composition. Micropor. Mesopor. Mater. 2023, 348, 112331. https://doi.org/10.1016/J.MICROMESO.2022.112331.

(159) Bahmanzadegan, F.; Ghaemi, A. A Comprehensive Review on Novel Zeolite-Based Adsorbents for Environmental Pollutant. J. Hazard. Mater. Adv. 2025, 17, 100617. https://doi.org/10.1016/J.HAZADV.2025.100617.

(160) Lang, Q.; Lu, P.; Yang, X.; Valtchev, V. Zeolites for the Environment. Green Carbon 2024, 2 (1), 12–32. https://doi.org/10.1016/J.GREENCA.2024.02.007.

(161) Yu, N.; Wang, R. Z.; Wang, L. W. Sorption Thermal Storage for Solar Energy. Prog. Energy Combust. Sci. 2013, 39 (5), 489–514. https://doi.org/10.1016/J.PECS.2013.05.004.

(162) Krajnc, A.; Varlec, J.; Mazaj, M.; Ristic, A.; Zabukovec Logar, N.; Mali, G.; Krajnc, A.; Varlec, J.; Mazaj, M.; Ristic, A.; Logar, N. Z.; Mali, G. Superior Performance of Microporous Aluminophosphate with LTA Topology in Solar-

Energy Storage and Heat Reallocation. Adv. Energy Mater. 2017, 7 (11), 1601815. https://doi.org/10.1002/AENM.201601815.

(163) Hauer, A. Adsorption Systems for Test—Design and Demonstration Projects. In Thermal Energy Storage for Sustainable Energy Consumption; Paksoy, H. Ö., Ed.; Springer, Dordrecht, 2007; pp 409–427. https://doi.org/10.1007/978-1-4020-5290-3_25.

(164) Krönauer, A.; Lävemann, E.; Brückner, S.; Hauer, A. Mobile Sorption Heat Storage in Industrial Waste Heat Recovery. Energy Procedia 2015, 73, 272–280. https://doi.org/10.1016/J.EGYPRO.2015.07.688.

(165) Corma, A. From Microporous to Mesoporous Molecular Sieve Materials and Their Use in Catalysis. Chem. Rev. 1997, 97 (6), 2373–2419. https://doi.org/10.1021/CR960406N.

(166) Vermeiren, W.; Gilson, J. P. Impact of Zeolites on the Petroleum and Petrochemical Industry. Top. Catal. 2009, 52 (9), 1131–1161. https://doi.org/10.1007/S11244-009-9271-8.

(167) Primo, A.; Garcia, H. Zeolites as Catalysts in Oil Refining. Chem. Soc. Rev. 2014, 43 (22), 7548–7561. https://doi.org/10.1039/C3CS60394F.

(168) Da Silva, M. J. Synthesis of Methanol from Methane: Challenges and Advances on the Multi-Step (Syngas) and One-Step Routes (DMTM). Fuel Process. Technol. 2016, 145, 42–61. https://doi.org/10.1016/J.FUPROC.2016.01.023.

(169) Shamsul, N. S.; Kamarudin, S. K.; Rahman, N. A.; Kofli, N. T. An Overview on the Production of Bio-Methanol as Potential Renewable Energy.

Renew. Sustain. Energy Rev. 2014, 33, 578–588. https://doi.org/10.1016/J.RSER.2014.02.024.

(170) Dalena, F.; Senatore, A.; Marino, A.; Gordano, A.; Basile, M.; Basile, A. Methanol Production and Applications: An Overview. In Methanol: Science and Engineering; Basile. Angelo, Dalena. Francesco, Eds.; Elsevier, 2018; pp 3–28. https://doi.org/10.1016/B978-0-444-63903-5.00001-7.

(171) Wang, S.; Qin, Z.; Dong, M.; Wang, J.; Fan, W. Recent Progress on MTO Reaction Mechanisms and Regulation of Acid Site Distribution in the Zeolite Framework. Chem Catal. 2022, 2 (7), 1657–1685. https://doi.org/10.1016/J.CHECAT.2022.05.012.

(172) He, L.-N.; Rogers, R. D.; Su, D.; Tundo, P.; Conrad Zhang, Z. Zeolites in Sustainable Chemistry: Synthesis, Characterization and Catalytic Applications, 1st ed.; Xiao Feng-Shou, Meng Xiangju, Eds.; Springer Berlin Heidelberg, 2015. https://doi.org/10.1007/978-3-662-47395-5.

(173) Olsbye, U.; Svelle, S.; Bjrgen, M.; Beato, P.; Janssens, T. V. W.; Joensen, F.; Bordiga, S.; Lillerud, K. P. Conversion of Methanol to Hydrocarbons: How Zeolite Cavity and Pore Size Controls Product Selectivity. Angew. Chem. Int. Ed. 2012, 51 (24), 5810–5831. https://doi.org/10.1002/ANIE.201103657.

(174) Margarit, V. J.; Gallego, E. M.; Paris, C.; Boronat, M.; Moliner, M.; Corma, A. Production of Aromatics from Biomass by Computer-Aided Selection of the Zeolite Catalyst. Green Chem. 2020, 22 (15), 5123–5131. https://doi.org/10.1039/D0GC01031F.

(175) Teixeira, I. F.; Lo, B. T. W.; Kostetskyy, P.; Stamatakis, M.; Ye, L.; Tang, C. C.; Mpourmpakis, G.; Tsang, S. C. E. From Biomass-Derived Furans to

Aromatics with Ethanol over Zeolite. Angew. Chem. Int. Ed. 2016, 55 (42), 13061–13066. https://doi.org/10.1002/ANIE.201604108.

(176) Pacheco, J. J.; Davis, M. E. Synthesis of Terephthalic Acid via Diels-Alder Reactions with Ethylene and Oxidized Variants of 5-Hydroxymethylfurfural. Proc Natl Acad Sci U S A 2014, 111 (23), 8363–8367. https://doi.org/10.1073/PNAS.1408345111.

(177) De Clercq, R.; Dusselier, M.; Dijkmans, J.; Iacobescu, R. I.; Pontikes, Y.; Sels, B. F. Confinement Effects in Lewis Acid-Catalyzed Sugar Conversion: Steering Toward Functional Polyester Building Blocks. ACS Catal. 2015, 5 (10), 5803–5811. https://doi.org/10.1021/ACSCATAL.5B01344.

(178) Corma, A.; Nemeth, L. T.; Renz, M.; Valencia, S. Sn-Zeolite Beta as a Heterogeneous Chemoselective Catalyst for Baeyer–Villiger Oxidations. Nature 2001 412:6845 2001, 412 (6845), 423–425. https://doi.org/10.1038/35086546.

(179) Luo, H. Y.; Lewis, J. D.; Román-Leshkov, Y. Lewis Acid Zeolites for Biomass Conversion: Perspectives and Challenges on Reactivity, Synthesis, and Stability. Annu. Rev. Chem. Biomol. Eng. 2016, 7, 663–692. https://doi.org/10.1146/ANNUREV-CHEMBIOENG-080615-034551.

(180) Rodríguez-Fernández, A.; Di Iorio, J. R.; Paris, C.; Boronat, M.; Corma, A.; Román-Leshkov, Y.; Moliner, M. Selective Active Site Placement in Lewis Acid Zeolites and Implications for Catalysis of Oxygenated Compounds. Chem. Sci. 2020, 11 (37), 10225–10235. https://doi.org/10.1039/D0SC03809A.

(181) Zhang, H.; Samsudin, I. bin; Jaenicke, S.; Chuah, G. K. Zeolites in Catalysis: Sustainable Synthesis and Its Impact on Properties and Applications. Catal. Sci. Technol. 2022, 12 (19), 6024–6039. https://doi.org/10.1039/D2CY01325H.

(182) Corma, A.; Domine, M. E.; Valencia, S. Water-Resistant Solid Lewis Acid Catalysts: Meerwein–Ponndorf–Verley and Oppenauer Reactions Catalyzed by Tin-Beta Zeolite. J. Catal, 2003, 215 (2), 294–304. https://doi.org/10.1016/S0021-9517(03)00014-9.

(183) Borfecchia, E.; Beato, P.; Svelle, S.; Olsbye, U.; Lamberti, C.; Bordiga, S. Cu-CHA – a Model System for Applied Selective Redox Catalysis. Chem. Soc. Rev. 2018, 47 (22), 8097–8133. https://doi.org/10.1039/C8CS00373D.

(184) Di Iorio, J. R.; Bates, S. A.; Verma, A. A.; Delgass, W. N.; Ribeiro, F. H.; Miller, J. T.; Gounder, R. The Dynamic Nature of Brønsted Acid Sites in Cu-Zeolites During NOx Selective Catalytic Reduction: Quantification by Gas-Phase Ammonia Titration. Top. Catal. 2015, 58 (7–9), 424–434. https://doi.org/10.1007/S11244-015-0387-8.

(185) Paolucci, C.; Khurana, I.; Parekh, A. A.; Li, S.; Shih, A. J.; Li, H.; Di Iorio, J. R.; Albarracin-Caballero, J. D.; Yezerets, A.; Miller, J. T.; Delgass, W. N.; Ribeiro, F. H.; Schneider, W. F.; Gounder, R. Dynamic Multinuclear Sites Formed by Mobilized Copper Ions in NOx Selective Catalytic Reduction. Science (1979) 2017, 357 (6354), 898–903. https://doi.org/10.1126/SCIENCE.AAN5630.

(186) Yan, P.; Peng, H.; Wu, X.; Rabiee, H.; Weng, Y.; Konarova, M.; Vogrin, J.; Rozhkovskaya, A.; Zhu, Z. Impact of Varied Zeolite Materials on Nickel

Catalysts in CO2 Methanation. J. Catal. 2024, 432, 115439. https://doi.org/10.1016/J.JCAT.2024.115439.

(187) Bacariza, M. C.; Graça, I.; Lopes, J. M.; Henriques, C. Tuning Zeolite Properties towards CO2 Methanation: An Overview. ChemCatChem 2019, 11 (10), 2388–2400. https://doi.org/10.1002/CCTC.201900229.

(188) Ma, S.; Li, X.; Yang, Z.; Li, H. Size Effect of Encapsulated Metal within Zeolite: Biomass, CO2 and Methane Utilization. J. Catal. 2023, 417, 368–378. https://doi.org/10.1016/J.JCAT.2022.12.010.

(189) Liu, L.; Lopez-Haro, M.; Lopes, C. W.; Li, C.; Concepcion, P.; Simonelli, L.; Calvino, J. J.; Corma, A. Regioselective Generation and Reactivity Control of Subnanometric Platinum Clusters in Zeolites for High-Temperature Catalysis. Nat. Mater. 2019, 18 (8), 866–873. https://doi.org/10.1038/s41563-019-0412-6.

(190) Pappas, D. K.; Borfecchia, E.; Dyballa, M.; Pankin, I. A.; Lomachenko, K. A.; Martini, A.; Signorile, M.; Teketel, S.; Arstad, B.; Berlier, G.; Lamberti, C.; Bordiga, S.; Olsbye, U.; Lillerud, K. P.; Svelle, S.; Beato, P. Methane to Methanol: Structure-Activity Relationships for Cu-CHA. J. Am. Chem. Soc. 2017, 139 (42), 14961–14975. https://doi.org/10.1021/JACS.7B06472.

(191) Zhu, K.; Liang, S.; Cui, X.; Huang, R.; Wan, N.; Hua, L.; Li, H.; Chen, H.; Zhao, Z.; Hou, G.; Li, M.; Jiang, Q.; Yu, L.; Deng, D. Highly Efficient Conversion of Methane to Formic Acid under Mild Conditions at ZSM-5-Confined Fe-Sites. Nano Energy 2021, 82, 105718. https://doi.org/10.1016/J.NANOEN.2020.105718.

(192) Mortensen, R. L.; Noack, H. D.; Pedersen, K.; Mossin, S.; Mielby, J. Recent Advances in Complete Methane Oxidation Using Zeolite-Supported Metal Nanoparticle Catalysts. ChemCatChem 2022, 14 (16), e202101924. https://doi.org/10.1002/CCTC.202101924.

(193) Gélin, P.; Primet, M. Complete Oxidation of Methane at Low Temperature over Noble Metal Based Catalysts: A Review. App. Catal. B: Environ. 2002, 39 (1), 1–37. https://doi.org/10.1016/S0926-3373(02)00076-0.

(194) Wang, C.; Wang, L.; Zhang, J.; Wang, H.; Lewis, J. P.; Xiao, F. S. Product Selectivity Controlled by Zeolite Crystals in Biomass Hydrogenation over a Palladium Catalyst. J. Am. Chem. Soc. 2016, 138 (25), 7880–7883. https://doi.org/10.1021/JACS.6B04951.

(195) Liu, H.; Li, J.; Liang, X.; Ren, H.; Yin, H.; Wang, L.; Yang, D.; Wang, D.; Li, Y. Encapsulation of Pd Single-Atom Sites in Zeolite for Highly Efficient Semihydrogenation of Alkynes. J. Am. Chem. Soc. 2024, 146 (34), 24033–24041. https://doi.org/10.1021/JACS.4C07674.(196) Zhu, C.; Li, W.; Chen, T.; He, Z.; Villalobos, E.; Marini, C.; Zhou, J.; Woon Lo, B. T.; Xiao, H.; Liu, L. Boosting the Stability of Subnanometer Pt Catalysts by the Presence of Framework Indium(III) Sites in Zeolite. Angew. Chem. Int. Ed. 2024, 63 (41), e202409784. https://doi.org/10.1002/ANIE.202409784.

(197) Zhou, J.; Liu, H.; Xiong, C.; Hu, P.; Wang, H.; Wang, X.; Ji, H. Potassium-Promoted Pt–In Bimetallic Clusters Encapsulated in Silicalite-1 Zeolite for Efficient Propane Dehydrogenation. J. Chem. Eng. 2023, 455, 139794. https://doi.org/10.1016/J.CEJ.2022.139794.

(198) He, Z.; Yang, J.; Liu, L. Design of Supported Metal Catalysts and Systems for Propane Dehydrogenation. JACS Au 2024, 4 (11). https://doi.org/10.1021/JACSAU.4C00730.

(199) Wan, H.; Qian, L.; Gong, N.; Hou, H.; Dou, X.; Zheng, L.; Zhang, L.; Liu, L. Size-Dependent Structures and Catalytic Properties of Supported Bimetallic PtSn Catalysts for Propane Dehydrogenation Reaction. ACS Catal. 2023, 13 (11), 7383–7394. https://doi.org/10.1021/ACSCATAL.3C00548.

(200) Luo, L.; Zhou, T.; Li, W.; Li, X.; Yan, H.; Chen, W.; Xu, Q.; Hu, S.; Ma, C.; Bao, J.; Pao, C. W.; Wang, Z.; Li, H.; Ma, X.; Luo, L.; Zeng, J. Close Intimacy between PtIn Clusters and Zeolite Channels for Ultrastability toward Propane Dehydrogenation. Nano Lett. 2024, 24 (24), 7236–7243. https://doi.org/10.1021/ACS.NANOLETT.4C01131.

(201) Liu, L.; Corma, A. Bimetallic Sites for Catalysis: From Binuclear Metal Sites to Bimetallic Nanoclusters and Nanoparticles. Chem. Rev. 2023, 123 (8), 4855–4933. https://doi.org/10.1021/acs.chemrev.2c00733.

(202) Li, C.; Meyer, R. J.; Yacob, S.; Gomez, E.; Lopez-Haro, M.; Calvino, J. J.; Moliner, M.; Serna, P.; Corma, A. Highly Stable Subnanometric PtIn Clusters for the Selective Dehydrogenation of Alkanes. ChemSusChem 2025, 18 (2), e202401284. https://doi.org/10.1002/CSSC.202401284.

(203) Dijkmans, J.; Dusselier, M.; Gabriëls, D.; Houthoofd, K.; Magusin, P. C. M. M.; Huang, S.; Pontikes, Y.; Trekels, M.; Vantomme, A.; Giebeler, L.; Oswald, S.; Sels, B. F. Cooperative Catalysis for Multistep Biomass Conversion with Sn/Al Beta Zeolite. ACS Catal. 2015, 5 (2), 928–940. https://doi.org/10.1021/CS501388E.

(204) Iglesias, J.; Moreno, J.; Morales, G.; Melero, J. A.; Juárez, P.; López-Granados, M.; Mariscal, R.; Martínez-Salazar, I. Sn–Al-USY for the Valorization of Glucose to Methyl Lactate: Switching from Hydrolytic to Retro-Aldol Activity by Alkaline Ion Exchange. Green Chem. 2019, 21 (21), 5876–5885. https://doi.org/10.1039/C9GC02609F.

(205) Wang, C.; Zheng, M.; Li, X.; Li, X.; Zhang, T. Catalytic Conversion of Ethanol into Butadiene over High Performance LiZnHf-MFI Zeolite Nanosheets. Green Chem. 2019, 21 (5), 1006–1010. https://doi.org/10.1039/C8GC03983F.

(206) Sushkevich, V. L.; Ivanova, I. I. Ag-Promoted ZrBEA Zeolites Obtained by Post-Synthetic Modification for Conversion of Ethanol to Butadiene. ChemSusChem 2016, 9 (16), 2216–2225. https://doi.org/10.1002/CSSC.201600572.

(207) Koninckx, E.; Mendes, P. S. F.; Thybaut, J. W.; Broadbelt, L. J. Ethylene Oligomerization on Nickel Catalysts on a Solid Acid Support: From New Mechanistic Insights to Tunable Bifunctionality. App. Catal. A: Gen. 2021, 624, 118296. https://doi.org/10.1016/J.APCATA.2021.118296.

(208) Mohamed, H. O.; Velisoju, V. K.; Hita, I.; Abed, O.; Parsapur, R. K.; Zambrano, N.; Hassine, M. Ben; Morlanes, N.; Emwas, A. H.; Huang, K. W.; Castaño, P. Highly Productive Framework Bounded Ni2+ on Hierarchical Zeolite for Ethylene Oligomerization. J. Chem. Eng. 2023, 475, 146077. https://doi.org/10.1016/J.CEJ.2023.146077.

(209) Rajapaksha, R.; Samanta, P.; Quadrelli, E. A.; Canivet, J. Heterogenization of Molecular Catalysts within Porous Solids: The Case of Ni-Catalyzed Ethylene Oligomerization from Zeolites to Metal–Organic

Frameworks. Chem. Soc. Rev. 2023, 52 (22), 8059–8076. https://doi.org/10.1039/D3CS00188A.

(210) Martínez Gómez-Aldaraví, A.; Paris, C.; Moliner, M.; Martínez, C. Design of Bi-Functional Ni-Zeolites for Ethylene Oligomerization: Controlling Ni Speciation and Zeolite Properties by One-Pot and Post-Synthetic Ni Incorporation. J. Catal. 2023, 426, 140–152. https://doi.org/10.1016/j.jcat.2023.07.010.

CHAPTER 2:
OBJECTIVES

This doctoral thesis explores innovative methodologies and synthesis strategies for producing zeolites with well-defined crystalline structures and tailored physicochemical, textural, and catalytic properties, enabling their application as heterogenous catalysts in industrial and environmentally relevant chemical processes. To achieve this goal, the thesis focuses on optimizing synthesis processes by selectively modifying the species involved in the formation of the final zeolitic catalyst, as well as adjusting key synthesis parameters that influence the resulting material properties. Across the various chapters, this doctoral thesis aims to achieve the following objectives.

- The first objective of this doctoral thesis, discussed in **Chapter 4**, is to enhance the catalytic performance of bimetallic clusters encapsulated within MFI-type zeolitic catalysts by optimizing the chemical composition of the initial synthesis gel. This study proposes a rational design approach, evaluating the synergistic effect of charge counter-balance alkali cations in combination with additional metal species. This strategy aims to maximize the dispersion and stabilization of the bimetallic clusters through the controlled formation of alloys with superior properties, improving both the catalytic activity and stability of the catalysts in the non-oxidative dehydrogenation of propane.

- The second and third objectives of this PhD thesis, explored in **Chapter 5**, are: (i) to enhance the catalytic performance of purely siliceous MFI-type zeolites with noble metal active centres in the semi-hydrogenation of phenylacetylene by precisely controlling the final particle size of the zeolite supports, improving their diffusive

properties. This is achieved by adjusting the crystallization temperature, which directly impacts the nucleation and growth processes of the crystals; and (ii) to improve the materials stability against undesired leaching or sintering phenomena through the development of hydrophobic crystalline coatings, utilizing an ultrafast hydrothermal synthesis approach.

- The fourth objective of this doctoral thesis, explored in **Chapter 6**, is the development of bifunctional medium-pore (MFI) and large pore (BEA) zeolite-type catalysts containing Brønsted acid sites and non-noble metal centres, for the evaluation of their catalytic performance in ethylene oligomerization under varying reaction conditions. The tailored catalytic properties are achieved through a combined strategy involving: (i) the method of metal incorporation, (ii) the rational design of the chemical composition of the synthesis gel, and (iii) the controlled modulation of the final crystalline particle size by employing specific organic structure-directing agents (OSDAs). This approach enables the synthesis of zeolitic catalysts with finely tuned physicochemical characteristics (acidity, nature of the metal centre) and diffusive properties (crystal size, topology).

CHAPTER 3:
METHODOLOGY

3.1 SYNTHESIS OF THE ORGANIC STRUCTURE DIRECTING AGENTS SYNTHESIS (OSDAs)

The Organic Structure Directing Agents (OSDAs) employed in the present thesis are summarized in **Figure 3.1**, including their names and internal nomenclature.

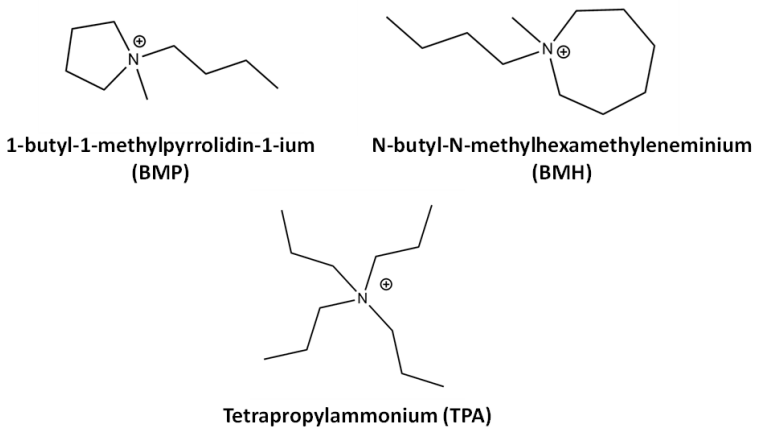

Figure 3.1. OSDA molecules employed in the present thesis.

Tetrapropylammonium (TPA) hydroxide sources are commercially available, including one from Fisher (40 wt%, K-free) and one from Sigma-Aldrich (1 M in H_2O, K traces ≈ 0.6 wt%).

In addition to the above commercially available OSDA molecules, other two organic cations, 1-butyl-1-methylpyrrolidin-1-ium (BMP) and N-butyl-N-methylhexamethyleneminium (BMH), were synthetized as described below.

The molecular structures were characterized by ^{1}H and ^{13}C, DEPT-^{13}C NMR and elemental analysis.

3.1.1. Synthesis of the 1-butyl-1-methylpyrrolidin-1-ium (BMP)

The BMP was synthetized following the procedure described by Gallego *et al*[1]. First, 15 g of 1-butylpyrrolidine (Sigma-Aldrich, 98 wt%) was dissolved in 200 mL of chloroform (J.T Baker, 99 wt%) inside a two-neck round flask fitted a stirrer and a glass condenser. The flask was immersed in an ice bath to maintain the system cooled at 0°C for 30 min under stirring. Then, 33.47 g of iodomethane (Sigma-Aldrich, 99 wt%) was added dropwise. The resulting solution was left under stirring for 3 days at room temperature. Once the reaction finished, the solvent was removed under low-pressure, and the product was crystallized in an ethyl acetate-ethanol solution. Finally, the crystallized 1-butyl-1-methylpyrrolidin-1-ium was recovered by filtration, obtaining 27.6 g of the OSDA halide salt (86.9% molar product yield).

3.1.2. Synthesis of the N-butyl-N-methylhexamethyleneiminium (BMH)

The former procedure described by *Chiappe* and *et al*[2] was modified to obtain the BMH molecule. First, 44.1 g of hexamethylenediamine (Sigma-Aldrich, 99 wt%) was added to 250 mL of anhydrous dimethylformamide (Sigma-Aldrich, 99.8%wt) under an inert atmosphere (Ar). Subsequently, 60.9 g of 1-bromobutane (Sigma-Aldrich, 99 wt%) was added dropwise to the previous mixture under vigorous stirring. The resultant solution was heated to 70°C and maintained under stirring for 16 hours. Once the solution was cooled, at room temperature, the resulting N-butylacepane bromide (whitish salt) was separated by filtration. The salt crystals were washed with a mixture of hexane (Sigma-Aldrich, 99 wt%) and ethyl acetate (Sigma-Aldrich, 99.5 wt%) to remove the remaining dimethylformamide and dried under reduced

pressure. Later, 50.4 g of the obtained intermediate was diluted in 400 mL of MilliQ® water and right after, 22.6 g of anhydrous sodium carbonate (Sigma-Aldrich, 99.5 wt%) was added to the solution and allowed to react under vigorous stirring at room temperature. As the reaction progressed, the reactant medium began to be separated into a biphasic mixture due to the free amine formation. The phases were separated using a glass decanting funnel, and the organic phase was washed with 100 mL of a saturated solution of NaCl (Sigma-Aldrich, 99.5 wt%).

The remaining water was removed mixing the organic phase with anhydrous $MgSO_4$ (Scharlab, 99.99 wt%) and the resulting liquid media was filtered to remove the inorganic salt. The final N-butylhexamethylenimine was obtained as a dense colourless liquid.

In the last step, 21.8 g of the N-butylhexamethylenimine was diluted in 200 mL of chloroform (J.T Baker, 99 wt%). The mixture was cooled in an ice bath at 0^{o}C, and then, 39.9 g of iodomethane (Sigma-Aldrich, 99 wt%) was added dropwise. After the reaction reached room temperature, the mixture was maintained under stirring for 72 hours. After finishing, the solvent was evaporated followed by the addition of a large quantity of ethyl acetate to force the compound precipitation. 40.0 g of N-butyl-N-methylhexamethyleneiminium iodide was achieved (94% molar product yield).

3.1.3. Ionic Exchange of the OSDAs to their hydroxide forms.

The employed OSDAs to synthetize the zeolites in the present thesis were in their OH^- form. In this way, during the gel preparation, they can provide basic pH to favour the Si and Al mobility beyond their directing roles. To exchange the halide form of the OSDAs (X=Cl^-, I^-, Br^-), an ionic exchange resin (Amberlite IRN-78) was employed.

First, the halide OSDA is dissolved in ultrapure water (MilliPore) in a proportion of 2 g per mmol of OSDA. 1 g of resin per OSDA milliequivalent was added after being washed for 4-5 times with distilled water and one last time with ultrapure water. The mixture was maintained under stirring overnight.

The final OSDA molecules, in their OH form, were obtained by filtration and then, titrated with HCl 0.1 N (Sigma-Aldrich), employing a phenolphthalein (0.2 w/w %) - ethanol solution as pH indicator.

The exchange yield, typically above 90%, was determined as follows:

$$Yield\ (\%) = \frac{mol\ OSDA{-}(OH)_n}{mol\ OSDA{-}(X)_n} \cdot 100 \qquad \textbf{Eq 3.1}$$

Where:

- mol OSDA-$(OH)_n$: molar amount of OSDAs in their hydroxide form (and the number of OH groups)
- mol OSDA-$(X)_n$: molar amount of OSDAs in their halide form (and the number of halide groups)

3.2 SYNTHESIS OF MICROPOROUS SOLIDS

3.2.1. Chemical Reagents

The chemical reagents employed to synthesize the zeolites studied in this PhD thesis are listed below:

- The previous described OSDAs molecules in their hydroxide form
- Tetraethylortosilicate (Sigma-Adrich, 98 wt%)
- Colloidal Silica (LUDOX® AS-40, Sigma-Aldrich, 40 wt%)
- Aluminium Hydroxide (Sigma-Aldrich, 85.65 wt%)
- Hydrofluoric Acid (Sigma-Aldrich, 48 wt%)
- Calcium Oxide (Sigma-Aldrich, Reagent Grade)
- Ultra-Pure MilliQ Water (MilliPore)
- CBV3024E (Si/Al=15) Commercial MFI structure (Zeolyst)
- CBV5524 (Si/Al=25) Commercial MFI structure (Zeolyst)
- CBV8020 (Si/Al=40) Commercial MFI structure (Zeolyst)
- CP814E (Si/Al=12.5) Commercial BETA structure (Zeolyst)
- $NiCl_2 \cdot 6H_2O$ (Sigma-Aldrich ,99.9 wt%)
- $Ni(NO_3)_2 \cdot 6H_2O$ (Sigma-Aldrich, 99.99 wt%)
- H_2PtCl_6 (Sigma-Aldrich, 8 wt%)
- $Pd(NH_3)_4(NO_3)_2$ (Sigma-Aldrich, 10 wt%)
- Ethylenediamine (Sigma-Aldrich, 99 wt%)
- $SnCl_4 \cdot 5H_2O$ (Sigma-Aldrich, 98 wt%)

3.2.2. Hydrothermal Synthesis Conditions

The syntheses of the zeolites along the present thesis were carried out by hydrothermal treatment. Homogeneous aqueous gels were prepared by introducing/mixing the required precursor reactants in the adequate molar proportions. Once the gels reached the required compositions, they were transferred into a stainless autoclave with Teflon liners. The autoclaves were heated at temperatures between 100 and 200ºC, permitting the required autogenous pressure to facilitate the crystallization. The autoclave can be heated under static or dynamic conditions.

Once zeolites crystallization was achieved, the autoclaves were cooled down and the content filtered or centrifuged (if the crystal size was too small to be retained by the filters), washing multiple times with abundant water and finally, the solids were dried at 100ºC. The crystalline materials were characterized by powder X-Ray diffraction. The "as prepared" materials were calcined in air at temperatures between 550ºC and 600ºC to remove the organic molecules.

To wash and reutilize the autoclave Teflon liners, a 20% hydrofluoric acid (HF) solution was prepared diluting the commercially available HF solution (Sigma-Aldrich, 48%wt) to dissolve the potential remaining zeolite seeds. After washing multiple times with water, the remaining HF solution was neutralized with CaO, taking place the reaction.

$$2HF + CaO \rightarrow CaF_2 + H_2O$$

CaO was added under vigorous stirring until reaching pH≈7, employing an ice bath to cooldown the HF solution. pH indicator strips (Merck, pH 5-10) were used to check the pH. The neutralization was performed with thicker

reinforced latex gloves (208 Natural Rubber, Sylprotec®) due to the corrosivity of the reaction[3].

3.2.3. Specific Zeolite Syntheses

The following sections describe the experimental procedures followed to synthetize the zeolites employed in this thesis as well as the characterization procedures employed to analyse their physico-chemical properties.

3.2.3.1. Synthesis of MFI type zeolites

The MFI type materials, both in their aluminosilicate and pure silica forms, were synthesized employing 1-butyl-1-methylpyrrolidin-1-ium (BMP) hydroxide and tetrapropylammonium hydroxide, respectively. Besides the OSDA molecules, different precursor reagents were used in each synthesis. The physico-chemical and textural properties, morphology and catalytic behaviour of the zeolites obtained are discussed in more detail in the following chapters.

The synthesis recipes to obtain the different MFI type zeolites, classified according to the employed OSDA and/or the Si and Al sources, are described below.

3.2.3.1.1. Synthesis of the nanosized MFI type zeolite employing amorphous silicon and aluminium sources and 1-butyl-1-methylpyrrolidin-1-ium (BMP) as OSDA.

The nanosized MFI zeolites employed in chapter 6 were synthetized using a similar preparation method to one previously reported[1], using the BMP molecule as OSDA. 0.26 g of $Al(OH)_3$ (Sigma-Aldrich, 85.65 wt%) were mixed with 14.34 g of a 17.8 wt% aqueous solution of the BMP (OH form) and the mixture was maintained under stirring. After homogenizing, 6.01 g of

LUDOX® AS-40 (Sigma-Aldrich, 40 wt%) were added and the mixture was maintained under stirring to evaporate the excess of water until reaching the desired composition.

$$1SiO_2: 0.0167\ Al_2O_3: 0.4\ BMP(OH): 15\ H_2O$$

The final gel was transferred into a Teflon liner inside a stainless-steel autoclave and kept at 150ºC for 7 days under dynamic conditions. After that period, the final solid was recovered by filtration, washed with abundant water and, finally, dried at 80ºC overnight.

3.2.3.1.2. Synthesis of the nanosized Ni-containing MFI type zeolite employing amorphous Silicon/Aluminium sources and 1-butyl-1-methylpyrrolidin-1-ium (BMP) as OSDA.

The nanosized Ni-containing MFI zeolites employed in chapter 6 were synthetized using a similar preparation method to one previously reported[1], using the BMP molecule as OSDA.

0.26 g of $Al(OH)_3$ (Sigma-Aldrich, 85.65 wt%) were mixed with 14.34 g of a 17.8 wt% aqueous solution of the BMP (OH form) and the mixture was maintained under stirring. Simultaneously, 0.26 g of ethylenediamine were mixed with 0.26 g of a 20 wt% aqueous solution of $NiCl_2$ (Sigma-Aldrich, 99 wt%) and diluted in 1.5 g of water under vigorous stirring. Then, the metal containing solution was mixed and homogenized with the previous solution. After homogenizing, 6.01 g of LUDOX® AS-40 (Sigma-Aldrich, 40 wt%) were added and the mixture was maintained under stirring to evaporate the excess of water until reaching the desired composition.

$$1SiO_2: 0.0167\ Al_2O_3: 0.4\ BMP(OH): 0.1\ EDA: 0.0102\ NiCl_2: 15\ H_2O$$

The final gel was transferred into a Teflon liner inside a stainless-steel autoclave and kept at 150°C for 7 days under dynamic conditions. After that period, the final solid was recovered by filtration, washed with abundant water and, finally let dried at 80°C overnight. To obtain the acidic zeolite, the solid was calcined at 550°C in air for 4 hours employing a heating ramp of 1°C/min.

3.2.3.1.3. Synthesis of nano-sized Pd-MFI type zeolite employing amorphous Si sources, inorganic alkaline cations and commercially available tetrapropylammonium hydroxide (TPAOH) as OSDA.

The nano-sized MFI-type zeolites containing Pd species in their channel system and employed in chapter 5 were synthesized using amorphous Si sources, a Pd salt precursor and tetrapropylammonium hydroxide as OSDA. The procedure has been slightly modified from the one described by Liu *et al*[4].

3.30 g of an aqueous solution of TPAOH (Fisher, 40 wt%) were mixed with 1.52 g of an aqueous solution of TPAOH 1.0 M (Sigma-Aldrich 0.6 K wt%), 4.12 g of tetraethylortosilicate (Sigma-Aldrich) and 5 gs of miliQ water and maintained under stirring overnight to hydrolyse the TEOS. After that, 0.046 g of an aqueous solution of $Pd(NH_3)_4(NO_3)_2$ (Sigma-Aldrich, 10 wt%) were added to 0.12 g of ethylenediamine and 4.38 g of miliQ water and dispersed inside an ultrasound bath. The resulting metal-complex suspension was added to the previous alkaline solution and maintained under stirring. The composition of the final gel was:

$$1SiO_2 : 4\ EtOH : 0.405\ TPAOH : 0.0118\ K : 0.0008\ Pd : 0.101\ EDA : 35\ H_2O$$

The final gel is transferred into a Teflon liner inside a stainless-steel autoclave and kept at 80°C for 4 days under dynamic conditions. After that, the final solid was recovered by centrifugation, washed with abundant water until reaching pH≈7, and dried drying al 80°C overnight.

3.2.3.1.4. Synthesis of micron-sized Pd-MFI type zeolite employing amorphous Si sources, inorganic alkaline cations and commercially available tetrapropylammonium hydroxide (TPAOH) as OSDA.

The micro-sized MFI-type zeolites containing in their channel system Pd species employed in chapter 5 were synthesized employing Silicon amorphous sources, a Pd salt precursor and tetrapropylammonium hydroxide as OSDA. The procedure has been slightly modified from the one described by Liu *et al*[4].

2.50 g of an aqueous solution of TPAOH (Fisher, 40 wt%) were mixed with 3.12 g of an aqueous solution of TPAOH 1.0 M (Sigma-Aldrich 0.6 K wt%), 4.12 g of tetraethylortosilicate (Sigma-Aldrich, 98 wt%) and 4.5 g of miliQ water and stirred overnight to hydrolyse the TEOS. After that, 0.082 g of an aqueous solution of $Pd(NH_3)_4(NO_3)_2$ (Sigma-Aldrich, 10 wt%) were added to 0.12 g of ethylenediamine and 4 g of miliQ water and dispersed inside an ultrasound bath. The resulting metal-complex suspension was added to the previous alkaline solution and maintained under stirring. The composition of the final gel was:

$$1\ SiO_2 : 4\ EtOH : 0.405\ TPAOH : 0.0242\ K : 0.0014\ Pd : 0.101\ EDA : 35\ H_2O$$

The final gel was transferred into a Teflon liner inside a stainless-steel autoclave and kept at 175°C for 4 days under dynamic conditions. After that,

the final solid was recovered by centrifugation, washed with abundant water until reaching pH≈7, and dried at 80ºC overnight.

3.2.3.1.5. Synthesis of nano-sized Pt-MFI type zeolite employing amorphous Si sources, inorganic alkaline cations and commercially available tetrapropylammonium hydroxide (TPAOH) as OSDA.

The nanosized MFI-type zeolites containing Pt species in their channel system and employed in chapter 5 were synthesized using amorphous Si sources, a Pt acid precursor and tetrapropylammonium hydroxide as OSDA. The procedure is a slight variation of the one described before by Liu *et al*[4].

3.30 g of an aqueous solution of TPAOH (Fisher, 40 wt%) were mixed with 1.52 g of an aqueous solution of TPAOH 1.0 M (Sigma-Aldrich 0.6 K wt%), 4.12 g of tetraethylortosilicate (Sigma-Aldrich, 98 wt%) and 5 g of miliQ water and let under stirring overnight to hydrolyse the TEOS. After that, 0.079 g of an aqueous solution of H_2PtCl_6 (Sigma-Aldrich, 8 wt%) were added to 0.12 g of ethylenediamine and 4.4 g of miliQ water and dispersed inside an ultrasound bath. The resulting metal-complex suspension was added to the previous alkaline solution and maintained under stirring. The composition reached in the final gel was:

$$1SiO_2 : 4\ EtOH : 0.405\ TPAOH : 0.0118\ K : 0.0008\ Pt : 0.101\ EDA : 35\ H_2O$$

The final gel is transferred into a Teflon liner inside a stainless-steel autoclave and kept at 80ºC for 4 days under dynamic conditions. After that, the final solid was recovered by centrifugation, washed with abundant water until reaching pH≈7, and dried at 80ºC overnight.

3.2.3.1.6. Synthesis of PtSn-MFI type zeolite employing amorphous Si sources, inorganic alkaline cations and commercially available tetrapropylammonium hydroxide (TPAOH) as OSDA.

The MFI-type zeolites employed in chapter 4, hosting in their channel system well dispersed Pt and Sn species, were synthesized employing a procedure similar to that described by Liu *et al*[4], employing amorphous Si sources, a Pt acid as precursor and tetrapropylammonium hydroxide as OSDA.

2.5 g of an aqueous solution of TPAOH (Alfa Aesar, 40 wt%) were mixed with 3.12 g of an aqueous solution of TPAOH 1.0 M (Sigma-Aldrich, 0.6 K wt%). Then, 4.12 g of tetraetylortosilicate (Sigma-Aldrich, 98 wt%) and 6 g of miliQ water were added and stirred overnight to hydrolyse the TEOS. Right after this, 0.18 g of a 20 wt% aqueous solution of $SnCl_4 \cdot 5H_2O$ (Sigma-Aldrich, 98 wt%) were added and stirred for 5 minutes.

Simultaneously, 0.14 g of an aqueous solution of H_2PtCl_6 (Sigma-Aldrich, 8 wt%) were added to 0.12 g of ethylenediamine and 2.5 g of miliQ water and mixed under stirring for 20 min. The resulting metal-complex suspension was added to the previous alkaline solution and maintained under vigorous stirring for 20 min. The composition reached in the final gel was:

$$1SiO_2 : 4\ EtOH : 0.405\ TPAOH : 0.0242\ K : 0.0012\ Pt : 0.005Sn : 0.11\ EDA : 35\ H_2O$$

The final mixture was transferred to a Teflon liner inside a stainless-steel autoclave and heated in an oven at 175°C for 4 days under static conditions. The solid product was filtered and washed with distilled water and acetone and dried overnight at 80°C.

3.2.3.1.7. Synthesis of PtSn-MFI type zeolite employing amorphous Si sources, inorganic alkaline cations provided by inorganic potassium salt and commercially available tetrapropylammonium hydroxide (TPAOH) as OSDA

The MFI-type zeolites employed in chapter 4, hosting in their channel system well dispersed Pt and Sn species, were synthesized using a procedure similar to the one described by Liu *et al*[4] but adding the potassium cations by using an inorganic salt.

Firstly, 8.12 g of an aqueous solution of TPAOH (Alfa Aesar, 40 wt%) were mixed with 6.15 g of a KCl aqueous solution (0.95 wt%) at room temperature, 8.24 g of tetraetylortosilicate (Sigma-Aldrich, 98 wt%) and 13.93 g of miliQ water and stirred overnight to hydrolyse the TEOS. Right after, 0.50 g of a 20% aqueous solution of $SnCl_4 \cdot 5H_2O$ (98 wt%, Sigma-Aldrich) were added and stirred and let for 5 minutes.

Simultaneously, 0.25 g of an aqueous solution of H_2PtCl_6 (Sigma-Aldrich, 8 wt%) were added to 0.27 g of ethylenediamine and maintained under stirring for 20 min. The resulting metal-complex suspension was added to the previous mixture and maintained under vigorous stirring for 20 min. The composition reached in the final gel was:

$$1SiO_2 : 4\ EtOH : 0.404\ TPAOH : 0.02\ K : 0.0012\ Pt : 0.007Sn : 0.11\ EDA : 35\ H_2O$$

The final mixture was transferred to a Teflon liner inside a stainless-steel autoclave and heated in an oven at 175ºC for 4 days under static conditions. The solid product was filtered and washed with distilled water and acetone and dried overnight at 80ºC.

In **Chapter 4**, some modifications will be made to the basic recipe (used for preparing the sample named as PtSn2) to explore a wider range of materials

and how slight variations in the chemical composition may affect the final catalytic behaviour. The synthesis of these additional PtSn-containing catalysts differs from that of the PtSn2-MFI catalyst, specifically in the amounts of K and Sn introduced into the synthesis gel. These variations require the same sources as those used for the PtSn2-MFI synthesis, and their respective molar compositions presented in **Table 3.1** below.

Table 3.1. Chemical composition modifications for the different PtSn-containing MFI type catalyst synthesized in **Chapter 4**.

Catalyst	*KCl*	*Pt*	*Sn*
MFI-PtSn3	0.02	0.0014	0.005
MFI-PtSn4	0.02	0.0014	0.004
MFI-PtSn5	0.02	0.0014	0.003
MFI-Pt6	0.02	0.0014	0
MFI-7	0.02	0	0
MFI-PtSn8	0.01	0.0014	0.007
MFI-PtSn9	0.01	0.0014	0.005
MFI-PtSn10	0.01	0.0014	0.003
MFI-PtSn11	0.01	0.0014	0.001

3.2.3.2. Synthesis of Beta type zeolites (BEA)

Beta zeolites were synthetized as aluminosilicates employing N-butyl-N-methylhexamethyleneiminium (BMH) hydroxide as OSDA. Different syntheses were performed to achieve the acid and Ni-containing Beta zeolites. Their physico-chemical and textural properties, morphology and catalytic behaviours are discussed in more detail in chapter 6.

The synthesis recipes to obtain the different Beta type zeolites, classified according the employed OSDA and the final Si/Al in the resulting solids, are described below.

3.2.3.2.1. Synthesis of nano-sized Beta type zeolite employing amorphous Si and Al sources and N-butyl-N-methylhexamethyleneiminium (BMH) as OSDA

The nano-sized Beta zeolites employed in chapter 6 were synthetized using a preparation method similar to the one previously reported[1], using the BMH molecule as OSDA.

0.15 g of $Al(OH)_3$ (Sigma-Aldrich, 85.65 wt%) were mixed with 19.66 g of a 20.5 wt% aqueous solution of the BMH (OH form) and the mixture was maintained under stirring. After homogenizing, 7.51 g of LUDOX® AS-40 (Sigma-Aldrich, 40 wt%) were added and the mixture was maintained under stirring to evaporate the excess of water until reaching the desired composition.

$$1SiO_2: 0.0167\ Al_2O_3: 0.4\ BMH(OH) : 15\ H_2O$$

The final gel was transferred into a Teflon liner inside a stainless-steel autoclave and kept at 150°C for 10 days under static conditions. After that period, the final solid was recovered by filtration, washed with abundant water and, finally dried at 80°C overnight.

3.2.3.2.2. Synthesis of the nano-sized Ni-containing Beta type zeolite employing amorphous Si and Al sources and N-butyl-N-methylhexamethyleneiminium (BMH) as OSDA

The nano-sized Ni-containing Beta zeolites employed in chapter 6 were synthetized using a similar preparation method to the one previously reported[1], using the BMH molecule as OSDA.

0.15 g of $Al(OH)_3$ (Sigma-Aldrich, 85.65 wt%) were mixed with 14.34 g of a 20.5 wt% aqueous solution of the BMP (OH form) and the mixture was maintained under stirring. Simultaneously, 0.33 g of ethylenediamine (Sigma-Aldrich, 99 wt%) were mixed with 0.33 g of a 20 wt% aqueous solution of $NiCl_2$ (Sigma-Aldrich, 99 wt%) and diluted in 1.5 g of water under vigorous stirring. Then, the metal containing solution was mixed and homogenized with the previous solution. After homogenizing, 7.51 g of LUDOX® AS-40 (Sigma-Aldrich, 40 wt%) were added and the mixture was maintained under stirring to evaporate the excess of water until reaching the desired composition.

$$1SiO_2 : 0.0167\ Al_2O_3 : 0.4\ BMH(OH) : 15\ H_2O$$

The final gel was transferred into a Teflon liner inside a stainless-steel autoclave and kept at 150°C for 10 days under static conditions. After that period, the final solid was recovered by filtration, washed with abundant water and, finally dried at 80°C overnight. To obtain the acidic zeolite, the solid was calcined at 550°C in air for 4 hours employing a heating ramp of 1°C/min.

3.2.3.3. Post-synthetic procedures

In the following section, different post-synthetic treatments applied to the zeolitic supports prepared in this thesis are presented. The main goal is to supply the adequate physico-chemical properties for the final catalytic application.

3.2.3.3.1. Nickel ion exchange incorporation over Al-rich BEA and MFI aluminosilicates.

Ni species were added via a post-synthetic method within the commercially available Al-containing MFI and BEA structures (CBV3024E and CP814E respectively) employed in chapter 6. In particular, Ni species were added via ion exchange to compare the final Ni speciation against other Ni incorporation methods such as Ni impregnation or direct incorporation in the zeolite synthesis. The ion-exchange procedure was carried out employing an aqueous solution of $Ni(NO_3)_2$ with the required concentration required to achieve a Ni content of 1 wt% in the solids, using a liquid/solid weight ratio of 40 and maintaining the solution under stirring overnight at 80ºC. The product was recovered by filtration and dried at 80ºC overnight.

3.2.3.3.2. Nickel impregnation on Al-containing MFI and BEA zeolites.

The Ni species in the MFI and BEA type materials prepared in **Chapter 6** were incorporated via wet impregnation to compare the different final Ni speciation when prepared by different methods (*i.e.* one-pot synthesis). The wet impregnation was carried out employing an aqueous solution of $Ni(NO_3)_2 \cdot 6H_2O$ in the required amount to obtain a final Ni concentration of 1 wt% in the solids and using a liquid/solid weight ratio of 10. The final solid was recovered and dried at 80ºC.

3.2.3.3.3. Platinum and tin impregnation on amorphous silica.

The synthesis of the $PtSn/SiO_2$ as comparative catalyst has been prepared according to the methodology described in the literature[5]. In particular, 0.52 g of a H_2PtCl_6 solution (Sigma-Aldrich, 8 wt%) and 16 mg of $SnCl_4$ (Sigma-Aldrich, 98 wt%) were added to 0.8 ml of 0.1 M HCl solution. 5 gram of silica (Sigma-Aldrich, pore size 60 Å) were impregnated using the previous solution by incipient wetness impregnation. The final catalyst was dried overnight at 80°C.

3.2.3.3.4. Removal of tin impurities on MFI by washing with a basic solution

The as-synthesized PtSn containing materials presenting Sn-Silicate precipitates were treated with a 20 wt.% NaOH aqueous solution (liquid/solid ratio of ~10) at 60°C, maintaining the mixture under stirring for 1 h. The solid product was filtered and washed with distilled water and acetone and, finally, dried at 60°C.

3.2.3.3.5. Calcination and reduction procedure to remove the OSDA molecules from the "as-prepared" zeolites and activate the noble metal active centres containing zeolites.

During a typical calcination process, the desorption of physisorbed water occurs first at temperatures above 100ºC. The OSDA molecules start to decompose at different temperatures depending on their size and polarity. Moreover, most of the organic species decompose at temperatures between 400ºC and 600ºC.

- Calcination procedure in metal-free synthesized zeolites

The typical calcination process to obtain the acid zeolites used in this thesis was carried out using a quartz fixed bed reactor which was heated using a slope of 2°C/min and feeding 100 mL/min of air until reaching 580°C, maintaining this temperature for 3 hours.

In the case of metal-containing zeolites, the calcination procedures were the followings:

- Calcination procedure for Pt containing zeolites

Regarding the calcination procedure applied to noble metal containing zeolites employed in **Chapters 4** and **5**, the temperature reached must be adequate to both calcine the OSDA molecules and provide enough thermal energy to disperse the noble metal (alloyed or non-alloyed) through the zeolitic matrix. To achieve this purpose, a fixed bed reactor was used, with an air flow of 75mL/min and a heating ramp of 2°C/min until reaching 600°C and maintaining that temperature for 4 hours.

- Reduction procedure for Pt or Pd containing zeolites

Regarding the reduction procedure applied to noble metal containing zeolites employed in **Chapter 5**, the temperature reached must be adequate to make the hydrogen gas flow able to reduce the noble metal oxide species dispersed in the previous calcination step to form the noble metal nanoparticles. The reduction process was carried out in a fixed bed reactor employing 100 mL/min of H_2 with a heating ramp of 10°C/min until reaching 600°C and maintaining that temperature for 2 hrs. Finally, the H_2 gas flow was replaced by a N_2 gas flow while cooling down the material.

- Reduction procedure for PtSn containing zeolites

Regarding the reduction procedure applied to bimetallic alloy containing zeolites employed in **Chapter 4,** the temperature reached must be adequate to make the hydrogen gas flow able to reduce the noble metal oxide species dispersed in the previous calcination step to form the noble metal nanoparticles. To achieve this purpose, the reduction process was carried out in a fixed bed reactor employing 75 mL/min of H_2 with a heating ramp of 10°C/min in a H_2 gas flow until reaching 600°C and maintaining that temperature for 2 hrs.

- Calcination procedure applied to the Nickel containing zeolites

Regarding the calcination procedure applied to the Ni-containing zeolites employed in **Chapter 6**, as prepared the samples were calcined in a fixed bed reactor employing 100 mL/min of air using a heating ramp of 1°C/min until reaching 550°C, and that temperature was maintained for 4 hours.

3.2.3.3.6. Developing hydrophobic shells for MFI zeolites employing Fast-synthesis techniques.

This section details the procedure carried out during the 3-months research stay at the University of Tokyo. The goal was to cover MFI-type zeolitic materials with a pure silica shell using a novel ultra-fast synthesis approach developed by the group of Professor Okubo at the University of Tokyo. This method involves modifying the geometry of the crystallization vessel to significantly improve heat transfer (see **Figure 3.2**), allowing crystallization processes to occur much faster than in the case of conventional hydrothermal synthesis, within minutes instead of days.

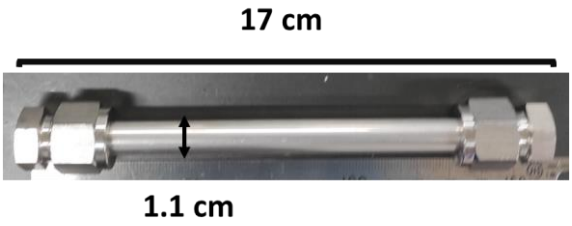

Figure 3.2. Stainless steel tubular reactor with increased X-axis length to maximize the heat transfer, allowing the fast-crystallization process. Developed and patented by Okubo's group at the University of Tokyo.

This post-synthetic treatment was applied to the noble metal containing MFI type materials introduced in **Chapter 5** and described for the first time by Peng *et al*[6]. The original protocol pursued to achieve the following gel composition.

$$1SiO_2{:}4\ EtOH{:}0.3\ TPAOH{:}120\ H_2O$$

For this process, TEOS (Tokyo Chemical Industry Co, 99 wt%), TPA-OH (Tokyo Chemical Industry Co, 40 wt%), and MilliQ water (MilliPore) were mixed and left to hydrolyse for 2 hours. Afterwards, required zeolites seeds were added to achieve a SiO_2-Core/SiO_2-Shell molar ratio of 1, and the mixture was stirred for one additional hour. The homogeneous mixture was then placed in a stainless-steel tubular reactor, which was introduced in a silicon thermal oil bath at 190°C for 10 minutes. After this period, the reactor was cooled in a water bath. Finally, the solid was separated by centrifugation and left to dry overnight at 80°C.

3.3 CHARACTERIZATION TECHNIQUES

The microporous materials studied in the present PhD thesis were characterized by the following techniques.

3.3.1. Powder X-Ray Diffraction (PXRD)

Powder X-Ray diffraction allows the identification of the crystalline structures. Every crystalline structure presents a specific and unique pattern which is unique and allows identifying the presence of a single crystalline phase or the presence of a mixture between crystalline phases. This technique is based on the Bragg Law, which mathematical expression is:

$$n \cdot \lambda = 2d \cdot sen\theta \qquad \textbf{Eq 3.2}$$

Where:

- n is an integer
- λ is the X-ray wavelength applied
- d is the distance among the crystal framework plane
- θ is the angle between the incidental beams and the dispersion planes

In the present PhD thesis, phase diffractograms were achieved using a Philips diffractometer, model X'Pert with a Bragg-Brentano geometry. The diffractometer is fitted with a graphite monochromator and an automatic divergent grid, employing Cu-Kα radiation. The device is equipped with a 3-axis mobile platform. This feature allows to measure in parallel different samples. The PXRD patterns were measured using a 1/16º fixed divergent gap, a 240 mm long arm goniometer, a Cu-Kα radiation source and a X'Pixcel

detector. The device tube works with an electric potential of 45 kV and an electric current of 40 mA. The measurements were taken between 1° and 35° (2θ) in a spread of 0.017° (2θ).

3.3.2. Chemical Analysis by Inductively Coupled Plasma Atomic Emission Spectroscopy (ICP-AES)

The Atomic Emission Spectroscopy is a determining technique that allows simultaneously the identification and the quantification of different chemical species with detection levels in the parts per billion magnitude order. The system requires an inductive coupled plasma that allows the ionization of the elements present in the sample. Those generated ions emit radiation in different wavelengths, being each one specific for each chemical element and an intensity directly related to the element concentration in the sample.

The solid/liquid samples were measured in a Varian 715-ES device and allows the determination of the amount of Si, Al, K, Ni, Pt, Pd within the samples. The procedure to set up the sample is described below.

The solid samples must be disintegrated, employing an acid mixture between hydrochloric acid, nitric acid and hydrofluoric acid in a volume proportion of 3:1:1 respectively. The system requires a previous calibration with standard dissolutions at different concentrations to obtain a calibration curve.

3.3.3. Elemental Analysis

The total amount of Carbon, Nitrogen and Hydrogen in the samples were determined employing a Fison EA1108 device. The organic species stored inside the samples were burnt in presence of air at 1000°C, producing the simplest combustion gases for each compound (CO_2, N_2 and H_2O). Those

gasses are retained and separated by a chromatography column. The device is fitted with a Thermal Conductivity Detector (TCD) and employs sulphanilamide as inner standard to quantify the elemental species.

3.3.4. Thermogravimetric Analysis

Thermogravimetric analysis allows determining the mass variation suffered by the material with the temperature. This technique is used to determine the organic content trapped in the "as-prepared" zeolite materials, as well as the water amount adsorbed in the microporous structure.

The analyses were performed in a Mettler-Toledo TGA/STDA851e, using air to assure the organic removal. For each analysis, between 5 and 10 mg of the solid material were used, heating from 20°C to 800°C at a heating rate of 10°C/min to guarantee the total organic elimination.

3.3.5. Textural Properties Analysis: N_2 adsorption

The preferred technique to study the textural properties in the microporous solids is N_2 adsorption isotherms, allowing to estimate the surface area expressed in terms of surface per mass unit, the micropore volume per mass unit and pore size distribution in porous solid materials. These parameters give information about the accessibility to the active centres of the microporous solid catalysts.

The surface area was determined employing the Brunauer-Emmet-Teller (BET) model[7] which suppose the following hypothesis to simplify the mathematical models.

- The adsorbent surface is not porous, and it is assumed to be uniform

- The gas molecules are adsorbed by successive layers and the side interactions between the molecules are neglected

Therefore, this model can be only applied working at very low relative pressures. The mathematical equation to describe an adsorption isotherm behaviour is:

$$\frac{P}{v\cdot[P_0-P]} = \left(\frac{K-1}{v_m\cdot K}\right)\cdot\left(\frac{P}{P_0}\right) + \left(\frac{1}{v_m\cdot K}\right) \qquad \textbf{Eq 3.3}$$

Where:

- v is the volume of gas adsorbed per mass unit of adsorbent at the working pressure P
- v_m is the volume of gas adsorbed per mass unit in the adsorbent's monolayer
- P is the equilibrium pressure
- P_0 is the saturation pressure
- K is the adsorption equilibrium constant

The equation allows to obtain a linear curve in which the equilibrium constant, and the monolayer volume can be determined from the slope and the origin ordinate. These two parameters permit estimating the BET area.

$$S_{total} = \frac{v_m\cdot N_A\cdot s}{V} \qquad \textbf{Eq 3.4}$$

$$S_{BET} = \frac{S_{Total}}{m_{solid}} \qquad \textbf{Eq 3.5}$$

Where:

- v_m is the volume of gas adsorbed per mass unit in the adsorbent's monolayer
- N_A is the Avogadro's Number
- V is the molar volume of the adsorbate in STP conditions
- s is the adsorption cross-section of the adsorbent species (0.162 nm^2 for the N_2 molecules)

The micropore volume and micropore area were determined employing the procedure called the *t*-plot method introduced by Boer *et al*[8]. The N_2 volume adsorbed against the adsorbed layer average thickness (*t*) is represented. This value (t) for the N_2 molecule were reported by Jura *et al*[9] from the relative pressure employing Harkins-Jura equation applied to non-porous titanium oxide.

$$t = \left(\frac{13.99}{0.034} - \log\left(\frac{P}{P_0}\right)\right)^{\frac{1}{2}} \qquad \textbf{Eq 3.6}$$

The plot of the adsorbed N_2 volume against the t-value according to the equation proposed by Boer[9,10] in which the N_2 monolayer thickness was reported as 3.54 Å, so the t-value expression results as follows:

$$t = 3.54 \cdot \left(\frac{v}{v_m}\right) \text{Å} \qquad \textbf{Eq 3.7}$$

The micropore volume ($V_{Micropore}$) can be obtained from the linear curve generated intercepting the y-axis.

$$V_{Micropore}\left(\frac{cm^3}{gr}\right) = 0.00157 \cdot Y_{Axis-Int} \qquad \textbf{Eq 3.8}$$

Those parameters are obtained from the quantitative adsorption/desorption N_2 isotherms at N_2 liquid temperature (-196ºC). To run the analysis, 250 mg of the pelletized sample (0.2-0.4 mm) was degassed under vacuum for 24 hrs while heating the sample at 400ºC to fully desorb physisorbed species. Textural properties were obtained by adsorption/desorption isotherms of N_2 using a Micrometrics ASAP-2020 device at -196ºC. Microactive v4.06 software using the Rouquerol Criteria[11] was employed to process the data.

3.3.6. Study of the active centre nature by Fourier Transform Infrared Spectroscopy

Fourier Transform Infrared Spectroscopy (FT-IR) is one of the most employed techniques for the characterization of solid catalyst because very relevant chemical structure information can be achieved using this spectroscopic technique. In the present PhD thesis, this technique has been employed to determine properties associated to the -OH group vibrations, giving information about the presence of trivalent cations in framework positions, such as Al, or about zeolite defects[12] at wavenumbers comprised between 3000 and 4000 cm^{-1}.

The band associated to Si-OH involved in the hydrogen bonding with other silanols or with framework oxygens are found about 3500 cm^{-1}, and this band is an indicator of weak acidity. Additionally, the OH band associated to hydroxyl groups attached to framework aluminium atoms (so-called aluminols, Si-OH-Al), which are known for possessing a strong acid behaviour, is found between 3500 and 3650 cm^{-1}. On the other hand, the band associated to the extra-framework aluminols is found near 3660 and 3670 cm^{-1}, and it is an indicator about the Lewis acidity as the redox behaviour of

the catalyst[13]. Finally, the vibrational signal assigned to external silanols are found among 3700 and 3745 cm^{-1}, related to a weak acid behaviour. In the present PhD thesis, the FT-IR spectra obtained were normalized according to the Overtone's signal area (1750 – 2300 cm^{-1}), which is associated to the silicon content in the samples, facilitating the comparison of the different samples at various temperatures.

3.3.6.1 Zeolite Acidity determination by Fourier Transform Infrared Spectroscopy using Pyridine as probe molecule

The bands associated with the vibration of the deformation of organic molecules that can be adsorbed inside the zeolite framework are found at low wavenumbers (1300 - 1700 cm^{-1}). In the present PhD thesis, pyridine molecule was used as a probe molecule to determine the nature of the acid centres in the catalyst by its adsorption/desorption study. Indeed, the strength and the availability of these acid centres can be estimated by the pyridine desorption at rising temperatures. The pyridine molecule, when interacting with a Brønsted acid site, forms the pyridinium cation, which shows a very specific signal at 1545 cm^{-1}. However, when the pyridine molecule interacts with a Lewis acid site[14] transferring an electron pair, it coordinates with the metallic atom and shows a signal at 1455 cm^{-1}.

The Brønsted acid site (BAS) and the Lewis acid site (LAS) concentration was determined by measuring the intensities of the bands placed at 1545 cm^{-1} and 1450 cm^{-1}, respectively, normalizing by the Si-O overtone area (1730 - 2100 cm^{-1}), using a numerical variation of the molar extinction coefficients given by Emeis[15] to avoid inconsistency of measurement due to zeolite structure effects, as reported by Zholobenko *et al*[16].

$$C_{Bronsted} = 1270 \cdot \frac{AO_{Av}}{AO_{AT}} \cdot H_B \quad \textbf{Eq 3.9}$$

$$C_{Lewis} = 570 \cdot \frac{AO_{Av}}{AO_T} \cdot H_L \quad \textbf{Eq 3.10}$$

Where:

- $C_{Brønsted}$ is the concentration of the pyridine molecules attached on the Brønsted acid sites (expressed as µmol of pyridine per gram of catalyst)
- C_{Lewis} is the concentration of the pyridine molecules attached on the Lewis acid sites (expressed as µmol of pyridine per gram of catalyst)
- AO_T is the measured area of Si-O overtone region, measured for each temperature (cm^{-1})
- AO_{Av} is the average area of Si-O overtone region of the sample (cm^{-1})
- H_B is the height of the Brønsted peak at 1545 cm^{-1}
- H_L is the is the height of the Lewis peak at 1450 cm^{-1}

The acidity was determined by using a Nicolet 710 FTIR device. Self-supported wafers were made (until reach a normalized mass density of 10 mg/cm^2) and were dehydrated overnight at 400ºC using a turbomolecular vacuum pump until reaching 10^{-6} mbar. After the activation step, the base spectrum was recorded, and the pyridine vapour ($6.5 \cdot 10^2$ Pa) was admitted into the IR cell and adsorbed by the zeolite. The desorption was carried out under vacuum for 3 different one-hour periods at 150ºC, 250ºC and 350ºC, respectively, measuring in each period the IR spectra once the temperature reached room temperature.

3.3.6.2 Zeolite metal active sites state determination by Fourier Transform Infrared Spectroscopy using CO as probe molecule

The nature and oxidation state of the metallic species hosted in some of the catalysts were studied employing CO as a probe molecule. The spectra were registered employing a Nexus (Thermo) 8700 FTIR spectrometer, using a deuterated triglycine sulphate detector (DTGS) and scanning at 4 cm^{-1}. The calcined samples were pressed to obtain self-supported wafers of 10 mg/cm^2, thermally activated in all cases with their pre-reaction conditions, cooled until room temperature, and after recording the base spectrum, the metal speciation was assessed by titration with CO upon cooling the sample to -176^oC under dynamic vacuum of 10^{-5} mbar and gradually, bringing in the CO doses from 0.1 to 2 mbar and recording the spectrum in each dose. For the later analysis, all the spectra were normalized to the area of the corresponding Si-O overtones (1700-2100 cm^{-1})[17].

3.3.7. Nuclear Magnetic Resonance Spectroscopy

Nuclear Magnetic Resonance (NMR) spectroscopy is a widely employed technique for molecular structure analysis. It is based on the interaction between the angular spin momentum of certain magnetically active atomic nuclei and an external magnetic field (B_o) applied to the sample. The magnetic moments of these nuclei exhibit different orientations due to their non-zero spin, leading to the splitting of distinct energy levels[18]. In the absence of an external magnetic field, the nuclear spins are randomly oriented. However, when a magnetic field is applied, the spins align in two possible states: those with positive spins align with the magnetic field, while

those with negative spins align against it, resulting in the minimum energy states, known as α and β, as illustrated in **Figure 3.3.**

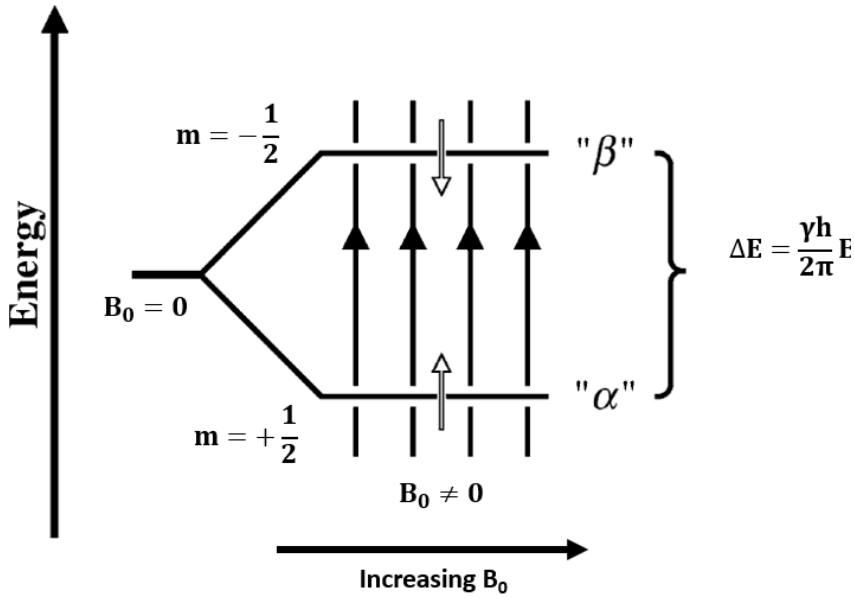

Figure 3.3. Energy levels of a ½ nuclear spin when it is submitted under an external magnetic field. Figure obtained from Jacobsen *et al*[18].

The energy difference between these two spin states is directly proportional to the strength of the applied external magnetic field ($B_1 >> B_o$). When the sample absorbs electromagnetic radiation, nuclei with a spin state of +1/2 are induced to transition to the -1/2 state. Upon cessation of the magnetic field, the nuclei return to their initial energy levels, emitting signals at frequencies that allow for the collection of the NMR spectra.

The electrons surrounding the atoms in a molecule are in constant motion, generating a weak magnetic field that opposes the externally applied magnetic field, thereby diminishing its strength. As a result, the magnetic field experienced by the nuclei is reduced. This shielding effect depends on

the electron density around the nucleus and the local atomic environment, allowing for differentiation between nuclei. The chemical shift measures these variations in NMR absorption frequencies due to the shielding effect. Typically expressed in parts per million (ppm), these shifts are relative magnitudes compared to standard molecules with minimally perturbed electronic distributions.

The solid-state NMR gives wider signals with less resolution because the mobility of atoms is significantly hindered, and then the dipolar and quadrupolar interactions and the chemical shifting anisotropy. Those interactions are described below[19-21].

- Dipolar interactions: These interactions are produced by a dipole-dipole interaction between the magnetic momentum of two adjacent nuclei caused by the spin magnetic field generated when are exposed to the external magnetic field, interacting two close atoms.
- Quadrupolar Interactions: Produced in those nuclei that does not have a spherical shape related to a quadrupolar momentum. This momentum interacts with the electric fields gradient result of the non-symmetric electric charges distribution.
- Chemical Shift Anisotropy: it is due to the interaction between magnetic field induced by the nuclei surrounding electron movement and the external magnetic field. The electron distribution does not have a perfect spherical shape so the resonant frequency changes are closely linked with the electron cloud resulting in an orientation when it is exposed to the external magnetic field.

In order to increase the signal quality and the information obtained, there is used the experimental technique of the Magic Angle Spinning procedure, (MAS-NMR), which decreases the shifting anisotropy and gets rid of the first order quadrupolar interactions and eliminates the dipolar interactions between the different nuclei[22]. In this procedure the sample spins in an angle of 54° 44' regarding the external magnetic field axis. In addition to the MAS-NMR it is widely used cross polarization, in this technique is transferred the magnetization of one abundant atom, generally is used the ^{1}H, to another much less abundant.

In order to assure that the non-commercially available OSDAs were properly synthetized, liquid NMR, ^{1}H and the ^{13}C NMR were used. The liquid NMR spectra were collected in a Bruker Avance-300 Ultrashield Spectrometer, working at 300 MHz to obtain the ^{1}H signal and 75 MHz to obtain ^{13}C NMR signal.

The solid NMR spectra were collected in a Bruker AVII HD 400 MAS. The main nucleus studied were ^{29}Si and ^{27}Al, allowing to determine the local environment of the TO_4 atoms. PtSn-MFI zeolites synthetized in chapter 4 were analysed by ^{1}H MAS NMR and ^{1}H Double Quantum (DQ)-Single Quantum (SQ) MAS NMR. Prior to expose the samples to the magnetic field, they were evacuated in vacuum while heated at 150°C to dehydrate the zeolite. All the spectra were collect using a Bruker 3.2 mm probe by spinning the sample at 20KHz. Back-to-Back (BaBa) dipolar recoupling sequence was used to excite and reconvert DQ coherences employing an excitation time of 100 us (2 periods).

3.3.7.1. ^{29}Si MAS-NMR

The ^{29}Si nucleus presents very limited sensitivity due to its low content in nature (≈4.68% in weight) and its gyromagnetic average radius (8.47 MHz/T). Because of these two features, it produces a wide chemical shift range and sharp peaks, allowing accurate determinations of the chemical surrounding environments of the silicious compounds.

Si atoms present in zeolitic frameworks in tetrahedral coordination with other SiO_4 atoms are named Q_4. Those atoms can also be found close to aluminium atoms, having an oxygen bridge between them (Lowenstein Rules), resulting in 5 Si-O-nAl (Q_{4-n}) feasible combinations (n ϵ 0,1,2,3,4). For each additional Al atom located in the second coordination, a different chemical shift is obtained in the spectrum, as summarized in **Figure 3.4.**

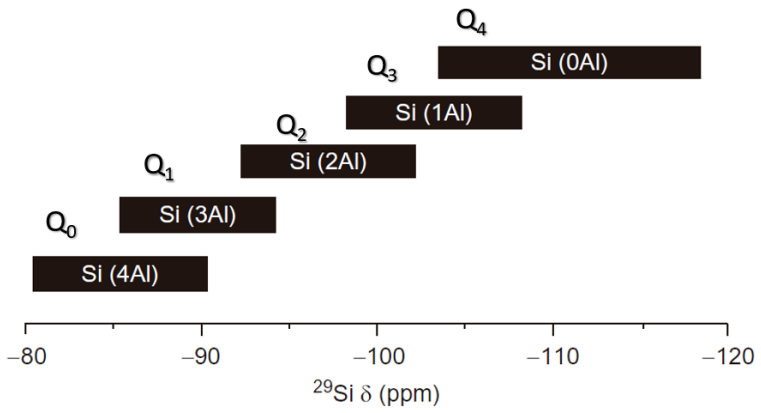

Figure 3.4. Scheme of ^{29}Si NMR chemical shifts for different silicon coordination with different numbers of aluminium atoms.

In a similar way, when the TO_4 is linked to silanol groups, the chemical shift is similar to the observed when the coordinating element is the aluminium but producing wider and less clear signals. The signals can generally be mathematically deconvoluted to identify correctly the Q_n species.

The ^{29}Si MAS-NMR spectra along the present PhD thesis were collected at 79.5 MHz and a rotational speed of 5KHz, using a pulse length of 55º and 3.5 μs and a repetition time 180 s, and tetramethylsilane (TMS) as standard to measure the chemical shift.

3.3.7.1. ^{27}Al MAS-NMR

The nuclear magnetic resonance of the aluminium nucleus applied to solid materials allows the study of the coordination of the Al atoms. Al nucleus is quadrupolar and, thus, it produces wide signals (I=5/2) in the recorded spectra due to the second order quadrupolar interactions.

In the zeolite research field, ^{27}Al MAS-NMR is widely used to determine the coordination of Al in tetrahedral positions, generally associated to Brønsted acid sites, which chemical shifts are located near to 55 ppm. The other most common Al species in zeolites are those in octahedral coordination. The octahedral Al species are located in extra-framework positions, which characteristic chemical sift is placed at 0 ppm and are mostly related to Lewis acid sites[23,24]. Other less common signals are those connected to distorted tetrahedral or pentacoordinated Al species, with chemical shifts close to 30 ppm[25]. As stated above, the main drawback associated with this nucleus is the strong quadrupolar effects, particularly when the zeolite is dehydrated, in this case the recorded signals give wide and very weak gaps related to "invisible aluminium", avoiding accurate quantifications[26,27].

The ^{27}Al MAS-NMR spectra were recorded at 104.2 MHz with a rotational speed of 10 kHz and a pulse length of 9º of 0.5 µs and a repetition time of 1 s. The chemical shift represented in the ^{27}Al MAS-NMR spectra were referred to $Al_3^+(H_2O)_6$, used as standard.

3.3.8. X-Ray adsorption spectroscopy (XAS)

X-Ray absorption spectroscopy (XAS) is a powerful analysis technique widely used to study the bulky characteristics of a solid material. It gives information about the atomic local structure of the chemical elements composing the material. In heterogenous catalysis this technique provides valuable information about element speciation (discerning among oxidation states). Synchrotron radiation facilities are required to provide an adjustable X-Ray energy source.

The X-ray absorption phenomena is explained through the Lambert-Beer Law[28]:

$$I = I_0 \cdot e^{-\mu \cdot x} \qquad \textbf{Eq 3.11}$$

Where:

- *I* is the intensity transmitted once the photon is attenuated after running through the sample
- I_0 is the intensity given by the incident X-Ray radiation on the sample
- µ is the absorption coefficient and it is specific of the material composition
- x is the sample thickness

The absorption coefficient depends on the material composition and the incident energy (E). Indeed, an increase of the incident radiation implies a decrease in this coefficient, as described by the equation that predicts the absorption coefficient.

$$\mu(E) \approx \frac{Z^4 \cdot \rho}{A \cdot E^3} \qquad \textbf{Eq 3.12}$$

Where:

- ρ is the material density
- Z is the atomic number of the studied specie
- A is the atomic mass of the studied specie
- E is the incident energy of the X-Ray radiation

If the incident radiation can provide an energy similar to the binding energy of a core level electron (closer to nucleus attaching the orbitals and do not participate in bonding), then a sharp rise of the energy absorbed (called absorption edge) is produced, which corresponds to the foster of this core level to the continuum level (negligible energy gaps than electrons are not trapped anymore). Since each atom possesses a specific core level electron, the study of different absorption edges modifies the energy of the incident X-ray beam. Generally, almost all the elements can be registered between 5-35 keV, permitting the use of XAS as a selective element technique. A typical XAS spectrum is divided in two main regions, where the gap ±50 eV of the absorption edge of the element is the limit separating both regions.

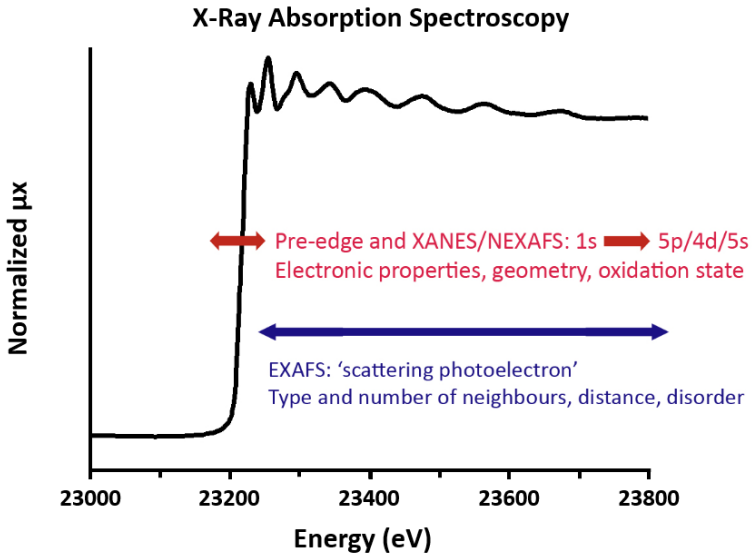

Figure 3.5. XAS spectra scheme, including both XANES and EXAF regions.

XANES (X-Ray Absorption Near-Edge Spectroscopy) region: This region surrounding the absorption edge gives information about the unoccupied states near Fermi level of the absorbing atom, informing about the element oxidation state, bond angles and local symmetry surrounding the absorber atoms. For this reason, XANES technique is used very often as a fingerprint comparison tool, where the samples are compared with standards of crystalline structures and oxidation states. Unfortunately, developing a mathematical model of the XANES region is difficult due to multi-scattering phenomena of low-energy electrons that happen in this region[29].

EXAFS (Extended X-Ray Absorption Fine Structure): This region is located after the XANES region up to 1000 eV approximately or even above the absorption edge. In this area the oscillations start to be controlled mainly by single-scattering effects. These characteristics are explained by the interaction

between the absorber material photoelectrons propagated outward in all the directions and the backscattered radiant energy emitted by the bordering atoms (**Figure 3.6**). The peaks registered in the EXFAS regions, are produced by constructive and destructive interferences of the X-Ray waves penetrating and leaving the absorbent.

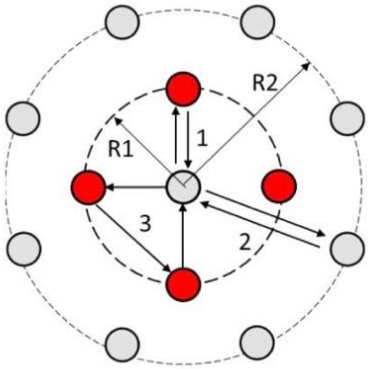

Figure 3.6. A central absorbing atom surrounded by two coordination shells at difference distances (R1 and R2, respectively). The scheme shows multiple scattering paths despite the two direct path pointed by 1 and 2. Scheme reproduced from Patience *et al*[30].

Those interactions are described in the following equation by the function χ(E), describing only the interactions with neighboring atoms:

$$\chi(E) = \frac{\mu(E) - \mu_0(E)}{\Delta\mu_0(E)} \qquad \textbf{Eq 3.13}$$

Where:

- μ(E)is the measured absorption coefficient.
- μ_0(E)is the background function that represents the theoretical absorption of an isolated atom.

- $\Delta\mu_0(E)$ is the experimental variation of the absorption coefficient at the threshold energy E_0.

Generally, the magnitude of the X-Ray energy units to wavenumbers (k) changes through the De Broglie hypothesis[30], expressed as follows:

$$k = \sqrt{\frac{2 \cdot m \cdot (E - E_0)}{h^2}} \qquad \textbf{Eq 3.14}$$

Where:

- m is the electron mass.
- E is the measured energy.
- E_0 is the energy in the absorption edge.
- h is the Planck constant.

The addition of the frequencies composing the EXAFS oscillations are related to different near bordering coordination shells. Then, the EXAFS spectrum can be mathematically modelled according to the following k-dependent equation:

$$\chi(k) = \sum_j \frac{N_j \cdot f_j(k) \cdot S_j(k) \cdot e^{\frac{-2R_j}{\mu_j(k)}} \cdot e^{-2 \cdot k^2 \cdot \sigma_j^2}}{k \cdot R_j^2} \cdot sin\big(2kR_j + \delta_j(k)\big) \qquad \textbf{Eq 3.15}$$

Where:

- fj (k) is the adjoining atoms scattering amplitudes.
- δj (k) is the adjoining atoms scattering phase-shifts functions.
- N_j is the number of the coordination atom placed in the j coordination shell.

- R_j is the distance between the absorber specie and the bordering atom.
- σ^2 is the Debbie-Waller factor.
- $e^{-2\cdot k^2\cdot \sigma_j^2}$ represents the atomic disorder.
- $e^{\frac{-2R_j}{\mu_j(k)}}$ quantifies the inelastic losses during the scattering process, μ_j symbolizes the free path of the photoelectron ejected.

Unfortunately, all the feasible scattering paths simultaneously overlap. Therefore, the function is mathematically modified by Fourier transform from the *k* domain to the R domain (interatomic distance), resulting the final equation as follows.

$$\chi(R) = \int_{k_i}^{k_f} W(k)k^n \cdot \chi(k)(\cos(2k\pi R) + i\sin 2k\pi R)\, dk \qquad \textbf{Eq 3.16}$$

Where:

- W (k) is Hanning window function dk=1.
- k^n is the k-weight.

The resolution of these equations allows processing, analysing and translating the information given by the XAS spectra, thus, resulting in a technique suitable to analyse the chemical information of crystalline and amorphous solids.

The XAS experiments to characterize the PtSn based zeolites employed in Chapter 4 was carried out by Dr. Randall from ExxonMobil Research and Engineering (Annandale, New Jersey). The measurements were done at the 8-ID ISS beamline at National Synchrotron Light Source-II at Brookhaven

National Lab. The spectra were gathered in fluorescence mode employing a 4-element solid state detector with reference foils for edge alignment. The data for the different experiments were collected approximately 200 eV before the edge jump up to 1000 eV after the edge area. Before acquiring the data, samples were powdered and 4 mg loaded into a 1.5 mm outer diameter x 1.3 inner diameter quartz capillary. The samples were adequate to the correct heigh using quart wool plugs. The gas flows were fed in the range between 5-10 mL/min at standard conditions. The samples were heated using two resistive heaters located in a distance of approximately 1 mm from the sample and employing heating ramps of 10°C/min. The gas flow compositions were 10 mL/min (5%O_2/95%He) for the calcination treatments and 10 mL/min of pure H_2 for the reduction treatment. The scans were set in a typical experiment at 2 min. The experimental data was analyzed using the Demeter Software package[32,33]. The data ranges were estimated based on the quality of data generally between k=3-12 Å and R=1.2-3.4 Å. The amplitude factor for Pt was estimated to be 0.83 from a Pt foil spectra, setting the coordination number to a fixed value of 12 to capture the fcc structure. The Debye-Waller factors, E_0 and the bond distances for all the bonds were optimized fitting simultaneously k, k^2 and k^3 weighted Fourier transforms.

3.3.9. Temperature Programmed Reduction (H_2-TPR)

This technique has been widely used to study the reducibility of the metal species, which is an indicator of the strength in the interaction between the microporous support and the hosted metal species. The temperature required to reduce metal species sheds light on the metal species stored in the support. To carry out this technique, a Micrometrics Autochem 2910 instrument was employed. 50 mg of the solid, with a particle size of 0.4-0.6

mm, was fed with a controlled flow of 50 mL/min of a gaseous mixture of H_2 and Ar (10% and 90%, respectively) and heated from 25°C until 800°C with a heating ramp of 10°C/min. The hydrogen consumed in reducing the metal species were measured by employing a Thermal Conductivity Detector (TCD).

3.3.10. High Resolution Field Emission Scanning Electron Microscope (HR-FESEM)

Scanning Microscopy is widely used and provides information about crystal size and morphology. This technique is very useful to detect impurities in the solid sample as a result of the presence of secondary phases blended with the main crystalline phase[34]. Unlike the commonly used Scanning Electron Microscopes, the High-Resolution Field Emission allows distinguishing nanoscale crystal sizes employing lower electric potentials (among 0.02-5 kV). This major advantage facilitates working with materials which can charge themselves electrically due to their electric insulator behaviour or those that can be damaged by the electric field exposure. The microscope also allows to work in dark field, allowing to detect atomically heavier species on the solid surface[35]. This useful feature helped along the present PhD thesis to search if the metallic species form aggregates on the external surface of the zeolite crystals instead of remaining encapsulated. A Zeiss (model Ultra 55) scanning electron microscope was used to characterize all the materials, employing an electric potential of 2.0 kV.

Samples were carried inside the microscope employing a double-faced adhesive Carbon tape, stuck to the sample holder without any additional coating.

3.3.11. High Resolution Transmission Electron Microscope (HR-TEM)

In transmission electron microscopy (TEM), a beam of electrons with a uniform current density at very high electric potentials (between 100 and 200 keV) is directed onto a very thin sample. Depending on the sample's thickness and atomic composition, some of these electrons will be scattered, while others will interact with the electronic structure of the atoms in the sample, resulting in different phenomena such as light emission, Auger electrons, secondary electrons, and energy in the X-ray spectrum.

By collecting all these signals, information about the nature and state of the sample can be gathered, including the arrangement of its crystalline planes, the morphology of the material particles, the chemical composition, and the electronic structure. TEM forms images from the projection of the 'shadow' created by the sample when it is irradiated and penetrated by the electron beam. Electron diffraction provides information about the crystalline structure of the material, while X-ray emission allows for chemical composition analysis, as each atom has characteristic X-ray emission values.

In this PhD thesis, a JEOL JEM 2100F transmission electron microscope was used. This microscope operates at an acceleration potential of 200 kV, with samples irradiated by a field emission electron gun. Images are collected using a high-resolution (2048 x 2048 pixels) GATAN charge-coupled device camera, model SC200, and processed with Digital Micrograph software. The microscope is equipped with a STEM unit and image detectors capable of working in both brightfield and high-angle darkfield modes. This setup allows for the rapid distinction of different phases with varying atomic numbers

based on visual contrast. Chemical analysis is conducted by collecting X-ray energy emitted by different atoms in the sample using an EDS X-Max 80 detector (Oxford Instruments). This system enables compositional analysis at specific points, within defined areas, or by scanning the entire microscope capture area (mapping).

To obtain images of enough visual quality, it is recommended that the sample thickness does not exceed 100 nm. Thinner samples allow to achieve a better electron transparency, resulting in clearer images. To prepare the sample, a small amount was dispersed in 2 mL of a volatile solvent (such as isopropanol or chloromethane) and placed in an ultrasonic bath for over 30 minutes. A few drops of this suspension were then placed onto a copper or nickel grid, as needed, and the solvent was allowed to evaporate, leaving the material particles fixed and dispersed on the grid.

3.4 CATALYTIC TEST

Once the materials have been synthetized and characterized to know information about their properties, their catalytic behaviour was evaluated for certain catalytic reactions. In this section, the employed catalytic systems and the reaction conditions are described in detail.

3.4.1. Non-oxidative Propane Dehydrogenation

The propane dehydrogenation reactions were conducted using a continuous flow fixed bed reactor Microactivity MAE (PID Eng&Tech) (**Figure 3.7**), equipped with a quartz reactor with a 10 mm inner diameter. The catalysts were pelletized to a size range of 0.2-0.4 mm. A 50 mg portion of the sieved catalyst was diluted with 400 mg of silicon carbide with a grain size of 0.6-0.8

mm and introduced into the reactor on a bed of 0.6 mm quartz wool. The catalyst was reduced with a hydrogen stream of 50 mL/min, heated at a rate of 10°C/min until reaching 600°C, and maintained at this temperature for 1 hour. After the reduction treatment, the reactor was purged with a stream of nitrogen. Then, the reaction mixture, consisting of 32 mL/min of N_2 and 10 mL/min of C_3H_8, was introduced, and the catalytic test was carried out for 8 hours.

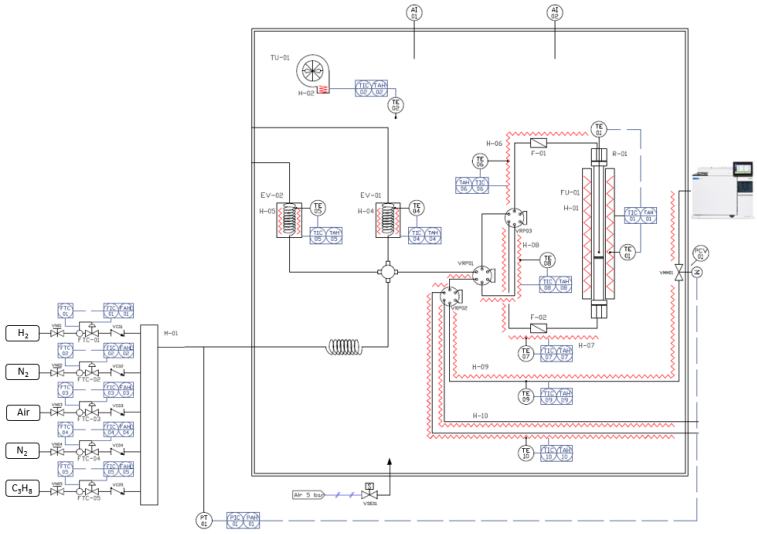

Figure 3.7. MAE PID reaction system diagram employed for the PDH reaction.

The outlet gas flow was collected and analysed on-line in an Agilent Chromatograph model 7890B equipped with a 25 m x 320 µm x 5 µm MAPD Al_2O_3 column ending in a Flame Ionization Detector (FID), which allowed quantifying the unreacted propane and the reaction products.

3.4.2. Selective hydrogenation of functional groups

The selective hydrogenation of functional groups was carried out in a Teflon cylinder inside a stainless-steel autoclave equipped with a pressure gauge, a gas inlet and a cannula to take samples as shown in **Figure 3.8**.

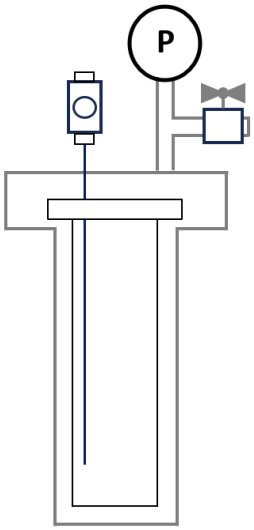

Figure 3.8. Scheme of the discontinuous Teflon-stainless steel batch reactor with pressure sensor, gas insertion opening and relief valve.

To carry out the phenylacetylene hydrogenation, 100 mg of the reduced catalyst was added to the Teflon liner followed by 60 mg of dodecane (inner standard) and 3200 mg of ethanol (Sigma Aldrich, 99.9 wt%). Finally, 200 mg of phenylacetylene (Sigma Aldrich, 99.9 wt%) was added, the autoclave was sealed and then H_2 was introduced until reaching the adequate pressure (6 bar). Then, the system was heated up to the desired temperature (30^{o}C) under stirring at 750 rpm. Samples were taken at different times and then analysed in a GC equipped with a 30 m x 250 µm x 0.50 µm HP-5 column connected to a Flame Ionized Detector (FID).

To facilitate the catalyst comparison, turnover number (TON) was calculated for the different reaction times measured using the following equation:

$$TON = \frac{N_{A0} - N_{At}}{n_M} = \frac{N_{A0} \cdot X_A}{n_M} \qquad \textbf{Eq 3.17}$$

Where:

N_A is the amount of the reactant molecule referred as mmol, N_{A0} is the reactant at the initial state and N_{At} is the reactant molecule content in the reaction time t.

n_M is the noble metal content within the material expressed as mmol.

3.4.3. Ethylene oligomerization

The ethylene oligomerization reactions were carried out using an automatized reactor Microactivity MAE (PID Eng&Tech) (**Figure 3.9**) equipped with a tubular Hastelloy stain-less steel reactor with a 10 mm inner diameter. The catalysts were pelletized to a size range of 0.2-0.4 mm. The reaction was performed at low and high pressure, as summarized in **Table 3.2.**

Table 3.2. Oligomerization reaction conditions used in the Microactivity MAE reaction system.

Ref	*Gounder et al*[36]	*Martínez et al*[37,38]
Pressure (bar)	2.5	35
Temperature (°C)	180	200
WHSV (hr^{-1})	16.3	2.1
m_{cat} (mg)	63	500
Q_{total} (mL/min)	600	100
% vol N_2	97.5	85
% vol C_2H_4	2.5	15

The adequate portion of the sieved catalyst was diluted with silicon carbide with a grain size of 0.6-0.8 mm until reaching a bed volume of 4 mL and introduced into the reactor.

The catalysts were activated in N_2 (53.8 mL/min) while increasing the temperature using a ramp of 5°C/min until reaching 550°C, maintaining this temperature for 6 hrs and finally cooling down until reaching the reaction temperature. The reactions were carried out for 6 hours.

The outlet gas flow was analysed on-line in an Agilent Chromatograph model 7890B equipped with two separated channels. The first one consists of a 30 m x 320 µm x 0.25 µm HP5 column connected to a Flame Ionization Detector (FID) and allows to measure the unreacted ethylene and the reaction products. The other channel contains a 30 m x 320 µm x 12 µm HP-Plot Molesieve, a 30 m x 320 µm x 20 µm HP-Q-Plot column and a Thermal Conductivity Detector (TCD), in order to quantify the amount of non-reacted ethylene and N_2 concentration (inner standard) by the following equation.

$$Q_{C2H4} = Q_{N2} \cdot \frac{A_{C2H4} \cdot f_{RC2H4}}{A_{N2} \cdot f_{N2}} \qquad \textbf{Eq 3.17}$$

Where:

- Q_{N2}, Q_{C2H4} are the volumetric flows of N_2 and Ethylene, respectively.
- A_{C2H4}, A_{N2} are the area values of the N_2 and C_2H_4 GC peaks, respectively.
- f_{RN2} is the response factor of the N_2.
- f_{RC2H4} is the response factor of the C_2H_4.

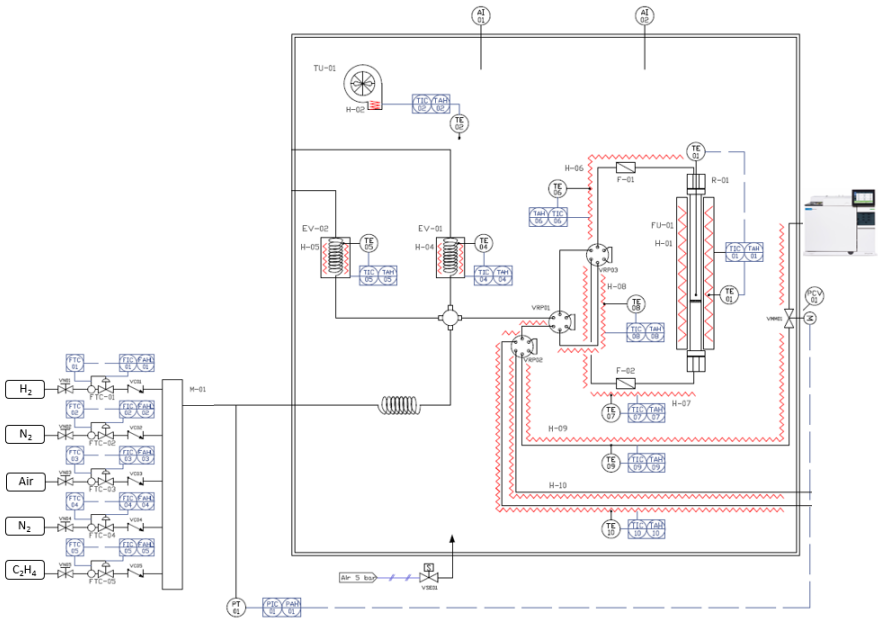

Figure 3.9. MAE PID reaction system diagram employed for the oligomerization reaction.

3.5 THEORETICAL CALCULATIONS

The theoretical calculations presented in Chapter 4, which analyse the optimal metal-alkaline cation distribution that maximize the PtSn interactions in the MFI zeolitic framework, were carried out by Dr. Reisel Millán and Dr. Mercedes Boronat.

To study the most thermodynamically stable configurations for the atom distribution in MFI-type materials, the calculations were performed using the Periodic Density Functional Theory[39] (DFT) methodology employing the Perdew-Burke-Ernzerhof (PBA) exchange-correlation functional within the generalized gradient approach (GGA)[40,41] as implemented in the Vienna Ab-initio Simulation Package (VASP 5.4) code[42]. The valence electron density was expanded in a plane wave basis set with a kinetic energy limit of 400 eV while

the influence of the core electrons on the valence density was accounted for using the projected augmented wave method[43] and the integration was carried out at the Γ-point of the Brillouin zone. Dispersion corrections to the energies were applied using Grimme's D3 method[44,45] with Becke-Johnson damping, as implemented in VASP[46]. The electronic energies values were set to converge to within 10^{-5} eV, and geometries were optimized until atomic forces were less than 0.05 eV/Å. During the geometry optimization process, all atomic positions were allowed to relax without constraints, while the unit cell parameters were kept constant.

Regarding the MFI modelled structure, orthorhombic cell with a chemical composition of $Si_{96}O_{192}$ was considered keeping constant their geometric parameters and being the lattice values *a*=20.090 Å, *b*=19.738 Å and *c*= 13.142 Å and the cell unit angles α=β=γ=90ºC.

5 MFI systems were generated assuming that the structure contains 4 tetrapropylammonium (TPA) cations (unit cell composition $Si_{92}O_{192}N_4C_{48}H_{124}$) placed in the 4 channel intersections present in each unit cell and with the associated 4 silanol/siloxy nest distributed in different ways, as summarized in the **Table 3.3.**

Table 3.3. Relative stability of six MFI-TPA models, each containing four TPA molecules and four associated silanol/siloxy nests positioned in various locations around the channel intersections within the MFI unit cell.

Model	E_{rel} *(kcal/mol)*
MFI-TPA-D1	0.0
MFI-TPA-D2	10.0
MFI-TPA-D3	11.4
MFI-TPA-D4	15.2
MFI-TPA-D5	17.0
MFI-TPA-D6	16.6

Setting as the referential point, the most stable MFI-TPA model (the one with less relative energy), one potassium cation and its counterbalance OH^- anion were introduced in different feasible crystallographic positions of the unit cell (cages, straight channels and the sinusoidal 10 membered ring channels), obtaining 12 MFI-TPA-K feasible systems with $Si_{92}O_{193}N_4C_{48}H_{125}K$ in each unit cell. For each one of these MFI-TPA-K models obtained, a pure silica zeolite containing 1 K^+ and its counter-member OH^- in the same initial position was optimized and used as reference.

Then, having the reference models and the MFI-TPA-K models, the energy required to add the K^+ cations (E_{INC}) was calculated as follows:

$$E_{INC} = E_{MFI-4TPA-K} + E_{MFI} - E_{MFI-4TPA} - E_{MFI-K} \quad \textbf{Eq 3.18}$$

Where:

- $E_{MFI\text{-}4TPA\text{-}K}$ is the total energy of the zeolite when contains the 4 TPA molecules, the K^+ cation and the pertinent defect.
- E_{MFI} is the energy belonging to the pure silica zeolitic framework.
- $E_{MFI\text{-}4TPA}$ is the total energy of the system when 4 TPA and their defects are present.
- $E_{MFI\text{-}K}$ is the total energy of the reference pure silica zeolite containing the K^+ and their defect in the same crystallographic position as it were $E_{MFI\text{-}4TPA\text{-}K}$.

The energy required to include a second K^+ cation was calculated with the next mathematical expression:

$$E_{INC} = E_{MFI-4TPA-2K} + E_{MFI-4TPA} - 2 \cdot E_{MFI-4TPA-K} \quad \textbf{Eq 3.19}$$

Where:

- $E_{MFI\text{-}4TPA\text{-}2K}$ is the total energy of the zeolite when contains the 4 TPA molecules and their associated silanol/siloxy nest, 2 K^+ cations and their pertinent defects, resulting in a unit cell composition of $Si_{92}O_{194}N_4C_{48}H_{126}K_2$.

3.6 REFERENCES

(1) Gallego, E. M.; Paris, C.; Rocío, M. D.-R.; Martínez-Armero, M. E.; Martínez-Triguero, L. J.; Martínez, C.; Moliner, M.; Corma, A. Simple Organic Structure Directing Agents for Synthesizing Nanocrystalline Zeolites. Chem Sci 2017, 8 (12), 8138–8149. https://doi.org/10.1039/c7sc02858j.

(2) Chiappe, C.; Pomelli, C. S.; Rajamani, S. Influence of Structural Variations in Cationic and Anionic Moieties on the Polarity of Ionic Liquids. J. Phys. Chem. B 2011, 115 (31), 9653–9661. https://doi.org/10.1021/jp2045788.

(3) Byer, S. G.; Wong, C.; Yang, R. T.; Reinhardt, J. R. Kinetics of the Reaction between HF and CaO for Fluoride Emission Control. Environ. Sci. Technol 1983, 17 (2), 84–88. https://doi.org/10.1021/es00108a004.

(4) Liu, L.; Lopez-Haro, M.; Lopes, C. W.; Li, C.; Concepcion, P.; Simonelli, L.; Calvino, J. J.; Corma, A. Regioselective Generation and Reactivity Control of Subnanometric Platinum Clusters in Zeolites for High-Temperature Catalysis. Nat. Mat 2019, 18 (8), 866–873. https://doi.org/10.1038/s41563-019-0412-6.

(5) Motagamwala, A. H.; Almallahi, R.; Wortman, J.; Igenegbai, V. O.; Linic, S. Stable and Selective Catalysts for Propane Dehydrogenation Operating at Thermodynamic Limit. Science (1979) 2021, 373 (6551), 217–222. https://doi.org/10.1126/science.abg7894.

(6) Peng, C.; Liu, Z.; Yonezawa, Y.; Yanaba, Y.; Katada, N.; Murayama, I.; Segoshi, S.; Okubo, T.; Wakihara, T. Ultrafast Post-Synthesis Treatment to Prepare ZSM-5@Silicalite-1 as a Core-Shell Structured Zeolite Catalyst.

Microporous Mesoporous Mater. 2019, 277, 197–202. https://doi.org/10.1016/j.micromeso.2018.10.036.

(7) Brunauer, S.; Emmett, P. H.; Teller, E. Adsorption of Gases in Multimolecular Layers. J Am Chem Soc 1938, 60 (2), 309–319. https://doi.org/10.1021/ja01269a023.

(8) De Boer, J. H.; Lippens, B. C.; Linsen, B. G.; Broekhoff, J. C. P.; Van Den Heuvel, A.; Osinga, T. J. The T-Curve of Multimolecular N2-Adsorption. J Colloid Interface Sci 1966, 21 (21), 405–414. https://doi.org/10.1016/0095-8522(66)90006-7.

(9) Jura, G.; Harkins, W. D. A Vapor Adsorption Method for the Determination of the Solid without the Assumption of a Molecular Area, and the Areas Ocuppied Bt Nitrogen and Other Molecules on the Surface Solid. J. Am. Chem. Soc 1994, 66, 1366–1373. https://doi.org/10.1021/ja01236a048.

(10) Lippens, B. C.; Linsen, B. G.; Boer, J. H. de. Studies on Pore Systems in Catalysts I. The Adsorption of Nitrogen; Apparatus and Calculation. J Catal 1964, 3 (1), 32–37. https://doi.org/10.1016/0021-9517(64)90089-2.

(11) Rouquerol, J.; Llewellyn, P.; Rouquerol, F. Is the Bet Equation Applicable to Microporous Adsorbents? Stud Surf Sci Catal 2007, 160, 49–56. https://doi.org/10.1016/S0167-2991(07)80008-5.

(12) Farneth, W. E.; Gorte, R. J. Methods for Characterizing Zeolite Acidity. Chem Rev 1995, 95 (3), 615–635. https://doi.org/10.1021/cr00035a007.

(13) Campbell, S. M.; Jiang, X.-Z.; Howe, R. F. Methanol to Hydrocarbons: Spectroscopic Studies and the Significance of Extra-Framework Aluminium.

Microporous Mesoporous Mater. 1999, 29 (1–2), 91–108. https://doi.org/10.1016/S1387-1811(98)00323-0.

(14) Brodu, N.; Manero, M. H.; Andriantsiferana, C.; Pic, J. S.; Valdés, H. Role of Lewis Acid Sites of ZSM-5 Zeolite on Gaseous Ozone Abatement. J. Chem. Eng, 2013, 231, 281–286. https://doi.org/10.1016/j.cej.2013.07.002.

(15) Emeis, C. A. Determination of Integrated Molar Extinction Coefficients for Infrared Absorption Bands of Pyridine Adsorbed on Solid Acid Catalysts. J Catal 1993, 141, 347–354. https://doi.org/10.1006/jcat.1993.1145.

(16) V. Zholobenko, C. Freitas, M. Jendrlin, P. Bazin, A. Travert, F. Thibault-Starzyk, Probing the acid sites of zeolites with pyridine: Quantitative AGIR measurements of the molar absorption coefficients, J. Catal. 385 (2020) 52–60. https://doi.org/https://doi.org/10.1016/j.jcat.2020.03.003

(17) Sheppard, T.; Daly, H.; Goguet, A.; Thompson, J. M. Improved Efficiency for Partial Oxidation of Methane by Controlled Copper Deposition on Surface-Modified ZSM-5. ChemCatChem 2016, 8 (3), 562–570. https://doi.org/10.1002/CCTC.201500980.

(18) Jacobsen, N. E. NMR Spectroscopy Explained: Simplified Theory, Applications and Examples for Organic Chemistry and Structural Biology, 1st ed.; John Wiley and Sons: Hoboken, New Jersey, 2007. https://doi.org/10.1002/9780470173350.

(19) Reif, B.; Ashbrook, S. E.; Emsley, L.; Hong, M. Solid-State NMR Spectroscopy. Nat Rev Methods Primers 2021, 1 (2). https://doi.org/10.1038/s43586-020-00002-1.

(20) Hunger, M.; Brunner, E. NMR Spectroscopy. Mol. Sieves 2004, 4, 201–293. https://doi.org/10.1007/B94236.

(21) Bakhmutov, V. I. Solid-State NMR in MATERIALS SCIENCE, 1st ed.; Taylor and Francis Group, Ed.; CRC Press: Boca Ratón, Florida, 2011. https://doi.org/10.1201/b11301.

(22) Andrew, E. R.; Bradbury, A.; Eades, R. G. Removal of Dipolar Broadening of Nuclear Magnetic Resonance Spectra of Solids by Specimen Rotation. Nature 1959 183:4678 1959, 183 (4678), 1802–1803. https://doi.org/10.1038/1831802a0.

(23) Batool, S. R.; Sushkevich, V. L.; van Bokhoven, J. A. Correlating Lewis Acid Activity to Extra-Framework Aluminum Species in Zeolite Y Introduced by Ion-Exchange. J Catal 2022, 408, 24–35. https://doi.org/10.1016/j.jcat.2022.02.010.

(24) Babić, V.; Koneti, S.; Moldovan, S.; Debost, M.; Gilson, J. P.; Valtchev, V. Chromic Acid Dealumination of Zeolites. Microporous Mesoporous Mater, 2022, 329, 1–10. https://doi.org/10.1016/j.micromeso.2021.111513.

(25) Yan, Z.; Ma, D.; Zhuang, J.; Liu, X.; Liu, X.; Han, X.; Bao, X.; Chang, F.; Xu, L.; Liu, Z. On the Acid-Dealumination of USY Zeolite: A Solid State NMR Investigation. J Mol Catal A Chem 2003, 194 (1–2), 153–167. https://doi.org/10.1016/S1381-1169(02)00531-9.

(26) Deng, F.; Yue, Y.; Ye, C. Observation of Nonframework Al Species in Zeolite by Solid-State NMR Spectroscopy. J. Phys. Chem. B 1998, 102, 5252–5256. https://doi.org/10.1021/jp9801929.

(27) Fyfe, C. A.; Bretherton, J. L.; Lam, L. Y. Solid-State NMR Detection, Characterization, and Quantification of the Multiple Aluminum Environments in US-Y Catalysts by 27Al MAS and MQMAS Experiments at Very High Field. J Am Chem Soc 2001, 123 (22), 5285–5291. https://doi.org/10.1021/ja003210k.

(28) Joly. Y; Grenier. S. X-Ray Absorption and X-Ray Emission Spectroscopy: Theory and Applications; Bokhoven J, Lamberti C, Eds.; John Wiley & Sons, Inc., 2016. https://doi.org/10.1002/9781118844243.

(29) Noguera, C.; Spanjaard, D.; Friedel, J. Dynamic Screening of Core Hole. I. Semiclassical Model. J. Phys. F: Met. Phys. 1979, 9 (6), 1189. https://doi.org/10.1088/0305-4608/9/6/022.

(30) Boffito. D.C; Neagoe. C; Gerrato. G; Boffito. C; Chiarello. G.L; Bianchi. C.L; Rigamonti. M.G; Benamer. A; Patience. G.S. Experimental Methods and Instrumentation For Chemical Engineers, 2nd ed.; Patience. G, Ed.; John Fedor, 2017. https://doi.org/10.1016/C2015-0-05570-8.

(31) Iglesias-Juez, A.; Chiarello, G. L.; Patience, G. S.; Guerrero-Pérez, M. O. Experimental Methods in Chemical Engineering: X-Ray Absorption Spectroscopy—XAS, XANES, EXAFS. Can. J. Chem. Eng 2022, 100 (1), 1–22. https://doi.org/10.1002/cjce.24291.

(32) Zabinsky, S. I.; Rehr, J. J.; Ankudinov, A.; Albers, R. C.; Eller, M. J. Multiple-Scattering Calculations of x-Ray-Absorption Spectra. Phys Rev B Condens Matter 1995, 52 (4), 2995–3009. https://doi.org/10.1103/PHYSREVB.52.2995.

(33) Ravel, B.; Newville, M. ATHENA, ARTEMIS, HEPHAESTUS: Data Analysis for X-Ray Absorption Spectroscopy Using IFEFFIT. J. Synchrotron Rad. 2005, 12 (4), 537–541. https://doi.org/10.1107/S0909049505012719.

(34) G.Fierro, J. L. Studies in Surface Science and Catalysis. Stud Surf Sci Catal 1990, 57, B391–B394. https://doi.org/10.1016/S0167-2991(08)61519-0.

(35) Joy, D. C.; Cowley, J. M. Handbook of Microscopy : Applications in Materials Science, Solid-State Physics, and Chemistry. Methods II, 1st ed.; Amelinckx, S., Van Dyck, Dirk., Van Landuyt, J., Van Tendeloo, G., Eds.; John Wiley & Sons, 2008; Vol. 2. https://doi.org/10.1002/9783527620647.

(36) Saxena, A.; Joshi, R.; Seemakurthi, R. R.; Koninckx, E.; Broadbelt, L. J.; Greeley, J.; Gounder, R. Effect of Nickel Active Site Density on the Deactivation of Ni-Beta Zeolite Catalysts during Ethene Dimerization. ACS Engineering Au 2021, 2 (1), 12–16. https://doi.org/10.1021/ACSENGINEERINGAU.1C00014.

(37) Moon, S.; Chae, H. J.; Park, M. B. Oligomerization of Light Olefins over ZSM-5 and Beta Zeolite Catalysts by Modifying Textural Properties. Appl Catal A Gen 2018, 553, 15–23. https://doi.org/10.1016/J.APCATA.2018.01.015.

(38) Martínez, A.; Arribas, M. A.; Concepción, P.; Moussa, S. New Bifunctional Ni–H-Beta Catalysts for the Heterogeneous Oligomerization of Ethylene. Appl Catal A Gen 2013, 467, 509–518. https://doi.org/10.1016/J.APCATA.2013.08.021.

(39) Kohn, W. Nobel Lecture: Electronic Structure of Matter-Wave Functions and Density Functionals*. Rev Mod Phys 1998, 71 (5), 1253–1266.

(40) Perdew, J. P.; Chevary, J. A.; Vosko, S. H.; Jackson, K. A.; Pederson, M. R.; Singh, D. J.; Fiolhais, C. Atoms, Molecules, Solids, and Surfaces: Applications of the Generalized Gradient Approximation for Exchange and Correlation. Phys Rev B 1992, 46 (11), 6671. https://doi.org/10.1103/PhysRevB.46.6671.

(41) Perdew, J. P.; Wang, Y. Accurate and Simple Analytic Representation of the Electron-Gas Correlation Energy. Phys Rev B 1992, 45 (23), 13244. https://doi.org/10.1103/PhysRevB.45.13244.

(42) Kresse, G.; Furthmüller, J. Efficient Iterative Schemes for Ab Initio Total-Energy Calculations Using a Plane-Wave Basis Set. Phys Rev B 1996, 54 (16), 11169. https://doi.org/10.1103/PhysRevB.54.11169.

(43) Blöchl, P. E. Projector Augmented-Wave Method. Phys Rev B 1994, 50 (24), 17953. https://doi.org/10.1103/PhysRevB.50.17953.

(44) Goerigk, L.; Grimme, S. A Thorough Benchmark of Density Functional Methods for General Main Group Thermochemistry, Kinetics, and Noncovalent Interactions. Phys. Chem. Chem. Phys. 2011, 13 (14), 6670–6688. https://doi.org/10.1039/C0CP02984J.

(45) Grimme, S. Semiempirical GGA-Type Density Functional Constructed with a Long-Range Dispersion Correction. J Comput Chem 2006, 27 (15), 1787–1799. https://doi.org/10.1002/JCC.20495.

(46) Grimme, S.; Ehrlich, S.; Goerigk, L. Effect of the Damping Function in Dispersion Corrected Density Functional Theory. J Comput Chem 2011, 32 (7), 1456–1465. https://doi.org/10.1002/JCC.21759.

CHAPTER 4:

RESOLVING COMPLEX K-Pt-Sn INTERACTIONS IN PtSn@K-MFI CATALYSTS FOR ALKANE DEHYDROGENATION

4.1. INTRODUCTION

In the past decade, the availability of low-cost C_2-C_4 light alkanes has abruptly raised with the increase in shale gas production[1], providing new opportunities to commodity chemicals outside conventional syngas and steam cracking processes[2,3]. Among the numerous routes to selectively turn light alkanes into useful building blocks, their direct dehydrogenation to olefins is an industrial reality, thanks to highly active and selective commercial catalysts that make the overall operation[4-6]. Among the entire direct olefin dehydrogenation routes, the direct dehydrogenation of propane has gained particular industrial importance due to its high selectivity towards the formation of solely propylene, avoiding the formation of hybrid products[7]. The reaction equations of direct propane dehydrogenation and competitive side pathway reactions are shown below[8].

$$C_3H_8 \rightarrow C_3H_6 + H_2 \quad \left(\Delta H^{\theta}_{298} = 124.3\ kJ \cdot mol^{-1}\right) \qquad \textbf{Eq 4.1}$$

$$C_3H_8 \rightarrow CH_4 + C_2H_4 \quad \left(\Delta H^{\theta}_{298} = 98.9\ kJ \cdot mol^{-1}\right) \qquad \textbf{Eq 4.2}$$

$$C_3H_8 + H_2 \rightarrow C_2H_6 + CH_4 \quad \left(\Delta H^{\theta}_{298} = -37.7\ kJ \cdot mol^{-1}\right) \qquad \textbf{Eq 4.3}$$

$$C_2H_4 + H_2 \rightarrow C_2H_6 \quad \left(\Delta H^{\theta}_{298} = -136.6\ kJ \cdot mol^{-1}\right) \qquad \textbf{Eq 4.4}$$

$$C_3H_8 \rightarrow 3C + 4H_2 \quad \left(\Delta H^{\theta}_{298} = 119.5\ kJ \cdot mol^{-1}\right) \qquad \textbf{Eq 4.5}$$

Nevertheless, as illustrated in **Eq 4.1**, thermodynamic limitations of this transformation impose high reaction temperatures to reach the high conversions, making the process energy intensive, while triggering non-trivial

catalyst deactivation challenges that negatively impact both economic and environmental metrics[3,5].

Supported-Pt catalysts have been broadly investigated to promote the direct dehydrogenation of light alkanes to olefins, mainly propane to propylene, due to their remarkable ability to activate C-H bonds, while largely avoiding C-C bond cleavage (**Eq 4.2**)[9,10]. The active phase in supported-Pt catalysts typically exists either as a Pt metal cluster or as crystalline nanoparticles. Previous density functional theory (DFT) studies revealed that Pt(111) exhibits comparable energy barriers for the dehydrogenation step and the subsequent desorption of the propylene molecule[11]. In contrast, Pt(211) shows a significantly lower energy barrier for dehydrogenation (0.29 eV) compared to the barrier for propylene desorption (1.43 eV). This difference in energy barriers contributes to the formation of coke during deep dehydrogenation processes. In addition to the coke formation issue, conducting the propane dehydrogenation process at elevated temperatures (Tamman temperature for Pt is 750°C) leads to migration and further sintering of Pt nanoparticles[12-14]. These effects are driven by the Ostwald ripening mechanism and the nanoparticles become larger, leading to non-desired side reactions, such as cracking (**Eq 4.2**), hydrogenolysis (**Eq 4.3**), ethylene hydrogenation (**Eq 4.4**) or more coke formation (**Eq 4.5**). Then, despite exhibiting adequate propane dehydrogenation activity, its inclination to sintering and coking and their expensive manufacturing cost still requires the development of low Pt-content and highly stable catalysts, by means of special preparation methods, based on promoter species effects and metal-support interaction improvement.

The incorporation of promoter metals aims to pair platinum (Pt) with other metals (M), resulting in either Pt-M composites or the formation of a PtM bimetallic alloy. This approach has been shown to enhance both the activity and selectivity for propylene production while reducing the amount of Pt required in the catalyst support. Numerous studies have explored the influence of these promoter species on the performance of bimetallic Pt catalysts, considering factors such as electronegativity, cost, toxicity, and chemical affinity. Among them, Sn has become in the recent years a typical, necessary, Pt promoter that further reduces undesired side transformations, such as hydrogenolysis and coke formation reactions [9,10,15]. There is still debate concerning the exact role of Sn, since it has been proposed to have both "geometric effects" and "electronic effects"[16-18]. In the first case, Sn promotes the separation of Pt ensembles, leading to the formation of small clusters, thus removing accessible sites for coke formation (as structure-sensitive undesired side reaction)[19-21]. Regarding its "electronic effect", previous studies showed a strong electron transfer between Sn and Pt atoms, turning the Pt atoms electron-richer, promoting the propylene desorption and decreasing the amount of coke formed[22,23]. Further DFT studies determined that the presence of Sn widens the Pt d-band, downshifting the d-band centre of Pt placed on PtSn bimetallic systems surface. This electronic structure modification results in a decrease of the energy barrier required to carry out the propylene desorption step and in an increase of the energy barrier to achieve the propane dehydrogenation, boosting the propylene selectivity while preventing coke or other subproducts formation[24]. In addition to Sn, another Pt promoters have also been described in the literature, such as Zn, Ge or In, among others (schematized in **Figure 4.1**.)[25-27].

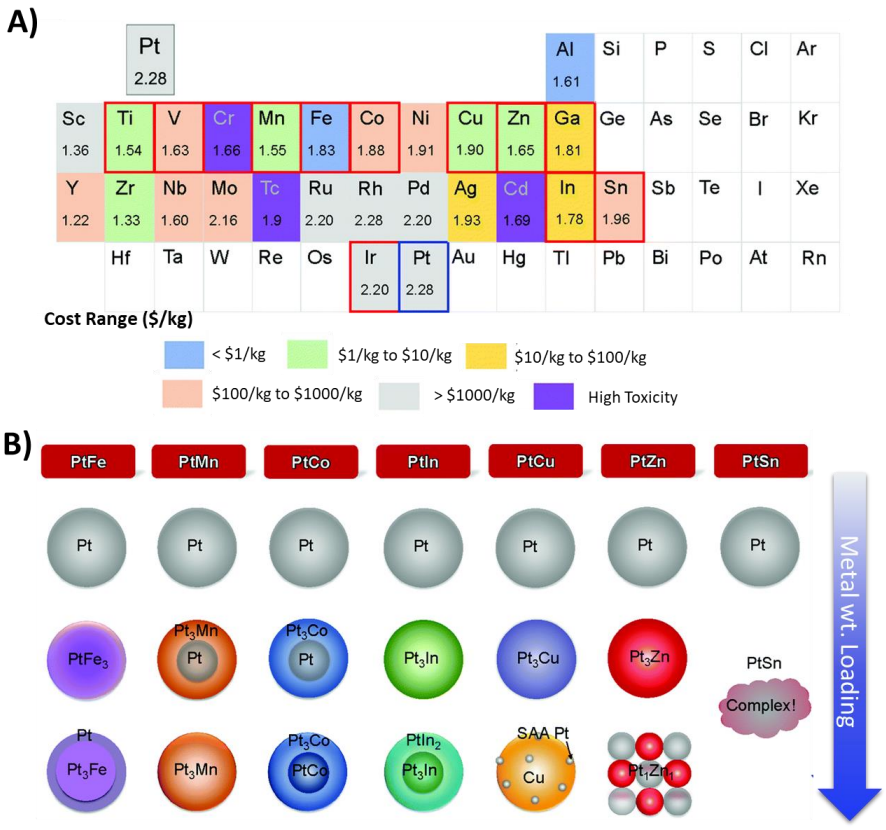

Figure 4.1. Structure scheme of different PtM bimetallic systems. **A)** shows a wide selection of different metal promoter M (electronegativity is indicated inside each metal frame), their cost and their potential toxicity. **B)** shows PtM structures obtained at different M %w/w contents. Scheme obtained from Cheng *et al*[8].

The main disadvantage of these common PtSn supported-metal catalysts is that they suffer permanent deactivation when subjected to severe redox stress, for example, during reaction and coke burn regeneration cycles in typical PDH processes, which causes extensive sintering of the metal nanoparticles[12,28].

Because of this deactivation problem, commercial PtSn catalysts must undergo complex continuous catalyst rejuvenation protocols (*i.e.* oxychlorination), which operate under increased cost, safety controls, and waste management regulations, to re-disperse the metal species and preserve proper levels of catalytic activity[29].

A recent strategy to boost the stability of metal nanoparticles has been the encapsulation of subnanometric PtSn clusters within the pores of pure silica MFI zeolite, a zeolite-type support widely reported to improve the propylene selectivity due to the absence of acid centers[30,31], following a one-pot synthesis approach that relies on the use of potassium cations to introduce negative charge into the zeolite framework, in the absence of trivalent elements (*i.e.* Al)[32,33]. HAADF-STEM and i-DCP imaging of the resultant PtSn@K-MFI catalyst demonstrated the regioselective stabilization of subnanometric PtSn clusters (~0.6-0.8 nm) in the sinusoidal 10-ring channels of MFI (as shown in **Figure 4.2**), associated with the formation of silanol/siloxy nests with potassium cations located at sinusoidal channels that connect with straight 10-ring pores[34] .

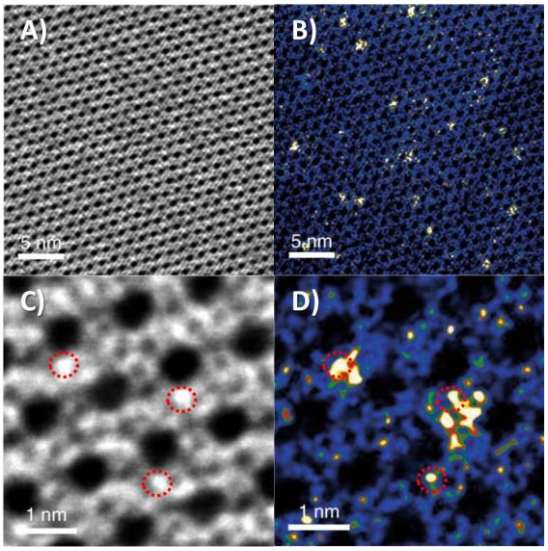

Figure 4.2. Identification of the location of subnanometric Pt clusters within the KPtSn@MFI catalyst. Large-area and detailed HR HAADF-STEM images (**A, C**) and the iDPC images on the same area (**B, D**) in the [010] orientation. Images reported by Liu L., *et al*[8].

As a result of these zeolite binding sites, outstanding resistance against metal sintering was observed compared to other zeolite-based catalysts prepared by conventional impregnation methods [32,33]. The resultant catalyst was not only sintering-resistant but could also catalyse the dehydrogenation of light alkanes to olefins with minimal cracking and coke formation (*i.e*. minimal time-on-stream deactivation).

Preliminary inspection of the influence of the Sn content in the original PtSn@K-MFI formulations revealed an optimal Sn content of ~0.9 wt.%, and the requirement of long reduction treatments to properly activate the catalyst in H_2 prior to the PDH reaction (*i.e.* reduction times longer than 12 h).[33] In this former study, by lowering the Sn content to 0.4 wt.% or lowering the activation times to < 12 h, a significant increase of the time-on-steam

(TOS) deactivation rates was observed in the catalytic tests, presumably as a result of decreased Pt-Sn interactions in the final material[33].

The present work was motivated by these results, and by previous observations reported on one-pot synthesis of Sn- and Ti-containing zeolites, where problematic synthesis outcomes where noticed when alkali cations were simultaneously present, due to the proneness of the latter to induce the formation of insoluble tin- or titano-silicates [35,36], thus altering the amount of metal available, in practice, inside the zeolite and decreasing the potential catalytic activity expected from them.

Keeping this in mind, this chapter pursues to provide a rational and systematic research about how the nominal formulation of PtSn@K-MFI catalysts affects the composition, structure, and performance of the final materials. To achieve this, a series of Pt-MFI catalysts were synthesized with specific and independently adjusted K and Sn contents. This chapter explores the impact of adjusting the atomic concentrations of K and Sn on the crystallinity and particle size distribution of both the crystalline MFI support and the bimetallic clusters encapsulated within the zeolite. Catalytic evaluations were conducted to identify the optimal compositional balance under the high-temperature conditions characteristic of the propane dehydrogenation (PDH) reaction. Finally, to correlate the influence of Sn content in the synthesis gel, reduction treatment parameters (temperature and duration), and time-on-stream (TOS) on the nature of Pt-Sn interactions, as well as their respective effects on catalytic performance, X-ray absorption spectroscopy (XAS) measurements were performed on the fresh and spent catalysts.

4.2. ONE-POT SYNTHESIS OF PtSn@K-MFI SAMPLES AND POST-SYNTHETIC TREATMENTS WITH NaOH: INFLUENCE OF K AND Sn CONTENTS

To enhance the clarity and traceability of the different samples examined, the nomenclature assigned to them, and the target compositions of the corresponding synthesis gels are summarized in **Table 4.1**. In order to evaluate the incorporation efficiency of the target species, the chemical composition of the resulting materials have been compared with the targeted K and Sn contents.

Table 4.1. ICP analyses of the different PtSn@K-MFI samples prepared by one-pot synthesis methods (note: the weight percentages both in the gel and solids are silica basis).

	Synthesis gels			***Solids recovered***		
Sample	**Pt (wt %)**	**K (wt %)**	**Sn (wt %)**	**Pt (wt %)**	**K (wt %)**	**Sn (wt %)**
MFI-PtSn1a	0.4	n.d.[a]	1	0.41	0.88	1.00
MFI-PtSn1b	0.4	n.d.[a]	1	0.40	1.15	1.05
MFI-PtSn2	0.4	1.3	1.4	0.41	1.05	1.38
MFI-PtSn2_NaOH[b]	---	---	---	0.43	0.73	0.77
MFI-PtSn3	0.4	1.3	1	0.45	1.03	0.98
MFI-PtSn4	0.4	1.3	0.7	0.42	0.87	0.72
MFI-PtSn5	0.4	1.3	0.5	0.43	0.81	0.49
MFI-Pt6	0.4	1.3	---	0.43	0.65	---
MFI-7	----	1.3	---	---	0.70	---
MFI-PtSn8	0.4	0.65	1.3	0.44	0.60	1.24
MFI-PtSn9	0.4	0.65	1	0.46	0.67	1.08
MFI-PtSn10	0.4	0.65	0.5	0.48	0.60	0.54
MFI-PtSn11	0.4	0.65	0.2	0.41	0.58	0.19

[a] Non-determined; [b] Treated with 20 wt.% NaOH aqueous solution at 60°C for 1 h (liquid/solid ratio=10)

The original recipe to synthesize PtSn@K-MFI used a commercially-available aqueous solution of tetrapropylammonium hydroxide (TPAOH) containing trace amounts of K in the solution [32,33]. This prior work (referred as MFI-PtSn1) showed that the presence of K cations within the final PtSn@K-MFI solids is critical to stabilize subnanometric PtSn clusters in the sinusoidal MFI channels, which do not sinter when subjected to cyclic high-temperature H_2/O_2 treatments, unlike most other catalysts reported in the literature [32,33].

Surprisingly, detailed FESEM and STEM (**Figure 4.3**) analysis of these samples indicates that small amounts of precipitates (*i.e.* impurities) are present in the as-prepared materials, mixed with the MFI crystals. The abundance of these impurities varies depending on the specific batch of TPAOH used while all other synthesis variables are maintained constant, as shown in **Figure 4.3**, for FESEM and STEM images (top panel) and STEM magnification (bottom panel). Energy-dispersive X-ray spectroscopy (EDX) shows that these regions are enriched in Sn relative to the average Sn composition in the final solids, Si/Sn= 76 and Si/Sn = 119 for Spectrum 1 and 2 in **Figure 4.3.C**, respectively, thus confirming the precipitation of part of the Sn as a tin-silicate phase.

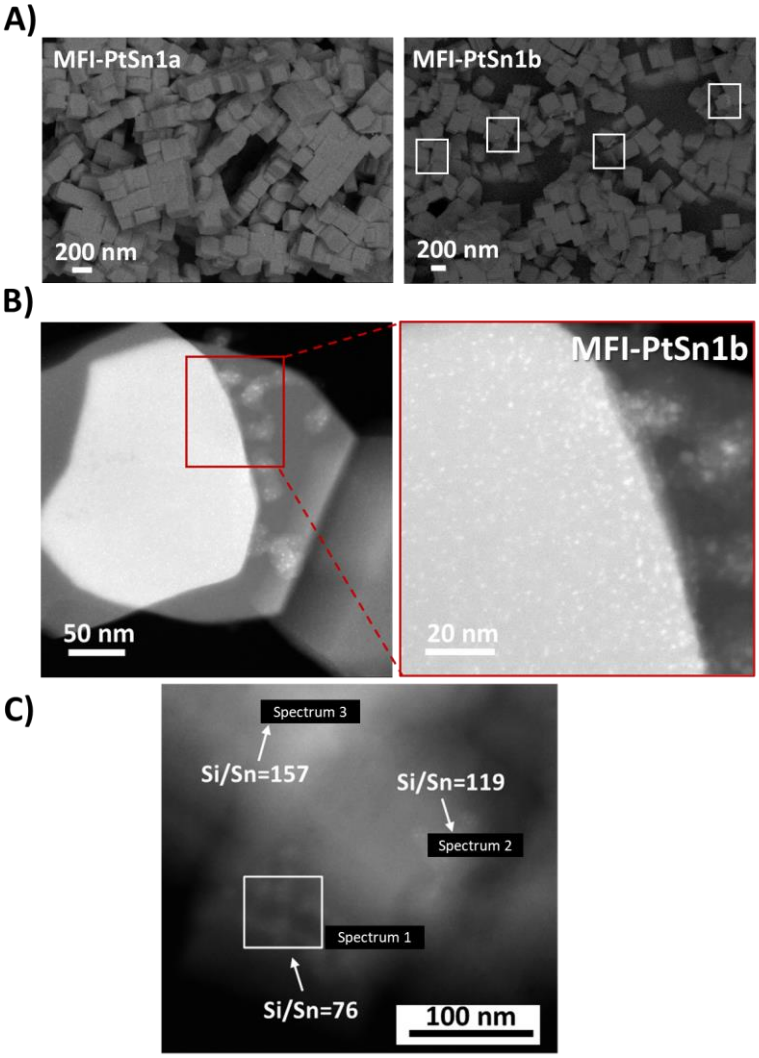

Figure 4.3. FESEM Dark Field and High-Angle Annular Dark Field (HAADF) TEM images of MFI-PtSn1 calcined sample **A)** FESEM images of the MFI-PtSn1 sample prepared using two different commercially-available TPAOH solution batches containing traces of K. White squares shown impurities areas. **B)** STEM images and zoom of the impurities (red square) and **C)** EDX/STEM analysis of the MFI-PtSn1b sample after being subjected to calcination and reduction treatments at 600°C in air and hydrogen, respectively. Red squares represent the zoom area to measure de EDX analysis; white squares shown the area for EDX spectrum measurement.

The results obtained seem to indicate that the precipitation of tin-silicates is promoted by the presence of K, whose concentration may vary slightly batch to batch in commercial TPAOH sources. This hypothesis finds roots in previous works on TS-1 materials, where it was observed that K in the synthesis gel induces the precipitation of titano-silicates[35,36]. The variability in results using different TPAOH batches suggests that the K, Sn and/or Pt speciation might be affected by subtle differences in the synthesis gels within a narrow compositional range, which triggered this new research.

To better understand and control the formation of active sites in one-pot synthesis of PtSn@K-MFI catalysts, while avoiding the variability provided by the different K traces content of the commercially available TPAOH, different preparations using a commercially available K-free TPA solution were prepared, employing KCl as a more reliable K source (see **Chapter 3**, section **3.2.3.1.6** for further details). For this initial study (samples MFI-PtSn2-5), the initial K content in the synthesis gel was fixed at 1.3 wt.%, whereas the Sn content was varied from 1.4 to 0.5 wt.%.

The PXRD patterns of these PtSn@K-MFI samples after calcination match the characteristic pattern of the MFI structure crystal phase (MFI-PtSn2-5 in **Figure 4.4**). The corresponding FESEM images confirm the formation of homogeneous zeolite crystallites with average sizes close to 200-300 nm (**Figure 4.5**). However, an amorphous contamination is also observed by FESEM in some cases (see squared areas in **Figure 4.5**), which becomes increasingly more prominent as the Sn content increases (thus, maximum at 1.4 wt.% Sn in MFI-PtSn2, and virtually inappreciable at 0.5 wt % Sn in MFI-PtSn5). STEM-EDX analysis of the samples calcined in air and reduced in

hydrogen at 600°C confirms the presence of these impurities in all cases, the size of which oscillates between ~ 10 nm, thus, too small to be observable by FESEM, when the amount of Sn is small (*i.e.* 0.5 wt.% in MFI-PtSn5, **Figure 4.5**-bottom right), and > 100 nm, when the amount of Sn is 1.4 wt.% (MFI-PtSn2, **Figure 4.5-**top left). Chemical analyses confirm, again, that these regions are Sn-enriched (Si/Sn < 20, compared to 110 in the zeolite crystals, **Figure 4.6**-bottom). The STEM images also show the formation of subnanometric metallic clusters in both materials[37], which appear preferentially located in areas of the MFI lacking other impurities (see **Figure 4.7**).

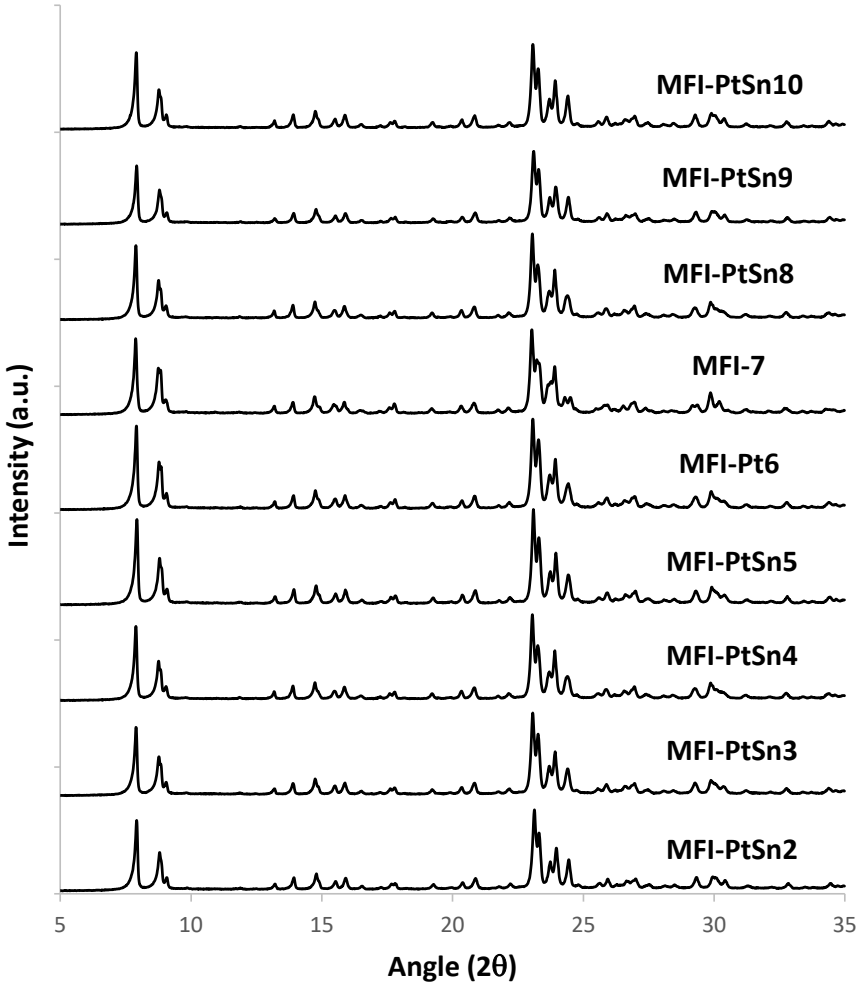

Figure 4.4. PXRD patterns of different PtSn@K-MFI samples in their calcined forms.

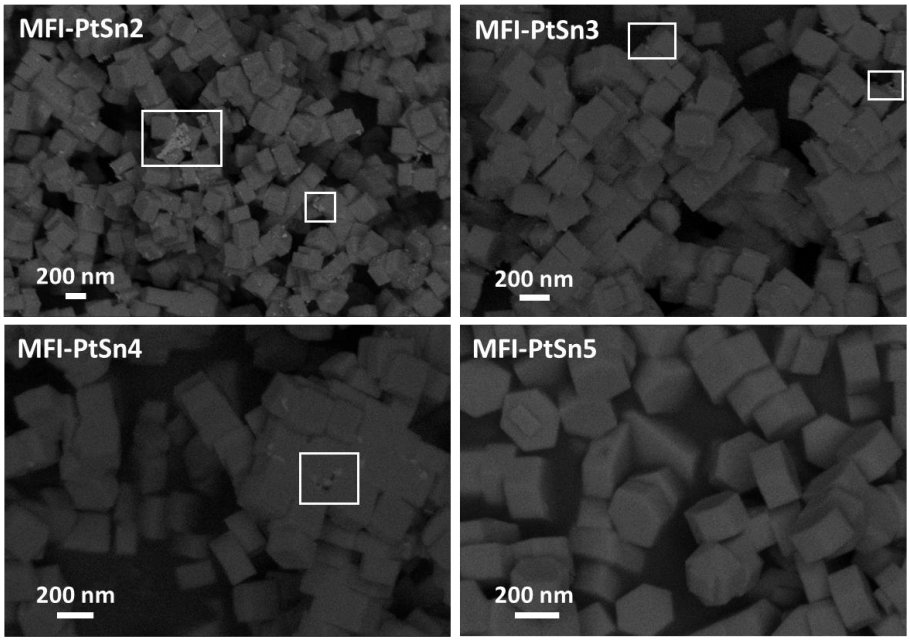

Figure 4.5. FESEM images of the as-prepared MFI-PtSn2-5 samples. White squares shown impurities areas.

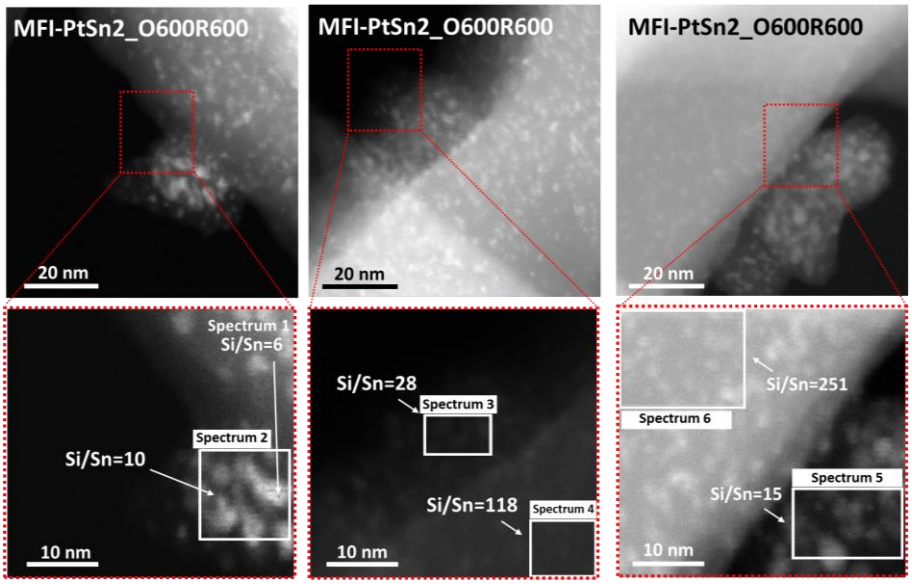

Figure 4.6. STEM (top) and EDX/STEM (bottom) analysis from the zoom area (red squares) of the MFI-PtSn2 sample after being subjected to calcination and reduction treatments at 600°C in air and hydrogen, respectively (O600R600). White squares show the selected area for EDX spectrum measurement.

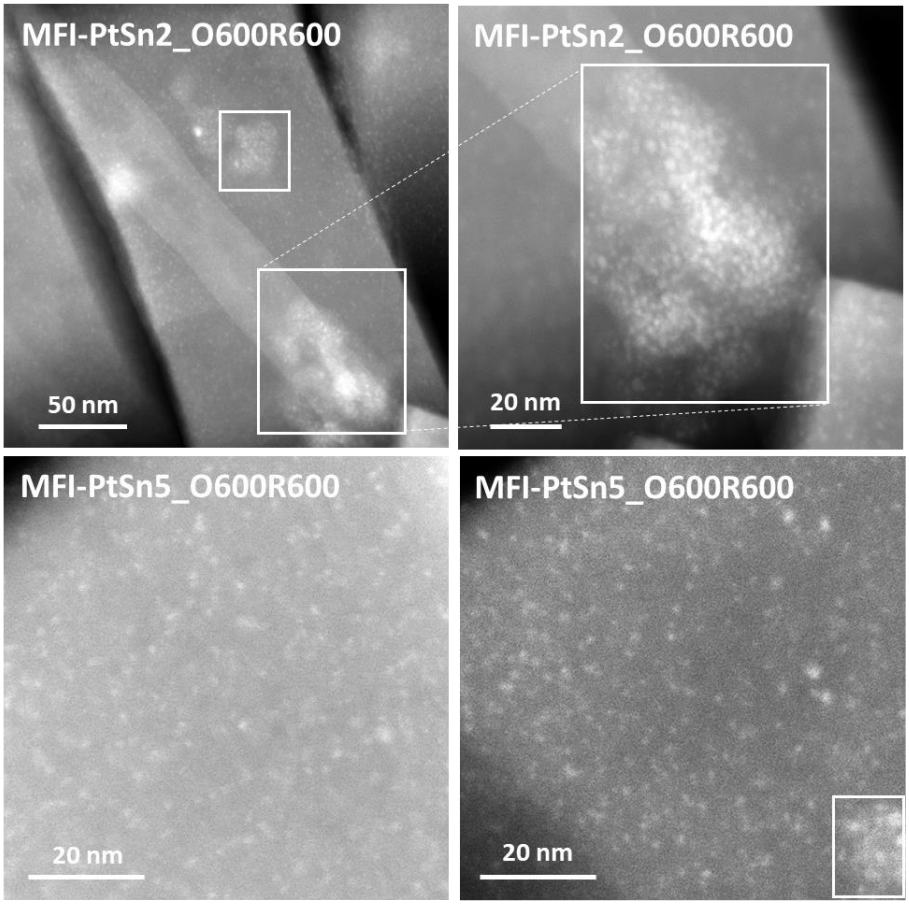

Figure 4.7. STEM images of the MFI-PtSn2 and MFI-PtSn5 samples after being subjected to calcination and reduction treatments at 600°C in air and hydrogen, respectively (O600R600)**.** White squares shown the impurities areas in both samples.

Interestingly, ICP analysis of MFI-PtSn2-5 samples show that the Pt and Sn contents in the final solids are analogous to those introduced in the corresponding synthesis gels, but the K content was lower (0.8-1 wt.% vs ~1.3 wt.% in the gels, MFI-PtSn2-5 in **Table 4.1**). Moreover, the amount of K incorporated decreased as the Sn content was lowered in the 1.4 to 0.5 wt.% range. The relationship between these two variables is linear (**Figure 4.8**) and

predicts that the maximum amount of K that incorporates into the final solid is 0.68 wt.%, when Sn is not present (extrapolation of the trendline to Sn wt.% = 0, *i.e. Y*-intercept at origin in **Figure 4.8**). This observation, and the fact that the concentration of amorphous precipitates in the final solids becomes more significant as the amount of Sn increases, led us to infer that K cannot be incorporated into the solids above this threshold (~0.68 wt.%), unless it is sequestered by Sn into the tin-silicates phase.

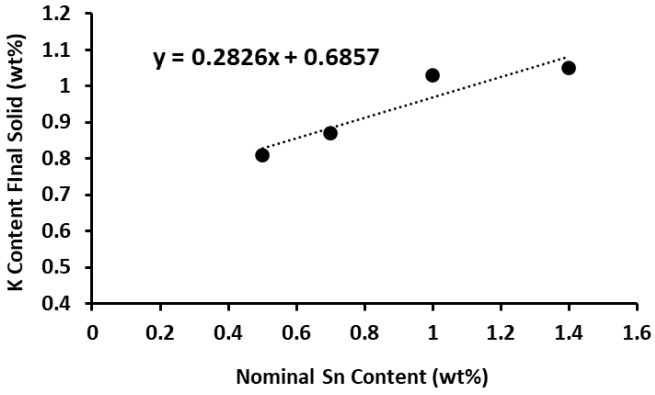

Figure 4.8. Amount of K (wt.%) incorporated in the final MFI-PtSn2-5 samples as the Sn content was decreased in the 1.4 to 0.5 wt.% range.

Chasing these preliminary evidences, an additional experiment was rationally designed to obtain better understanding of the correlation between K and Sn in these samples., after developing a protocol that selectively removes inorganic impurities from the external surface of the zeolite via controlled base-washing of uncalcined samples. For this experiment, as-prepared MFI-PtSn2 sample containing amorphous tin-silicate impurities was treated with 20 wt.% NaOH aqueous solution at 60°C for 1 h, at a fixed liquid/solid ratio of 10, leading to conditions alkaline enough to dissolve these non-desired

impurities (see **Chapter 3**, section **3.2.3.3.3** for further experimental details). The procedure does not remove the organic TPA inside the MFI pores, which we expected to protect the zeolite and any internal inorganic extra-framework cations from being reacted and extracted. FESEM images before and after these treatments demonstrate that the amorphous contamination on the surface of the MFI crystals is effectively removed through the process, without alteration of the zeolite particle morphology (**Figure 4.9.** lower images). The removal of these amorphous impurities is, moreover, accompanied by a substantial decrease in the K and Sn contents (K content drops from 1.05 to 0.73 wt.%, and Sn content drops from 1.38 wt.% to 0.77 wt.%, see MFI-PtSn2 and MFI-PtSn2_NaOH in **Table 4.1**). The Pt content, in contrast, appears unaffected by the NaOH treatment (0.41 and 0.43 wt.% for MFI-PtSn2 and MFI-PtSn2_NaOH, respectively, **Table 4.1**). These results confirm that the NaOH treatment removes the amorphous precipitates selectively, while maintaining metals inside the MFI crystals intact, thanks to the protecting role of TPA prior to calcination. The result also suggests that the vast majority of Pt is successfully encapsulated inside the zeolite pores during its crystallization.

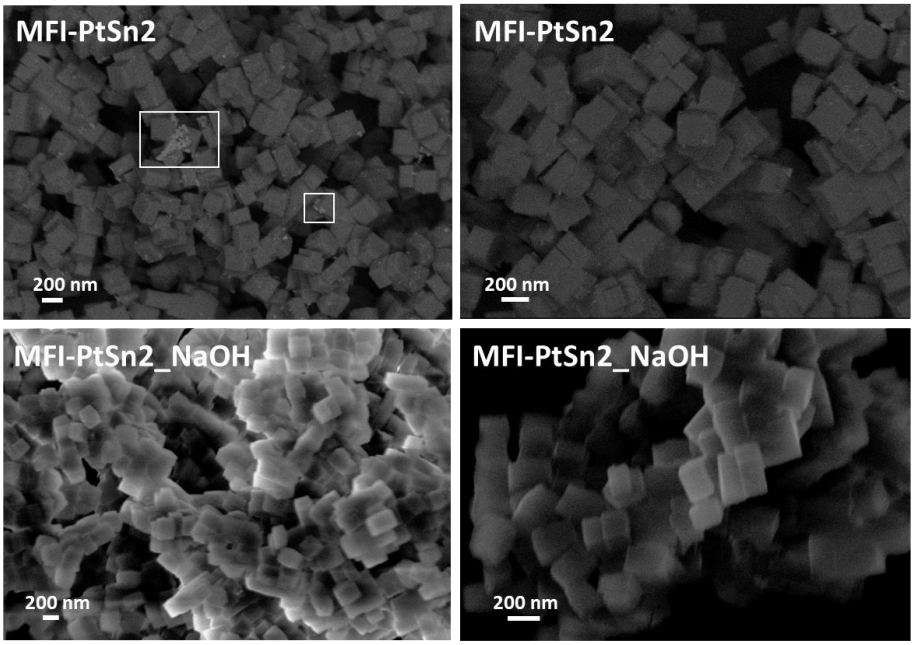

Figure 4.9. FESEM images of the as-prepared MFI-PtSn2 sample and after being subjected to a post-synthetic treatment with NaOH (20 wt.% aqueous solution) at 60°C for 1 h, liquid/solid ratio=10. White squares show the impurities areas.

Interestingly, the amount of K retained by the zeolite after the NaOH wash, once the vast majority of the tin-silicate has been removed, is very close to the maximum amount of K that is incorporated into the final solid according to **Table 4.1**, in experiments conducted at variable Sn concentrations in the synthesis gels. This observation supports the hypothesis that samples that avoid tin-silicate impurities cannot incorporate K above a certain stoichiometric concentration of about ~0.7 wt.% in the final product (see MFI-PtSn2_NaOH in **Table 4.1**).

In order to verify this postulate, further evidence was provided in the following sections through additional experiments run under Sn-free

conditions using TGA, ^{1}H 2D DQ/SQ NMR, and DFT calculations to rationalize the observed stoichiometry in a quantitative manner.

4.3. Sn-FREE Pt@K-MFI BLANK EXPERIMENTS: UNDERSTANDING THE REQUIRED STOICHIOMETRIC K CONTENT

In order to determine the maximum K content that can be incorporated through a one-pot method inside purely siliceous MFI crystals, two more experiments were performed, avoiding the Sn addition in the synthesis gels and, therefore, eliminating the possibility to form a K-doped tin-silicate impurity. Both of these samples were synthesized at high nominal K contents (*i.e.* 1.3 wt.%), but the first one targeted a nominal Pt content of 0.4 wt.% (MFI-Pt6), whereas the second was a Pt-free sample (MFI-7). MFI crystals in these samples maintain similar particle morphology and size compared to previous PtSn@K-MFI materials, as demonstrated by FESEM (**Figure 4.10**).

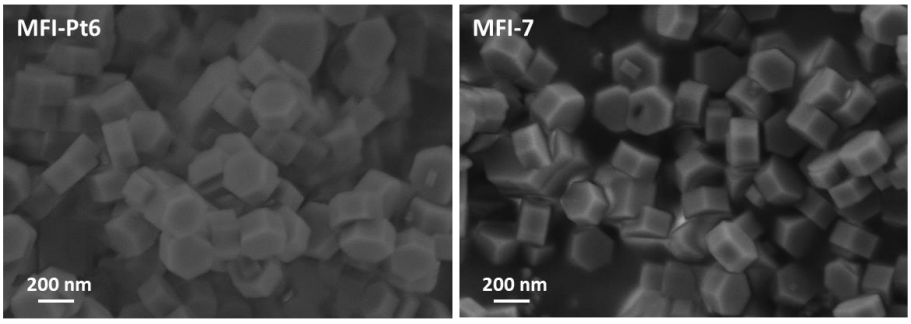

Figure 4.10. FESEM images of the as-prepared Sn-free MFI-Pt6 sample and the PtSn-free MFI-7 sample.

The loading of K in the final solids, measured by ICP, is similar in both materials, ~ 0.65-0.69 wt.%, which is almost half the amount introduced in

the synthesis gels, and is also significantly lower compared to syntheses run in the presence of Sn at equivalent nominal K values (**Table 4.1**, comparison between MFI-Pt6 and MFI-7 vs MFI-PtSn2-5). From these experiments, the maximum amount of K that can be incorporated into the MFI crystals via a one-pot synthesis method was estimated, obtaining again a content approximately of 0.7 wt.%, consistent with the prediction from **Figure 4.8**.

To understand the genesis of this limitation, elemental and thermogravimetric analyses were performed, determining that the as-prepared K-MFI samples incorporate ~4 molecules of TPA per unit cell of the zeolite, which contains ~ 96 T atoms (**Table 4.2**). TPA, thus, is expected to occupy the four pore intersections per unit cell of the zeolite, in good agreement with conventional MFI syntheses. In the absence of tetrahedrally coordinated elements such as Al, having 4 TPAs per unit cell locates one framework defect in every intersection of the zeolite, just to counterbalance the positive charge of the extra-framework organic cation.

At 0.7 wt.% K, which is the maximum amount of K that we could experimentally introduce into the MFI crystals under these conditions, materials are incorporating ~1 K atom per unit cell, thus, one extra framework defect every four intersections (**Table 4.2**).

Table 4.2. Elemental and thermogravimetric analyses of the K-MFI sample.

Sample	C (wt.%)[a]	N (wt.%)[a]	C/N (molar ratio)	TGA weight loss (wt.%)[b]	TPA/u.c[c]	K/u.c.
MFI-7	9.19	0.89	12.0	13.4	4.10	1.02

[a] Calculated from the elemental analysis; [b] Calculated from the thermogravimetric analysis (TGA) up to 600°C; [c] u.c.: unit cell of MFI (96 T atoms)

The ^{1}H MAS NMR spectrum of MFI-7 shows an asymmetric main signal centred at 2 ppm (see **Figure 4.11, A)**), whereas other smaller resonances appear at high field (10.2, 12.4 and 16.4 ppm, see **Figure 4.11, A)**). A detailed integration of the ^{1}H MAS NMR spectrum reveals ~112 protons for the signal centred at ~2 ppm, ~9 protons associated with the signal at 10.2 ppm, ~3 protons with the signal at 12.4 ppm, and ~1 proton to the signal at 16.4 ppm (see **Figure 4.11 A)**). The signal at 2 ppm has been assigned to protons of the methyl and methylene groups in TPA molecules (4 per MFI unit cell), whereas the signals at 10.2 and 12.4 ppm have been assigned to defective sites containing a Si-vacancy (see **Figure 4.11, C)**)[38], compensating the positive charge of the organic TPA cation in the TPA-MFI zeolite framework. These signals account for 12 protons, corresponding to the presence of four $(SiOH)_3{-}SiO^-$ clusters per unit cell (see **Figure 4.11, C)**)[38]. Finally, and to the best of our knowledge, the signal at 16.4 ppm, corresponding to ~1 proton per unit cell, has not been described in the literature. It is worth noting that this signal does not appear if the MFI is prepared under K-free conditions (see **Figure 4.11, B)**). To assign this signal, ^{1}H 2D DQ/SQ NMR experiments were performed. Because no DQ correlation is observed at 32.8 ppm (2*16.4 ppm, see circle in **Figure 4.11, B)**), and because DQ signals require at least a pair of

protons, we infer that the 16.4 ppm signal derives from a single proton. The low-field shift of this signal could suggest a strong hydrogen bond interaction, which is more pronounced than that observed in the $(SiOH)_3$-Si-O^- cluster. To maintain the neutral charge of the TPA-MFI structure, the signal at 16.4 ppm was tentatively assigned to a SiOH-SiO^- connectivity defect compensated by K^+ (see **Figure 4.11, D)**), in good agreement with the presence of ~1 K per MFI unit cell.

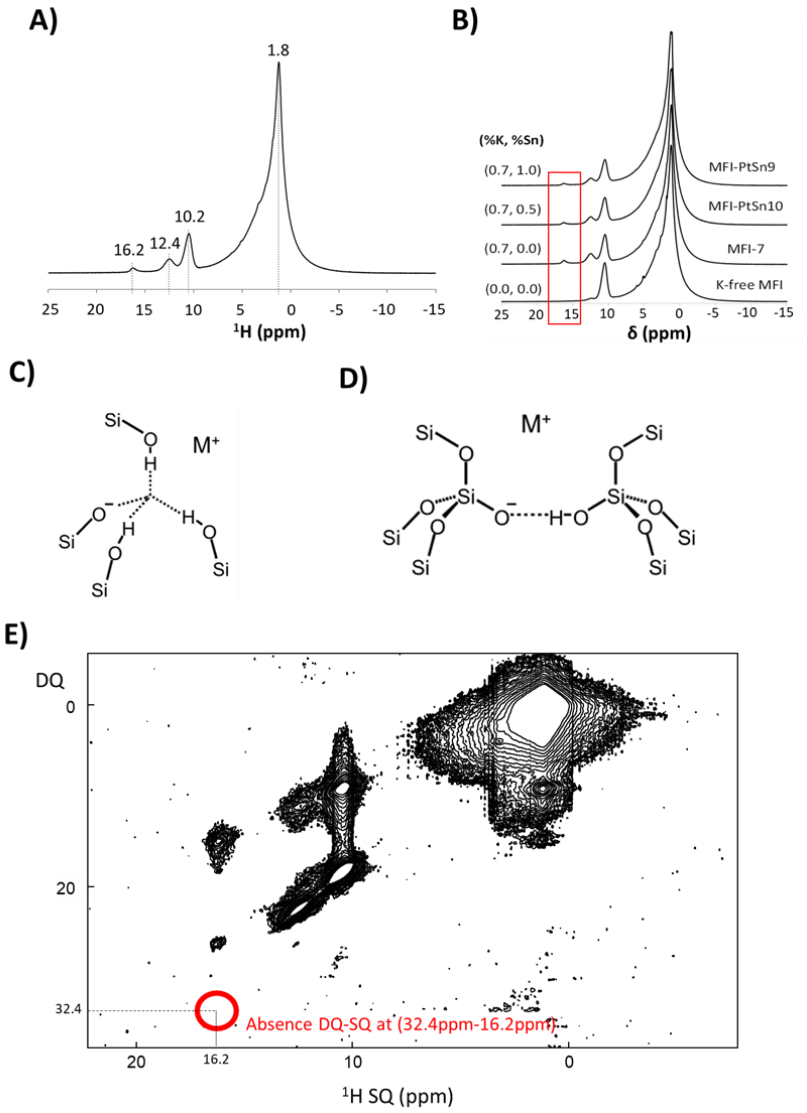

Figure 4.11. A) ^{1}H MAS NMR spectrum of the as-prepared MFI-7 sample. **B)** ^{1}H MAS NMR of different as-prepared MFI materials modifying the K and the Sn content. **C)** Nest that results from an absent T site to produce three surrounding silanols (Si–OH) and one siloxy (Si–O^{-}). **D)** Defect produced by breaking at least one siloxane (Si–O–Si) linkage to create one siloxy and one silanol. M^{+} can be TPA^{+} or K^{+} in the as-prepared K-MFI system. **E)** ^{1}H DQ-SQ MAS NMR spectrum of the as-prepared MFI-7 sample.

Periodic DFT methods have been employed to calculate the energy necessary to add one K per unit cell into the MFI-TPA system, with four TPA molecules and four associated silanol/siloxy nests placed in the four intersecting channels of the MFI unit cell. The K^+ cation and the associated OH^- counter-ion were placed in regions unoccupied by the TPA molecules, that is, around the pore intersections, in the sinusoidal channels, and in the lateral cages. K is too big to fit into the cages and, in the absence of TPA molecules, it is well stabilized in both types of channels (see relative energies for MFI-K models in **Table 4.3**). However, when the straight channels and the intersections are occupied by TPA molecules, K can be only stabilized in the sinusoidal channels (see relative energies for MFI-TPA-K models in **Table 4.3).**

Table 4.3. Relative stability of MFI-TPA-K and MFI-K models and energy of incorporation of K (E_{inc}) in different locations within the MFI unit cell.

	K location	*OH location*	*E_{rel} MFI-TPA-K (kcal/mol)*	*E_{rel} MFI-K (kcal/mol)*	*E_{inc} (kcal/mol)*
A	cage	sin	48.3	38.3	6.2
B	cage	str	50.7	34.8	12.1
C	str	sin	33.9	6.7	23.1
D	sin	str	22.6	8.1	10.7
E	str	cage	16.8	2.8	10.1
F	sin	cage	2.0	3.9	**-5.8**
G	cage	sin	41.4	34.5	3.1
H	sin	cage	**0.0**	1.9	**-5.7**
I	cage	str	47.9	39.3	4.8
J	str	sin	35.5	1.0	30.6
K	str	cage	13.2	**0.0**	9.3
L	sin	str	11.9	3.3	4.7

In the most stable systems, F and H, K is located in a sinusoidal channel and the associated OH is in a lateral cage forming an additional H bond (see **Figures 4.12**). In these two cases, the calculated energies to incorporate K are negative, indicating that the process is thermodynamically favourable.

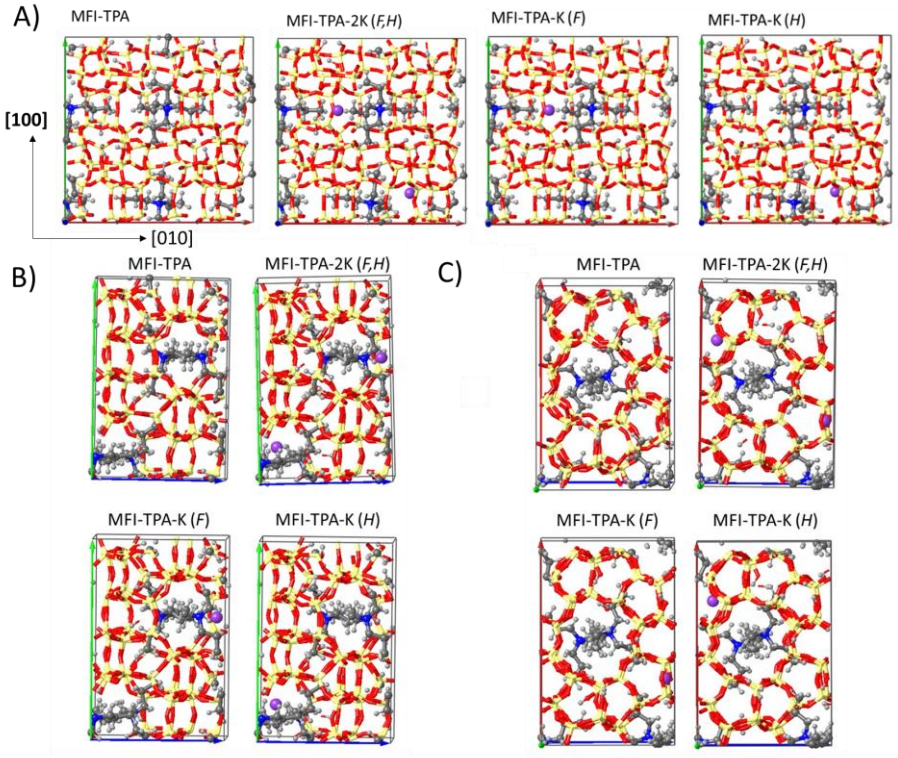

Figure 4.12. Optimized geometries of MFI-TPA, MFI-TPA-K and MFI-TPA-2K models. **A)** View from the [001] direction, showing the location of the TPA molecules at the intersections and the K cations in the sinusoidal channels **B)** View from the [100] direction showing the sinusoidal 10-ring channels and, **C)** View from the [010] direction showing the straight 10-ring channels. Framework Si and O atoms depicted as yellow and red sticks, N, C, H and K atoms depicted as blue, grey, white and pink balls.

Interestingly, the simultaneous incorporation of two K cations, and the associated OH, is clearly endothermic in these two favourable positions, with a calculated E_{inc} value of 14.9 kcal/mol. Analysis of the optimized geometries of these systems (**Figure 4.12.A)**) shows that the two K cations in the MFI-TPA-K2 model are separated by 11.974 Å, and that neither the silicate framework nor the interaction of K with the surrounding O atoms is modified (see optimized Si-Si and K-O distances in **Table 4.4**). The additional energy required to add a second K in the same unit cell might therefore be attributed to unfavourable fitting of TPA molecules upon a small displacement within the pores, caused by steric and electrostatic TPA/K repulsions. This is consistent with the experimental observation that samples never incorporate K above a 1:1 unit cell stoichiometry, unless other forms of species such as tin-silicates can be formed, in synthesis made with large amounts of Sn present.

Table 4.4. Optimized values of the Si-Si and K-O distances (in Å) involved in the incorporation of K in models F and H.

Label	***Composition***	***rSi-Si(F)***	***rSi-Si(H)***	***rK-O(F)***	***rK-O(H)***
MFI	$Si_{96}O_{192}$	3.196	3.201	-	-
MFI-D1	$Si_{96}O_{192}H_{16}$	3.209	3.178	-	-
MFI-D1-K	$Si_{96}O_{192}H_{17}K$	2.962	2.787	-	-
MFI-4TPA	$Si_{92}O_{192}N_4C_{48}H_{124}$	3.208	3.190	-	-
MFI-4TPA-K	$Si_{92}O_{193}N_4C_{48}H_{125}K_1$	2.995	2.802	2.964	2.654
MFI-4TPA-2K	$Si_{92}O_{194}N_4C_{48}H_{126}K_2$	3.002	2.792	2.926	2.623

4.4. SYNTHESIS AND CHARACTERIZATION OF PtSn@K-MFI MATERIALS AT STOICHIOMETRIC K CONTENTS

Once the K placement mechanism was elucidated, it became necessary to analyse the properties of new PtSn@K-MFI materials made with a stoichiometric content of K in the synthesis gels, corresponding to the maximum amount of K that the MFI structure can theoretically adsorb without the precipitation of tin-silicates (~0.7 wt.% K, as shown previously). In other words, these syntheses aimed at locating all added K inside the MFI crystals, a result that, presumably, should happen even if Sn was present in a large excess (according to the results obtained from the base-washing experiment exposed above). For this study, 0.7 wt.% K was fixed in the gels, and three Sn contents were evaluated, at 1.3, 1.0 and 0. 5 wt.% (MFI-PtSn8, MFI-PtSn 9, and MFI-PtSn10 in **Table 4.1**, respectively).

The PXRD patterns of the MFI-PtSn8-10 show the formation of MFI as a pure phase (**Figure 4.4**), and the corresponding FESEM and STEM images confirm the virtual absence of amorphous tin-silicate particles (**Figure 4.13**). However, the sample with the highest Sn content, MFI-PtSn8, shows symptoms of metal aggregation after calcination, something that is not observed at lower Sn contents. Analysis of MFI-PtSn8 by STEM confirms the presence of significant amounts of Pt nanoparticles on the surface of the MFI crystals (**Figure 4.13.(left panel)**), but the zeolite appears also full of very tiny metal clusters of lower Z-contrast, only observable at high magnifications (**Figure 4.13.(right panel)**). Taking into account that the silanol/K-siloxy nests are inferred critical to stabilize ~1 nm Pt clusters after multiple high-temperature reduction-oxidation-reduction cycles, one plausible explanation

to the decreasing catalyst stability with increasing Sn contents, at K loadings below the maximum allowed K stoichiometry of ~0.7 wt.%, is that extra-framework Sn species outcompete Pt for occupying those positions (when Sn is in large excess. At lower Sn contents, in contrast, brighter clusters, well-dispersed throughout the MFI crystals, can be observed in the corresponding STEM images after one oxidation-reduction cycle at 600°C (see MFI-PtSn9_O600R600 and MFI-PtSn10_O600R600 in **Figure 4.13** (**right panel**)).

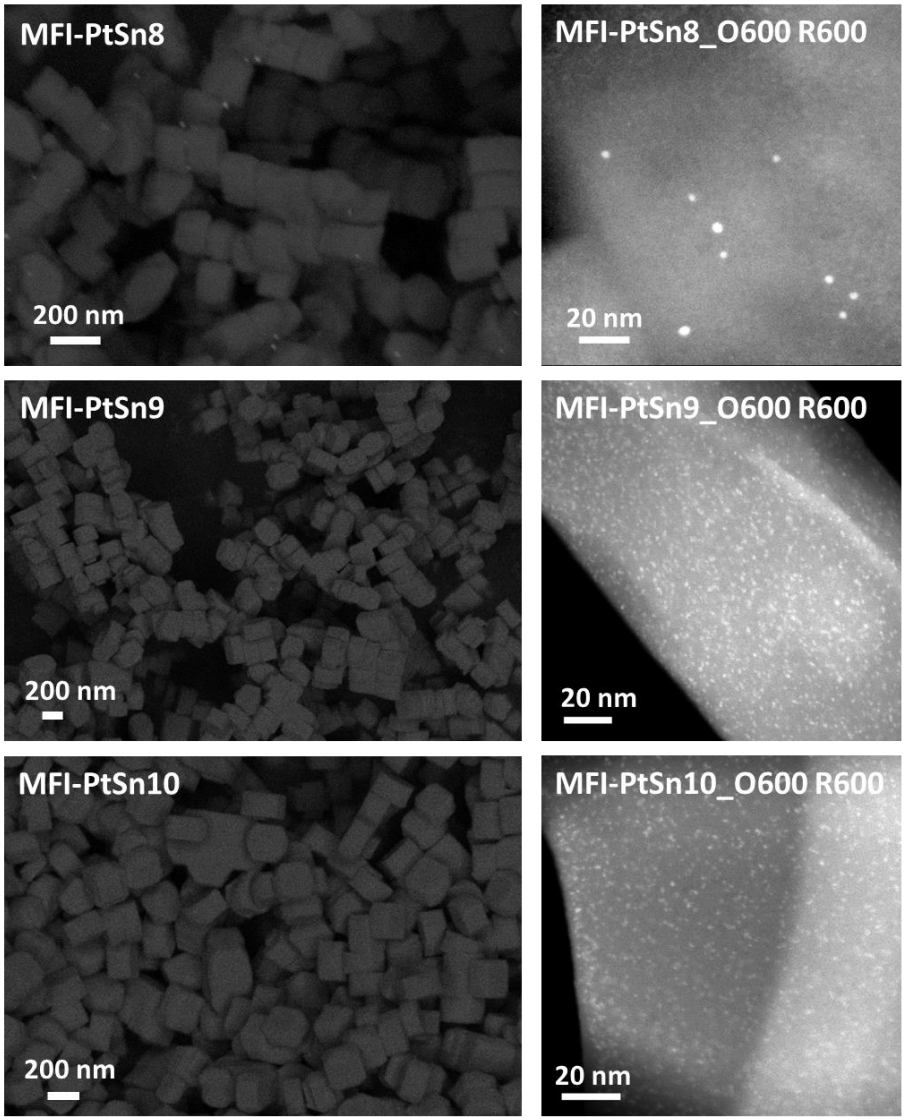

Figure 4.13. FESEM images of the calcined MFI-PtSn8, MFI-PtSn9 and MFI-PtSn10 samples (left panel). STEM images of the MFI-PtSn8, MFI-PtSn9 and MFI-PtSn10 samples after being subjected to calcination and reduction treatments at 600°C in air and hydrogen, respectively (O600R600) (right panel).

ICP analysis demonstrates that the Sn and K contents in the final solids agrees with a ~ 100 % incorporation of the metals in the synthesis gels (**Table 4.1**). To test that the K and Sn fully incorporate into the zeolite crystals at these concentrations of K and Sn in the synthesis gels, we proceeded to wash the as-prepared samples with NaOH, as previously done, and confirmed that content of K and Sn (as well as Pt) remain unaffected by the base-treatment. This result is a strong indication that tin-precipitates are avoided when the amount of K introduced in the synthesis gel is < 0.7 wt.%, even if the amount of Sn is high.

Once the catalysts were prepared, the impact of the synthesis conditions and the resulting metal structures on the performance of K-PtSn@MFI catalysts for the PDH reaction was evaluated.

4.5. PDH CATALYTIC PERFORMANCE

Our results demonstrate that the distribution and uniformity of metal species in PtSn@K-MFI samples made via one-pot methods is very sensitive to changes in the K and Sn contents in the synthesis gels, and that these two variables are closely interconnected due to competing amorphous phases that precipitate as impurities when K and Sn are in excess.

To correlate these structures with their catalytic performance in the PDH reaction, we tested catalysts MFI-PtSn3 (synthesized at high K and Sn loadings, thus containing significant amounts of tin-silicates), MFI-PtSn8 (stoichiometric K content, and high Sn loading), MFI-PtSn9 (stoichiometric K content, and intermediate Sn loading) and MFI-PtSn10 (stoichiometric K content, and low Sn loading) after calcination and reduction in O_2 and H_2,

respectively, at 600°C for 1h. The evolution of the propane conversion with time-on-stream is summarized in **Figure 4.14** and includes data over three consecutive reaction/regeneration cycles at 600°C in O_2 and H_2 (needed to remove coke and reactivate the catalyst). For comparison purposes, the performance of a Sn-free, Pt@K-MFI sample (MFI-Pt6) is also reported after one use, along with the performance of a $PtSn/SiO_2$ [39] after three reaction/regeneration cycles. The selectivity of these catalysts exceeds, in all cases, 92 % (see **Figure 4.14, D-F**), except that of the MFI-Pt6 sample, which stays 85-90 % due to enhanced hydrogenolysis and coking when Sn is absent, consistent with the well-known role of this promoter on the selectivity of Pt [40,41]. Accordingly, **Figure 4.14, A)** shows that the time-on-stream deactivation is also the greatest with this catalyst. The selectivity of the best catalysts in this series, at high Sn contents, is > 96 % (see **Figure 4.14 D)**).

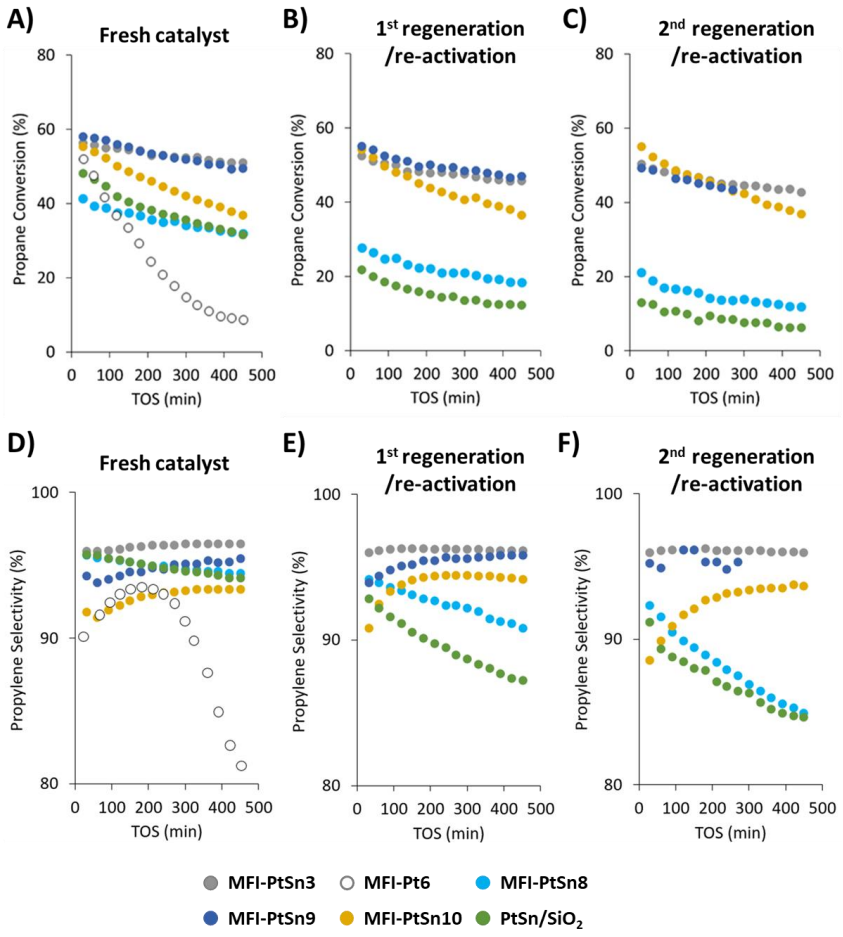

Figure 4.14. Propane conversion (**A-C**) and propylene selectivity (**D-F**) as a function of the time-on-stream for the direct propane dehydrogenation reaction using representative PtSn@K-MFI catalysts. **A,D)** Catalysts after a first calcination in air and reduction in H_2 for 1h at 600°C. **B,E)** Catalysts after one consecutive regeneration in air at 600°C for 1 h, followed by re-activation in H_2 at 600°C for 1h; **C,F)** Catalysts after a second consecutive regeneration in air at 600°C for 1 h, followed by re-activation in H_2 at 600°C for 1h. Colour of the symbols correspond to: MFI-PtSn3 (grey); MFI-Pt6 (white); MFI-PtSn8 (light blue); MFI-PtSn9 (dark blue); MFI-PtSn10 (yellow) and $PtSn/SiO_2$ synthesized according to Linic *et al* [39] (green). Catalyst compositions indicated in **Table 4.1**. Reaction conditions: WHSV = 17.3 h^{-1} (on a propane basis); atmospheric pressure; 600°C; 3:1 N_2/propane molar ratio.

On the other hand, it is very clear that compared to other state-of-the-art PtSn catalysts, for example, recent $PtSn/SiO_2$ catalysts[39], the optimized PtSn@K-MFI materials showed to be substantially more active after the first H_2 activation (results close to 58 % conversion, very close to the theoretical equilibrium conversion under the selective reaction conditions, vs ~40 % with the reference $PtSn/SiO_2$ (**Figure 4.14, A)**), both tested at a propane WHSV of 17.3 h^{-1}), deactivating slower over time-on-stream (~4 times slower). The materials exhibit similar catalytic behaviour without significant deactivation after being regenerated in O_2 (decay from ~58 % conversion to ~50 – 55 %, depending on the Sn content, vs ~48 to ~13 % in the case of $PtSn/SiO_2$) (**Figure 4.14, B)** and **C)**). Furthermore, the PtSn@K-MFI materials showed being more selective to propylene than the reference $PtSn/SiO_2$, particularly after O_2 regeneration (~96 % vs < 90 %), as observed in **Figures 4.14 D-F**. STEM images of the spent $PtSn/SiO_2$ catalyst demonstrate the transition from well-dispersed ~ 2 nm PtSn nanoparticles, before reaction, to particles between 2 and 15 nm after reaction and regeneration (**Figure 4.15**). The bimodal particle size distribution is consistent with an Ostwald-ripening sintering mechanism typical of supports unable to stabilize atomically dispersed PtO_x species in O_2 at moderate-to-high temperatures [42]. Similar problems affect to commercial $PtSn/Al_2O_3$ formulations, which must be subjected to additional oxychlorination processes to recuperate and re-impregnate Pt after coke burn operation, to mitigate activity loses caused by Pt sintering [29,43].

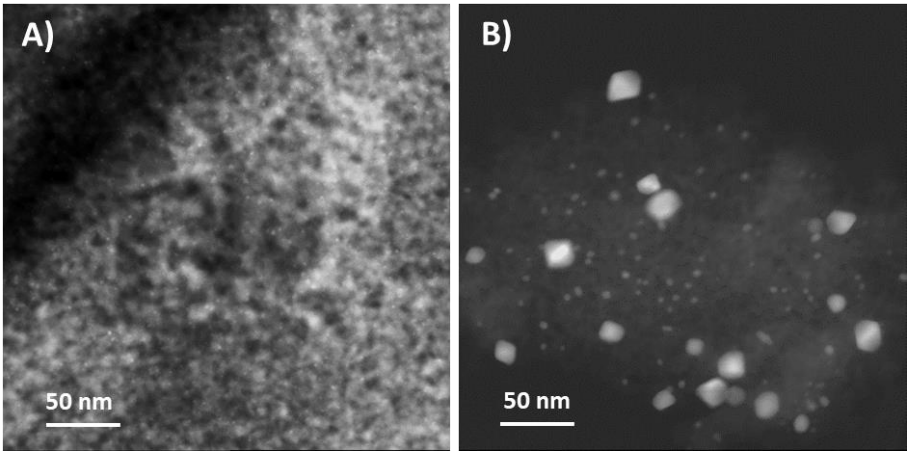

Figure 4.15. A) STEM images of the fresh $PtSn/SiO_2$ catalyst and **B)** after two consecutive PDH reaction cycles.

The best PtSn@K-MFI catalysts developed here also outperform the $PtSn/SiO_2$ reference when tested in the PDH reaction at high concentrations of propane (**Figure 4.16**). More specifically, sample MFI-PtSn9 is able to attain equilibrium conversion (close to 30 % at 550°C) at a WHSV of 300 h^{-1}, whereas the $PtSn/SiO_2$ reference stays at ~ 15 % conversion at a WHSV of 150 h^{-1}; and after regeneration in air at 600°C, the zeolite-supported sample maintains a clear conversion and selectivity advantage relative to the amorphous SiO_2 counterpart (**Figure 4.16**). Nevertheless, we note that both TOS deactivation and stability upon regeneration appear more challenging when highly concentrated propane streams are reacted, as expected.

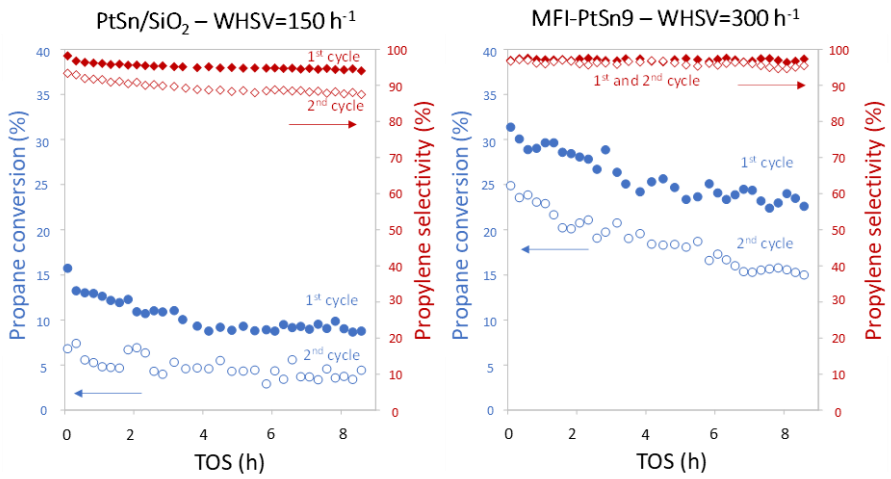

Figure 4.16. Propane conversion (blue) and propylene selectivity (red) for the PDH reaction using a highly concentrated propane stream for $PtSn/SiO_2$ (left) and MFI-PtSn9 (right) in their fresh forms (filled symbols) and after being regenerated (empty symbols) using a weight hourly space velocitie (WHSV) of 150 and 300 h^{-1} for the $PtSn/SiO_2$ and MFI-PtSn9, respectively. Reaction conditions: T = 550°C; P = 1 atm; feed gas, N_2: propane = 1:9 (molar). After each cycle, the catalyst was regenerated by calcination in air at 600°C for 3 h.

Because sample MFI-PtSn8 incorporates a non-negligible amount of Pt outside the MFI crystals (**Figure 4.13**), it is not surprising that this catalyst also deactivates relatively fast both during the PDH reaction (slope of the conversion vs time curve in **Figure 4.14, A)**), and upon regeneration. Samples MFI-PtSn3 and MFI-PtSn9, in contrast, provide the slowest TOS deactivation in this series, and a moderate loss of activity upon regeneration. These two samples, surprisingly, behave virtually identical in the PDH test, despite obvious differences in the composition and structures in the final solids (as proved previously by the different procedures, and summarized in **Figure 4.17**). Thus, it is reasonable to speculate that both samples contain similar active sites, even when synthesized at different nominal gel compositions,

and even when the former incorporates impurities of K and Sn as large external tin-silicates, which appear to behave as mere spectators. Our data does not inform, however, if only one or otherwise various types of Sn species, finely dispersed inside the MFI crystals, are involved in the formation of Pt-Sn bonds during the H_2 treatments.

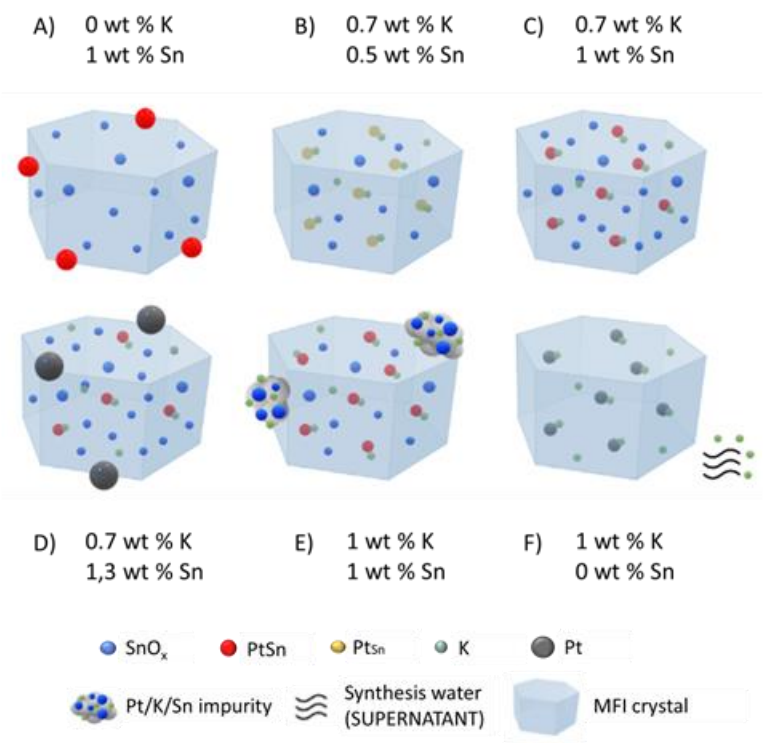

Figure 4.17. Summary of structures in calcined and reduced Pt-Sn@K-MFI materials synthesized by a one-pot methodology, as inferred in this work by EDX-STEM, FESEM, ICP analysis, EXAFS, NMR, and DFT calculations for synthesis gels with variable nominal compositions. The indicated K and Sn contents are the wt.% of Sn and K, respectively, in the synthesis gels, on a SiO_2 basis. The loading of Pt is 0.4 wt.% in all cases. **A)** The lack of K results in the formation of large PtSn outside the MFI crystals, which leads to low catalytic activity; **B)**, **C)** and **D)** are structures synthesized with the maximum K that can be introduced into the zeolite (0.7 wt.% K), at variable Sn content. Up to ~ 1 wt.% Sn, increasing the amount of Sn increases the number of Pt-Sn interactions (red species suggest more Sn-enrichment compared to yellow species). Beyond that point, part of the Pt escapes the zeolite crystals and grows as large Pt-rich particles. Samples at stoichiometric K amounts and moderate Sn deliver optimal activity, TOS deactivation and regenerability; **E)** the excess of K above 0.7 wt.% results in the precipitation of tin-silicates that are mere spectators in the PDH reaction; **F)** in the absence of Sn, the excess of K does not incorporate into the final solid, and leaves the material during synthesis washing operations. In all these synthesis, K-silanol-siloxy nests play critical roles in the stabilization of subnanometric PtSn clusters located in the sinusoidal channels of MFI, near the K centres.

Finally, comparison between samples MFI-PtSn8, MFI-PtSn9 and MFI-PtSn10 is interesting, because these three samples are synthesized with the correct stoichiometric amount of K in the synthesis gels, but at increasing Sn loadings. This situation largely avoids the formation of external tin-silicate precipitates and induces the vast majority of the Sn to penetrate into the zeolite pores, probably enhancing the Sn distribution/speciation within the resultant MFI crystals and maybe explaining the shortened reduction time observed. In this scenario, the higher the Sn content inside the zeolite, the greater the amount of Pt that we infer escapes from the zeolite channels after redox stress, corresponding to a loss of conversion after regeneration that follows the order MFI-PtSn8 (greatest loss) > MFI-PtSn9 > MFI-PtSn10 (comparison of the conversions at times = 0 in **Figure 4.14, A)**). FESEM and STEM images of the spent catalysts show that the abundancy of large (undesired) Pt ensembles also follows the same order, being minimal in MFI-PtSn10 (see **Figure 4.18**), where the vast majority of the metal remains as subnanometric metal clusters after this strenuous test.

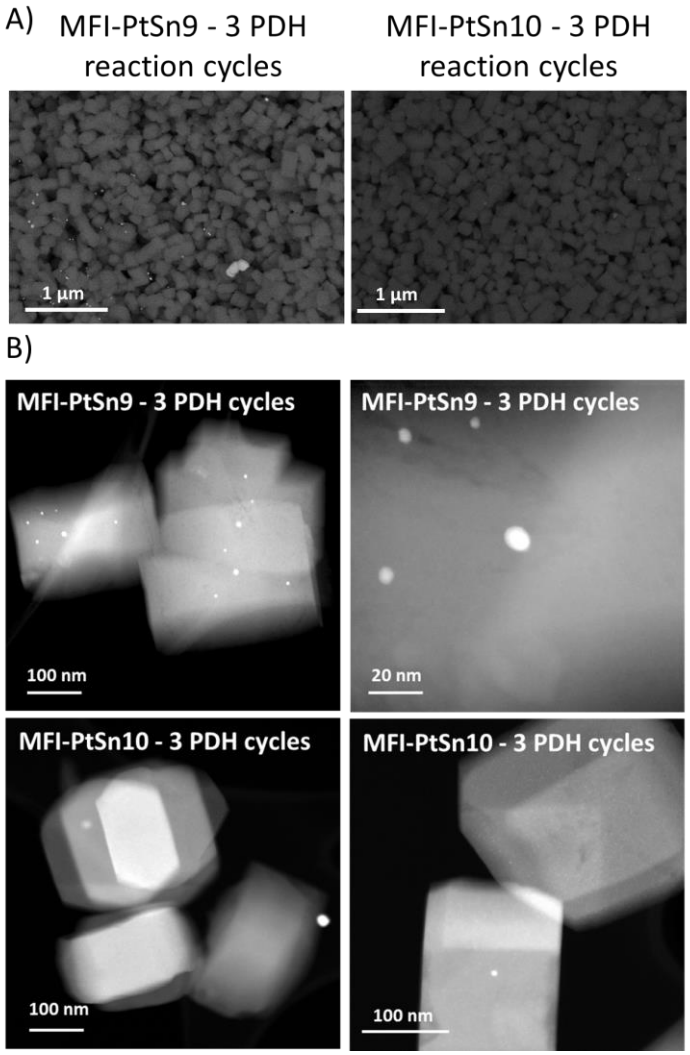

Figure 4.18. A) FESEM and **B)** STEM images of the MFI-PtSn9 and MFI-PtSn10 catalysts after three consecutive PDH reaction cycles.

Sample MFI-PtSn10, most stable upon regeneration, deactivates, however, faster over time-on-stream. To understand the different on-stream deactivation behaviour of MFI-PtSn9 and MFI-PtSn10, both presenting negligible amounts of tin-silicate impurities and negligible amounts of Pt

outside the MFI crystals, we characterized these samples by X-ray absorption spectroscopy (XAS) to unravel the nature of the PtSn interactions after their exposure to hydrogen at 600°C for 1 h. Extended X-ray absorption fine structure (EXAFS) spectrum of the reduced PtSn@K-MFI samples (see **Figure 4.19**), along with quantitative fitting of the EXAFS parameters in **Table 4.5**, provide direct evidence of the Pt-Sn bonding, indicating that short reduction times in H_2 (~1 h) at 600°C are sufficient to form the Pt-Sn bonds. The metal-metal bond distances are found within 2.71-2.74 Å for Pt-Pt, and 2.57-2.62 for Pt-Sn. Interestingly, the Pt-Pt and Pt-Sn coordination numbers for the MFI-PtSn9 sample (1 wt.% Sn) are 4.6 and 1.5, respectively, while those for MFI-PtSn10 (0.5 wt.%) are 5.8 and 0.6, respectively, clearly indicating the formation of Pt-rich nanoparticles in both cases, more so when the Sn content is the lowest (MFI-PtSn10, see **Table 4.5**). The increased number of Pt-Sn bonds in sample MFI-PtSn9, containing a higher Sn content, correlates well with the less pronounced conversion vs time deactivation in **Figure 4.14, A)**. This sample attains similar TOS deactivation to previous PtSn@K-MFI catalysts, without the requirement of long activation times in H_2 prior to the reaction[12]. In agreement with these results, dropping the Sn content below that of MFI-PtSn10, for example, by incorporating only 0.2 wt % Sn into the final solid (sample MFI-PtSn11), further aggravates the TOS deactivation problem (**Figure 4.20**). Moreover, in cases where the catalyst lacks sufficient PtSn bonds after a short H_2 activation (*i.e.* typically, in catalysts that include relatively small amounts of mobile Sn species, such as in MFI-PtSn10), it is possible to promote the formation of new PtSn interactions by increasing the exposure to H_2 (**Table 4.5**, and **Figure 4.19, C)**), which leads to decreased TOS deactivation (**Figure 4.20, B)**), as previously reported.[33]

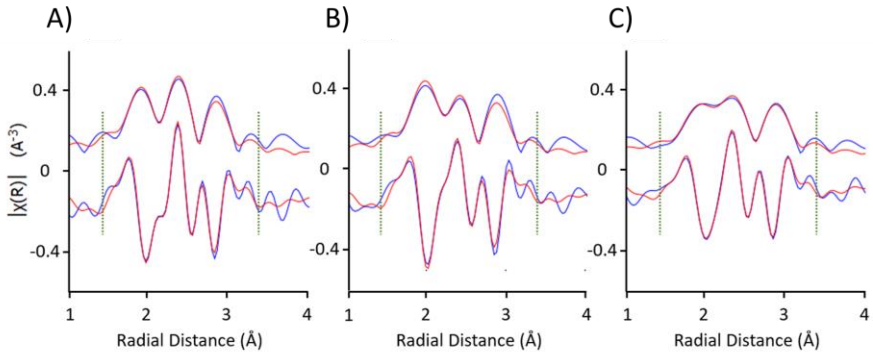

Figure 4.19. Magnitude and real parts of the Fourier Transform EXAFS spectra (R-space without phase-correction) at k-weight = 2 for the MFI-PtSn9, and MFI-PtSn10 samples after reduction in H_2 for 1 h at 600°C (**A** and **B** plots, respectively), and for sample MFI-PtSn10 after reduction in H_2 for 12 h at 600°C (plot **C**). The green dotted lines indicate the fit window. All spectra taken at 50°C.

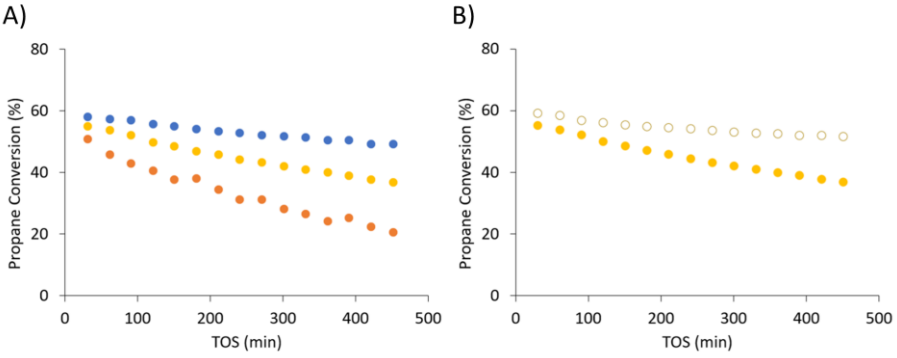

Figure 4.20. A) Propane conversion as a function of the time-on-stream for the direct propane dehydrogenation reaction using MFI-PtSn9 (blue), MFI-PtSn10 (yellow) and MFI-PtSn11 (orange), at constant Pt and K contents of ~0.4 wt % Pt and ~0.6 wt % K, and variable Sn content of ~1, ~0.5, and ~0.2 wt % Sn, respectively, after calcination in air and reduction in H_2 for 1 h at 600°C. **B)** Propane conversion as a function of the time-on-stream for the direct propane dehydrogenation reaction using the MFI-PtSn10 reduced in H_2 at 600°C for 1h (solid yellow) and 12 h (empty symbols) Reaction conditions: WHSV = 17.3 h^{-1} (on a propane basis); atmospheric pressure; 600°C; 3:1 N_2/propane molar ratio.

Figure 4.17. helps to illustrate once again the importance of relationships between gel (nominal) composition, composition and structures in the final solids and how the PtSn alloy evolves according to the atomic proportion. They reveal subtle, complex surface chemistries that are important to rationalize the characteristics of K/Sn/Pt catalysts synthesized by one-pot methodologies to maximize the catalytic activity and stability.

Table 4.5. EXAFS data at the Pt LIII edge characterizing the PtSn@K-MFI samples after being reduced in H_2 for 1 h at 600°C.[a]

Sample	*Shell*	*N*	*R (Å)*	*$\Delta\sigma^2$ (Å^2)*	*ΔE_0 (eV)*
MFI-PtSn9	Pt-Pt	4.6	2.74	0.01	4.9
	Pt-Sn	1.5	2.57	0.008	0.6
MFI-PtSn10	Pt-Pt	5.8	2.72	0.011	4.5
	Pt-Sn	0.6	2.62	0.003	1.9

[a] Notation: N, coordination number; R, distance between absorber and backscatterer atoms; $\Delta\sigma^2$, Debye‑Waller factor; ΔE_0, inner potential correction. Error bounds (accuracies) characterizing the structural parameters obtained by EXAFS spectroscopy are estimated to be as follows: coordination number N, ~20%; distance R, ~0.02; Debye‑ Waller factor $\Delta\sigma^2$, ~20%; and inner potential correction ΔE0, ~20%.

4.6. CONCLUSIONS

The K and Sn contents have been systematically varied in the synthesis of the PtSn@K-MFI system to evaluate the metal dispersion and stability along the MFI crystallites. Experimental and theoretical calculations demonstrate that K is no longer incorporated in siliceous MFI crystals above ~ 0.7 wt.%,

corresponding to a stoichiometry of ~1 K per unit cell of MFI. Above this stoichiometry, K is not incorporated into the final solids, unless significant amounts of Sn are simultaneously present, leading to the formation of tin-silicate precipitates.

The performance of different optimized PtSn@K-MFI catalysts and standard references materials was tested in the PDH reaction. Higher TOS deactivation catalytic profiles are observed with low Sn loadings (below 0.5 wt.%), but these materials present excellent regenerability after consecutive PDH reactions. In contrast, Sn content close to 1 wt.% seems optimal to minimize TOS deactivation in the PDH reaction due to the maximization of Pt-Sn bonds, as revealed by EXAFS, but consecutive regenerations after long-time PDH reaction cycles result in significant metal sintering. Increasing Sn contents within MFI crystallites facilitate Pt sintering and, thus, occurring catalyst deactivation upon regeneration cycles. The performance of optimized catalysts in this work is also markedly superior relative to well-established literature references, as $PtSn/SiO_2$. The results obtained here clearly highlight the remarkable relevance that fine-tuning rationalizations of simple one-pot synthesis approaches can have on the final atomic and subnanometric metal interactions, as a result of complex interconnected nucleation/crystallization processes, and, consequently, in the catalytic and sintering-resistance properties when exposed to highly demanding industrial conditions.

The results obtained from this chapter have been published in “Journal of American Chemical Society” in the work entitled “Resolving complex K-Pt-Sn interactions in PtSn@K-MFI catalysts for alkane dehydrogenation”, which DOI is: https://doi.org/10.1021/jacs.5c01536.

4.7. REFERENCES

(1) Middleton, R. S.; Gupta, R.; Hyman, J. D.; Viswanathan, H. S. The Shale Gas Revolution: Barriers, Sustainability, and Emerging Opportunities. Appl. Energy 2017, 199, 88–95. https://doi.org/10.1016/J.APENERGY.2017.04.034.

(2) McFarland, E. Unconventional Chemistry for Unconventional Natural Gas. Science (1979) 2012, 338 (6105), 341–342. https://doi.org/10.1126/science.1226840.

(3) Del Campo, P.; Martínez, C.; Corma, A. Activation and Conversion of Alkanes in the Confined Space of Zeolite-Type Materials. Chem. Soc. Rev. 2021, 50 (15), 8511–8595. https://doi.org/10.1039/D0CS01459A.

(4) Nawaz, Z. Light Alkane Dehydrogenation to Light Olefin Technologies: A Comprehensive Review. Chem. Eng. Rev 2015, 31 (5), 413–436. https://doi.org/10.1515/revce-2015-0012.

(5) Sattler, J. J. H. B.; Ruiz-Martinez, J.; Santillan-Jimenez, E.; Weckhuysen, B. M. Catalytic Dehydrogenation of Light Alkanes on Metals and Metal Oxides. Chem. Rev. 2014, 114 (20), 10613–10653. https://doi.org/10.1021/cr5002436.

(6) Vora, B. V. Development of Dehydrogenation Catalysts and Processes. Top. Catal. 2012, 55 (19–20), 1297–1308. https://doi.org/10.1007/s11244-012-9917-9.

(7) Wang, G.; Zhu, X.; Li, C. Recent Progress in Commercial and Novel Catalysts for Catalytic Dehydrogenation of Light Alkanes. Chem. Rec. 2020, 20 (6), 604–616. https://doi.org/10.1002/TCR.201900090.

(8) Chen, S.; Chang, X.; Sun, G.; Zhang, T.; Xu, Y.; Wang, Y.; Pei, C.; Gong, J. Propane Dehydrogenation: Catalyst Development, New Chemistry, and Emerging Technologies. Chem. Soc. Rev. 2021, 50 (5), 3315–3354. https://doi.org/10.1039/D0CS00814A.

(9) Dai, Y.; Gao, X.; Wang, Q.; Wan, X.; Zhou, C.; Yang, Y. Recent Progress in Heterogeneous Metal and Metal Oxide Catalysts for Direct Dehydrogenation of Ethane and Propane. Chem. Soci. Rev. 2021, 50 (9), 5590–5630. https://doi.org/10.1039/D0CS01260B.

(10) Liu, L.; Corma, A. Metal Catalysts for Heterogeneous Catalysis: From Single Atoms to Nanoclusters and Nanoparticles. Chem.l Rev. 2018, 118 (10), 4981–5079. https://doi.org/10.1021/acs.chemrev.7b00776.

(11) Yang, M. L.; Zhu, Y. A.; Fan, C.; Sui, Z. J.; Chen, D.; Zhou, X. G. DFT Study of Propane Dehydrogenation on Pt Catalyst: Effects of Step Sites. Phys. Chem. Chem. Phys. 2011, 13 (8), 3257–3267. https://doi.org/10.1039/C0CP00341G.

(12) Im, J.; Choi, M. Physicochemical Stabilization of Pt against Sintering for a Dehydrogenation Catalyst with High Activity, Selectivity, and Durability. ACS Catal. 2016, 6 (5), 2819–2826. https://doi.org/10.1021/acscatal.6b00329.

(13) Zhu, J.; Yang, M. L.; Yu, Y.; Zhu, Y. A.; Sui, Z. J.; Zhou, X. G.; Holmen, A.; Chen, D. Size-Dependent Reaction Mechanism and Kinetics for Propane Dehydrogenation over Pt Catalysts. ACS Catal. 2015, 5 (11), 6310–6319. https://doi.org/10.1021/acscatal.5b01423.

(14) Wang, L.; Wang, L.; Meng, X.; Xiao, F.-S.; Wang, L.; Xiao Key, F.; Meng, X.; Xiao, F. New Strategies for the Preparation of Sinter-Resistant Metal-

Nanoparticle-Based Catalysts. Adv. Mater. 2019, 31 (50), 1901905. https://doi.org/10.1002/ADMA.201901905.

(15) Liu, L.; Corma, A. Bimetallic Sites for Catalysis: From Binuclear Metal Sites to Bimetallic Nanoclusters and Nanoparticles. Chem. Rev. 2023, 123 (8), 4855–4933. https://doi.org/10.1021/acs.chemrev.2c00733.

(16) Hauser, A. W.; Gomes, J.; Bajdich, M.; Head-Gordon, M.; Bell, A. T. Subnanometer-Sized Pt/Sn Alloy Cluster Catalysts for the Dehydrogenation of Linear Alkanes. Phys. Chem. Chem. Phys. 2013, 15 (47), 20727–20734. https://doi.org/10.1039/C3CP53796J.

(17) Virnovskaia, A.; Morandi, S.; Rytter, E.; Ghiotti, G.; Olsbye, U. Characterization of Pt,Sn/Mg(Al)O Catalysts for Light Alkane Dehydrogenation by FT-IR Spectroscopy and Catalytic Measurements. J. Phys. Chem. C 2007, 111 (40), 14732–14742. https://doi.org/10.1021/jp074686u.

(18) Gorczyca, A.; Raybaud, P.; Moizan, V.; Joly, Y.; Chizallet, C. Atomistic Models for Highly-Dispersed PtSn/γ-Al2O3 Catalysts: Ductility and Dilution Affect the Affinity for Hydrogen. ChemCatChem 2019, 11 (16), 3941–3951. https://doi.org/10.1002/CCTC.201900429.

(19) Zhang, Y.; Zhou, Y.; Shi, J.; Zhou, S.; Sheng, X.; Zhang, Z.; Xiang, S. Comparative Study of Bimetallic Pt-Sn Catalysts Supported on Different Supports for Propane Dehydrogenation. J. Mol. Catal. A. 2014, 381, 138–147. https://doi.org/10.1016/J.MOLCATA.2013.10.007.

(20) Zhang, J.; Deng, Y.; Cai, X.; Chen, Y.; Peng, M.; Jia, Z.; Jiang, Z.; Ren, P.; Yao, S.; Xie, J.; Xiao, D.; Wen, X.; Wang, N.; Liu, H.; Ma, D. Tin-Assisted Fully Exposed Platinum Clusters Stabilized on Defect-Rich Graphene for

Dehydrogenation Reaction. ACS Catal 2019, 9 (7), 5998–6005. https://doi.org/10.1021/ACSCATAL.9B00601.

(21) Zhu, Y.; An, Z.; He, J. Single-Atom and Small-Cluster Pt Induced by Sn (IV) Sites Confined in an LDH Lattice for Catalytic Reforming. J. Catal. 2016, 341, 44–54. https://doi.org/10.1016/J.JCAT.2016.06.004.

(22) Batzill, M.; Beck, D. E.; Koel, B. E. Electronic Contrast in Scanning Tunneling Microscopy of Sn–Pt(111) Surface Alloys. Surf. Sci. 2000, 466 (1–3), L821–L826. https://doi.org/10.1016/S0039-6028(00)00803-7.

(23) Santhosh Kumar, M.; Chen, D.; Holmen, A.; Walmsley, J. C. Dehydrogenation of Propane over Pt-SBA-15 and Pt-Sn-SBA-15: Effect of Sn on the Dispersion of Pt and Catalytic Behavior. Catal. Today 2009, 142 (1–2), 17–23. https://doi.org/10.1016/J.CATTOD.2009.01.002.

(24) Yang, M. L.; Zhu, Y. A.; Zhou, X. G.; Sui, Z. J.; Chen, D. First-Principles Calculations of Propane Dehydrogenation over PtSn Catalysts. ACS Catal. 2012, 2 (6), 1247–1258. https://doi.org/10.1021/CS300031D.

(25) Iida, T.; Zanchet, D.; Ohara, K.; Wakihara, T.; Román-Leshkov, Y. Concerted Bimetallic Nanocluster Synthesis and Encapsulation via Induced Zeolite Framework Demetallation for Shape and Substrate Selective Heterogeneous Catalysis. Angew. Chem. Int.l Ed. 2018, 57 (22), 6454–6458. https://doi.org/10.1002/ANIE.201800557.

(26) Ma, Y.; Song, S.; Liu, C.; Liu, L.; Zhang, L.; Zhao, Y.; Wang, X.; Xu, H.; Guan, Y.; Jiang, J.; Song, W.; Han, Y.; Zhang, J.; Wu, P. Germanium-Enriched Double-Four-Membered-Ring Units Inducing Zeolite-Confined

Subnanometric Pt Clusters for Efficient Propane Dehydrogenation. Nat. Catal. 2023, 6 (6), 506–518. https://doi.org/10.1038/s41929-023-00968-7.

(27) Li, C.; Meyer, R. J.; Yacob, S.; Gomez, E.; Lopez-Haro, M.; Calvino, J. J.; Moliner, M.; Serna, P.; Corma, A. Highly Stable Subnanometric PtIn Clusters for the Selective Dehydrogenation of Alkanes. ChemSusChem 2025, 18 (2), e202401284. https://doi.org/10.1002/CSSC.202401284.

(28) Iglesias-Juez, A.; Beale, A. M.; Maaijen, K.; Weng, T. C.; Glatzel, P.; Weckhuysen, B. M. A Combined in Situ Time-Resolved UV–Vis, Raman and High-Energy Resolution X-Ray Absorption Spectroscopy Study on the Deactivation Behavior of Pt and PtSn Propane Dehydrogenation Catalysts under Industrial Reaction Conditions. J. Catal. 2010, 276 (2), 268–279. https://doi.org/10.1016/J.JCAT.2010.09.018.

(29) Morgan, K.; Goguet, A.; Hardacre, C. Metal Redispersion Strategies for Recycling of Supported Metal Catalysts: A Perspective. ACS Catal. 2015, 5 (6), 3430–3445. https://doi.org/10.1021/ACSCATAL.5B00535.

(30) Sun, Q.; Wang, N.; Fan, Q.; Zeng, L.; Mayoral, A.; Miao, S.; Yang, R.; Jiang, Z.; Zhou, W.; Zhang, J.; Zhang, T.; Xu, J.; Zhang, P.; Cheng, J.; Yang, D. C.; Jia, R.; Li, L.; Zhang, Q.; Wang, Y.; Terasaki, O.; Yu, J. Subnanometer Bimetallic Platinum–Zinc Clusters in Zeolites for Propane Dehydrogenation. Angew. Chem. Int. Ed. 2020, 59 (44), 19450–19459. https://doi.org/10.1002/ANIE.202003349.

(31) Zhang, B.; Zheng, L.; Zhai, Z.; Li, G.; Liu, G. Subsurface-Regulated PtGa Nanoparticles Confined in Silicalite-1 for Propane Dehydrogenation. ACS Appl. Mater. Interfaces. 2021, 13 (14), 16259–16266. https://doi.org/10.1021/ACSAMI.0C22865.

(32) Liu, L.; Lopez-Haro, M.; Lopes, C. W.; Li, C.; Concepcion, P.; Simonelli, L.; Calvino, J. J.; Corma, A. Regioselective Generation and Reactivity Control of Subnanometric Platinum Clusters in Zeolites for High-Temperature Catalysis. Nat. Mat 2019, 18 (8), 866–873. https://doi.org/10.1038/s41563-019-0412-6.

(33) Liu, L.; Lopez-Haro, M.; Lopes, C. W.; Rojas-Buzo, S.; Concepcion, P.; Manzorro, R.; Simonelli, L.; Sattler, A.; Serna, P.; Calvino, J. J.; Corma, A. Structural Modulation and Direct Measurement of Subnanometric Bimetallic PtSn Clusters Confined in Zeolites. Nat. Catal. 2020, 3 (8), 628–638. https://doi.org/10.1038/s41929-020-0472-7.

(34) Burton, A.; Terefenko, E.; Wang, H.; Paccagnini, M.; Sattler, A. Structure-Property Relationships That Influence Platinum Stability in All-Silica or Highly Siliceous Zeolites. Micropor. Mesopor. Mater. 2023, 350. https://doi.org/10.1016/j.micromeso.2022.112411.

(35) Bellussi, G.; Fattore, V. Isomorphous Substitution in Zeolites: A Route for the Preparation of Novel Catalysts. Stud. Surf. Sci. Catal. 1991, 69 (C), 79–92. https://doi.org/10.1016/S0167-2991(08)61557-8.

(36) Khouw, C. B.; Davis, M. E. Catalytic Activity of Titanium Silicates Synthesized in the Presence of Alkali-Metal and Alkaline-Earth Ions. J Catal 1995, 151 (1), 77–86. https://doi.org/10.1006/JCAT.1995.1010.

(37) The Uncertainty of This Particle Size Distribution and Average Particle Size Is Greater than in Other Sample with Slightly Larger Pt Clusters, Because of Detection Limitation under Our Microscope.

(38) Brunklaus, G.; Koller, H.; Zones, S. I. Defect Models of As-Made High-Silica Zeolites: Clusters of Hydrogen-Bonds and Their Interaction with the Organic Structure-Directing Agents Determined from 1 H Double and Triple Quantum NMR Spectroscopy. Angewandte Chemie International Edition 2016, 55 (46), 14459–14463. https://doi.org/10.1002/anie.201607428.

(39) Motagamwala, A. H.; Almallahi, R.; Wortman, J.; Igenegbai, V. O.; Linic, S. Stable and Selective Catalysts for Propane Dehydrogenation Operating at Thermodynamic Limit. Science (1979) 2021, 373 (6551), 217–222. https://doi.org/10.1126/science.abg7894.

(40) Xiong, H.; Lin, S.; Goetze, J.; Pletcher, P.; Guo, H.; Kovarik, L.; Artyushkova, K.; Weckhuysen, B. M.; Datye, A. K. Thermally Stable and Regenerable Platinum–Tin Clusters for Propane Dehydrogenation Prepared by Atom Trapping on Ceria. Angewandte Chemie International Edition 2017, 56 (31), 8986–8991. https://doi.org/10.1002/anie.201701115.

(41) Siri, G. J.; Ramallo-López, J. M.; Casella, M. L.; Fierro, J. L. G.; Requejo, F. G.; Ferretti, O. A. XPS and EXAFS Study of Supported PtSn Catalysts Obtained by Surface Organometallic Chemistry on Metals. Appl Catal A Gen 2005, 278 (2), 239–249. https://doi.org/10.1016/j.apcata.2004.10.004.

(42) Moliner, M.; Gabay, J. E.; Kliewer, C. E.; Carr, R. T.; Guzman, J.; Casty, G. L.; Serna, P.; Corma, A. Reversible Transformation of Pt Nanoparticles into Single Atoms inside High-Silica Chabazite Zeolite. J Am Chem Soc 2016, 138 (48), 15743–15750. https://doi.org/10.1021/jacs.6b10169.

(43) Arteaga, G. J.; Anderson, J. A.; Becker, S. M.; Rochester, C. H. Influence of Oxychlorination Treatment on the Surface and Bulk Properties of a Pt–

Sn/Al2O3 Catalyst. J Mol Catal A Chem 1999, 145 (1–2), 183–201. https://doi.org/10.1016/S1381-1169(99)00092-8.

CHAPTER 5:

ONE-POT ENCAPSULATED METAL ZEOLITE WITH CONTROLLED PARTICLE SIZES: FROM NANO TO SUBMICRON ZEOLITE PARTICLES

5.1. ZEOLITE PARTICLE SIZE AND METAL STABILIZATION: STATE OF ART

Various strategies and approaches have been discussed in the introduction of the present thesis to enhance the final properties of zeolite-based catalysts, with the primary goal of maximizing their catalytic performance (*i.e.*, activity, selectivity, reusability or stability under reaction conditions). Among these approaches, maximizing the dispersion of active sites through rational modifications of the synthesis gel composition has been deeply explored in Chapter 4, enabling the synthesis of MFI-type catalyst with optimal PtSn bimetallic dispersion by controlling the potassium role.

Herein, the synthesis of zeolite-based catalyst with different zeolite particle sizes following one-pot metal encapsulation strategy has been studied, as well as the influence of their properties in catalytic applications where having adequate diffusive pathways can be key to enhance the catalytic performance. In general, different approaches have been described in the literature to selectively control the zeolite accessibility, mainly classified in:

- Bottom-up methodologies: From simple and small initial precursors, larger and more complex architectures can be generally built by classical hydrothermal synthesis procedures[1]. The resulting particle size of the crystallized microporous materials can be fine-tuned by adequately controlling target synthetic parameters (as it will be discussed later).
- Top-Down methodologies: Involving already formed or pre-formed complex structures as the starting point, which will be broken down into smaller units through various post-synthetic strategies, such as

the selective removal of specific species by chemical processes, strategies for reorganizing crystalline particle agglomerates, or tribochemical treatments to modify the size and morphology of the particles[2].

The adequate selection of the appropriate methodology depends on the desired final properties of the target materials. For applications requiring materials with homogenous morphological, textural, and chemical features, the bottom-up approach is generally more convenient. Conversely, certain top-down procedures, such as desilication, dealumination, or metal extraction, may result in an undesired alteration of the final properties of the materials if not carefully controlled. This thesis has emphasized the bottom-up methodology. Although the methodology can offer advantages for producing nanozeolites with consistent properties, obtaining a precise regulation of crystal size remains one of the major challenges due to the inherent complexity of the crystallization process and the multitude of factors that influence it, as discussed in **Chapter 1**.

Figure 5.1 below shows a scheme summarizing the most relevant factors that can have a direct influence in controlling the final size of the crystalline particles when rationalizing a reaction medium for zeolite crystallization, as generally described in the literature[3-6].

Synthesis Gel Composition	Si and Al sources and Si/Al ratio	
	pH media (OH-, F-) and other counterions (CO_3^{2-}, HPO_4^{2-}, $C_2O_4^{2-}$...)	
	Charge Balancing Cations (NH_4^+, Na^+, K^+, Cs^+...)	
	Other Heteroatoms	T^{III}/T^{IV}
		Metallic Dopants (Noble metal, Non-noble metal, Alloys
	SDAs Nature	Inorganic (desired cristal seeds, mineralizing agents...)
		Organic
	Syntesis Solvent Media (H_2O, H_2O/R-OH, Organic Solvent...)	
Crystallization Conditions	Crystallization Time	
	Crystallization Temperature	

Figure 5.1. Summary of those controllable factors in the zeolite synthesis process that can tailor the final properties of the zeolite-type material.

Controlling the particle size can offer an enhancement of different key properties, including a significant increase of the external surface area and improving the accessibility of reactants to the active centres, a fact that can boost the activity[7,8]. Moreover, the decrease of the reaction path length along the "nanoreactor" also facilitates the release of the reaction products before they undergo undesirable secondary reactions, which in many cases lead to catalyst deactivation due to blockage or poisoning of the active sites[9].

The current challenge in controlling the final zeolite crystal size arises from the complexity of the crystal formation/growth mechanisms, involving many parallel reactions and condensation steps that are unique for every specific crystalline system. In a common hydrothermal synthesis, the crystal formation and growth processes are mainly ruled by kinetic and thermodynamic factors[10]. Indeed, minor variations in the synthesis gel composition and for the operational conditions can lead to very significant changes in the crystallization kinetics, resulting in undesired phases.

The literature provides numerous examples demonstrating how those variations in the thermodynamic and kinetic parameters of a system are induced by the use of precursors of different nature, influencing directly in the crystallization process, and maybe leading to obtain different particle sizes. Some of the reported studies have extensively examined the influence of the Si precursor species on the final particle size, revealing that Si sources with higher activity, higher specific surface area and more soluble (*i.e.*, TEOS, fumed SiO_2) promote faster nucleation processes (in absence of seeds of the desired phase), thereby yielding smaller particle sizes compared to those syntheses employing more polymerized silicon sources, such as silica polymeric sources which promote the crystal growth steps[11,12].

Alkalinity, directly linked to the dissolution capacity of precursor species, is another factor that significantly influences the final size of the zeolites obtained. Elevated alkalinity facilitates the deprotonation of Si-O bonds in the precursor species, leading to the formation of electrically charged silicate ions within the reaction medium. These ions polymerize into silicate frameworks in the presence of OH^- anions. High alkalinity conditions favour an increased dissolution of Si species, and consequently, the decrease of the viscosity of the synthesis gel[13,14]. This process markedly accelerates nucleation times[15], as observed in studies reported by Martin *et al*.[16] and Gallego *et al*.[17], where only synthesis conditions with noticeable high alkalinity were able to produce the targeted CHA-type zeolites with the smallest crystalline particle sizes. However, it is important to acknowledge that the rapid nucleation kinetics induced by the alkalinity excess in the medium also heightens the risk of forming nuclei of undesired crystalline phases due to charge imbalances in the crystallization environment. The H_2O/Si ratio also plays a pivotal role in

the synthesis process, as it directly influences the pH of the medium, thereby affecting the solubility of Si species. While a decrease in pH generally restricts the dissolution of Si species, combining a high pH (particularly in the absence of mineralizing agents such as alkaline inorganic cations) and an intermediate-high dilution level ($H_2O/Si \approx 20–40$) provides an adequate rheological environment, promoting the formation of smaller crystalline particles[6,18,19].

In addition to the difficulties of controlling the phase obtained from the chemical composition variations, there are no characterization tools that can provide clear and unequivocal information about the nucleation phenomena associated with the formation of zeolite crystals at nanoscale levels in the gel medium. In general, the combination of different techniques, such as HRTEM, AFM, High Energy XRD, Solid State NMR and Computational Calculations are employed to elucidate the formation mechanism of a given crystalline system[20-22].

Among the factors outlined in **Figure 5.1** that can influence the final particle size of zeolites, temperature and crystallization time are the most easily traceable. By maintaining the composition of the synthesis gel unchanged (specifically its composition and rheological properties), the kinetics of the synthesis process (arranging both initial nucleation and subsequent growth steps) can be systematically studied, provided that the synthesis temperature is high enough to surpass the energetic threshold required for crystallization[23,24].

In previous studies reported by X. Zhang *et al.*[25], meticulous research about the impact of key factors such as chemical composition, temperature, and

crystallization time on the final zeolite particle size obtained was conducted. The study revealed several noticeable insights, with two main points being outlined. In one hand, under isothermal conditions, the system requires a specific induction period to generate a sufficient number of nuclei, which is essential for achieving measurable crystallinity in the final material. On the other, temperature plays an even more relevant role in every step involved in the crystallization process of zeolitic structures. It accelerates the kinetic constants governing species dissolution, nucleation, and crystal growth processes carried out during hydrothermal synthesis. By increasing the reaction kinetics through increasing the crystallization temperatures, the system can reach rapidly the crystallization equilibrium, thereby reducing synthesis time and typically yielding larger crystalline particles[26,27], although the chance to reach other phase energy barrier is feasible, subsequently leading to form additional crystalline phases. Likewise, Petushkov *et al.* conducted screening studies that established a measurable and intuitive correlation between the synthesis temperature and crystallization time while maintaining the same composition and precursors, and the resulting crystalline particle size in MFI zeolites[5]. Their findings, illustrated in **Figure 5.2** below, identify the influence of the synthesis parameters for achieving the smallest possible particle size.

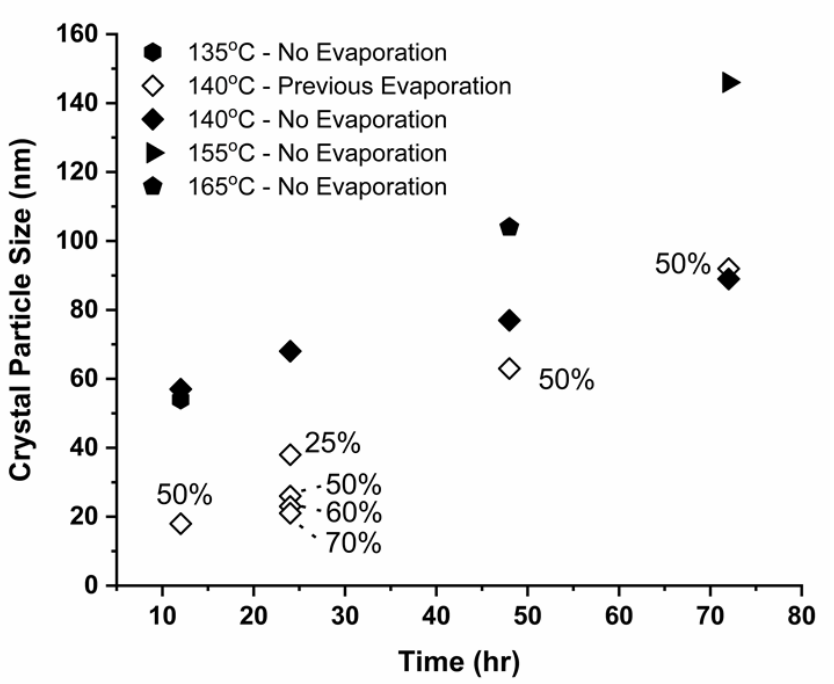

Figure 5.2. Correlation between crystallization time and temperature to modulate the final particle crystal size in MFI zeolites developed by Petushkov *et al*[5]. Percentage numbers represent the degree of previous evaporation carried out before hydrothermal synthesis process.

Conversely, lower temperatures favour nucleation over crystal growth. For zeolites belonging to the MFI family, as explored in this chapter, a temperature of 80°C has been described previously by Hu *et al.* as adequate for fostering the maturation of the precursor species and the formation of crystal nucleus[28].

In Metal@Zeolites systems, as illustrated in **Figure 5.3**, metal species are mainly categorized into two types according to their final size: encapsulated metallic structures and fixed metallic structures. Encapsulated metals include extra-framework isolated atoms and extra-framework nanoclusters (<1 nm),

whose dimensions are smaller than the size micropores/cages present in the zeolite. On the other hand, fixed metals are metal nanoparticles with higher sizes than the micropore (>1nm) of the zeolite in which they are stuck, breaking the zeolite framework lattice to fit the nanoparticle inside the crystal[29].

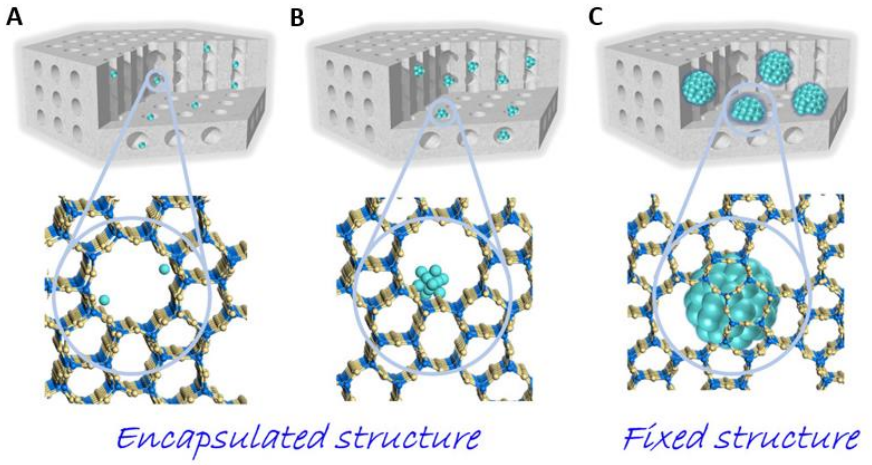

Figure 5.3. Metal@Zeolite systems with encapsulated and structure-fixed metals. Scheme for isolated metal centres **A)**, for encapsulated nanoclusters **B)** and for nanoparticle fixed in the zeolite matrix **C)**. Figure presented by Wang. H *et al*[30].

Depending on the size, geometry or electronic structure of the metallic species within the support, it will be possible to maximizing the catalytic activity of those processes catalysed by metal centres. For instance, Corma *et al*. studied the importance of achieving the adequate metal particle size in the final catalytic activity for CO oxidation and the Water-Gas Shift reaction (WGS). In the first case, the Pt-containing catalyst was more active for CO oxidation when the Pt active sites were in nanoparticle form, being almost inactive when the Pt sites were dispersed as isolated atoms within the structure[31]. For the WGS study, improved performance was observed for Au

nanoparticles of ~ 2nm, where the activation of the reactant was achieved even at low temperature[32].

As the influence of the metallic particle size, especially in noble metal-catalysed reactions, is of a relevant importance, controlling the dispersion and stability of the expensive Pd and Pt elements has received large attention. Examples of reactions involving these noble metals and where the particle size influences catalytic activity are the non-oxidative alkane dehydrogenation, discussed previously in Chapter 4, the utilization of liquid organic agents as hydrogen carriers (*i.e.*, methylcyclohexane, ammonia)[33-35], and the selective semihydrogenation of multifunctional molecules of significant interest, such as phenylacetylene[36-38] (see **Figure 5.4**).

This chapter pursues to study how controlling the size of the zeolite particles would affect the final catalytic performance of metal-encapsulated zeolites. Herein, Silicalite-1 (pure silica MFI) was synthesized at different temperatures, resulting in different crystal sizes and, therefore, diffusion pathway lengths. The effect of crystal size modifications was evaluated in the selective semi hydrogenation of a bulky molecule as phenylacetylene (involving steric hinderance of the zeolite support).

5.2. SYNTHESIS AND CHARACTERIZATION OF THE NOBLE METAL CONTAINING ZEOLITES AT DIFFERENT TEMPERATURES: CONTROLLING ZEOLITE PARTICLE SIZE

The one-pot synthesis of Pt and Pd containing purely siliceous Silicalite-1were carried out at different crystallization temperatures (80, 100, 150 and 175°C), as described in sections 3.2.3.1.3 and 3.2.3.1.4. in Chapter 3. First, the synthesis of the Pt-containing molecules has been explored. **Figure 5.4** shows

the diffractograms of the PtK@Silicalite-1 materials synthesized at different temperatures after 4 days. The expected trend is observed in these diffractograms, where the intensities of the most characteristic peaks of the MFI structures increase as the crystallization temperature also increases, especially for the two peaks located within the 7-9 degrees and in the trident-like peak above 23°C.

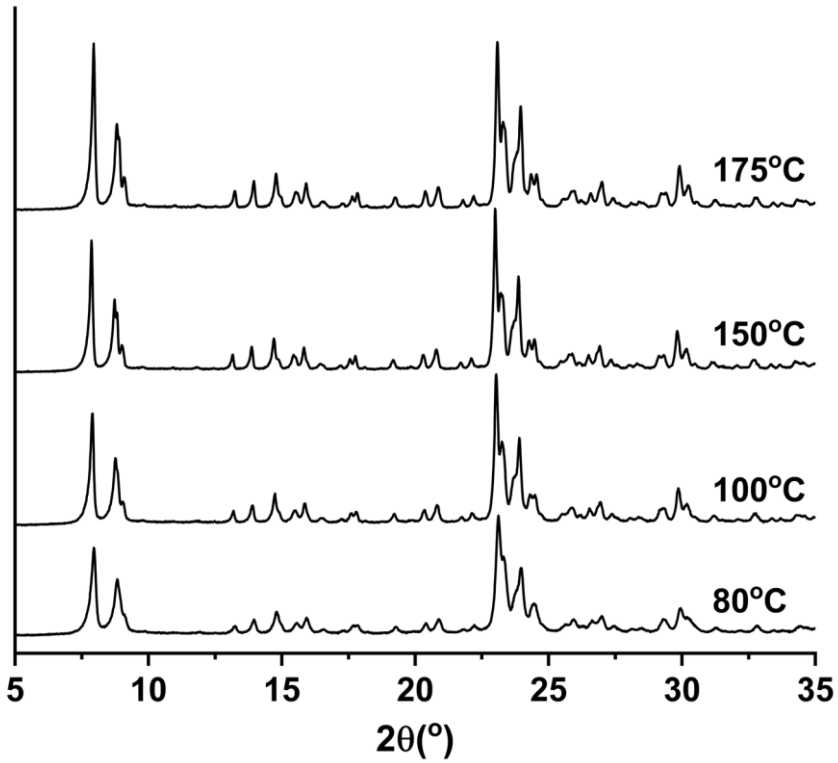

Figure 5.4. PXRD patterns of the different PtK@S-1 type materials synthesized at different temperatures varying from 80 to 175°C.

The composition of the materials obtained in this initial study is presented in **Table 5.1.** At lower synthesis temperatures (80–100°C), it was necessary to adjust the theoretical quantities of the synthesis gel to achieve a final

incorporation of 0.6% wt% of K and 0.4% wt% of Pt in the crystallized material. As stated previously, low temperatures favour nucleation vs. crystal growth but, in addition, the low temperatures also hinder the incorporation of Si species in the S-1 framework crystallites, resulting in lower solid yields (~ 55-60%).

Conversely, at higher synthesis temperatures, the overall incorporation yields were significantly higher, almost matching the desired theoretical proportions in the synthesis gels.

Table 5.1. Theoretical compositions in the synthesis gels and experimental chemical compositions of the PtK@S-1 materials, obtained by ICP spectroscopy for the different synthesis temperatures studied.

	Synthesis gel		**Solids (ICP)**	
Temperature (°C)	K (wt%)	Pt (wt%)	K (wt%)	Pt (wt%)
80	0.3	0.24	0.65	0.40
100	0.3	0.24	0.62	0.41
150	0.6	0.4	0.70	0.48
175	0.6	0.4	0.59	0.44

To evaluate the effect of the different crystallization temperatures on the final zeolite particle size and the metal encapsulation within the pores, the as-prepared materials were first subjected to calcination in air at 600°C to remove the organic molecules. The calcined samples were subsequently examined by FESEM. **Figure 5.5** presents the dark-field FESEM images obtained for all the zeolitic supports at different temperatures where not only the zeolite particle sizes can be evaluated, but the potential undesired metal sintering on the external zeolite surfaces can also be observed. A gradual increase in the zeolite particle sizes is observed as the crystallization

temperature rises (see **Figure 5.5**). The absence of bright spots in the dark-field images, generally associated to the presence of denser metal particles, such as metal agglomerates with higher atomic weight compared to the zeolitic matrix, suggests that massive migration or sintering of Pt has not occurred during the calcination process with air to remove the OSDAs molecules.

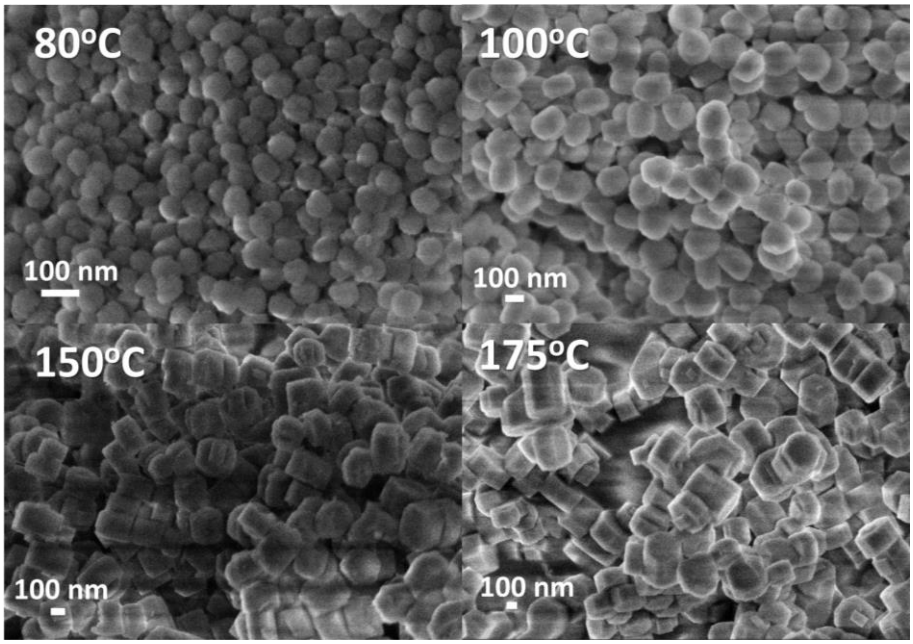

Figure 5.5. FESEM dark-field images of PtK@S-1 catalysts prepared at different crystallization temperatures and maintaining the crystallization time for 4 days.

The average zeolite particle sizes measured for the PtK@S-1 materials synthesized at different crystallization temperatures has been estimated by quantifying 100 measurements from different images for each material, resulting in a range of particle sizes from 84 to 335 nm for the PtK@S-1 materials synthesized at 80 and 175ºC, respectively.

The textural properties of these materials have been determined by N_2 adsorption analysis and illustrated below (see **Table 5.2**).

Temperature (ºC)	*Particle Size (nm)*	BET Area (m^2/gr)	Micropore Area (m^2/gr)	External Surface (m^2/gr)	Micropore Volume (cm^3/gr)
80	84 ± 8.9	543	460	83	0.18
100	158 ± 17	459	394	65	0.17
150	290± 38	397	371	26	0.17
175	336± 43	393	372	21	0.17

Table 5.2. Textural properties of the S-1 materials synthetized at different temperatures using N_2 adsorption technique.

As expected, the materials with lower particle size present higher external surface area (~ 83 m^2/gr, see **Table 5.2**) while the external surface area is significantly lower for the materials prepared at higher temperatures (~ 20 m^2/gr for the sample prepared at 175ºC, see **Table 5.2**)[39-42].

The presence of nanoparticles and their dispersion within the zeolite supports was examined using High-Angle Annular Dark Field (HAADF) TEM across all materials synthesized at different crystallization temperatures (**Figure 5.6**), after being calcined in air at 600ºC followed by a reduction treatment with hydrogen at 600ºC (**Chapter 3.2.3.3.3**) After the reduction step, the distribution of Pt metal nanoparticles was assessed, and their sizes were studied within the Silicalite-1 (see **Figure 5.6**).

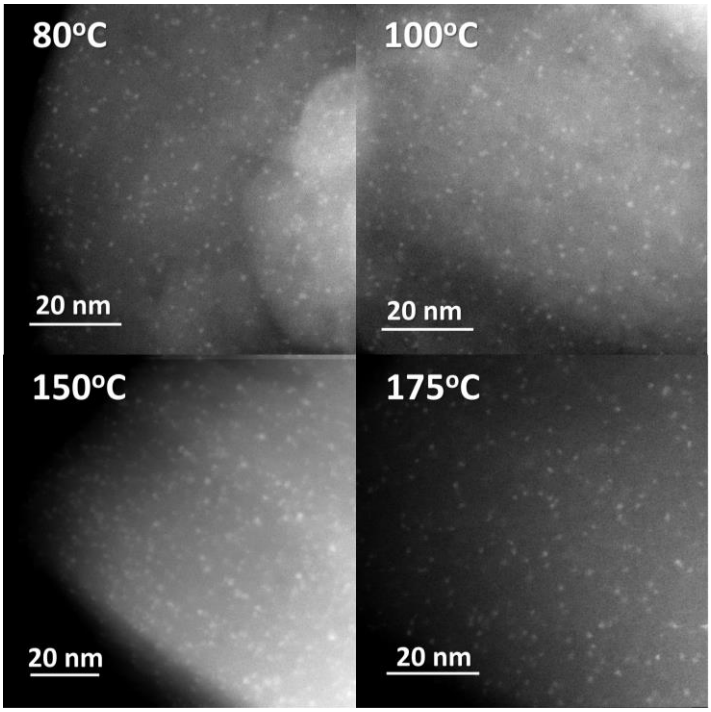

Figure 5.6. High-Angle Annular Dark Field (HAADF) TEM images of reduced PtK@S-1 catalysts for the different crystallization temperatures after being calcined in air at 600ºC and reduced in H_2 at 600ºC.

The dispersion of Pt nanoparticles within the Silicalite-1 matrix remains homogenous, regardless of the crystallization temperature used to synthesize the zeolites. The average experimental size of the Pt nanoparticles is comparable across all materials studied, being close to ~ 1 nm (see **Figure 5.6**). These outcomes indicate that the crystallization temperature does not significantly influences the dispersion or final size of the Pt nanoparticles. Instead, the primary factor governing the dispersion of Pt nanoparticles is the presence of K^+ ions, as demonstrated by previous works[43-46] and corroborated in Chapter 4 of this manuscript.

Similarly, Pd-containing Silicalite-1 catalyst were synthesized at the lowest (80ºC, KPd@nS-1) and at the highest temperatures (175ºC, KPd@µS-1) of the study to obtain the materials with the most differentiated diffusive properties and to compare them with their Pt-containing counterparts (maintaining the same Pd active centres moles than the Pt active sites contained in the PtK@S-1 catalysts . The chemical and textural properties of the Pd-containing Silicalite-1 with different zeolite particle sizes and Pt-containing nanosized after being calcined are shown in **Table 5.3**. The Pd and K contents are analogous for both Pd-containing S-1 materials, but as it could be expected, the external surface area of the material prepared at lower temperatures (~ 80 m^2/gr) is larger than the external surface area of the sample synthesized at 175ºC (~ 30 m^2/gr).

Table 5.3. Chemical and **t**extural properties of the KPd-containing S-1 materials synthetized at different temperatures using N_2 adsorption technique and chemical composition analysis obtained by ICP technique.

Sample	*ICP K (wt%)*	*ICP M (wt%)*	*BET Area (m^2/g)*	*Micropore Area (m^2/g)*	*Ext. Surface Area (m^2/g)*	*Micropore Volume (cm^3/g)*
KPd@ nS-1	0.6	0.2	518	437	81	0.18
KPd@ µS-1	0.6	0.2	402	368	34	0.16
KPt@ nS-1	0.65	0.4	543	460	83	0.18

The samples were reduced as described in **Chapter 3.2.3.3.4**, employing H_2 in a gas flow of 100 ml/min, a heating ramp of 10°C/min until reaching 600°C and then, maintained for 3 hrs. The samples were characterized using HAADF TEM to evaluate both the dispersion and the metal nanoparticle size gained in each reduction treatment (see **Figure 5.7**).

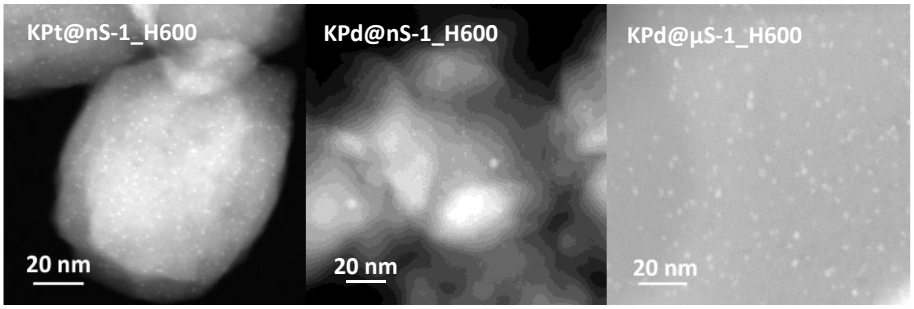

Figure 5.7. High-Angle Annular Dark Field (HAADF) TEM images of reduced K-Noble Metal containing@S-1 catalysts for the different crystallization temperatures after being calcined in air at 600°C and reduced in H_2 at 600°C with a heating rate of 10°C/min (samples H600).

Good dispersion of metallic nanoparticles was achieved for the Pd-containing zeolites, with almost the totality of the Pd species being effectively encapsulated within the zeolite crystals. The nanoparticle sizes estimated, resulting in similar nanoparticles sizes of ~ 1.8-2 nm (see **Table 5.4**) for both Pd-containing Silicalite-1 materials. Although currently, a definitive explanation is not available of why the average Pd nanoparticles are slightly larger than the Pt nanoparticles (~ 1 nm), the similar sizes in both Pd-containing S-1 materials would allow a fair comparison of these materials in the catalytic tests.

Table 5.4. Average metal nanoparticle sizes determined for Pt- and Pd-containing S-1 catalysts, considering different zeolite particle sizes, reduced in H_2 at 600ºC with a heating rate of 10ºC/min.

Catalyst	*Ø (nm)*
KPt@nS-1_H600	1.0 ± 0.2
KPd@nS-1_H600	1.8 ± 0.4
KPd@µS-1_H600	2.0 ± 0.3

It is worth noting that larges metal nanoparticle sizes have been previously reported in the literature for Pd-encapsulated species compared to Pt in zeolite crystals[47]. Once the catalysts with different crystallite particle sizes and incorporating encapsulated metal nanoparticles have been prepared and characterized, the impact of these parameters on catalytic performance and their stability upon reuse is examined in the following section.

5.3. SELECTIVE REDUCTION OF FUNCTIONAL BULKY MOLECULES IN LIQUID PHASE: HYDROGENATION OF PHENYLACETYLENE

To investigate the influence of diffusional pathways associated to zeolite particle sizes of S-1 supports synthesized at different temperatures, the materials prepared at 80ºC and 175ºC with encapsulated Pt or Pd have been selected. This selection intended to examine rationally the effect of the diffusive properties and the choice of the metal as active centre in the catalyst for the transformation of a bulky model molecule, phenylacetylene. The phenylacetylene molecule has been selected given its potential to produce styrene, a valuable intermediate extensively used in the plastic industry[48,49].

As shown in **Figure 5.8**, styrene is the primary product, but susceptible of being further hydrogenated to ethylbenzene. Thus, the selectivity to styrene will strongly depend on its residence time within the zeolite structure, which is directly dependent on the crystal size and diffusional path lengths of the zeolite.

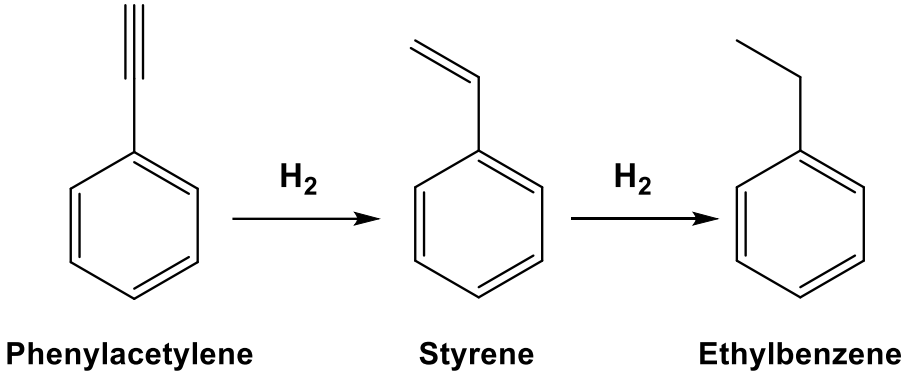

Figure 5.8. Hydrogenation mechanism described for phenylacetylene molecule.

The catalytic tests were carried out as described in **Chapter 3.4.2**. To achieve this, catalytic tests were conducted on both nanoscaled and microscaled zeolites (see **Figure 5.9**).

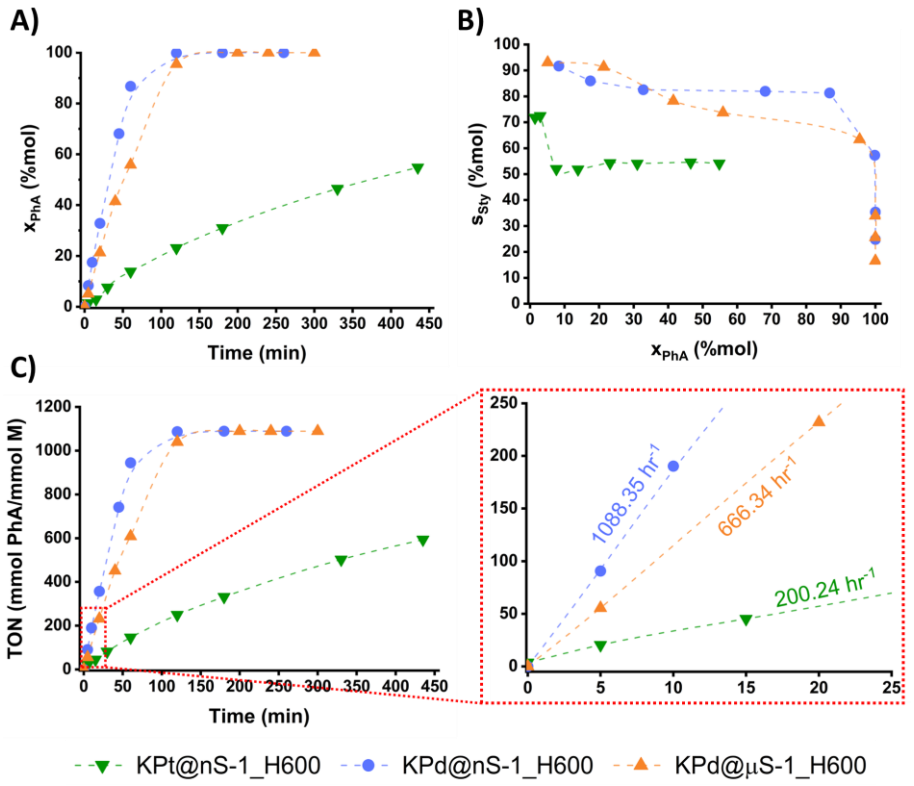

Figure 5.9. Catalytic behaviour of noble metal containing catalysts reduced at 600°C with a ramp of 10°C/min, employed for the reaction of semi-hydrogenation of phenylacetylene to produce styrene. The study includes **A)** the progression of catalytic activity over time, **B)** the evolution of selectivity for styrene formation as a function of phenylacetylene conversion, and **C)** the normalization of reacted phenylacetylene with respect to metal content, with the turnover frequency (TOF, in hr^{-1}) calculated from the slope of the turnover number (TON) at short reaction times.

The enhancement of diffusive properties in the materials is clearly reflected in the catalytic performance, with the KPd@nS-1 sample exhibiting higher conversion rates at earlier stages and maintaining higher selectivity towards the styrene formation, even at high conversion values, compared to its submicron-sized counterpart (see **Figure 5.9A** and **Figure 5.9B**). This disparity

in reaction rates is particularly evident when analyzing the TOF values, where the TOF of the Pd nanozeolite is 1.5 times greater (see **Figure 5.9C**) than that of the KPd@µS-1 sample. In contrast, Pt nanoparticles demonstrate significantly lower catalytic activity, yielding intermediate levels of both activity and selectivity (~50% in both cases) for styrene formation, indicating substantially lower reactivity compared to Pd nanoparticles, despite the enhancement of the diffusional properties provided by the small zeolite crystal size in KPt@nS-1 catalyst.

Once the reaction was finished, the spent catalysts were recovered by filtration using EtOH to remove residual phenylacetylene and dodecane adhered to the catalyst, and dried at a temperature of 100^{o}C for 16 hrs. The Pd-containing materials were then subjected to a reusability test to assess their catalytic stability after being used. The catalytic performance of the materials after reuse and the comparison with the fresh catalyst activity is illustrated in **Figure 5.10**, where it is observed that the catalytic activity of the different catalysts does not decline noticeably during the second reaction cycle, exhibiting conversion values comparable to those obtained with the fresh catalyst (see **Figure 5.10, A)**). However, differences emerged in the selectivity toward styrene formation, with a significant decline in the initial selectivity observed upon reuse of the KPd@µS-1 sample (see **Figure 5.10, B)**). As depicted in **Figure 5.10, C)**, a reduction in TOF values was noted for reused catalysts, confirming that the initial activity of the catalysts has been reduced upon their use, despite remaining the activity similar to the fresh catalysts.

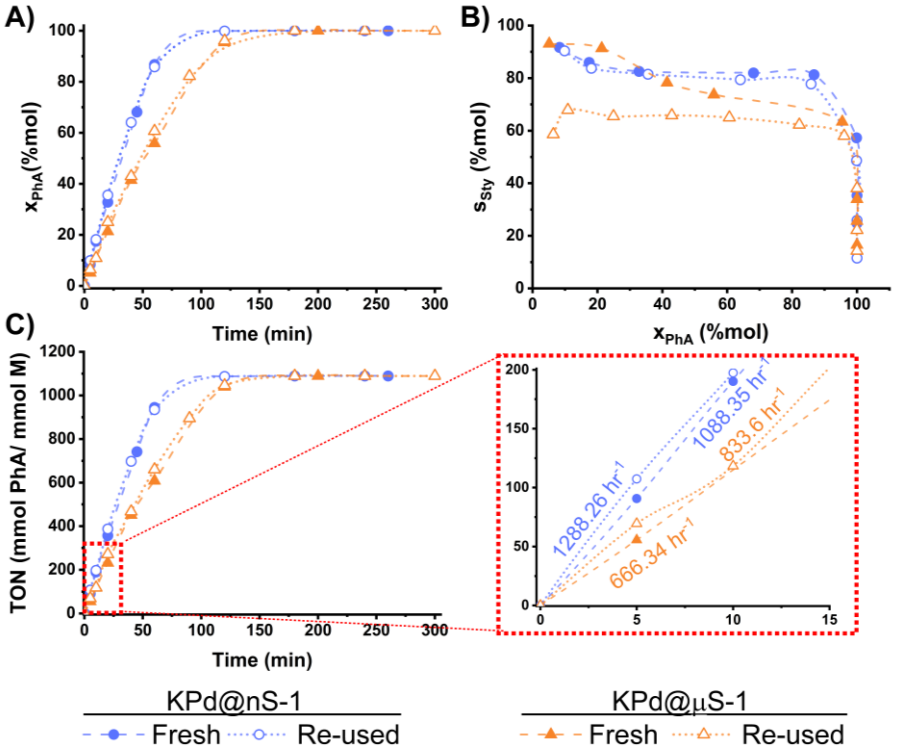

Figure 5.10. Catalytic behaviour of noble metal containing catalysts reduced at 600°C with a ramp of 10°C/min, employed for the reaction of semi-hydrogenation of phenylacetylene to produce styrene. The study includes **A)** the progression of catalytic activity over time for fresh catalyst and re-utilized in a second reaction cycle, **B)** the evolution of selectivity for styrene formation for fresh catalyst and re-utilized in a second reaction cycle as a function of phenylacetylene conversion, and **C)** the normalization of reacted phenylacetylene with respect to metal content, with the turnover frequency (TOF, in hr^{-1}) calculated from the slope of the turnover number (TON) at short reaction times.

To determine whether the catalyst reuse resulted in any loss of chemical species through leaching into the liquid reaction medium, the catalysts were recovered and analysed chemically using ICP. The results of this analysis are presented in **Table 5.5** below.

Table 5.5. Chemical compositions in the KPd-S-1 materials employed as catalysts for the semi-hydrogenation of phenylacetyene molecule obtained by ICP spectroscopy for both the fresh and the re-used materials.

Catalyst	ICP K (wt%)	ICP Pd (wt%)
Pd@nS-1_H600	0.60	0.20
Pd@nS-1_H600_Re-used	0.53	0.19
Pd@µS-1_H600	0.60	0.20
Pd@µS-1_H600_Re-used	0.53	0.20

The compositional analysis confirms the retention of metallic species within the materials, with loss of the 11% of potassium species (0.53 wt% in the re-used catalyst), regardless of zeolite particle size, thereby excluding metal leaching phenomenon. Consequently, the state of the metallic nanoparticles after reaction recycle was examined to determine whether sintering phenomena took place following exposure to the reaction conditions by High-Angle Annular Dark Field (HAADF) TEM. The images obtained of the materials are shown in **Figure 5.11** below.

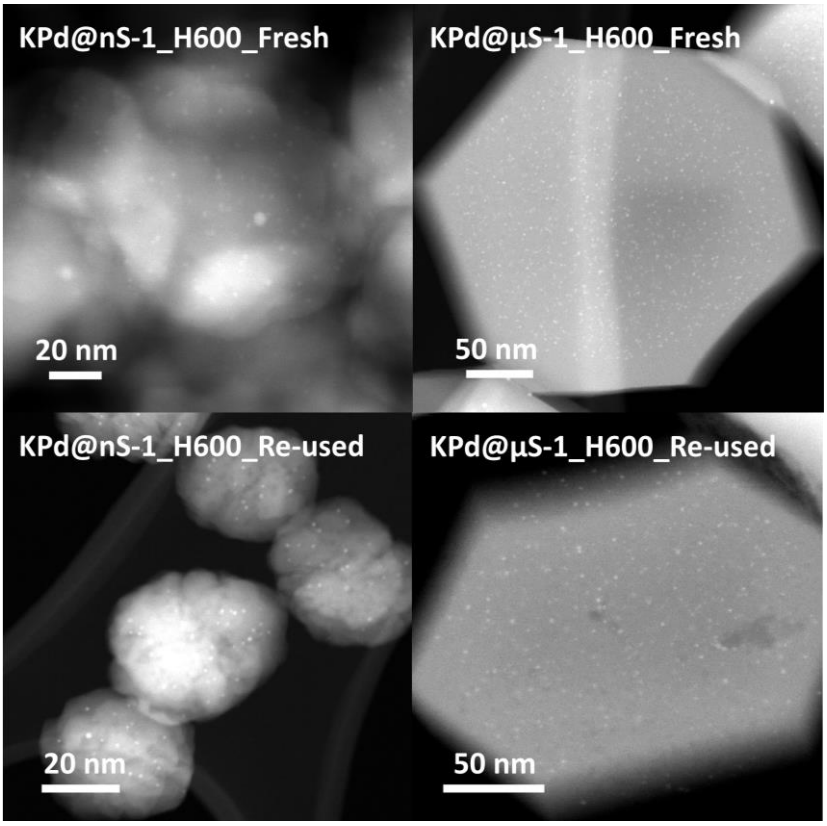

Figure 5.11. HAADF TEM images of the different Pd-containing materials for the catalytic reusability study, both in fresh state and re-used after been recovered and dried overnight at temperature.

In the KPd@nS-1 samples, an increase in the size of Pd nanoparticles is observed after recovering the material from the recycle reaction, along with the emergence of a few particles on the zeolite surface (see KPd@nS-1_H600_Re-used in **Figure 5.11**). These observations, combined with the ICP analyses confirming the maintenance of metallic species (Pd, K^+), rule out leaching phenomena. However, they indicate the phenomena of undesired surface sintering. In contrast, the KPd@µS-1 sample does not exhibit Pd

nanoparticles on its surface, and its composition remains unchanged, further confirming the stability of the incorporated species.

Given the promising catalytic behaviour of nanosized materials in the semi-hydrogenation reaction due to their high values of activity and selectivity, it is crucial to develop alternative strategies for stabilizing Pd nanoparticles within the zeolite framework, thereby preventing migration and surface sintering. One of the most effective approaches to mitigate these issues involves the creation of external protective coatings, as for instance, by means of the preparation of core-shell structured materials. The following section explores the application of ultrafast hydrothermal synthesis technology as an innovative method for generating hydrophobic crystalline coatings, which could enhance the confinement of Pd nanoparticles within the S-1 zeolite matrix, particularly for nanosized crystals.

5.4. DEVELOPMENT OF CORE-SHELL ZEOLITES THROUGH ULTRA-FAST SYNTHESIS TECHNIQUE TO IMPROVE CATALYST ACTIVITY. STATE OF ART.

Various strategies can be employed to tailor the final physicochemical properties of materials, focusing on the rational design of their architecture. These approaches range from functionalization with chemical species, which reduce the effects of the reaction medium on the material, to the development of protective crystalline layer coatings composed of chemically inert species, significantly enhancing the materials resistance to potential adverse conditions. One of the most widely adopted strategies involves the fabrication of core-shell hybrid materials. Core-shell zeolites represent a type of composite materials in which crystals of one zeolitic structure (shell) grow

on the surface of another zeolite (core), forming a continuous and protective outer layer[50].

These hybrid materials have garnered significant interest due to their ability to integrate the advantageous properties of the shell zeolite with the unique properties of the core zeolite. This synergy enables the production of novel composite materials with tailorable multifunctional properties, while maintaining the typically diffusive properties of the microporous materials, making them more suitable for specific catalytic applications than individual zeolitic structures[51,52].

Among the examples described in the state of the art of how the successful strategic development of zeolitic core-shell catalysts has improved catalytic behaviour and stability we can highlight: **(i)** the development of composed materials formed by a SAPO-34 core and a ZSM-5 shell for the ethanol dehydration reaction to produce propylene, increasing the selectivity to propylene formation and the stability of the catalyst by favouring the diffusion of the product molecules as they move from a small-pore to a medium-pore channel system, decreasing the coke formation[53]; **(ii)** the preparation of a ZSM-5@S-1 core-shell structure by coating MFI zeolite crystals containing acidic centres with a hierarchical Silicalite-1 shell[54], a modification that neutralized surface acidity while enhancing molecular diffusion due to the presence of mesopores. As a result, the catalyst exhibited significantly improved stability and catalytic performance in the production of light aromatic compounds, including benzene, toluene, ethylbenzene, xylene, and naphthalene, from volatile products derived from the pyrolysis of lignocellulose[54]; **(iii)** the fabrication of hydrophobic S-1 coatings with varying thicknesses surrounding Fe-ZSM-5 cores, materials that were explored for the

NH_3-SCR reaction[55]. This modification not only improved catalytic activity but also ensured its stability even in the presence of water vapor[55].

The development of zeolite-zeolite core-shell materials represents a promising strategy for enhancing zeolitic catalysts in industrial processes. However, its widespread application remains constrained by several challenges, including difficulties in achieving uniform coatings across the entire crystal surface (particularly in large crystals surfaces), the unintended migration of active species from the core due to partial redissolution[56], the non-desired secondary crystallization where new nucleus are made instead of developing the crystalline shell and the potential loss of diffusive properties resulting from disruptions in the continuity of porous channel systems caused by uncontrolled desilication[57]. These phenomena frequently happen as a result of long secondary crystallization times, which can trigger undesirable secondary processes. Therefore, it is essential to develop strategies to accelerate the crystallization process and mitigate the emergence of these secondary chemical phenomena.

In order to mitigate the challenges associated with different time-dependent phenomena happened during crystallization and crystal growth, the implementation of ultra-fast hydrothermal synthesis technology presents a viable solution. This innovative approach, developed and patented by the Okubo-Wakihara research group at the University of Tokyo, optimizes heat transfer efficiency, enabling significantly accelerated crystallization processes.

Conventional autoclaves offer a safe environment to hold the typical conditions under which a traditional hydrothermal synthesis needs to be

carried out. However, their main container is made of Teflon, offering a low thermal conductivity and requiring long induction periods for the autoclave to reach the actually required synthesis temperature, making difficult to determine, in an accurate way, the changes happening in the crystallization process during these stages prior to reaching the desired temperature. For this reason, the Okubo-Wakihara group changed the conventional design of the autoclave for a stainless-steel tubular reactor of 13.5 cm of effective length, sealed by two caps provided by the Swageslok® company (see **Chapter 3.2.3.4.4** of this manuscript).

Those feature changes are based on the objective of optimizing the heat transfer capacity thought increasing the surface-to-volume ratio, enhancing many times the heat transfer rate as shown in **Figure 5.12**, where a heating rate comparison between the tubular reactor and a Parr Instrument Company conventional Teflon-lined autoclave is analysed.

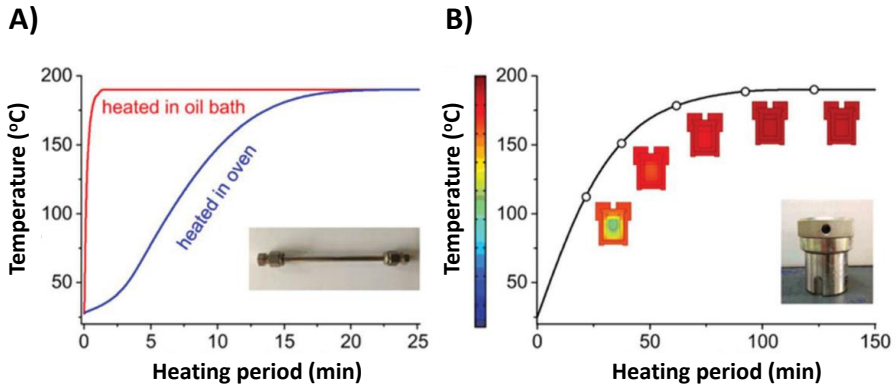

Figure 5.12. Temperature profile for **A)** ultrafast synthesis stainless steel reactor and **B)** conventional hydrothermal synthesis in a stainless autoclave with a Teflon cylinder. Reproduced from Liu Z *et al*[58].

As shown in the **Figure 5.12**, the thermal induction period is decreased to the range of one minute if working in a pre-heated oil bath, whereas the required time decreases from 100 min to 20 min if working in conventional air convection ovens. This improvement not only allows observing changes at short times, but in combination with a rational selection of the precursor species included in the synthesis gel (*i.e*. seeding or aging), also permits decreasing the necessary crystallization time to the order of minutes. **Figure 5.13** summarizes the different steps involved during the fast crystallization synthesis.

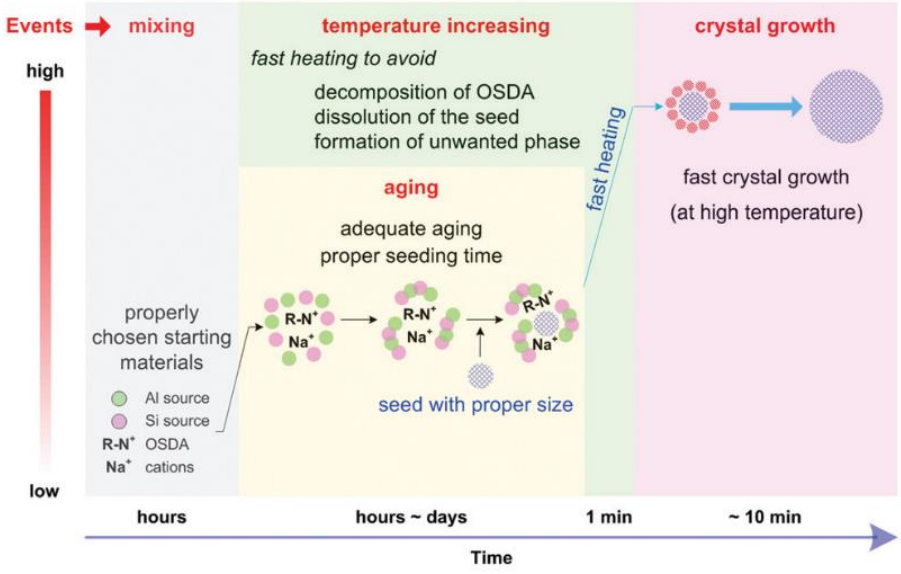

Figure 5.13. Scheme for a typical ultrafast synthesis procedure, encompassing the events taking place at different stages under temperatures and time scales. Reproduced from Liu *et al*[58].

As shown, several factor must be taken into account to develop a fully controlled synthesis, such as rationalizing the precursor species and the intermediate steps required (stirring, seeds, aging...). The ultrafast synthesis was demonstrated to offer promising results in the zeolite synthesis with adequate properties[59-62].

The same fundamental principle behind ultrafast hydrothermal synthesis for zeolite crystal formation can be extended to the fabrication of zeolite-based crystalline coatings. Indeed, the Okubo-Wakihara group employed the ultrafast synthesis methodology to produce ZSM-5@Silicalite-1[63]. In that work, they achieved a pure silicious coverage over an Al-containing MFI core zeolite. A time screening was performed to study the evolution of the shell thickness, and the resultant materials were tested for the cumene and 1,3,5-triisopropylbenzene (TIPB) cracking reactions. The results reported by the group show the cumene cracking yield remains the same while the TIPB cracking yield decreases with increasing the covering time as a result of decreasing the surface acidity[63]. The evolution of the Silicalite-1 shell formation at different times of ultrafast heating is shown in **Figure 5.14**.

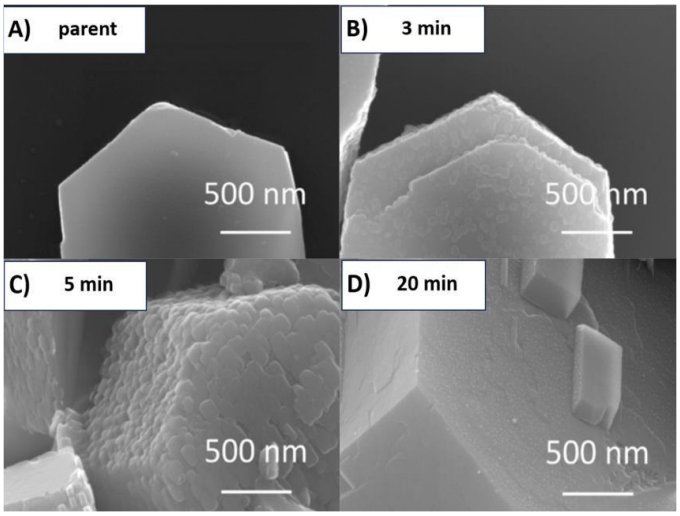

Figure 5.14. SEM images of ZSM-5@S-1 products reported by Ce Peng *et al*[63] employing commercial ZSM-5 (HSZ- 840NHA, Tosoh Chemicals) as core. **A)** Core ZSM-5 (Si/Al=19); **B)** Coated for 3 min (Si/Al=21); **C)** Coated for 5 min (Si/Al=23); **D)** Coated for 20 min (Si/Al=26).

Based on the idea of using the ultrafast synthesis methodology, this section of the chapter reports the results obtained during the PhD International Trainee Internship performed in the Okubo-Wakihara research group at the University of Tokyo. The Research Internship topic focused on the study of the influence of the water content in the synthesis gel to grow Silicalite-1 shells with controlled thickness, and to apply this strategy to the metal-containing Silicalite-1 zeolites with different crystallite sizes presented in the previous sections of this chapter. Thus, in the first stage, the optimal amount of water in the synthesis gel during the coating process was studied as a function of the size of the metal-free zeolites used as core. Once the initial screening was done, the coating process was applied to Pd-containing Silicalite-1 materials to provide them a coating that could help improving the catalyst stabilization against the undesired surface sintering phenomena observed before.

5.5. STUDY OF WATER CONTENT CORE PARTICLE SIZE ON THE SILICALITE-1 SHELL THICKNESS.

To evaluate the thickness of the Silicate-1 shell in the core-shell zeolite systems, two different MFI-type core materials were selected, a nano and a submicronsized, as reported in **Chapter 3**. For this preliminary study, the selected core samples were metal-free S-1, which were prepared as the nano- and micron-sized metal-containing S-1 samples described previously but without adding the metallic component. Once the core zeolites were obtained, they were coated by the ultra-fast synthesis process described in **Chapter 3**, but modifying the H_2O/Si molar ratio at 20, 40, 80 and 120. To facilitate the identification of the materials along the section, the selected nomenclatures were: **nS-1**, for the nanosized Silicalite-1 synthesized at **80ºC** **µS-1**, for the submicronsized Silicalite-1 (synthesized at **175ºC**).

Firstly, the ultra-fast coverage has been explored on the nS-1 materials. The Si content of the core and the Si content added for the coverage has been fixed at 1:1. However, the yield of the solid collected after the ultra-fast procedure varies with the H_2O/Si ratio (see **Table 5.6**).

Table 5.6. Experimental mass measurements of the nanosized as-prepared S-1 seeds (core), the shell theoretical mass content added during the synthesis and the amount of core-shell material obtained (as prepared) for the different H_2O/Si ratios studied.

Sample	*Core seeds (mg)*	*Shell added (mg SiO_2)*	*Solid Collected (mg)*
nS-1@S-1 H_2O/Si=20	226	232.6	368
nS-1@S-1 H_2O/Si=40	136	138.8	216
nS-1@S-1 H_2O/Si=80	76	81.2	120
nS-1@S-1 H_2O/Si=120	58	60.3	74

The different materials were characterized by PXRD (see **Figure 5.15**), presenting in all cases similar diffractograms after the coating process employing the ultrafast synthesis with different water contents in the synthesis gel. The PXRD patterns indicate that all the samples kept the crystallinity, confirming that the as-prepared nS-1 particles used as core did not dissolve during the process.

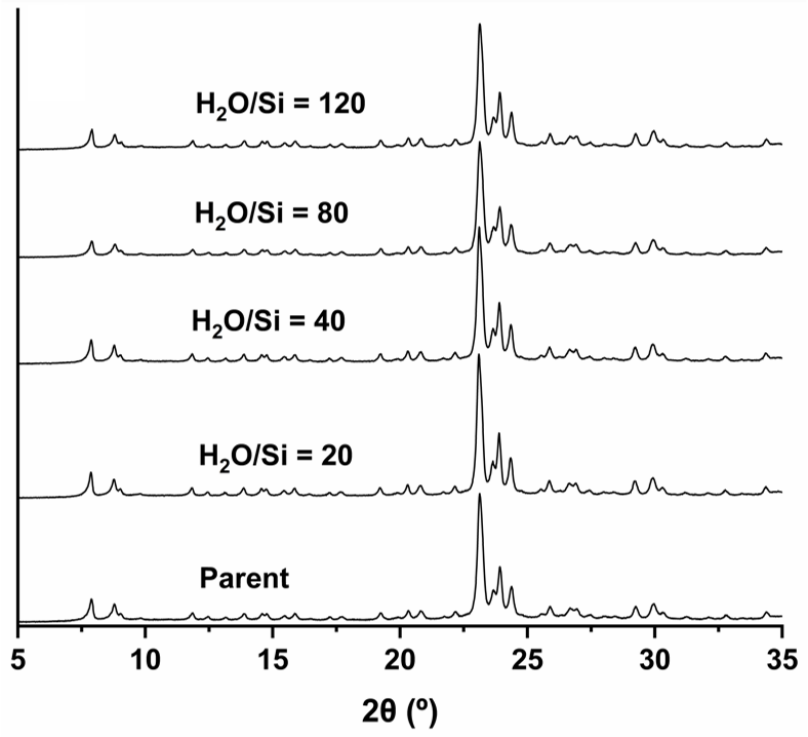

Figure 5.15. PXRD pattern of the different nS-1@Silicalite-1 structures obtained by ultrafast synthesis covering methodology carried out at 190ºC for 10 min with different H_2O/Si molar ratios.

In addition to the PXRD characterization, thermogravimetry test were carried out on the as-prepared composites to determine, through the mass of the solid recovered, whether there had been an increase in mass that could help

empirically to determine a feasible process of incorporation of more species in addition to the seeds, developing the shells.

Employing the experimental weight measurements of the recovered dry solids (see **Table 5.6**), in combination with the thermogravimetric analysis (see **Table 5.7**), it was possible to determine the "core-shell" yields and the ratio between the core and shell materials by employing the equations **Eq.5.1** and **Eq.5.2**.

$$R_{\frac{\text{Core-Shell}}{\text{Core}}} = \frac{m_{\text{solid collected}} \cdot \%TGA_{\text{solid collected}}}{m_{\text{Core zeolite}} \cdot \%TGA_{\text{Core zeolite}}} \qquad \textbf{Eq 5.1}$$

$$\%Yield_{Core-Shell} = \left(\frac{m_{solid\ collected} \cdot \%TGA_{solid\ collected}}{m_{Core\ zeolite} \cdot \%TGA_{Core\ zeolite} + m_{TEOS} \cdot \frac{Mw_{SiO_2}}{Mw_{TEOS}}} \right) \cdot 100 \qquad \textbf{Eq 5.2}$$

Where:

- $m_{solid\ collected}$: dry mass of the core@shell material collected after centrifugation.
- $m_{Core\ zeolite}$: zeolite mass added during the synthesis.
- $\%TGA_{solid\ collected}$: % of the core@shell sample recovered after the thermogravimetry essay.
- $\%TGA_{Core\ Zeolite}$: % of the zeolite sample recovered after the thermogravimetry essay.

The experimental values of the inorganic mass recovered after the thermogravimetry essays for the different samples are shown in **Table 5.7**, revealing a similar weight loss in all cases.

Table 5.7. Inorganic solids obtained after the thermogravimetric essays (as percentage of the initial mass loaded), mass ratios estimated between the mass of the materials recovered and the amount of zeolite incorporated as core, as well as the yield of the core-shell materials.

Sample	***%Solid TGA***	$R_{Core\text{-}Shell/Core}$	$\%Yield_{Core\text{-}Shell}$
Parent	83	----------	----------
nS-1@S-1 H_2O/Si=20	83.7	1.64	73.1
nS-1@S-1 H_2O/Si=40	83.3	1.59	71.6
nS-1@S-1 H_2O/Si=80	83.4	1.59	69.3
nS-1@S-1 H_2O/Si=120	83.5	1.28	57.1

The trend observed has to be noted, as the more concentrated synthesis seems more productive in terms of mass gained within the whole core-shell composite, compared to the materials obtained under more diluted conditions. These results suggest that more concentrated media favour the formation of thicker Silicalite-1 shells. To evaluate this point, the samples were studied by Scanning Electronic Microscopy, whose images are shown in **Figure 5.16**.

A perceptible increase of the crystallite particle sizes is observed through the SEM images after the covering treatment. Indeed, the more concentrated synthesis gels (lower H_2O/Si ratio) result in the higher increase of final particle size of the core-shell materials. The presence of additional particles is not shown in the SEM images, suggesting that undesired secondary nucleation processes have not occurred during the synthesis process. The overall particle size distributions can be observed in the following 3-D histogram (**Figure 5.17**).

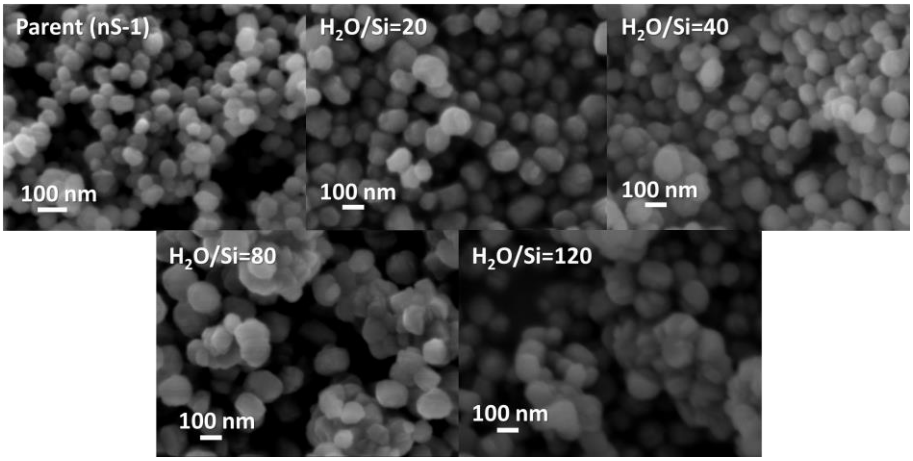

Figure 5.16. SEM images of the nS-1 samples coated using different H_2O/Si molar ratios in the synthesis gels for 10 minutes at 190^{o}C by ultrafast synthesis.

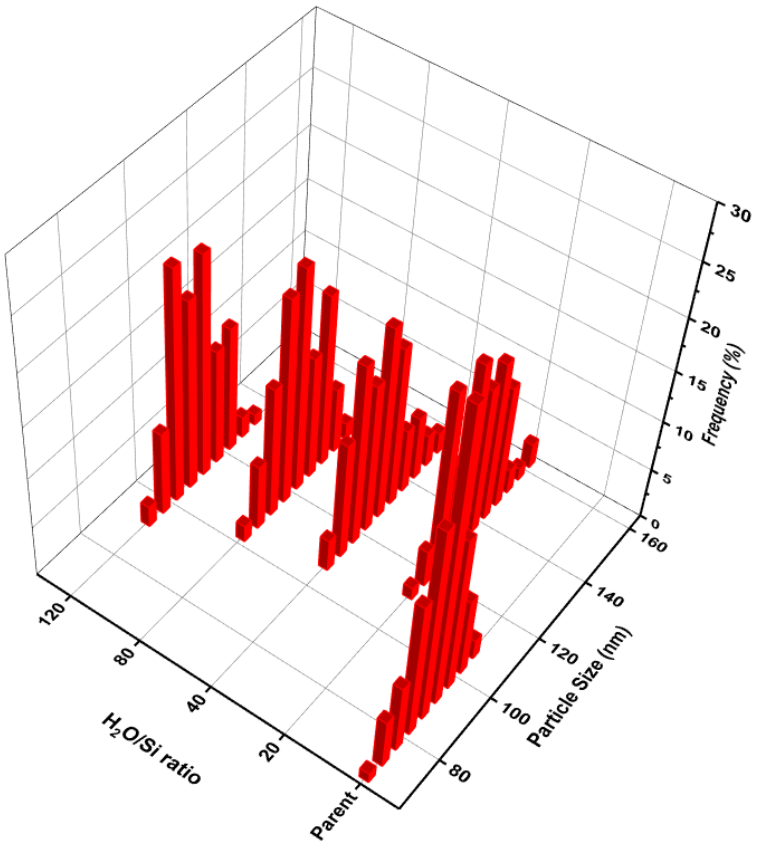

Figure 5.17. nS-1@S-1 composites particle size distribution measured by SEM microscopy (N=100 along different SEM images) for the samples prepared with different H_2O/Si ratios in the synthesis gels and carried out at 190°C for 10 min.

The particle size distribution trend observed after characterizing the materials clearly shows that concentrated media favor the increase of the thickness of the Silicalite-1, revealed by the increment of the particle size and also by preserving the highest mass of the collected solids after the synthesis. The average particle sizes of the materials obtained under different conditions are shown in **Table 5.8**, values that confirm that the lowest H_2O/Si

ratio favours the higher mass deposition and also the higher final core-shell composite particle size.

Table 5.8. Average particle sizes standard deviation obtained for the nS-1@S-1 composites synthetized with different H_2O/Si ratios with the ultrafast-synthesis process.

Sample	Average Particle Size (nm)	Standard Deviation (nm)
Parent	89.7	±8.0
nS-1@S-1 H_2O/Si=20	135.2	±10.6
nS-1@S-1 H_2O/Si=40	126.0	±10.2
nS-1@S-1 H_2O/Si=80	121.5	±8.9
nS-1@S-1 H_2O/Si=120	110.0	±8.7

Similarly, µS-1 material was covered using the ultra-fast approach and the same H_2O/Si ratios, while maintaining unaltered the other synthesis conditions. The obtained core-shell materials were characterized similarly to the nS-1-type composites. As in the case of the nS-1 sample, the mass content of the µS-1 zeolite powder added as core and the equivalent SiO_2 content added as shell were fixed at 1:1. After the coverage procedure, the composites were recovered after centrifugation and dried overnight at 80°C.

Table 5.9. Experimental mass measurements of the amount of micronsized as-prepared S-1 zeolite (core), the shell theoretical mass content added during the synthesis and the amount of core-shell material obtained (as prepared) for the different H_2O/Si ratios studied.

Sample	***Core seeds (mg)***	***Shell added (mg SiO_2)***	***Solid Collected (mg)***
µS-1@S-1 H_2O/Si=20	226	229.8	394
µS-1@S-1 H_2O/Si=40	136	137.8	235
µS-1@S-1 H_2O/Si=80	76	76.5	104
µS-1@S-1 H_2O/Si=120	58	56.1	77

The different materials were characterized by PXRD (see **Figure 5.18**), and present, in all cases, similar diffractograms after the coating process employing the ultrafast synthesis procedure with different water contents in the synthesis gel. The PXRD patterns evidence the high crystallinity of all the samples, confirming that the as-prepared µS-1 particles used as core does not dissolve during the process. Similarly to the previous nS-1@S-1 materials, the core-shell composites show analogous PXRD diffractograms, but with the intensity of the peaks being generally higher than that observed for the nS-1 type composites, as could be expected due to the larger zeolite particle sizes of µS-1@S-1.

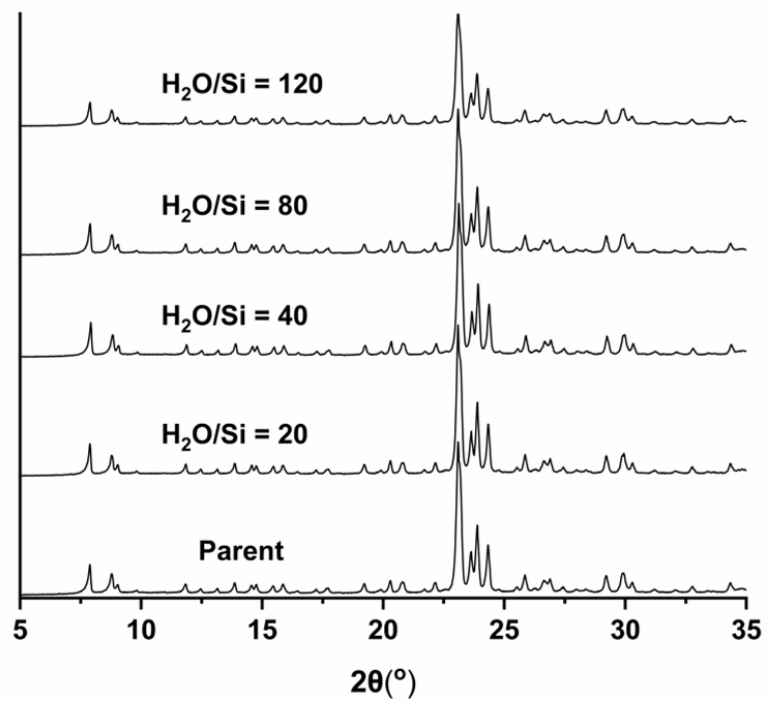

Figure 5.18. PXRD patterns of the different µS-1@S-1 materials composites obtained by ultrafast synthesis covering methodology carried out at 190ºC for 10 min with different H_2O/Si molar ratios in the synthesis gels.

To determine the efficiency of the coverage, the same quantification parameters presented previously ($R_{Core\text{-}Shell/Core}$ and $Yield_{Core\text{-}Shell}$) were employed here by using the results obtained through the thermogravimetry essays of the µS-1@Silicalite-1 samples. Considering the mass weight loss of the TGA analysis, different indicators to quantify the efficiency of the coating process were calculated by applying **Eq. 5.1** and **Eq. 5.2**, as shown in the **Table 5.10** below.

Table 5.10. Inorganic solids obtained after the thermogravimetric essays (as percentage of the initial mass loaded), mass ratio estimated between the mass of the materials recovered and the amount of zeolite incorporated as core, as well as the yield of the core-shell materials.

Sample	***%Solid TGA***	***$R_{Core\text{-}Shell/Core}$***	***%$Yield_{Core\text{-}Shell}$***
Parent	87	----------	----------
µS-1@S-1 H_2O/Si=20	85	1.7	78.3
µS-1@S-1 H_2O/Si=40	84.5	1.68	78.0
µS-1@S-1 H_2O/Si=80	85	1.34	61.6
µS-1@S-1 H_2O/Si=120	84.7	1.29	61.4

A similar trend is observed as compared to the nanometre-sized composites, and the syntheses conducted in more concentrated media allowed higher recovered mass quantities than those composites prepared under more diluted conditions. Noticeably, the core-shell synthesis yields were generally higher at bigger core particle size than those obtained when using nS-1 zeolite as core materials (78.3% for µS-1 versus 73.1% for nS-1 under the more concentrated conditions, whereas 61.4% versus 57.1% in the more diluted conditions, respectively). While this difference is evident, it is not large enough to indicate that the surface area of the core zeolites could significantly impact the nucleation and crystallization mechanisms of the coatings. This suggests that the covering effect is more closely related to the

applied technique and minimally influenced by the surface area of the seeds. In any case, future research could approach the use of larger MFI core materials within the micron-meter sizes in order to evaluate if lower surface areas than those studied here can clearly reveal the positive/negative roles of the external surface area.

Figure 5.19 shows the SEM images of the core-shell composites synthesized using submicrometric Silicalite-1 seeds for the different studied water contents in the synthesis gels.

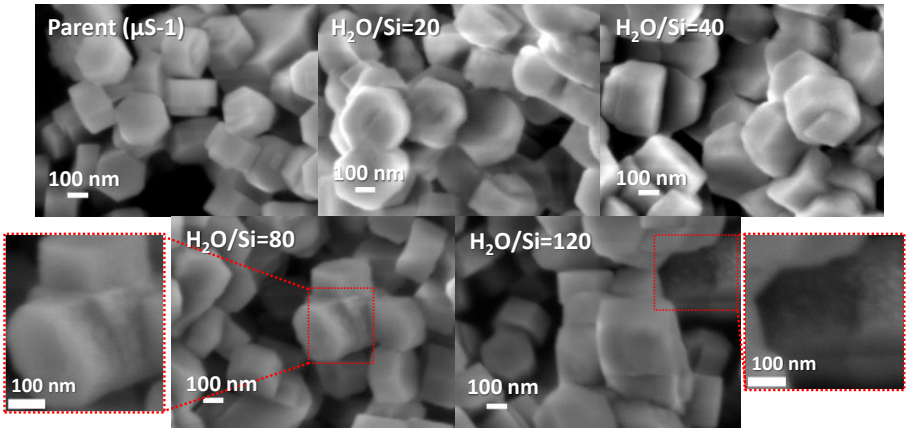

Figure 5.19. SEM images of the µS-1 samples coated using different H_2O/Si molar ratios in the synthesis gels for 10 minutes at 190ºC by ultrafast synthesis. Red squares show a magnification area of crystal surface.

In general, larger sizes are observed in the core-shell composites prepared under more concentrated media (see **Figures 5.19** and **5.20**), while those prepared under more diluted conditions reveals the appearance of dots on the surface of the crystalline particle (see $H_2O/Si=80$ and $H_2O/Si=120$ in **Figure 5.19**). The appearance of these dots suggests that the crystallization mechanism under diluted conditions might induce some secondary growth.

Conversely, the absence of these dots on the surface of the materials would suggest that high alkaline media would preferentially promote the epitaxial growth. However, further characterization (TEM images of the particle surface) may be needed before accepting this assumption.

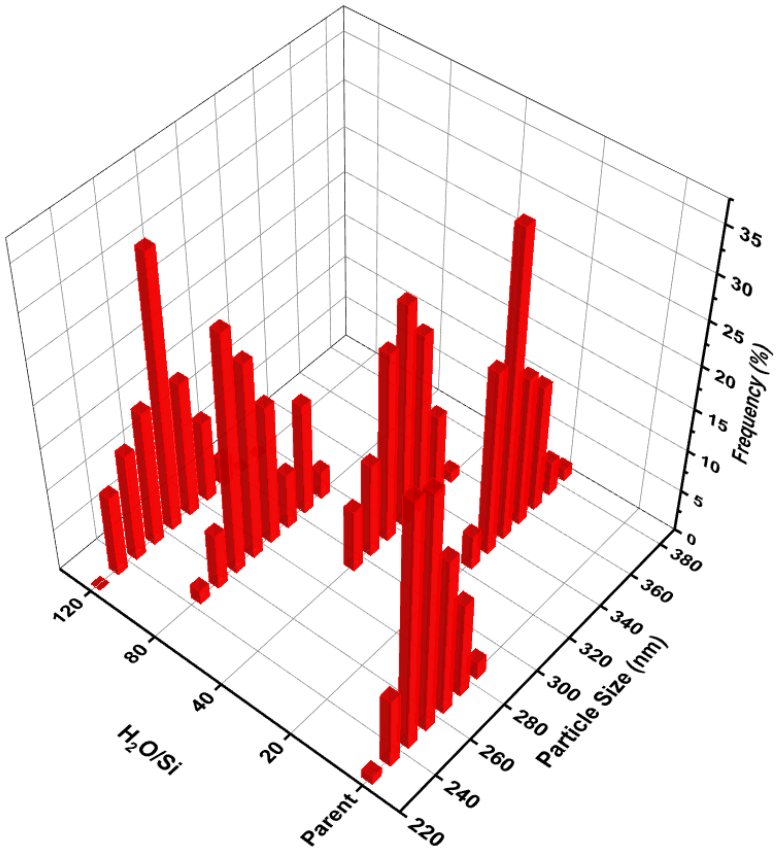

Figure 5.20. µS-1@S-1 composites particle size distributions measured by SEM microscopy (N=100 along different SEM images) for the samples prepared with different H_2O/Si ratios in the synthesis gel and carried out at 190ºC for 10 min.

The particle size distribution trend observed after characterizing the materials clearly shows that concentrated media favour the increase of the thickness of the Silicalite-1, revealed by the increment of the particle size and

also by preserving the highest mass of the collected solids after the synthesis. The average particle size of the materials obtained under different conditions are shown in **Table 5.11**, where it is confirmed that the lowest H_2O/Si ratio favours the highest mass deposition and also the largest final core-shell composite particle size.

Table 5.11. Average particle sizes standard deviation obtained for the µS-1@S-1 composites synthetized with different H_2O/Si ratios with the ultrafast-synthesis process.

Sample	Average Particle Size (nm)	Standard Deviation (nm)
Parent	254.6	±12.9
µS-1@S-1 H_2O/Si=20	343.5	±12.6
µS-1@S-1 H_2O/Si=40	317.6	±13.8
µS-1@S-1 H_2O/Si=80	278.5	±16.6
µS-1@S-1 H_2O/Si=120	262.0	±16.9

For comparison purposes, the crystalline coating process of µS-1 zeolite was attempted in a conventional autoclave, aiming to confirm the benefits of the ultrafast crystallization technique as a novel proposal to favour the preparation of zeolitic core-shell material systems over conventional hydrothermal synthesis to produce crystalline shells.

The composition of the synthesis gels to grow the Silicalite-1 shell was:

$$1SiO_2{:}4\ EtOH{:}0.3\ TPAOH{:}40\ H_2O$$

keeping the SiO_2 shell/SiO_2 core mass ratio ~ 1.

The conventional hydrothermal syntheses to study the S-1 covering evolution were evaluated at different times: 10 min, 1 hr, 24 hrs and 96 hrs, respectively at 190°C. The diffractograms of the resultant solids are shown in **Figure 5.21**.

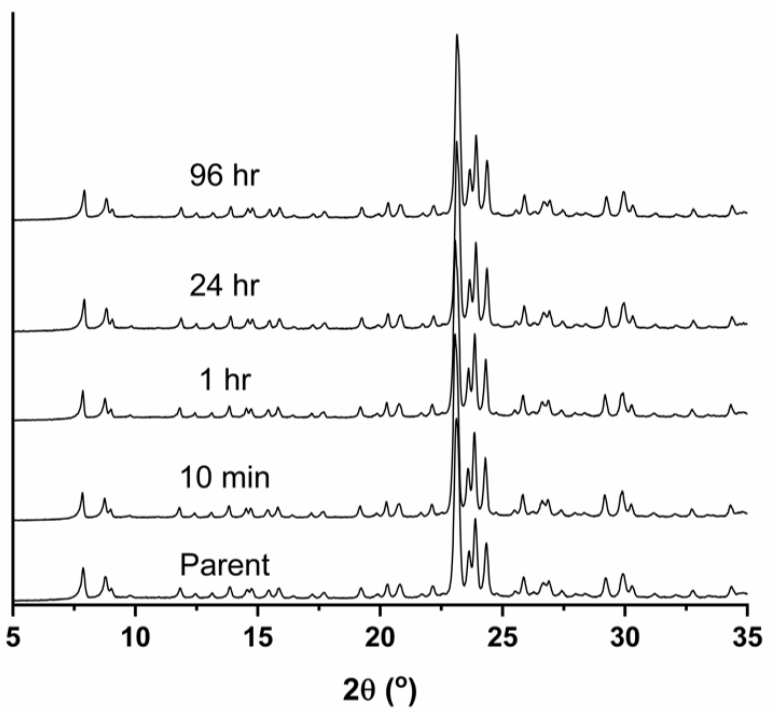

Figure 5.21. PXRD patterns of the µS-1@S-1 materials prepared following hydrothermal synthesis at different times: 10 min, 1 hr, 24 hr and 96 hr, respectively.

The persistence of the peaks confirms that the material does not suffer undesired amorphization at any stage when exposed to alkaline environments during the hydrothermal synthesis. These materials were also characterized by SEM microscopy to evaluate their morphology and particle size distribution (see **Figure 5.22**).

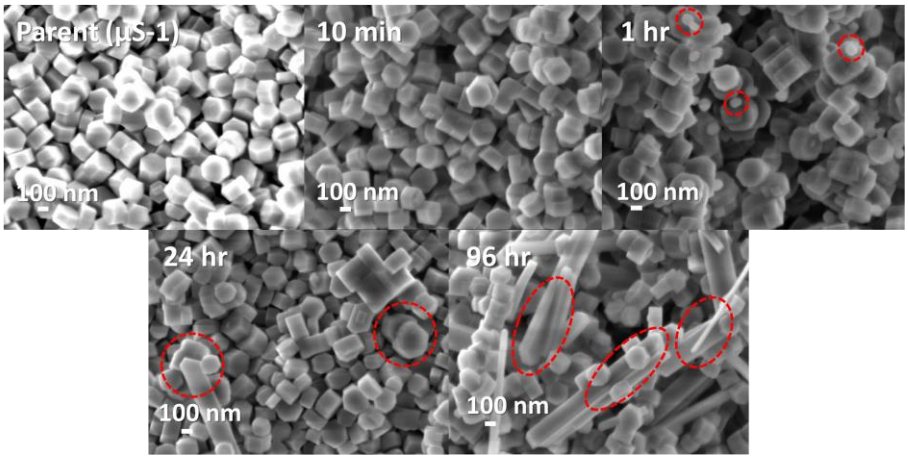

Figure 5.22. SEM images of µS-1 after being covered with S-1 by conventional hydrothermal synthesis at different times at 190°C.

Contrary to the core-shell covering achieved via ultrafast synthesis, the conventional synthesis does not yield any discernible growth of the crystalline particles after 10 min. This fact can be explained by the induction period required to reach the desired temperature, as previously showed in **Figure 5.12**. After 1 hour (**Figure 5.22, 1 hr**), the appearance of small crystalline particles, significantly smaller than the original seed particles, began to become noticeable. The formation of these additional particles suggests the occurrence of secondary crystallization issues as new crystalline nuclei rather than promoting the homogenous deposition of silica species on the surfaces of pre-existing crystalline particles, to obtain the core-shell zeolite composites.

As the synthesis time progresses (**Figure 5.22**, after 24 hrs and 96hrs, respectively), an uncontrolled growth of crystals was observed with very large dimensions, elongated mainly in one direction. This behaviour strongly indicates that employing conventional hydrothermal synthesis for producing

zeolite-type core-shell materials, at least under the selected conditions, present significant challenges to avoid secondary crystallization and/or undesired crystal growth.

In contrast, ultrafast synthesis technique, by maximizing the heating rate and ensuring more uniform temperature distribution due to the higher surface to volume ratio of the reactor, promotes the formation of homogeneous surface coatings on already existing particles. Consequently, this approach yields zeolitic core-shell composites with a remarkable particle size distribution uniformly.

5.6. COVERING OF KPd-CONTAINING ZEOLITES WITH A HYDROPHOBIC SHELL OF CRYSTALLINE ZEOLITE USING ULTRAFAST SYNTHESIS METHODOLOGY.

After studying the influence of the water content in the gel on the formation of the Silicalite-1 shell on cores with different sizes, the nanosized Pd-containing S-1 reported previously (**KPd-nS-1**) has been coated here by the ultrafast method. The idea behind this strategy is to provide a shell that could enhance the Pd nanoparticles stability against the metal sintering surface phenomena suffered and described in the previous sections.

For this purpose, the coating was carried out using the ultrafast crystallization methodology with the following composition:

$$1\ SiO_2 : 4\ EtOH : 0.3\ TPAOH : 40\ H_2O$$

keeping the SiO_2 shell/SiO_2 core mass ratio ~ 1.

As described previously in this Chapter, the coating was carried out at 190°C for 10 min. X-Ray diffraction shows the presence of the characteristic peaks of MFI crystallin structure (see **Figure 5.23**).

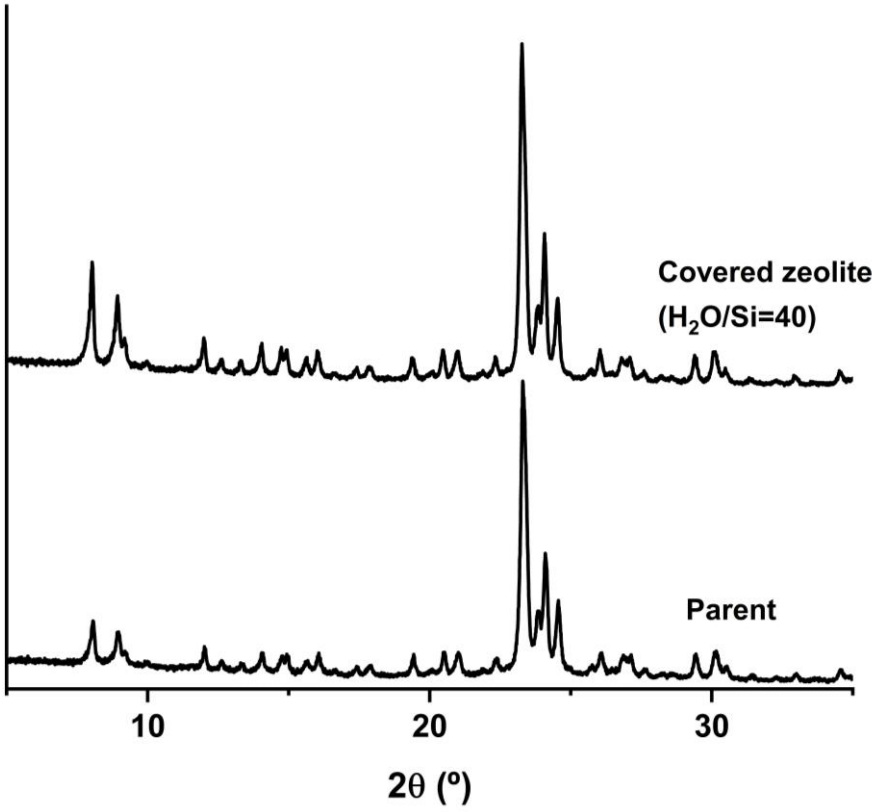

Figure 5.23. PXRD patterns of KPd-containing nanosized Silicalite-1 in the as-prepared form (parent) and after performing the covering with the ultrafast-synthesis methodology.

The variation of the chemical composition that must occur in the core-shell composite was measured to quantify the increase of the overall silica because of the shell formation. The composition of the materials, determined by ICP, is presented below in **Table 5.12.**

Table 5.12. Chemical composition of the parent zeolite (KPd-nS-1) and the covered zeolite (KPd-nS-1@S-1).

Sample	*ICP K(wt%)*	*ICP Pd(wt%)*
KPd-nS-1	0.62	0.22
KPd-nS-1@S-1	0.36	0.12

The decrease of the proportion of the different heteroatoms is noticeable after the coverage, a sign that the amount of Silicon increased due to the covering process. In order to assure that, the calcined and reduced samples were further characterized by High Annular-Dark Field Transmission Electronic Microscopy to verify that the metal particles hosted within the zeolitic matrix of the core material remained confined within the "core" after the obtention of the S-1 shell coating by ultrafast-synthesis technique. The corresponding image is shown in **Figure 5.24**.

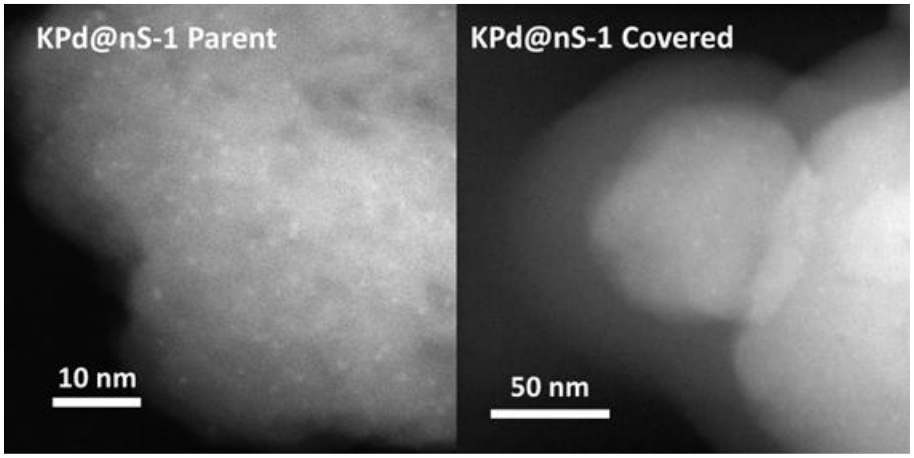

Figure 5.24. High Annular-Dark Field STEM images of the reduced KPd-nS-1 zeolites, both parent and covered with ultrafast-synthesis technique.

The transmission electron microscopy images obtained for both types of materials reveal a noticeable contrast in the distribution of metallic nanoparticles. In the parent material (KPd-nS-1), a homogenous dispersion of metal nanoparticles is observed within the crystal agglomerates. In contrast, in the core-shell material, a concentrated region of metallic particles is clearly evident in the core area, exhibiting the highest contrast, as shown in **Figure 5.24**. A less dense region of uniform thickness, surrounds this core, corresponding to the shell layer, where total absence of metal nanoparticles is observed.

Future research includes the characterization of the textural properties of these materials to unravel if the diffusive properties and accessibility of the porous channels in the parent zeolite were preserved after adding the shell layer. Deterioration of the diffusive properties could happen due to the growth of the new crystalline phase with planes oriented in different directions from those of the core structure or from the collapse of the interface between the core and the shell, potentially caused by surface dissolution of the crystalline particles under alkaline conditions at higher temperatures.

5.7. CONCLUSIONS.

In the first part of this chapter, S-1 zeolites with controlled crystalline nanoparticle sizes were successfully prepared by regulating the synthesis temperature, enabling a targeted modification of the final textural and diffusive properties of the obtained materials. This rational approach was applied to synthesize S-1 with enhanced diffusivity and encapsulated Pd

nanoparticles via direct synthesis. These properties were systematically evaluated in the semi-hydrogenation of the bulky phenylacetylene molecule.

Zeolitic materials with smaller particle sizes exhibited significantly improved catalytic performance, demonstrating higher activity and enhanced selectivity toward styrene formation compared to their larger counterparts. The results remark the critical role of rational catalyst design, particularly in tailoring textural and diffusive properties to achieve maximum conversion and selectivity values for the target reaction.

In the second part of this chapter, ultrafast synthesis methodology has been introduced as a potential methodology for hydrothermal zeolite synthesis. This approach significantly reduces the crystallization time required by maximizing the heat transfer surface area-to-volume ratio, allowing to produce uniform crystalline zeolite coatings that serve as a protective layer of the core zeolites in the resulting hybrid systems. A careful screening study was conducted to evaluate the effects of the synthesis gel concentration (expressed as the H_2O/Si ratio) and the size of the seed zeolite crystals used as crystallization centres, on the final dimensions of the core-shell materials obtained. The outcomes revealed that more concentrated media resulted in higher crystallization yields and larger final particle sizes compared to those obtained under diluted conditions.

Following this preliminary investigation, Pd-containing Silicalite-1 catalyst, previously described, was coated with a hydrophobic Silicalite-1 layer. The resulting core-shell zeolite-type composite was preliminarily characterized, demonstrating the retention of the metal nanoparticles within the core. Future research will focus on assessing the preservation of the materials'

textural properties and its effectiveness in enhancing catalyst lifetime under severe reaction conditions, findings that may reinforce the promising utility of this new coating approach to enhance catalyst deactivation resistance and improving overall performance in demanding applications like semihydrogenation of bulky molecules in liquid phase.

5.8. REFERENCES.

(1) Zhu, D.; Wang, L.; Fan, D.; Yan, N.; Huang, S.; Xu, S.; Guo, P.; Yang, M.; Zhang, J.; Tian, P.; Liu, Z. A Bottom-Up Strategy for the Synthesis of Highly Siliceous Faujasite-Type Zeolite. Adv. Mater. 2020, 32 (26), 1–7. https://doi.org/10.1002/adma.202000272.

(2) Valtchev, V.; Majano, G.; Mintova, S.; Pérez-Ramírez, J. Tailored Crystalline Microporous Materials by Post-Synthesis Modification. Chem. Soc. Rev. 2013, 42 (1), 263–290. https://doi.org/10.1039/c2cs35196j.

(3) Ren, N.; Bronić, J.; Subotić, B.; Song, Y. M.; Lv, X. C.; Tang, Y. Controllable and SDA-Free Synthesis of Sub-Micrometer Sized Zeolite ZSM-5. Part 2: Influence of Sodium Ions and Ageing of the Reaction Mixture on the Chemical Composition, Crystallinity and Particulate Properties of the Products. Micropor. Mesopor. Mater. 2012, 147 (1), 229–241. https://doi.org/10.1016/J.MICROMESO.2011.06.022.

(4) Chauhan, N. L.; Das, J.; Jasra, R. V.; Parikh, P. A.; Murthy, Z. V. P. Synthesis of Small-Sized ZSM-5 Zeolites Employing Mixed Structure Directing Agents. Mater. Lett. 2012, 74, 115–117. https://doi.org/10.1016/J.MATLET.2012.01.094.

(5) Petushkov, A.; Yoon, S.; Larsen, S. C. Synthesis of Hierarchical Nanocrystalline ZSM-5 with Controlled Particle Size and Mesoporosity. Micropor. Mesopor. Mater. 2011, 137 (1–3), 92–100. https://doi.org/10.1016/J.MICROMESO.2010.09.001.

(6) Alipour, S. M.; Halladj, R.; Askari, S. Effects of the Different Synthetic Parameters on the Crystallinity and Crystal Size of Nanosized ZSM-5 Zeolite. Rev. Chem. Eng. 2014, 30 (3), 289–322. https://doi.org/10.1515/revce-2014-0008.

(7) Ye, G.; Sun, Y.; Guo, Z.; Zhu, K.; Liu, H.; Zhou, X.; Coppens, M. O. Effects of Zeolite Particle Size and Internal Grain Boundaries on Pt/Beta Catalyzed Isomerization of n-Pentane. J. Catal. 2018, 360, 152–159. https://doi.org/10.1016/j.jcat.2018.01.033.

(8) Jang, H. G.; Min, H. K.; Lee, J. K.; Hong, S. B.; Seo, G. SAPO-34 and ZSM-5 Nanocrystals' Size Effects on Their Catalysis of Methanol-to-Olefin Reactions. Appl. Catal. A 2012, 437–438, 120–130. https://doi.org/10.1016/J.APCATA.2012.06.023.

(9) Itani, L.; Bozhilov, K. N.; Clet, G.; Delmotte, L.; Valtchev, V. Factors That Control Zeolite L Crystal Size. Chem. Eur. J 2011, 17 (7), 2199–2210. https://doi.org/10.1002/CHEM.201002622.

(10) Uzcátegui, D.; González, G. Study of the Kinetics of Crystallization of Zeolite MEL. Catal. Today 2005, 107–108, 901–905. https://doi.org/10.1016/J.CATTOD.2005.07.041.

(11) Mohamed, R. M.; Aly, H. M.; El-Shahat, M. F.; Ibrahim, I. A. Effect of the Silica Sources on the Crystallinity of Nanosized ZSM-5 Zeolite. Micropor.

Mesopor. Mater. 2005, 79 (1–3), 7–12. https://doi.org/10.1016/J.MICROMESO.2004.10.031.

(12) Pavlov, V. S.; Bruter, D. V.; Konnov, S. V.; Ivanova, I. I. Effect of Silica Source on Zeolite MFI Crystallization in Fluoride Media and Its Physicochemical and Catalytic Properties. Micropor. Mesopor. Mater 2022, 341, 112088. https://doi.org/10.1016/J.MICROMESO.2022.112088.

(13) Hu, S.; Song, G.; Xue, D.; Li, F. Influence of Alkalinity on the Synthesis of Hierarchical LTA Zeolite by Using Bridged Polysilsesquioxane. RSC Adv 2019, 9 (5), 2551–2558. https://doi.org/10.1039/C8RA08952C.

(14) Liu, L.; Du, T.; Li, G.; Yang, F.; Che, S. Using One Waste to Tackle Another: Preparation of a CO2 Capture Material Zeolite X from Laterite Residue and Bauxite. J. Hazard. Mater. 2014, 278, 551–558. https://doi.org/10.1016/J.JHAZMAT.2014.06.041.

(15) Chen, J.; Wiley, J. Chemistry of Zeolites and Related Porous Materials: Synthesis and Structure, First Edition.; John Wiley & Sons, Ed.; Wiley-Interscience, 2007. https://doi.org/10.1002/9780470822371.

(16) Martín, N.; Moliner, M.; Corma, A. High Yield Synthesis of High-Silica Chabazite by Combining the Role of Zeolite Precursors and Tetraethylammonium: SCR of NOx. Chem. Comm. 2015, 51 (49), 9965–9968. https://doi.org/10.1039/C5CC02670A.

(17) Gallego, E. M.; Li, C.; Paris, C.; Martín, N.; Martínez-Triguero, J.; Boronat, M.; Moliner, M.; Corma, A. Making Nanosized CHA Zeolites with Controlled Al Distribution for Optimizing Methanol-to-Olefin Performance.

Chem. Eur. J 2018, 24 (55), 14631–14635. https://doi.org/10.1002/CHEM.201803637.

(18) Van Grieken, R.; Sotelo, J. L.; Menéndez, J. M.; Melero, J. A. Anomalous Crystallization Mechanism in the Synthesis of Nanocrystalline ZSM-5. Micropor. Mesopor. Mater. 2000, 39 (1–2), 135–147. https://doi.org/10.1016/S1387-1811(00)00190-6.

(19) Chen, D.; Jiang, Z.; Jia, Y.; Wang, X.; Deng, W.; Chaianansutcharit, S.; Zhou, A.; Guo, L. Silicalite-1 Zeolites for Toluene Sorption: Effects of the Particle Size and Intracrystalline Mesopores. Micropor. Mesopor. Mater. 2023, 356, 112596. https://doi.org/10.1016/J.MICROMESO.2023.112596.

(20) Nikolakis, V.; Vlacho, D. G.; Tsapatsis, M. Modeling of Zeolite Crystallization: The Role of Gel Microstructure. Micropor. Mesopor. Mater. 1998, 21 (4–6), 337–346. https://doi.org/10.1016/S1387-1811(98)00017-1.

(21) Wakihara, T.; Okubo, T. Crystal Growth Behavior of Zeolites Elucidated by Atomic Force Microscopy. J. Chem. Eng. Jpn 2004, 37 (5), 669–674. https://doi.org/10.1252/jcej.37.669.

(22) Yu, H.; Cao, Y.; Liu, Y.; Fan, H.; Yu, X. Solid State NMR Studies of Silicalite-1 Obtained under the Non-Classic Growth Pathways. J. Alloys Compd. 2018, 747, 465–470. https://doi.org/10.1016/J.JALLCOM.2018.02.315.

(23) Zhan, B. Z.; White, M. A.; Lumsden, M.; Mueller-Neuhaus, J.; Robertson, K. N.; Cameron, T. S.; Gharghouri, M. Control of Particle Size and Surface Properties of Crystals of NaX Zeolite. Chem. Mater. 2002, 14 (9), 3636–3642. https://doi.org/10.1021/cm011635f.

(24) Kim, G. J.; Ahn, W. S. Synthesis and Characterization of Iron-Modified ZSM-5. Appl. Catal. 1991, No. 71, 55–68. https://doi.org/10.1016/0166-9834(91)85005-G

(25) Zhang, X.; Tang, D.; Zhang, M.; Yang, R. Synthesis of NaX Zeolite: Influence of Crystallization Time, Temperature and Batch Molar Ratio SiO2/Al2O3 on the Particulate Properties of Zeolite Crystals. Powder Technol. 2013, 235, 322–328. https://doi.org/10.1016/j.powtec.2012.10.046.

(26) Larlus, O.; Valtchev, V. P. Control of the Morphology of All-Silica BEA-Type Zeolite Synthesized in Basic Media. Chem. Mater. 2005, 17 (4), 881–886. https://doi.org/10.1021/cm048799r.

(27) Patuwan, S. Z.; Arshad, S. E. Important Synthesis Parameters Affecting Crystallization of Zeolite t: A Review. Materials 2021, 14 (11). https://doi.org/10.3390/ma14112890.

(28) Hu, Y.; Liu, C.; Zhang, Y.; Ren, N.; Tang, Y. Microwave-Assisted Hydrothermal Synthesis of Nanozeolites with Controllable Size. Micropor. Mesopor. Mater. 2009, 119 (1–3), 306–314. https://doi.org/10.1016/J.MICROMESO.2008.11.005.

(29) Zhang, Q.; Gao, S.; Yu, J. Metal Sites in Zeolites: Synthesis, Characterization, and Catalysis. Chem. Rev. 2023, 123 (9), 6039–6106. https://doi.org/10.1021/acs.chemrev.2c00315.

(30) Wang, H.; Wang, L.; Xiao, F. S. Metal@zeolite Hybrid Materials for Catalysis. ACS Cent. Sci. 2020, 6 (10), 1685–1697. https://doi.org/10.1021/acscentsci.0c01130.

(31) Liu, L.; Zakharov, D. N.; Arenal, R.; Concepcion, P.; Stach, E. A.; Corma, A. Evolution and Stabilization of Subnanometric Metal Species in Confined Space by in Situ TEM. Nat. Commun. 2018, 9 (1). https://doi.org/10.1038/s41467-018-03012-6.

(32) Yao, S.; Zhang, X.; Zhou, W.; Gao, R.; Xu, W.; Ye, Y.; Lin, L.; Wen, X.; Liu, P.; Chen, B.; Crumlin, E.; Guo, J.; Zuo, Z.; Li, W.; Xie, J.; Lu, L.; Kiely, C. J.; Gu, L.; Shi, C.; Rodriguez, J. A.; Ma, D. Atomic-Layered Au Clusters on α-MoC as Catalysts for the Low-Temperature Water-Gas Shift Reaction. Science (1979) 2017, 357 (6349). https://doi.org/10.1126/science.aah4321.

(33) Yan, J.; Wang, W.; Miao, L.; Wu, K.; Chen, G.; Huang, Y.; Yang, Y. Dehydrogenation of Methylcyclohexane over Pt-Sn Supported on Mg-Al Mixed Metal Oxides Derived from Layered Double Hydroxides. Int. J. Hydrogen Energy. 2018, 43 (19), 9343–9352. https://doi.org/10.1016/j.ijhydene.2018.04.003.

(34) Lee, S.; Lee, J.; Kim, T.; Han, G.; Lee, J.; Lee, K.; Bae, J. Pt/CeO2 Catalyst Synthesized by Combustion Method for Dehydrogenation of Perhydro-Dibenzyltoluene as Liquid Organic Hydrogen Carrier: Effect of Pore Size and Metal Dispersion. Int. J. Hydrogen Energy. 2021, 46 (7), 5520–5529. https://doi.org/10.1016/J.IJHYDENE.2020.11.038.

(35) Chan, C. H.; Lee, S. Y.; Han, S. S. Origin of Enhanced Toluene Hydrogenation by Pt–Ru Catalysts for an Efficient Liquid Organic Hydrogen Carrier. Int. J. Hydrogen Energy. 2023, 48 (86), 33590–33598. https://doi.org/10.1016/J.IJHYDENE.2023.05.118.

(36) Zhang, Z.; Liu, G.; Ding, L.; Hu, M.; Gu, J.; Xu, W.; Xiao, Q. Promotion Effect of the X-Zeolite Host on Encapsulated Platinum Clusters for Selective

Hydrogenation of Phenylacetylene to Styrene. Inorg. Chem. 2021, 60 (24), 19120–19127. https://doi.org/10.1021/ACS.INORGCHEM.1C02917.

(37) Liu, H.; Li, J.; Liang, X.; Ren, H.; Yin, H.; Wang, L.; Yang, D.; Wang, D.; Li, Y. Encapsulation of Pd Single-Atom Sites in Zeolite for Highly Efficient Semihydrogenation of Alkynes. J. Am. Chem. Soc. 2024, 146 (34), 24033–24041. https://doi.org/10.1021/JACS.4C07674.

(38) Domínguez-Domínguez, S.; Berenguer-Murcia, Á.; Linares-Solano, Á.; Cazorla-Amorós, D. Inorganic Materials as Supports for Palladium Nanoparticles: Application in the Semi-Hydrogenation of Phenylacetylene. J. Catal. 2008, 257 (1), 87–95. https://doi.org/10.1016/J.JCAT.2008.04.008.

(39) Louis, B.; Vicente, A.; Fernandez, C.; Valtchev, V. Crystal Size-Acid Sites Relationship Study of Nano- and Micrometer-Sized Zeolite Crystals. J. Phys. Chem. C 2011, 115 (38), 18603–18610. https://doi.org/10.1021/jp204234d.

(40) Ding, L.; Zheng, Y.; Hong, Y.; Ring, Z. Effect of Particle Size on the Hydrothermal Stability of Zeolite Beta. Micropor. Mesopor. Mater. 2007, 101 (3), 432–439. https://doi.org/10.1016/J.MICROMESO.2006.12.008.

(41) Larsen, S. C. Nanocrystalline Zeolites and Zeolite Structures: Synthesis, Characterization, and Applications. J. Phys. Chem. C 2007, 111 (50), 18464–18474. https://doi.org/10.1021/jp074980m.

(42) Li, Q.; Yang, S.; Navrotsky, A. Energetics of a Nanophase Zeolite Independent of Particle Size. Micropor. Mesopor. Mater. 2003, 65 (2–3), 137–143. https://doi.org/10.1016/S1387-1811(03)00480-3.

(43) Liu, L.; Lopez-Haro, M.; Lopes, C. W.; Li, C.; Concepcion, P.; Simonelli, L.; Calvino, J. J.; Corma, A. Regioselective Generation and Reactivity Control

of Subnanometric Platinum Clusters in Zeolites for High-Temperature Catalysis. Nat. Mat 2019, 18 (8), 866–873. https://doi.org/10.1038/s41563-019-0412-6.

(44) Gong, N.; Zhou, R.; Wan, H.; Hou, H.; Dou, X.; Gong, J.; He, P.; Liu, L. Tuning the Selectivity in the Nonoxidative Alkane Dehydrogenation Reaction by Potassium-Promoted Zeolite-Encapsulated Pt Catalysts. JACS Au 2024. https://doi.org/10.1021/jacsau.4c00949.

(45) Zhou, J.; Liu, H.; Xiong, C.; Hu, P.; Wang, H.; Wang, X.; Ji, H. Potassium-Promoted Pt–In Bimetallic Clusters Encapsulated in Silicalite-1 Zeolite for Efficient Propane Dehydrogenation. Chem. Eng. J. 2023, 455. https://doi.org/10.1016/j.cej.2022.139794.

(46) Yang, X.; Su, X.; Chen, X.; Duan, H.; Liang, B.; Liu, Q.; Liu, X.; Ren, Y.; Huang, Y.; Zhang, T. Promotion Effects of Potassium on the Activity and Selectivity of Pt/Zeolite Catalysts for Reverse Water Gas Shift Reaction. Appl. Catal. B 2017, 216, 95–105. https://doi.org/10.1016/j.apcatb.2017.05.067.

(47) Moliner, M.; Gabay, J.; Kliewer, C.; Serna, P.; Corma, A. Trapping of Metal Atoms and Metal Clusters by Chabazite under Severe Redox Stress. ACS Catal. 2018, 8 (10), 9520–9528. https://doi.org/10.1021/ACSCATAL.8B01717.

(48) Cui, L.; Chen, M.; Chen, C.; Liu, D.; Jian, Z. Systematic Studies on (Co)Polymerization of Polar Styrene Monomers with Palladium Catalysts. Macromol. 2019, 52 (19), 7197–7206. https://doi.org/10.1021/ACS.MACROMOL.9B01299.

(49) Schellenberg, J. Recent Transition Metal Catalysts for Syndiotactic Polystyrene. Prog. Pol. Sci. 2009, 34 (8), 688–718. https://doi.org/10.1016/J.PROGPOLYMSCI.2009.04.002.

(50) Wang, Z.; Wan, W.; Sun, J.; Carrillo-Cabrera, W.; Grüner, D.; Yin, X.; Qiu, S.; Zhu, G.; Zou, X. Epitaxial Growth of Core–Shell Zeolite X–A Composites. CrystEngComm 2012, 14 (6), 2204–2212. https://doi.org/10.1039/C2CE06432D.

(51) Bouizi, Y.; Rouleau, L.; Valtchev, V. P. Factors Controlling the Formation of Core-Shell Zeolite-Zeolite Composites. Chem. Mater. 2006, 18 (20), 4959–4966. https://doi.org/10.1021/cm0611744.

(52) Zou, H.; Luo, Z.; Yang, X.; Xie, Q.; Zhou, Y. Toward Emerging Applications Using Core–Shell Nanostructured Materials: A Review. J. Mater. Sci. 2022, 57 (24), 10912–10942. https://doi.org/10.1007/S10853-022-07328-Z.

(53) Li, X.; Rezaei, F.; Ludlow, D. K.; Rownaghi, A. A. Synthesis of SAPO-34@ZSM-5 and SAPO-34@Silicalite-1 Core-Shell Zeolite Composites for Ethanol Dehydration. Ind. Eng. Chem. Res 2018, 57 (5), 1446–1453. https://doi.org/10.1021/acs.iecr.7b05075.

(54) Feng, X. B.; Cao, J. P.; Yao, N. Y.; He, Z. M.; Zhang, L. Y.; Liu, T. L.; Zhao, X. Y.; Gao, X. H. Simultaneous Enhancement of Aromatic Products and Catalytic Lifetime for Catalytic Re-Forming of Lignite Pyrolysis Volatiles over a Self-Assembled Hierarchical Core-Shell ZSM-5@Silicalite-1 Zeolite. ACS Sustainable Chem. Eng. 2021, 9 (38), 12960–12969. https://doi.org/10.1021/ACSSUSCHEMENG.1C04439.

(55) Du, T.; Qu, H.; Liu, Q.; Zhong, Q.; Ma, W. Synthesis, Activity and Hydrophobicity of Fe-ZSM-5@silicalite-1 for NH3-SCR. J. Chem. Eng. 2015, 262, 1199–1207. https://doi.org/10.1016/J.CEJ.2014.09.119.

(56) Zheng, J.; Sun, X.; Du, Y.; Qin, B.; Zhang, Y.; Zhang, H.; Pan, M.; Li, R. Structural Features of Core–Shell Zeolite–Zeolite Composite and Its Performance for Methanol Conversion into Gasoline and Diesel. J. Mater. Res. 2016, 31 (15), 2302–2316. https://doi.org/10.1557/JMR.2016.208.

(57) Le, T. T.; Shilpa, K.; Lee, C.; Han, S.; Weiland, C.; Bare, S. R.; Dauenhauer, P. J.; Rimer, J. D. Core-Shell and Egg-Shell Zeolite Catalysts for Enhanced Hydrocarbon Processing. J. Catal. 2022, 405, 664–675. https://doi.org/10.1016/j.jcat.2021.11.004.

(58) Liu, Z.; Zhu, J.; Wakihara, T.; Okubo, T. Ultrafast Synthesis of Zeolites: Breakthrough, Progress and Perspective. Inorg. Chem. Front. 2019, 6 (1), 14–31. https://doi.org/10.1039/c8qi00939b.

(59) Zhu, J.; Liu, Z.; Iyoki, K.; Anand, C.; Yoshida, K.; Sasaki, Y.; Sukenaga, S.; Ando, M.; Shibata, H.; Okubo, T.; Wakihara, T. Ultrafast Synthesis of High-Silica Erionite Zeolites with Improved Hydrothermal Stability. Chem. Comm. 2017, 53 (50), 6796–6799. https://doi.org/10.1039/C7CC03166A.

(60) Liu, Z.; Wakihara, T.; Nomura, N.; Matsuo, T.; Anand, C.; Elangovan, S. P.; Yanaba, Y.; Yoshikawa, T.; Okubo, T. Ultrafast and Continuous Flow Synthesis of Silicoaluminophosphates. Chem. Mater. 2016, 28 (13), 4840–4847. https://doi.org/10.1021/acs.chemmater.6b02141.

(61) Shang, S.; Ren, L.; Liu, Q.; Zhou, A.; Zhang, J.; Liu, B.; Zhang, A.; Guo, X. Ultrafast Synthesis and Regulating Al Status of Mesoporous ZSM-48 Zeolite

via a Pretreated-Seed-Solution-Assisted Strategy. Cryst Growth Des 2023, 23 (7), 5008–5018. https://doi.org/10.1021/acs.cgd.3c00245.

(62) Liu, Z.; Wakihara, T.; Oshima, K.; Nishioka, D.; Hotta, Y.; Elangovan, S. P.; Yanaba, Y.; Yoshikawa, T.; Chaikittisilp, W.; Matsuo, T.; Takewaki, T.; Okubo, T. Widening Synthesis Bottlenecks: Realization of Ultrafast and Continuous-Flow Synthesis of High-Silica Zeolite SSZ-13 for NOx Removal. Angew. Chem. Int. Ed. 2015, 54 (19), 5683–5687. https://doi.org/10.1002/ANIE.201501160.

(63) Peng, C.; Liu, Z.; Yonezawa, Y.; Yanaba, Y.; Katada, N.; Murayama, I.; Segoshi, S.; Okubo, T.; Wakihara, T. Ultrafast Post-Synthesis Treatment to Prepare ZSM-5@Silicalite-1 as a Core-Shell Structured Zeolite Catalyst. Microporous Mesoporous Mater. 2019, 277, 197–202. https://doi.org/10.1016/j.micromeso.2018.10.036.

CHAPTER 6:

DESIGN OF BIFUNCTIONAL Ni-ZEOLITES FOR ETHYLENE OLIGOMERIZATION. CONTROLLING NICKEL SPECIATION AND ZEOLITE PROPERTIES THROUGH ONE-POT SYNTHESIS AND POST-SYNTHETIC NICKEL INCORPORATION

6.1. INTRODUCTION.

Light olefins ($C_2^=$-$C_6^=$) are unsaturated molecules with the empiric chemical formula of C_nH_{2n} presenting at least one double bond. These organic compounds are "key" building-blocks, used as intermediates to synthetize high value industrial organic molecules employed in the production of plastics, textiles, drugs or fuels[1].

The current estimated global Market of ethylene is 316.8 million Tons in 2023, a demand that is predicted to rise up to 406.5 million Tons in 2030. Traditionally, light olefins are obtained by steam cracking processes of different feedstocks, including light paraffins (C_1-C_3) and petroleum liquids (naphtha and distillate fuel oil)[2,3], with ethylene and propylene yields ranging between 23%-42% and 14%-21%, respectively depending on the feedstock.

Besides steam cracking, other on-purpose processes have been widely studied for the production of olefins, such as the direct transformation of methanol following the Methanol-to-Olefins (MTO)[4] or Methanol to Propylene (MTP)[5] routes, or the direct obtention of heavy olefins in the Methanol to Gasoline reaction (MTG) yielding a mixture of hydrocarbons with a similar composition to conventional gasoline[6].

Although there is an increasing demand for light olefins, the high energy required in the conventional routes (40 GJ/ton C_2H_4) such as steam cracking and the carbon foodprint associated (1.8-2 kg of CO_2/kg C_2H_4)[7,8], forces the development of new and more long term sustainable chemical routes to obtain them, such as photocatalytic conversion of CH_4 or their production from biomass-derived products (mainly intermediates with alcohol

functional groups)[9]. Some industrial trends or demands are summarized in **Figure 6.1**.

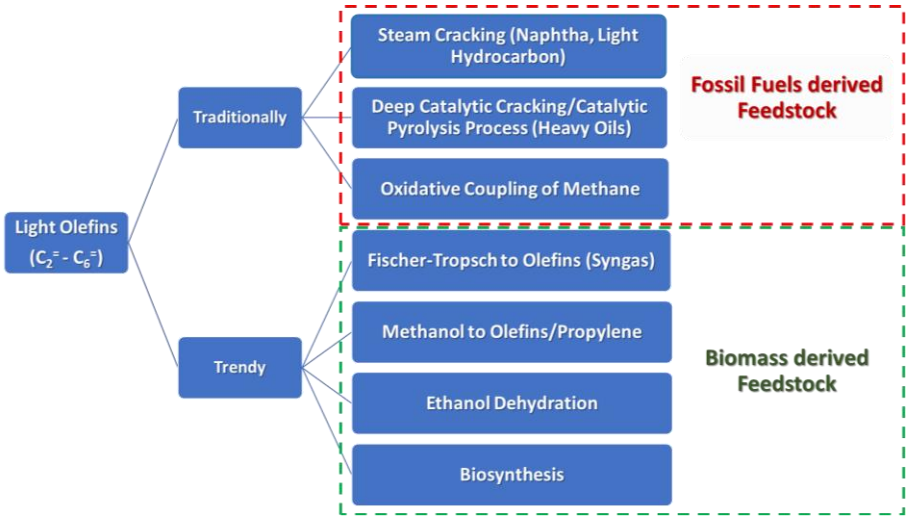

Figure 6.1. Flowchart of the different pathways to obtain olefins. Figure adapted from the info obtained from *Corma et al*[10] and *Zhao et al*[2].

The "green ethylene" processes that nowadays can be industrially scalable are mainly classified in two goups[11], **(i)** direct routes from bioalcohols and **(ii)** indirect routes, in which the biomass and syngas are transformed into methane and dimethyl ether, being converted into bioethanol through methyl acetate hydrolysis.

The next step after producing ethylene should involve an efficient transformation into higher olefins. The oligomerization of light olefins is the most relevant industrial pathway since different key products can be obtained, including liquid fuels (gasoline, diesel or the currently high demanded jet fuel), plasticizers, solvents or other intermediates easy to be functionalized, thanks to its high versatility in terms of the olefin fed and the

number of the oligomerization steps, directly influencing the final molecular weight range of the products[10,12-14]

Generally, the commercial processes for the ethylene oligomerization to obtain long-chain olefins involve the use of homogenous catalysts, such as trialkylaluminium (Chevron-Phillips)[15] and Nickel organometallic complexes (Shell Higher Olefin Process)[16]. Currently the search of novel and efficient heterogeneous catalysts is a matter of great interest for industry and academia, revealed by the numerous research works that are published every year (see **Figure 6.2**).

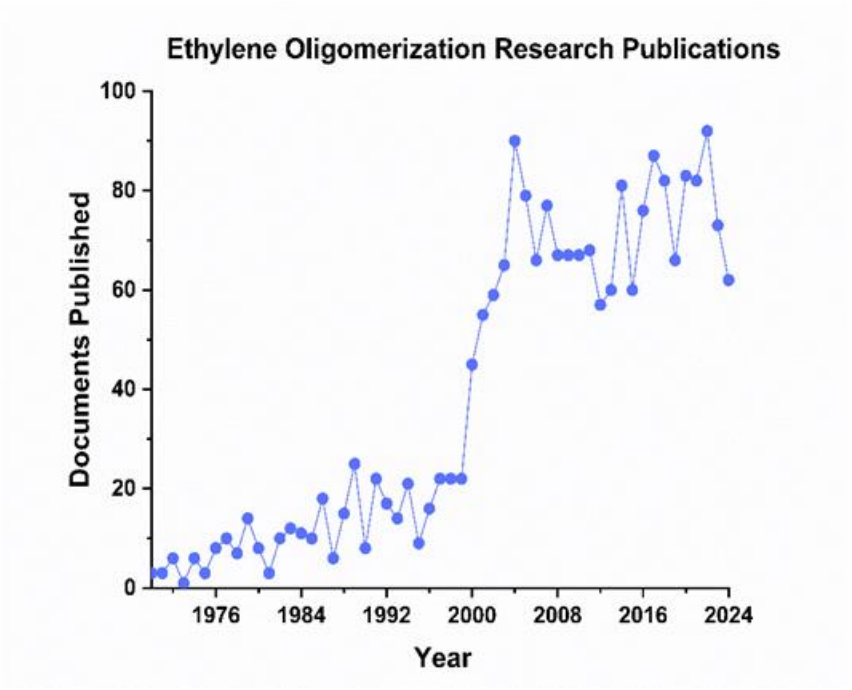

Figure 6.2. Research paper published in the last 50 years on oligomerization of light olefins. Data supplied by Scopus Database.

Considering the green chemistry principles, the use of heterogenous catalysts is a more environmentally friendly alternative due to the easy separation of

the catalyst from the reaction media, fact that facilitates its recyclability and reuse. In this sense, different solid catalysts have been employed for olefin oligomerization, including alumina, supported phosphoric acid, microporous sulphonic resins and more recently, zeolites. Zeolite catalysts are very promising heterogenous catalysts for ethylene oligomerization due to their tuneable properties, such as the Brønsted or Lewis acidity, the high surface available and the diffusional and confinement advantages that the microporous channels can offer. These properties and the shape selectivity given by the zeolite framework are well-known to facilitate the formation of products with certain characteristics[17,18], for instance the high-quality diesel fractions composed by high value linear or low-branched hydrocarbons obtained when medium pore zeolites were used or the production of highly branched bulkier products when tri-dimensional large-pore zeolites were employed[19-21], leading to fast deactivation problems as soon as the pore system is blocked by high molecular weight products. Decreasing zeolite particle size substantially reduces the diffusional pathways, allowing the molecules to escape before undesired consecutive reactions can take place and increasing significantly the zeolite resistance against deactivation[22,23].

Although solid acid catalysts show excellent catalytic behaviour for the oligomerization of olefins with more than 3 carbons, the rate of oligomerization of ethylene at mild temperatures is negligible as compared to other olefins. To circumvent this problem, different transition metals (Co, Cr, Fe, Ni) based catalysts[24,25] were proposed due to their capability to activate C=C, being Ni, the most employed transition metal considering economic cost and high activity and selectivity towards dimerization.

The reaction mechanism of ethylene dimerization in the presence of Ni-based catalyst follows the Cosse-Arlman mechanism described in the **Figure 6.3**, where two ethylene molecules interact with a Ni active site, forming a Ni-di-ethene complex that result in the formation of a 1-butene molecule (coordination step). Additionally, another ethylene molecule present in the media can coordinate to the Ni active site while the previous butene remains attached, steeping towards higher olefins (insertion step).

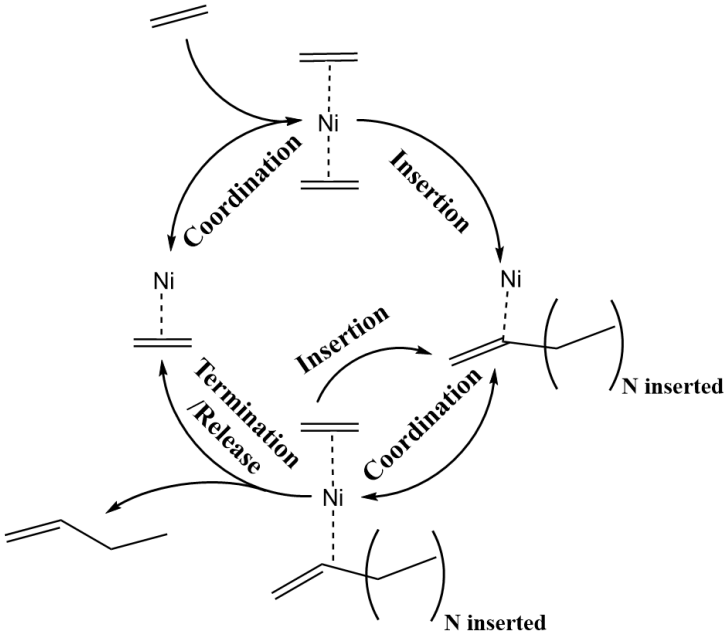

Figure 6.3. Cosse-Arlman Mechanism for Ni sites involved in the dimerization process[26].

Kinetic modelling and theoretical calculations have revealed that the acid sites present in the zeolitic support play a key role in the Cosse-Arlman mechanism[26], since they would help stabilizing the Nickel species attached as cations, counterbalancing the net negative charge of the zeolitic framework given by trivalent aluminium atoms placed in framework positions[27].

Unravelling the oxidation state of Ni under working conditions is one of the most controversial issues in the ethylene oligomerization reaction. The first approaches to this topic in the 80's claimed that the Ni atoms with zero valence were the active ones, according to results obtained by electron paramagnetic resonance techniques[28,29]. This hypothesis was rebutted later by several works that proved the role of Ni cations. Moreover, the roles of the Ni^{+} [30-35] or Ni^{2+} [36-40] were not fully clarified for years, but recent spectroscopy studies using CO as probe molecule revealed that the metallic active centres were Ni^{2+} cations.

However, it must be remarked that Ni^{2+} cations are not always connected in the same way to the zeolite host. On the one hand, Ni^{2+} in ion exchange positions attached to the acid centres, show stronger Lewis acidity and are more active in the first stages of the reaction and then deactivate fast due to the fact that longer alkyl complexes adsorbed on the Ni^{2+} are no able to be detached from the Ni^{2+} active site. On the other hand, Ni^{2+} species also can be grafted to silanols with milder acidity[41].

Although the Cosse-Arlman mechanism has been widely associated with Nickel (II) complexes for the ethylene dimerization, Moussa and co-workers recently proposed an alternative mechanism for Beta zeolite based on the Ni^{2+} grafted to silanol groups. (**Figure 6.4**). This proposal relies on the *in situ* FTIR spectroscopy and kinetics modelling and supports that the ethylene molecule coordinates with Ni^{2+} site via π-coordination with the subsequent formation of a Nickel ethenyl hydride intermediate[42].

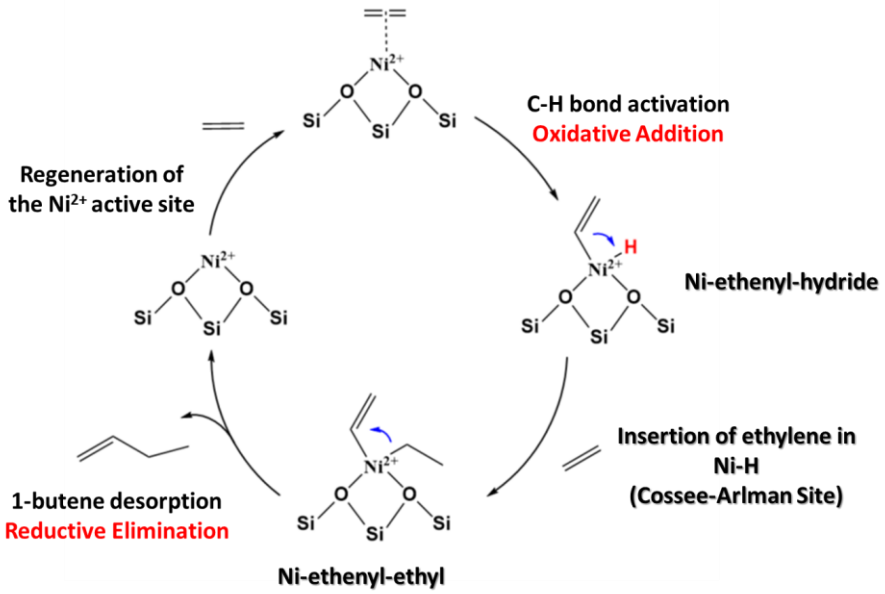

Figure 6.4. Simplified dimerization mechanism carried through Ni^{2+} active sites grafted to zeolitic silanol groups on Ni-Beta zeolites proposed by Moussa et al[42].

It is worth noting that, when the oligomerization is performed by bifunctional zeolites with both Brønsted acid centres and Ni^{2+} cationic sites, once the olefin begins to grow on the Ni active site following any of the mechanism showed to an olefin presenting more than 3 carbons, the resulting carbanion is prone to be converted through different side/consecutive acid reactions catalysed by the acid sites (**Figure 6.5**)[26], modifying the final product distribution. Thus, developing zeolite-based catalysts with controlled acidity and/or fine tunned Ni/Al ratios may modify the reaction towards light olefins or the formation of higher molecular weight hydrocarbons. Thus, the optimization of the yields towards desired oligomerization products with specific size, molecular weight and branching degree[43], could be achieved by

properly designing the zeolite-based support with the adequate pore topology and zeolite particle size.

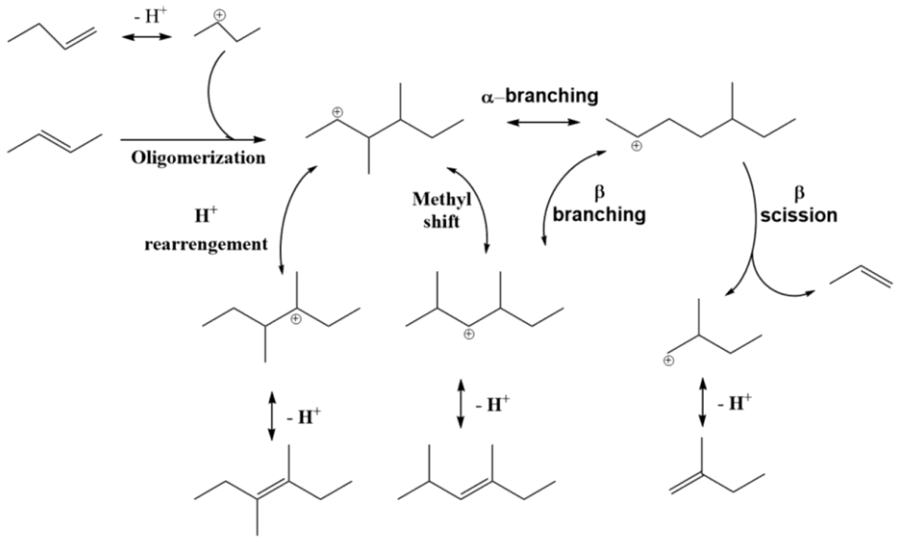

Figure 6.5. Acid catalysed reactions promoted by the zeolite acid sites for carbanions with more than 3 carbons[26].

Traditionally, Ni is incorporated in the zeolite particles via post-synthesis methodologies like ion exchange or impregnation procedures[40,44-46]. In addition, post-synthetic heterogenization of well-defined Ni-complexes on different zeolites with different pore topologies, as zeolite Y (FAU)[47], ZSM-5 (MFI)[48], Beta (BEA)[49] or ITQ-2 (delaminated MWW)[50] has been described, showing adequate catalytic behaviour for the ethylene dimerization reaction. However, incorporation of Ni species via one-pot synthesis strategies in high silica zeolites, their characterization and their catalytic evaluation for the ethylene oligomerization reaction has not been studied so far, even though, several one-pot metal approaches to improve metal dispersion and metal

stability within microporous materials have been developed in the last years [51-53].

In this chapter, a rational design of different Ni-containing zeolitic materials following diverse synthesis strategies is presented. Two different crystalline structures (MFI and BEA) with two crystal particle sizes (from micron- to nano-sized particles) and variable chemical composition to obtain different acidities (Si/Al molar ratios from 10 to 40) are selected where Ni will be incorporated by different methods. On the one hand, Ni species will be added by the classical post-synthetic approaches and, on the other hand, the Ni species will be added by one-pot synthesis approaches employing N-ligand molecules. All the materials will be further characterized and tested for the ethylene oligomerization reaction under low[54] and high pressure conditions[55].

6.2. SYNTHESIS AND CHARACTERIZATION OF THE NICKEL CONTAINING ZEOLITES

The following section details the synthesis procedures and the characterization results of selected zeolite-based catalysts. Zeolites with MFI (**Section 3.2.3.1.1**) and Beta (BEA) (**Section 3.2.3.2.1**) structure and nanosized crystals have been prepared following the recipe described elsewhere[56]. Ni structure was introduced in these materials following two methods: post-synthetically via wet impregnation (**Section 3.2.3.3.3.2**), and directly during the synthesis process by using a Ni-polyamine complex in the synthesis gel (**Sections 3.2.3.1.2 and 3.2.3.2.2.2**). Additionally, commercial materials have been selected for comparison purposes[42,46,57], where Ni species were incorporated post-synthetically, either by ion exchange in Al-

rich commercial zeolites (as detailed in **Section 3.2.3.3.3.1**) or by wet impregnation in more siliceous zeolites (**Section 3.2.3.3.2**). For clarification, a summary of the prepared catalysts is presented in **Tables 6.1 and 6.2**, along with their corresponding names.

Table 6.1. Nomenclature of the MFI-type zeolite materials**.**

Structure	***Sample Name***	***Catalyst***
MFI	MFI15-H	Commercially available MFI zeolite (CBV3024) in acidic form (Si/Al≈15)
	Ni-MFI15_ps	Commercially available MFI zeolite (CBV3024) with ≈ 1 wt% Ni added via ion exchange
	MFI25-H	Commercially available MFI zeolite (CBV5524) in acidic form (Si/Al≈25)
	Ni-MFI25_ps	Commercially available MFI zeolite (CBV5524) with ≈ 1 wt% Ni added via wetness impregnation
	MFI30-H	Commercially available MFI zeolite (CBV8020) in acidic form (Si/Al≈30)
	Ni-MFI30_ps	Commercially available MFI zeolite (CBV8020) with ≈ 1 wt% Ni added via wetness impregnation
	nMFI30-H	Nanosized MFI zeolite synthetized in acidic form (Si/Al≈30)
	Ni-nMFI30_ps	Nanosized MFI zeolite synthetized (Si/Al≈30) with ≈ 1 wt% Ni added via wetness impregnation
	Ni-MFI30_op	Nanosized MFI zeolite synthetized (Si/Al≈30) with ≈ 1 wt% Ni added via one-pot encapsulation

Table 6.2. Nomenclature of the BEA-type zeolite materials.

Structure	*Sample Name*	*Catalyst*
BEA	BEA11-H	Commercially available BEA zeolite (CP814) in acidic form (Si/Al≈11)
	Ni-BEA11_ps	Commercially available BEA zeolite (CP814) with ≈ 1 wt% Ni added via ion exchange
	nBEA15-H	Nanosized BEA zeolite synthetized in acidic form (Si/Al≈15)
	Ni-nBEA15_ps	Nanosized BEA zeolite synthetized (Si/Al≈15) with ≈ 1 wt% Ni added via wetness impregnation
	Ni-nBEA15_op	Nanosized BEA zeolite synthetized (Si/Al≈15) with ≈ 1 wt% Ni added via one-pot encapsulation
	nBEA30-H	Nanosized BEA zeolite synthetized in acidic form (Si/Al≈30)
	Ni-nBEA30_ps	Nanosized BEA zeolite synthetized (Si/Al≈30) with ≈ 1 wt% Ni added via wetness impregnation
	Ni-nBEA30_op	Nanosized BEA zeolite synthetized (Si/Al≈30) with ≈ 1 wt% Ni added via one-pot encapsulation

The resultant as-prepared MFI and BEA samples present the characteristic PXRD patterns of both structures (see PXRD patterns of MFI- and BEA-type materials in **Figure 6.6, A)** and **6.6, B)** respectively). The presence of broader but less intense peaks suggests the crystallization of these materials as nanosized crystals, as reported previously in the literature[56]. In addition, the incorporation of Ni species thought direct synthesis approaches does not alter the crystallization processes obtaining similar diffractograms when comparing the same synthesis in presence or absence of Ni-complex in the gel (see for instance nMFI30_ap and Ni-nMFI30_op in **Figure 6.6, A)**).

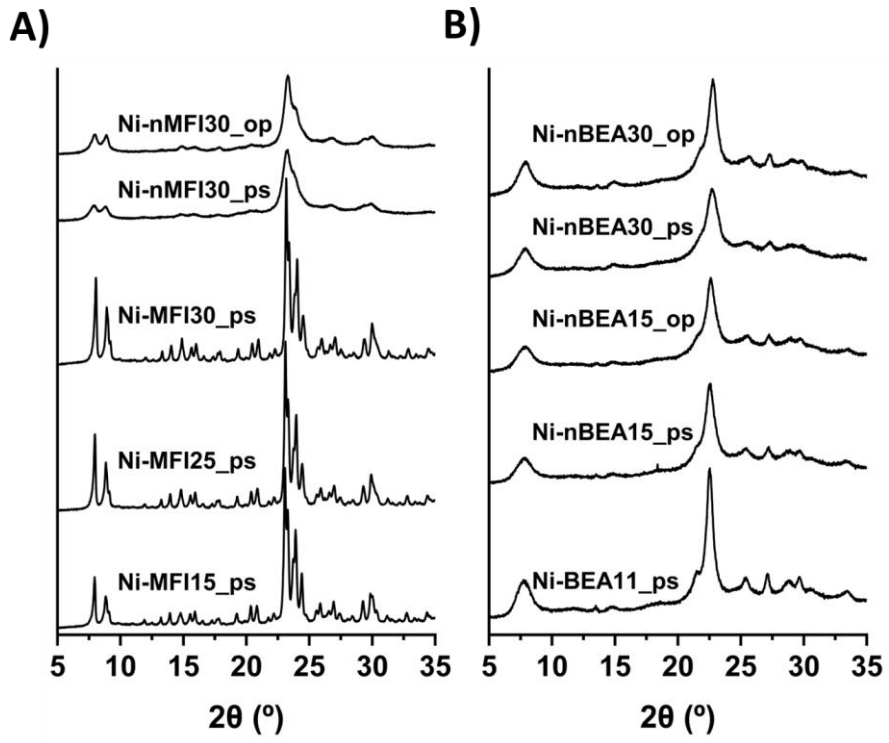

Figure 6.6. PXRD patterns of the different MFI **A)** and BEA zeolites considered in the present study **B)**.

To assess the final size of the zeolite particles, the morphological characterization has been initially conducted by FESEM (see images of MFI and BEA zeolites, in **Figure 6.7 and 6.8**, respectively). The nanosized MFI and BEA synthesized following the recent methodology described by Gallego *et al*[56] clearly shows the framework of agglomerates of small particles, approximately 10 nm in size (see nMFI30, nBEA15, and nBEA30 samples in **Figures 6.7 and 6.8**). Although FESEM provides a close estimation of the particle sizes within the agglomerates, further analysis was required using brightfield transmission electron microscopy. Images from the transmission electron microscopy confirm an average size of 10 nm for the primary

particles of these nanozeolites (see **Figure 6.9**), consistent with the previous description of Gallego *et al*[56].

In the case of the MFI-type samples, a noticeable difference in crystal size was observed between the synthesized (≈10 nm) and the commercial samples (0.1-0.2 µm) (see **Figure 6.7**). This size variation, along with differences in chemical composition, is expected to significantly impact the final catalytic performance. In fact, recent findings by our research group have demonstrated that the use of nanozeolites with sizes ranging from 10 to 20 nm as acid catalysts in the oligomerization of larger olefins, such as 1-pentene, significantly enhances the resistance to deactivation and increases the yield of liquid products within the gasoline and diesel range[58,59].

In contrast, for the BEA-type zeolites, the BEA11 sample also exhibits a relatively small crystal particle size (≈25-30 nm) closely resembling that of the synthesized nMFI30, nBEA15 and nBEA30 samples (10 nm) (see **Figure 6.8** and **Figure 6.9)**, but still larger. There are no significant differences between the sizes of the nanozeolites crystallites synthesized without Ni (nBEA15 and nBEA30, see **Figure 6.8**) and with Ni (Ni-nBEA15_op and Ni-nBEA30_op, see **Figure 6.8** and **Figure 6.9**) in good agreement with their similar PXRD patterns (see **Figure 6.6, B**).

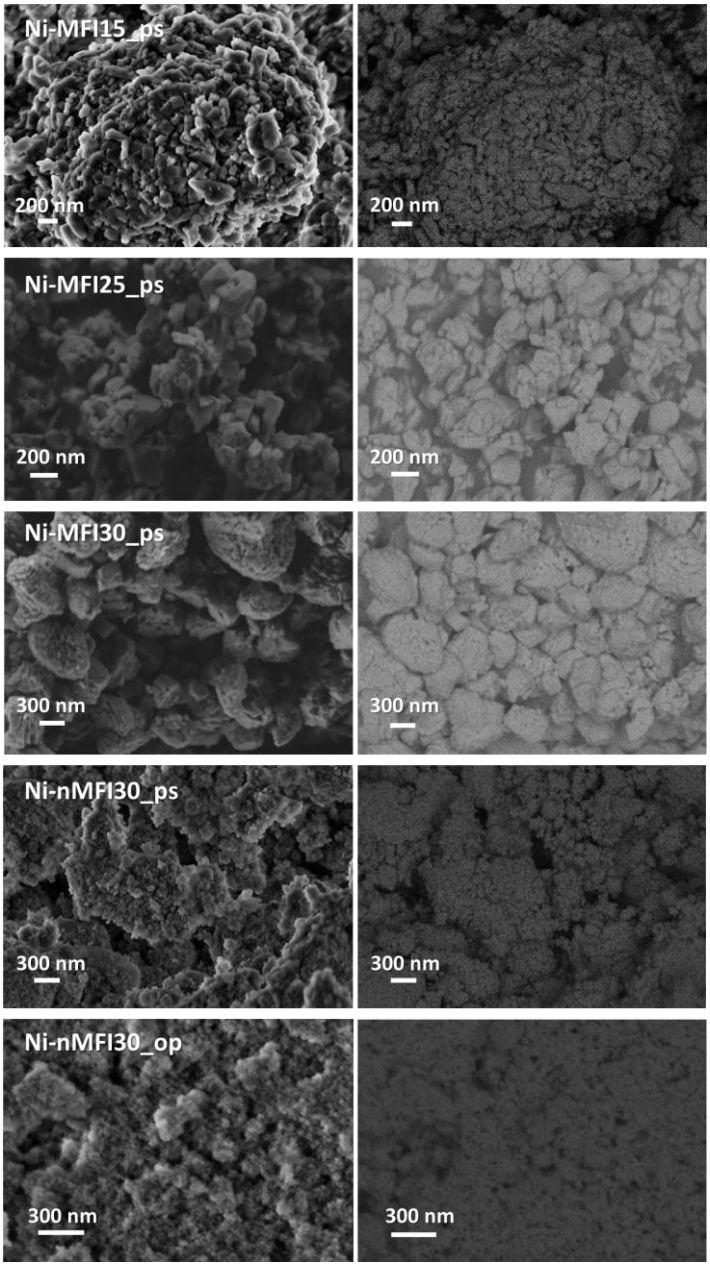

Figure 6.7. FESEM images for the MFI-type materials. Left column images are taken in bright field to estimate the crystal zeolite size. Right column is the dark field FESEM images taken to assure the absence of agglomerated Ni species on the zeolite crystal surface.

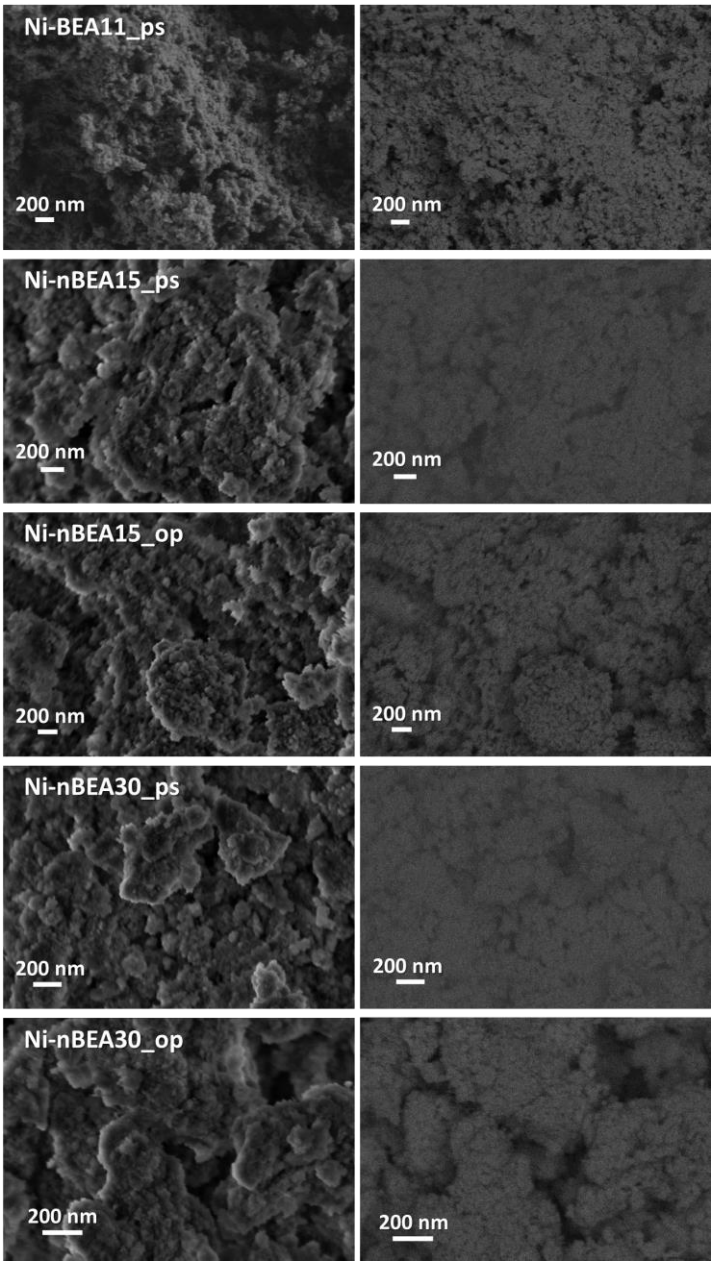

Figure 6.8. FESEM images for the BEA-type materials. Left column images are taken in bright field to estimate the crystal zeolite size. Right column images are the dark field FESEM images taken to assure the absence of agglomerated Ni species on the zeolite crystal surface.

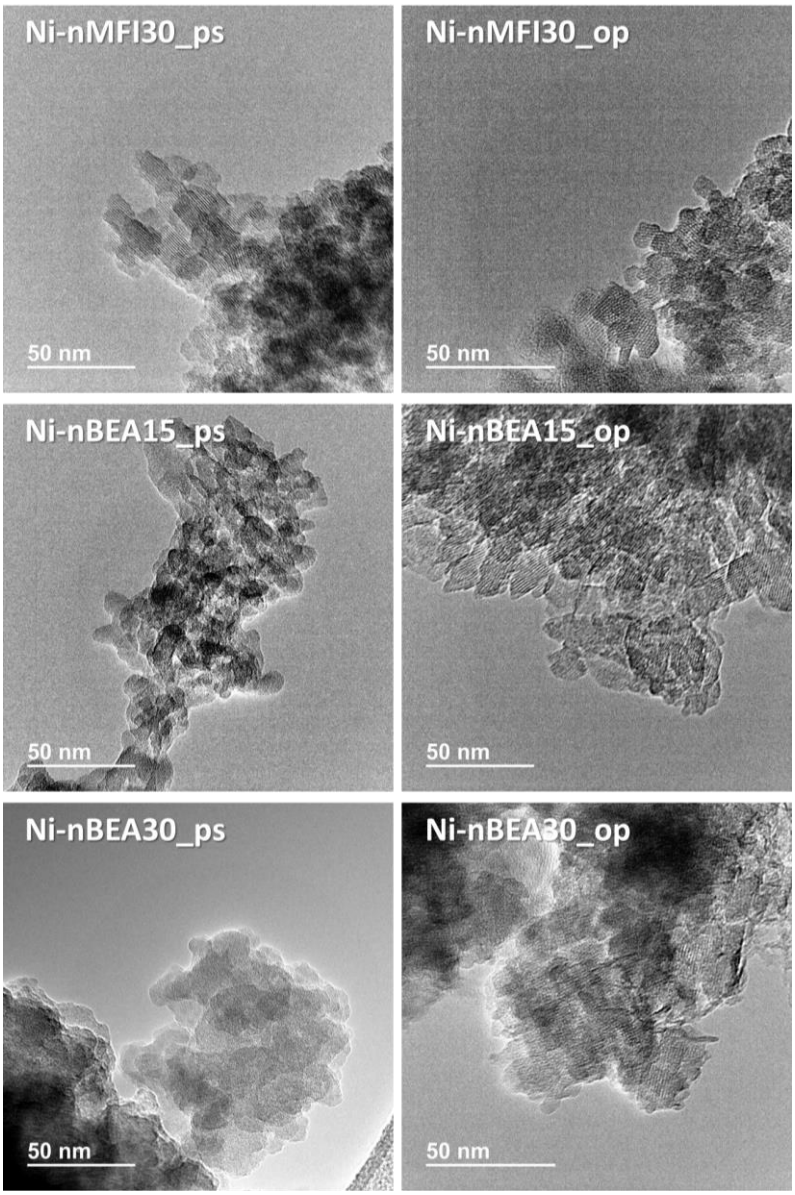

Figure 6.9. Bright Field Transmission Electronic Microscopy Images of the synthesized nanosized MFI and BEA zeolites.

The average particle sizes for each nanosized material has been calculated using at least 60 different particle measurements (see **Table 6.3**).

Table 6.3. Crystal particle size statistical summary

Sample	*Av. Part. Size (nm)*	*Std. dev (nm)*
Ni-nMFI30_ps	8.3	2.1
Ni-nMFI30_op	8.6	1.5
Ni-nBEA15_ps	8.8	2.1
Ni-nBEA15_op	10.1	3.0
Ni-nBEA30_ps	8.1	2.1
Ni-nBEA30_op	9.2	2.6

The ICP analysis permitted the estimation of the chemical composition of the different Ni-containing materials synthesized either by one-pot or post-synthetic approaches. The results indicate that the Si/Al ratios in the synthesized solids were similar to the target compositions in the synthesis gels (see nMFI30, nBEA15, and nBEA30 in **Table 6.4** and **Chapter 3).**

Table 6.4. Physico-chemical properties of the different Ni-containing zeolite catalyst.

Catalyst	*Si/Al*	*Ni wt%*	*BET Area (m^2/g)*	*Micropore Area (m^2/g)*	*External Surface (m^2/g)*	*Micropore Volume (cm^3/g)*
Ni-MFI15_ps	14.1	0.92	411	369	42	0.16
Ni-MFI25_ps	25.9	1.1	414	369	45	0.16
Ni-MFI30_ps	29	1.1	408	357	51	0.15
Ni-nMFI30_ps	24.3	1.1	523	280	243	0.11
Ni-nMFI30_op	28.1	1.2	528	320	208	0.13
Ni-BEA11_ps	10.8	1.1	633	441	192	0.18
Ni-nBEA15_ps	14	0.95	590	331	259	0.14
Ni-nBEA15_op	12.9	1.2	714	403	311	0.17
Ni-nBEA30_ps	22.2	1.2	668	358	310	0.15
Ni-nBEA30_op	21	1.3	744	433	311	0.18

ps: post-synthesis, **op**: one-pot

After calcining the materials in air at 580°C to remove occluded organic molecules, Ni was added via post-synthetically (ion exchange/wetness impregnation, being referred the samples with the Ni added by post-synthetic treatments as ps), exhibiting approximately 1 wt% of Ni after undergoing wet impregnation, as confirmed by ICP analysis (Ni-nMFI30_ps, Ni-nBEA15_ps, Ni-nBEA30_ps in **Table 6.4**). Similarly, the commercial materials that had undergone post-synthetic Ni addition showed a final Ni incorporation close to 1 wt% (Ni-MFI15_ps, Ni-MFI25_ps, Ni-MFI30_ps, and Ni-BEA11_ps, respectively).

According to the findings reported by Gallego *et al*[56], in the as-prepared nanoscale BEA structures with a Si/Al molar ratio of 15, the entire Al atoms were tetrahedrally coordinated. After calcining at 580°C, approximately 80% of the Al remained in framework positions. Comparing those previous results with the ^{27}Al MAS NMR spectra obtained in this study (**Figure 6.10**), the proportion of Al in extra-framework positions was found to be 26% for nBEA15-H and 19% for Ni-nBEA15_op. This suggests that the presence of Ni species in the synthesis gel partially stabilizes the zeolite structure against undesired dealumination. A plausible explanation for this stabilization is the formation of cationic Ni species during calcination, occupying then charge compensating sites, as it will be discussed more in detail later.

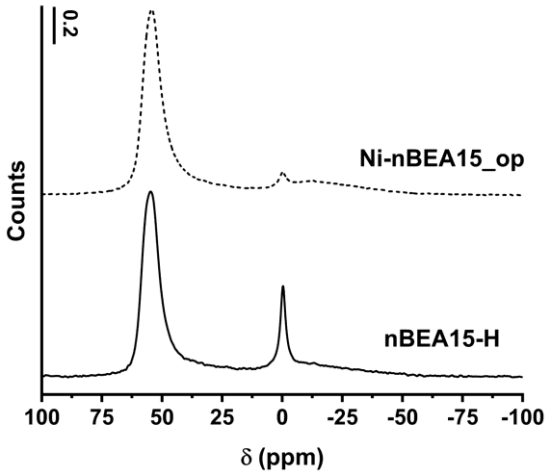

Figure 6.10. ^{27}Al MAS NMR spectra of the calcined nBEA15-H and Ni-nBEA15_op samples. Integration of the bands assigned to tetrahedrally (~59 ppm) and octahedrally coordinated Al (~0 ppm) for both samples result in 26 and 19 % of extra-framework Al for the acid and the Ni-loaded nano-Beta, respectively.

As expected, the external surface areas of the synthesized nanosized zeolites were significantly larger than those of the commercial zeolites, due to their smaller particle size (**Figures 6.7** and **6.8**). Specifically, the external surface areas for the synthesized MFI-type zeolites ranged from 200 to 250 m²/g, while those for the BEA-type nanosized zeolites ranged from 260 to 310 m²/g. In contrast, the commercial MFI zeolites (Ni-MFI15_ps, Ni-MFI25_ps, and Ni-MFI30_ps) exhibit surface areas of 40 to 50 m²/g, and the commercial Beta zeolite (Ni-BEA11_ps) has a surface area of approximately 190 m²/g.

The Brønsted and Lewis acidity of the different nickel-containing zeolites were determined using FT-IR combined with adsorption and desorption of pyridine at different temperatures. These values are summarized in **Table 6.5**, and the corresponding IR spectra in the pyridine region are shown in **Figure 6.11**.

All samples exhibit bands at 1545 and 1455 cm^{-1}, corresponding to the protonation of the basic probe molecule by the zeolite Brønsted acid sites (BAS) and the coordination of the pyridine molecule with Lewis acid sites, respectively. In commercial zeolites with Ni added post synthetically, a marked decrease of the Brønsted acid band and a corresponding increase in the Lewis acid band are observed, particularly for zeolites with lower Si/Al ratios (Ni-MFI15_ps and Ni-BEA11_ps). This trend suggests that a noticeable portion of the added Ni was incorporated as Ni^{2+} species stabilized in exchange positions, "neutralizing" the acidic sites and reducing then Brønsted acidity, compared to protonated parent zeolites[43,60].

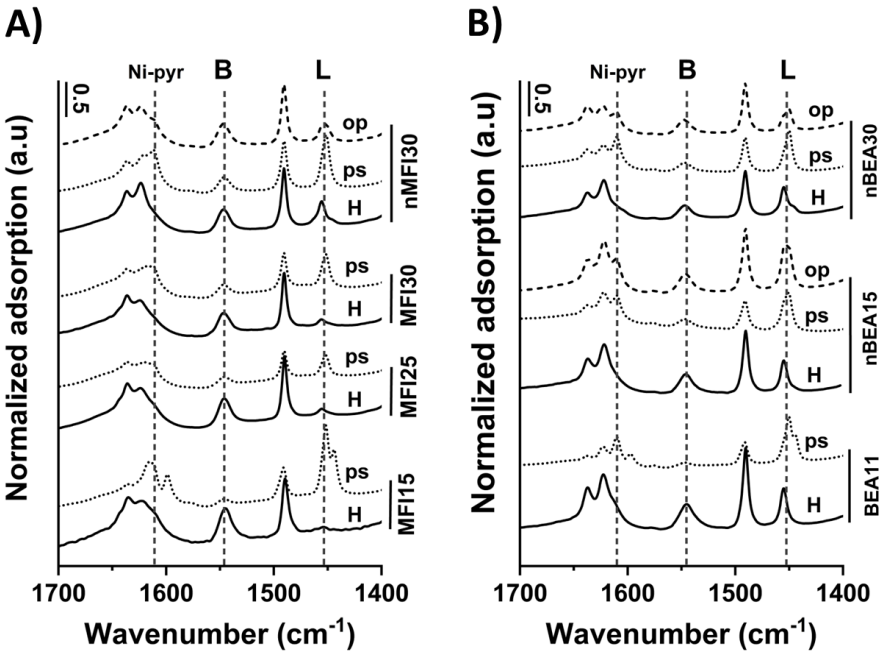

Figure 6.11. A) FTIR-pyridine spectra after the desorption treatment at 150ºC for the MFI and the **B)** BEA-type materials, including the parent zeolites in acidic form (H, solid trace), as well as the Ni-containing zeolites where Ni was incorporated either post-synthetically (ps, dot trace) or through one-pot synthesis (op, dash trace).

Table 6.5. Acidity of the different Ni-free and Ni-containing zeolites as determined by FT-IR combined with pyridine adsorption/desorption. [a] Acidities calculated as µmol of pyridine retained after desorption treatment at 150ºC. [b] Ratios of µmol of pyridine retained after desorption treatment at 350 and 150ºC.

Sample	*Brønsted acidity[a] (µmol Pyr/g cat)*	B_{350}/B_{150}[b]	*Lewis acidity[a] (µmol Pyr/g cat)*	L_{350}/L_{150}[b]
MFI15-H	548	0.7	16	1.0
Ni-MFI15_ps	104	0.4	477	0.2
MFI25-H	461	0.8	38	0.8
Ni-MFI25_ps	153	0.9	143	0.6
MFI30-H	372	0.8	38	0.6
Ni-MFI30_ps	200	0.6	208	0.3
nMFI30-H	382	0.8	133	0.6
Ni-nMFI30_ps	259	0.5	406	0.5
Ni-nMFI30_op	400	0.7	120	0.7
BEA11-H	469	0.5	269	0.8
Ni-BEA11_ps	74	0.1	366	0.5
nBEA15-H	345	0.6	227	0.8
Ni-nBEA15_ps	146	0.5	306	0.6
Ni-nBEA15_op	355	0.5	346	0.8
nBEA30-H	244	0.7	172	0.7
Ni-nBEA30_ps	169	0.4	352	0.6
Ni-nBEA30_op	272	0.5	166	0.8

In addition, all the commercial Ni-containing zeolites present a common band centred at 1610 cm^{-1}, assigned in the literature to pyridine coordinatively bonded to Ni^{2+} cations (Figure 6.11)[61]. The same bands are observed in those

nanosized materials where Ni was incorporated by wetness impregnation (Ni-nMFI30_ps, Ni-nBEA15_ps, Ni-nBEA30_ps).

Conversely, in materials with lower Al content, where Ni was incorporated through direct encapsulation (Ni-nMFI30_op, Ni-nBEA30_op), the final density of Brønsted and Lewis acid sites did not significantly decrease compared to their protonated forms. This, along with the low intensity of the 1610 cm^{-1} bands in their respective spectra (**Figure 6.11**), suggests that direct incorporation of Ni primarily leads to the formation of NiO species rather than promoting the formation of extra-framework Ni cations in charge compensation sites.

In the case of the synthesized high Al-containing nanosized Beta (Ni-nBEA15_op), an intermediate behaviour was observed. While the Brønsted acidity is similar to the Ni-free parent zeolite, the intensity of the band associated with Ni^{2+} cations is similar to that observed in the Ni-impregnated samples. This, combined with the increased Lewis acidity, suggests the coexistence of both NiO and Ni^{2+} cations. The presence of cationic Ni species is also linked to the stabilization against dealumination observed in Ni-BEA15_op, due to the presence of the Ni-EDA complex. Thus, Ni that does not form NiO species likely remains as Ni^{2+}, either grafted to silanol groups or occupying charge compensation sites, keeping its Brønsted acidity alongside its increase in Lewis acidity.

The same trend in the final Ni speciation is observed in the samples, independently from samples being MFI or Beta zeolites, only depending on the way in which Ni is incorporated. The results showed that post-synthetic incorporation of Ni favours the formation of cationic Ni^{2+} species, either in

charge-compensating positions or grafted to silanol groups. In contrast, Ni direct incorporation during synthesis predominantly leads to the formation of NiO species, regardless of the zeolite's crystalline structure.

To further investigate the Ni speciation within the materials, the samples were characterized by FTIR spectroscopy using CO as a probe molecule. The analyses were conducted both at low CO dosage, useful for identifying metallic species, and at CO saturation, which allows the identification of other zeolite species.

The first samples studied were the Ni-free commercial MFI zeolites with different Si/Al ratios (see **MFI15**, **MFI25** and **MFI30** in **Figure 6.12 CO-Low dosage**). In the protonated form, these zeolites exhibit signals at 2175 and 2138 cm^{-1}, which have been assigned in the literature to CO adsorbed on the Brønsted acid sites and to CO condensed within the zeolite pores ("liquid-like" behaviour), respectively[62]. Moreover, the commercial zeolite with lower Al content presents an additional signal at 2160 cm^{-1}, which has been identified as CO attached to silanol groups[63]. Notably, when CO is added in low dosage levels, those signals are almost totally absent in the FTIR spectra (**Figure 6.12 CO-Low dosage**), as the CO concentration is insufficient to show the Brønsted acid sites and silanol groups signals.

Following the post-synthetic incorporation of Ni, the infrared spectrum of the Al richest sample displays two specific signals located at 2204 and 2212 cm^{-1}, associated with the interaction between the CO and the Ni^{2+} in exchange position sites [41,63], whereas a band is observed at 2192 cm^{-1}, assigned to Ni^{2+} grafted to the silanol groups within the zeolite structure[41,63]. This is even more clear in the CO low dosage spectra (see **MFI15**, **MFI25** and **MFI30 in Figure**

6.12 CO-Low dosage) where only the signals of the CO interacting with the metal are displayed, concluding that the samples presenting high density of Brønsted acid sites, such as Ni-MFI15_ps, favour the incorporation of the metal incorporated as Ni^{2+} in exchange position sites. As the amount of Brønsted acid sites decreases and less ion-exchange sites are available, the Ni speciation is prone towards the formation of silanol grafted Ni^{2+} species (≈2190 cm^{-1}) and NiO nanoparticles (≈2150 cm^{-1}).

Indeed, a significant decrease of the bands associated to the Brønsted acid sites is clearly observed in **Figure 6.12** at CO-saturation levels when comparing the commercial MFI samples in their protonic form and with the Ni species added by impregnation, (see **Ni-MFI15_ps, Ni-MFI25_ps and Ni-MFI30_ps**) being these results in good agreement with the decrease of the Brønsted acid site band observed in FTIR-pyridine experiments[64], implying a decrease of the available Brønsted acid centres as result of the Ni^{2+} species incorporated in exchange positions. Regarding the nanosized MFI samples, the spectra obtained for nMFI30 in its protonated form and the one for the sample with Ni added by one-pot synthesis are quite similar at CO saturation levels (see **nMFI30_H** and **Ni-nMFI30_op** in **Figure 6.12)**). The intensity of the band at 2175 cm^{-1} in the Ni-nMFI30_op sample is slightly higher than in the parent nMFI30 spectrum. This band, typically associated with the interaction of CO with the Brønsted acid sites of the zeolite, has also been related in the literature to the presence of NiO species[63]. The intensity increase observed in the Ni-nMFI30_op spectrum supports the presence of these NiO species, a hypothesis further reinforced by the signal around 2150 cm^{-1} in the spectrum at lower CO coverage (see **Figure 6.12)**.

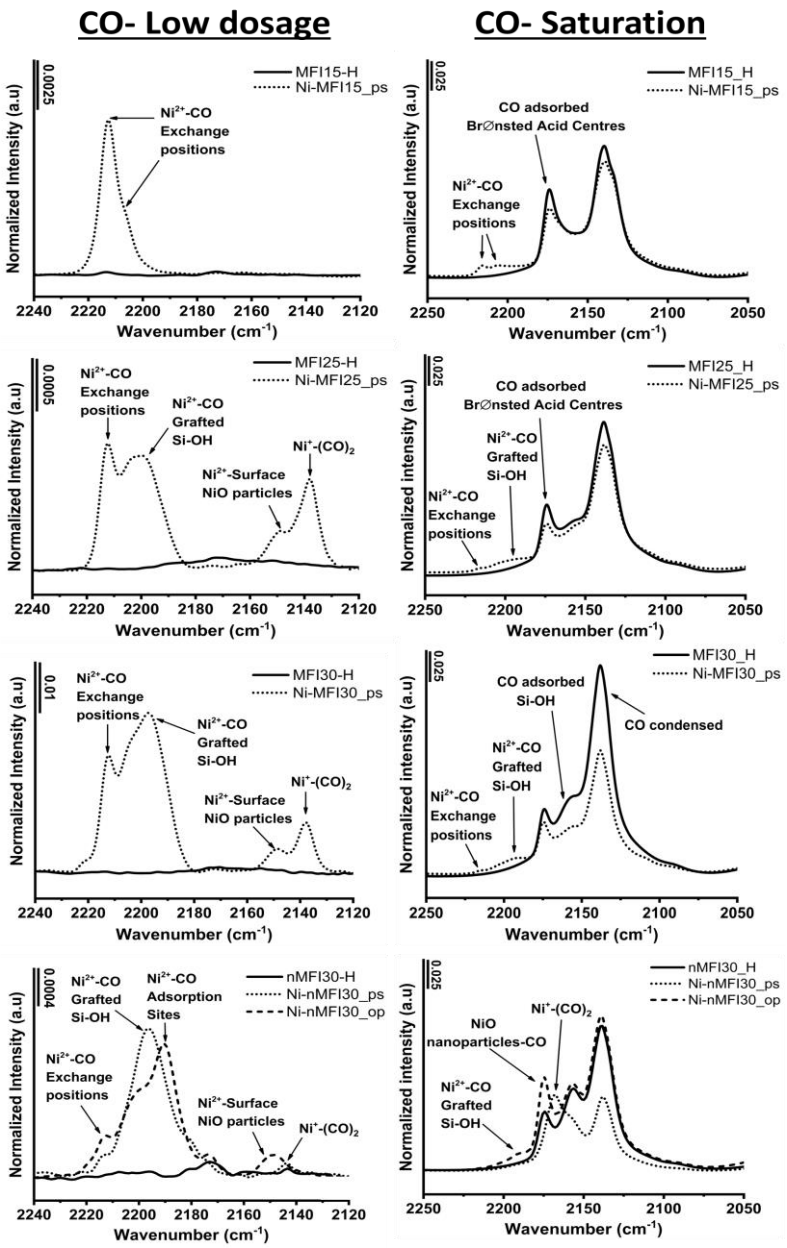

Figure 6.12. FTIR spectra using CO as probe molecule at CO low dosage adsorption (left column) and at CO saturation (right column) for the Ni-containing nanosized MFI zeolites. The panels include the parent zeolites (solid trace) and the Ni-containing zeolites where Ni has been added via post-synthetic (dot trace) and/or one-pot methods (dash trace).

Moreover, this sample exhibits a small fraction of Ni^{2+} species attached to Si-OH groups, as deduced from the signal at 2192 cm^{-1}, which appears in both the CO saturation spectrum (see **Ni-nMFI30_op** in **Figure 6.12)**) and the low CO dosage spectrum (see **Figure 6.12**). In contrast, the spectrum of the Ni-nMFI30_ps sample shows a significant decrease in the intensity of the band associated with Brønsted acid sites (2175 cm^{-1}, see **Ni-nMFI30_ps in Figure 6.12 CO-Saturation)**). This supports the conclusion obtained from the observed decrease in the Brønsted acid band in the FTIR-pyridine experiment (**Figure 6.11 A)**). Furthermore, the appearance of a characteristic band at 2168 cm^{-1} (**Ni-nMFI30_ps in Figure 6.12 CO-Saturation**), associated with the formation of Ni^{+}-CO species[65], suggests a self-reduction phenomenon during vacuum and high-temperature pretreatment, consistent with previous studies reported by various authors[41,62,65].

Similar patterns are observed in the BEA-type materials (see **Figure 6.13**). The spectrum of the parent nBEA30 sample displays two signals at 2175 cm^{-1} and 2160 cm^{-1}, corresponding to CO interactions with Brønsted acid sites and silanol groups, respectively (see **nBEA30_H** in **Figure 6.13 CO-Saturation**) The same signal as in the commercial MFI zeolites is observed at 2138 cm^{-1}, attributed to condensed CO within the pores. However, unlike the nMFI30 spectrum, post-synthetic incorporation of Ni does not result in a decrease in the Brønsted acid band (see **nBEA30_H** and **Ni-nBEA30_ps** in **Figure 6.13 CO-Saturation**).

The reason this band is preserved in the CO experiment, despite the reduction in Brønsted acid site density observed in the pyridine experiment, is the formation of NiO species, whose interaction with CO amplifies the signal at the same wavenumber. Indeed, the spectrum measured at low CO

concentration (**Figure 6.13 CO-Low dosage**) reveals the presence of NiO species. The broadening of the 2204 cm^{-1} band suggests that a significant fraction of the Ni species is in the form of Ni^{2+} cations grafted to silanol groups, as proposed by Martinez *et al*[63]. Additionally, a characteristic band at 2137 cm^{-1} is observed in the spectra of the nBEA30 samples, prepared by both post-synthetic and direct incorporation of Ni (see **nBEA30** sample in **Figure 6.13 CO-Low dosage**), indicating the presence of the Ni^{+}-CO complex, along with another shoulder in the spectrum associated to these species at 2109 cm^{-1} [62,66].

The increase in the band at 2175 cm^{-1} in the Ni-nBEA30_op spectrum, associated with Brønsted acid sites and the formation of NiO species (**Figure 6.13 CO-Saturation)**), is further supported by the appearance of a signal around 2150 cm^{-1}, more pronounced in the CO low dosage spectrum (**Figure 6.13 CO-Low dosage**). This trend is similar to the one observed in Ni-nMFI30_op, both at CO saturation and low dosage levels, with the effect being particularly noticeable at low CO concentrations (**Ni-nMFI30_op** in **Figure 6.12 CO-Low dosage** and **Figure 6.13 CO-Low dosage**).

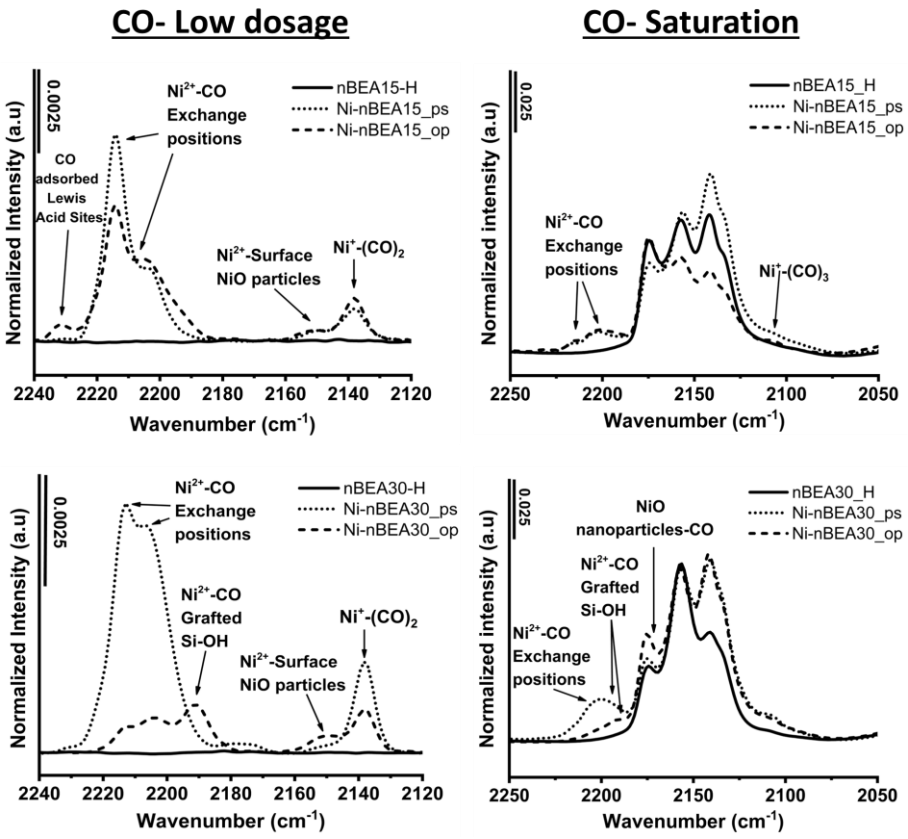

Figure 6.13. FTIR spectra using CO as probe molecule at CO-Low dosage adsorption (left column) and at CO-Saturation (right column) for the Ni-containing nanosized BEA zeolites. The panels include the parent zeolites (solid trace) and the Ni-containing zeolites where Ni has been added via post-synthetic (dot trace) and/or one-pot methods (dash trace).

For the high Al content nanosized Beta zeolites (nBEA15), there is a notable contribution of the band at 2212 cm^{-1} derived from the CO interaction with Ni^{2+} at exchange positions, especially in the Ni-NBEA15_ps sample, as observed in the IR spectrum under CO low dosage coverage. In contrast, the sample with Ni incorporated via direct encapsulation shows a stronger signal at 2175 cm^{-1}, similarly to what was observed in Ni-nBEA30_op. The

persistence of this band within this range (see **nBEA15** samples in **Figure 6.13 CO-Low dosage**), despite the decreased intensity for the same band in the Ni-nBEA15_ps spectrum, suggests the formation of NiO species, as indicated by the isolated contribution of this signal in the CO low dosage spectrum of Ni-nBEA15_op (**Figure 6.13 CO-Low dosage**). Pairing this result with the slight decrease in Brønsted acidity observed in the FTIR-pyridine spectrum (see Ni-nBEA15_op in **Figure 6.11**) reinforces the conclusion that a portion of the Ni species are present as NiO rather than Ni^{2+}, which could otherwise block available Brønsted acid sites. This trend is similar to what was observed for nBEA30, though more pronounced.

The analysis of the Ni-containing zeolites using FT-IR at low temperatures and CO molecule as a probe molecule reveals that, regardless of the zeolite's topological structure (MFI or BEA), the Ni incorporation methodology plays a decisive role in determining its final speciation within the zeolitic support. One-pot encapsulation promotes the formation of NiO species, while post-synthetic incorporation methodologies favour the formation of cationic Ni species, being high Al content materials more prone to estabilize Ni^{2+} species in exchange positions, attached to Brønsted acid centres and low Al content more favoured to form Ni^{2+} species grafted to silanol groups.

In addition to analysing the spectra in the specific region of CO interactions, potential changes in T-OH stretching region of the spectra, related to the presence of aluminols and silanols, were examined to assess the final speciation of Ni species based on their interactions with these functional groups. A noticeable decrease in the intensity of signals around 3600 cm^{-1}, corresponding to the hydroxyl groups responsible for the Brønsted acidity of the zeolite, was observed in all MFI-type commercial samples where Ni was

incorporated post-synthetically. Additionally, these spectra reveal a decrease in the signal intensities attributed to isolated internal silanol groups (≈3738 cm^{-1})[67,68], while the intensity of signals associated with isolated external silanols (≈3750 cm^{-1}) remained unchanged.

These results are consistent with those evidenced by low-temperature FTIR-CO spectra, reassuring that Ni^{2+} are preferentially grafted to isolated silanols within the micropore structure, especially in more siliceous zeolites. On the other hand, more Ni^{2+} species are positioned in exchange sites on zeolites containing higher Al contents, interacting with the aluminols of the Brønsted acid centres.

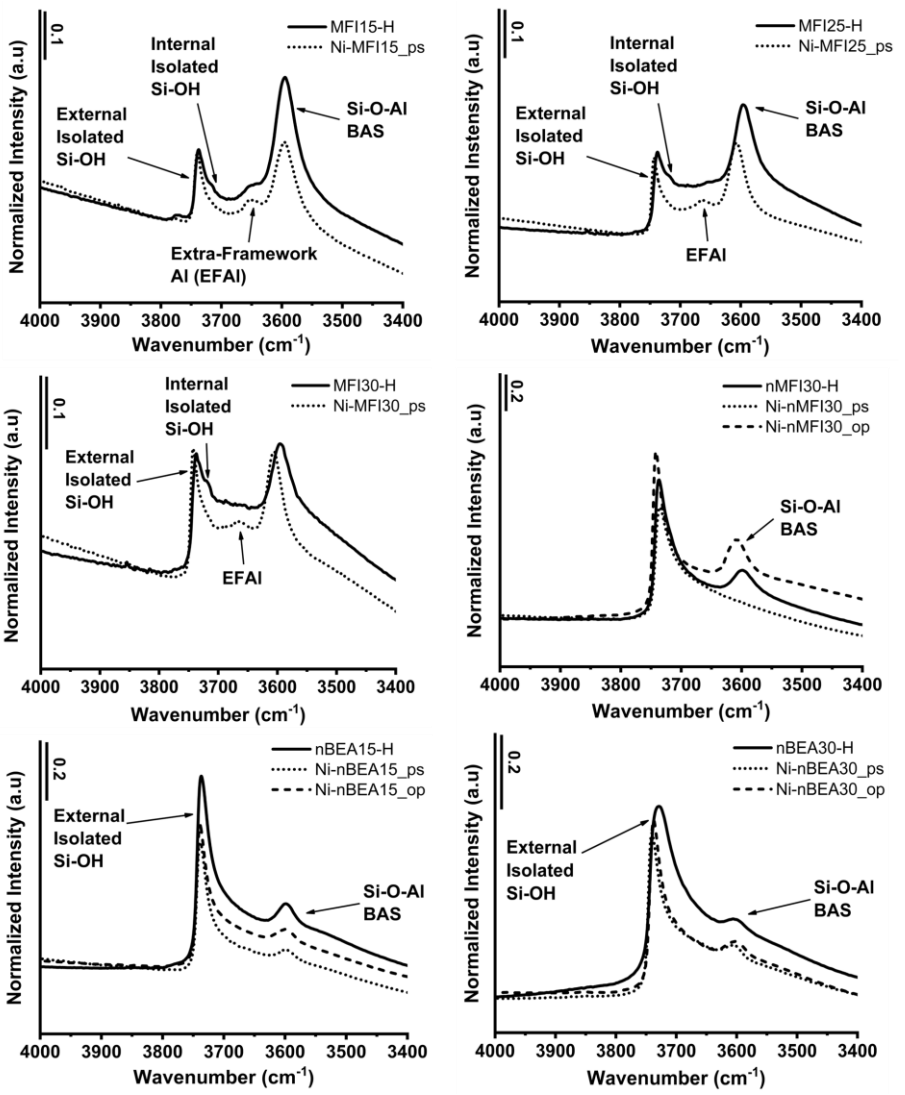

Figure 6.14. FTIR spectra in the –OH stretching region for commercial MFI zeolites and synthetized nanosized MFI and BEA zeolites. The panels include the parent zeolites (solid trace) and the Ni-containing zeolites where Ni has been added via post-synthetic (dot trace) and/or one-pot methods (dash trace).

Regarding the synthesized zeolites, a decrease in the signals associated with aluminols linked to Brønsted acid centres is observed in the spectra of both nMFI30 (**Figure 6.14**) and nanosized Beta (see **nBEA15** and **nBEA30** samples in **Figure 6.14**). This decrease is more pronounced in the Ni-nMFI30_ps sample, where the signal disappears entirely. Although there is a slight increase in this signal for the Ni-nMFI30_op sample, the overall trend across the other materials is a decline in this signal intensity. Indeed, a reduction of the Si-O-Al signal values is observed in the nanoBEA samples regardless the employed Ni incorporation methodology, especially in the sample with the highest Al content when Ni is added post-synthetically (**Figure 6.14**).

In terms of the isolated silanol signals (≈3750 cm^{-1}), most of the synthesized samples exhibit a decrease in this signal, with the exception of Ni-nMFI30_op where an increase is observed. For the Beta zeolites, a decrease in the intensity of the band associated with isolated external silanols is observed when compared to their Ni-free counterparts. Similar to the phenomena observed in the commercial zeolites spectra, the synthesized samples follow the same pattern, where Ni^{2+} cations are present in both forms. In the higher Al-content synthetized Beta, a higher proportion of Ni^{2+} cations might occupy exchange sites, while in the lower Al-content materials, Ni^{2+} cations are predominantly grafted onto the silanols. In contrast, in those samples where the Ni was added by one-pot synthesis, the decrease of those bands is much softer, suggesting that Ni could be incorporated as NiO species, remaining part of the silanol and aluminol groups free.

The potential presence of agglomerated Ni particles on the external surfaces of the synthetized MFI and BEA samples was initially investigated using scanning electron microscopy with an ESB darkfield detector (see **Figure 6.7**).

In contrast, the infrared spectra indicated the existence of NiO species for those samples where Ni was added by direct encapsulation. The samples were further examined through dark-field transmission electron microscopy (see **Figure 6.15**) to confirm the presence of encapsulated nanosized NiO particles within the zeolite crystal. Ni nanoparticles were not detected in the commercial samples Ni-MFI15_ps, Ni-MFI25_ps, and Ni-MFI30_ps, aligning these observations with the infrared spectra results, supporting that the majority of Ni species remained as divalent cationic form (see **Ni-MFI15_ps**, **Ni-MFI25_ps** and **Ni-MFI30_ps** in **Figure 6.12**). As for the synthesised nanoMFI (see **Figure 6.15**), STEM imaging confirmed the absence of particles when Ni was added by post-synthetic treatments, while in the Ni-nMFI30_op sample (see **Figure 6.15**), encapsulated NiO nanoparticles within the zeolite crystal were clearly observed.

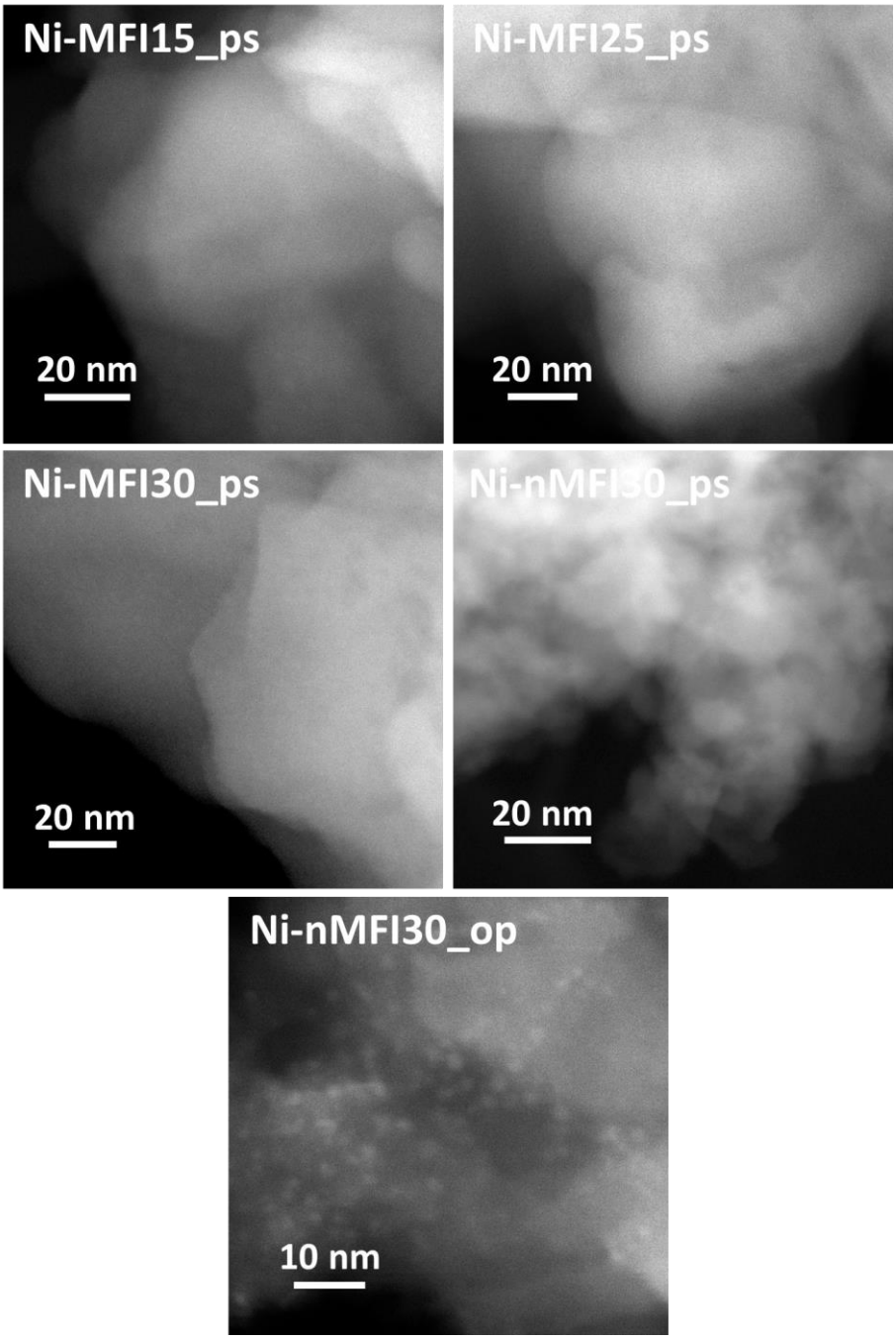

Figure 6.15. Dark field STEM images of the different Ni-containing MFI-type zeolites.

A similar trend is observed for BEA-type zeolites, particularly for Ni-BEA11_ps, Ni-nBEA15_ps, and Ni-nBEA30_ps. In case of the materials where Ni was incorporated post-synthetically, the formation of encapsulated particles was not detected, aligning these evidences with the results obtained by the infrared spectroscopy. The direct incorporation via one-pot synthesis primarily promotes the speciation of Ni as NiO while post-synthetic favours the formation of Ni^{2+} species.

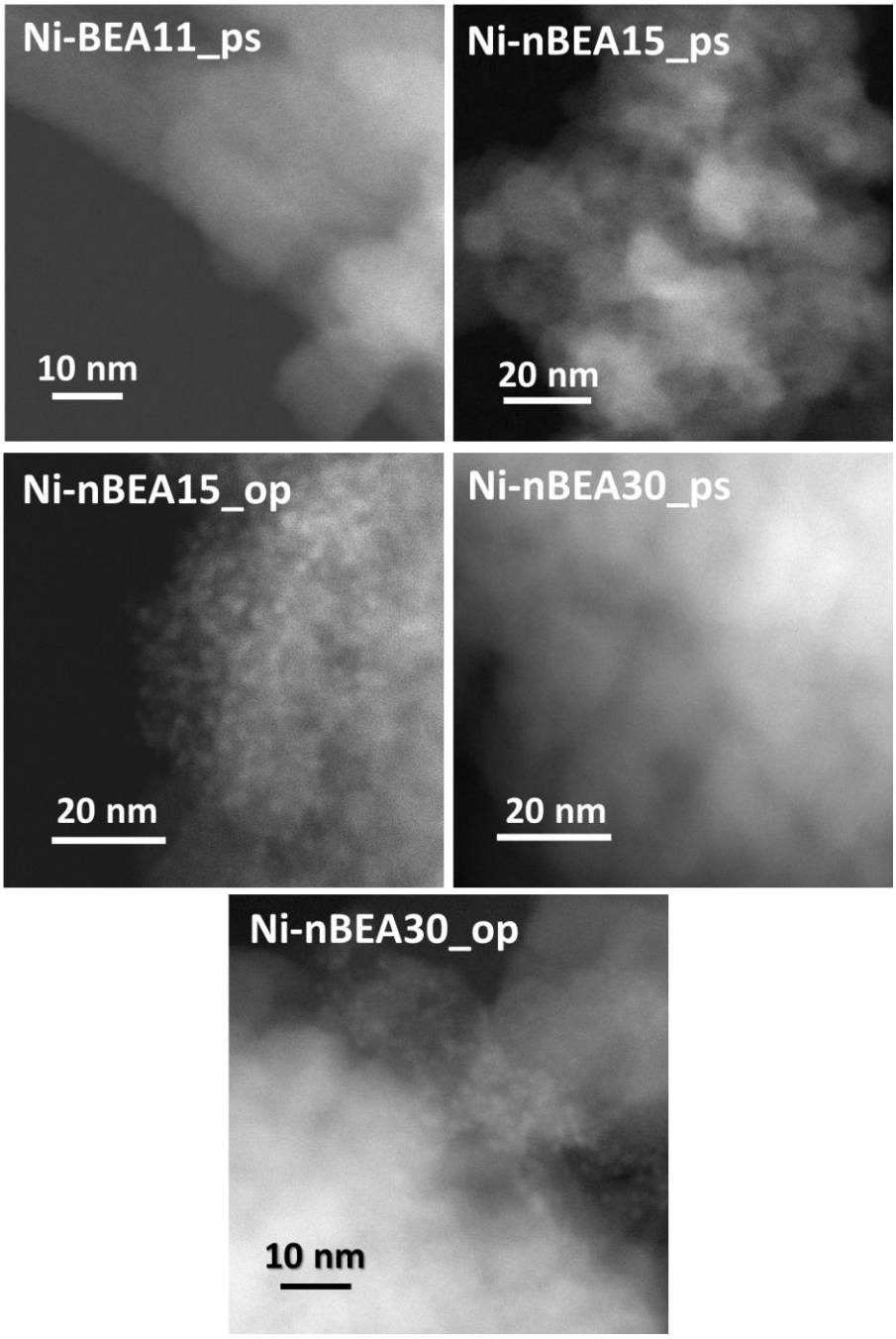

Figure 6.16. Dark field STEM images of the different Ni-containing BEA-type zeolites.

Temperature-programmed reduction (TPR) tests using H_2 were performed to investigate the metal-support interaction. By analysing the temperature at which metal species in the materials undergo reduction, it is possible to identify the different metal speciation. According to the literature, external bulky NiO nanoparticles with weak interactions with the support are reduced at temperatures below 300°C[41,54,69,70]. However, the reduction of Ni(II) to Ni(0) requires a higher energy input, typically occurring between 360 and 600°C, depending on the location of the cationic species and their degree of interaction with the support[41,54,65,69,70] (see **Figure 6.17**)

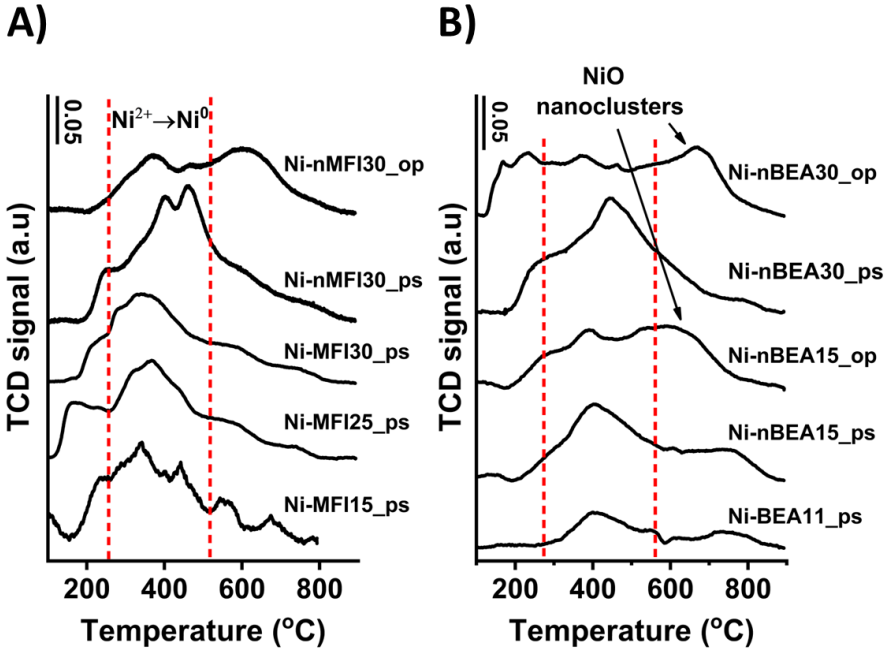

Figure 6.17. H_2-TPR profiles for the Ni-containing **A)** MFI-type and **B)** BEA-type materials.

All the Ni-containing samples exhibit the major reduction peaks within this intermediate temperature range of 350 to 600°C, associated to the Ni^{2+} reduction. Notably, samples where Ni was incorporated post-synthetically

show higher hydrogen consumption near the upper limit of this range (**Figure 6.15**), suggesting a strong interaction between the Ni^{2+} cations and the zeolite structure[41]. In contrast, materials synthesized through one-pot synthesis display significant hydrogen consumption at lower temperatures, indicative of NiO nanoparticles on the external surface, as well as a prominent reduction peak above 600°C. This last peak is associated with the reduction of encapsulated NiO nanoparticles (**Figure 6.15, Figure 6.16** and **Table 6.6**), showing a much stronger interaction with the support framework, consistent with findings by Li *et al*. on directly encapsulated Ni species[71].

Table 6.6. Relative hydrogen consumption estimated from the TPR measurements at the low, medium and high temperature regions for the different Ni-zeolites.

Sample	*%Ni Low T (T<300-350ºC)*	*% Ni Intermediate T (300-525ºC)*	*% Ni High T (T>525ºC)*
Ni-MFI15_ps	30	58	12
Ni-MFI25_ps	15	79	6
Ni-MFI30_ps	7	90	3
Ni-nMFI30_ps	8	67	25
Ni-nMFI30_op	39	2	59
Ni-BEA11_ps	3	67	30
Ni-nBEA15_ps	2	53	45
Ni-nBEA15_op	12	23	65
Ni-nBEA30_ps	6	60	34
Ni-nBEA30_op	26	34	40

These final results, together with those obtained by the FTIR spectroscopy, using both CO and pyridine as probe molecules, and by the STEM strongly evidence that the final state of Ni species within the same zeolite framework is mainly dependent on the incorporation method. Additionally, the Brønsted acid density of the materials is shown to vary based on the Ni incorporation strategy too.

6.3. THE INFLUENCE OF THE Ni SPECIES AND PHYSICO-CHEMICAL PROPERTIES OF ZEOLITE SUPPORTS ON THE CATALYTIC ACTIVITY AND FINAL PRODUCTS SELECTIVITY IN ETHYLENE OLIGOMERIZATION REACTION.

The catalytic performance of the Ni-containing zeolites, with fine tunned Ni species and physicochemical properties (surface area, particle size, crystal structure or Brønsted/Lewis acidity), was investigated for the ethylene oligomerization reaction under different conditions (see **Chapter 3**, **Table 3.1**). In a first approach, the reaction was examined at near-ambient pressures with a low ethylene partial pressure and high space velocity. Based on previous studies, high selectivity towards the dimerization of ethylene into butenes was expected working under these conditions, even for materials exhibiting elevated Brønsted acidity[54]. Additionally, the materials were tested under more demanding conditions, including high pressure, increased ethylene concentration, and lower space velocity, approaching the conditions to those employed in industry. According to the literature, these harsher conditions are expected to favour the formation of oligomers with molecular weights in the range of liquid fuels, where the acidity has a more significant contribution to the catalytic behaviour[55,61].

Figure 6.18 illustrates the ethylene conversion obtained by the different MFI and BEA catalysts. A noticeable pattern observed is that all the catalysts exhibit an initial decrease in their activity within the first 50 minutes of time-on-stream (TOS) and after that, the catalysts become stable. This initial activity drop is more pronounced in MFI zeolites compared to Beta zeolites and is more severe in samples with lower Si/Al ratios. Once the catalyst activity became stable, the final ethylene conversion values reached by the different materials appear to be similar.

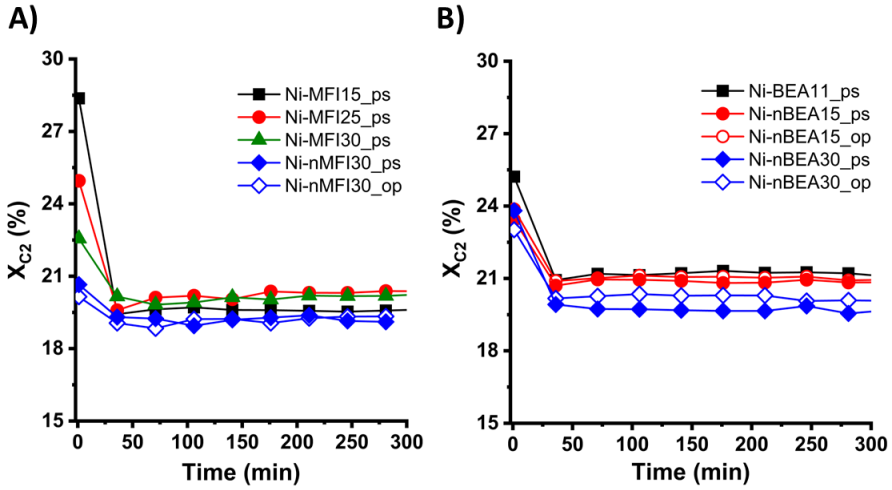

Figure 6.18. Reacted ethylene in Ni-containing **A)** MFI and **B)** BEA materials under near-ambient pressure. Reaction conditions: 180°C, 2.5 bar, WHSV = 16.3 hr^{-1}, Q_t = 600 mL/min (%vol N_2 = 97.5, %vol C_2H_4 = 2.5%), m_{cat} = 63 mg.

To gain a deeper understanding of the role played by the different Ni species in each catalyst, **Figure 6.19** presents the conversion values normalized to the Ni content of the respective materials.

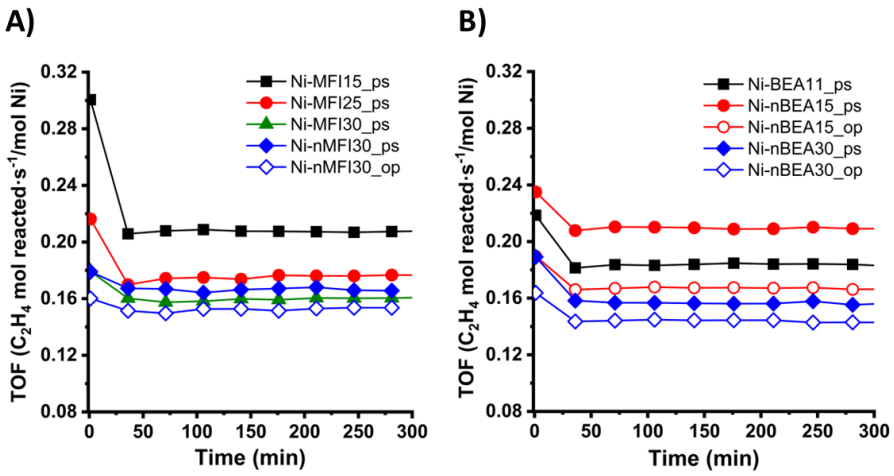

Figure 6.19. Reacted ethylene (mol) normalized by Ni content in Ni-containing **A)** MFI and **B)** BEA materials under near-ambient pressure. Reaction conditions: 180°C, 2.5 bar, WHSV = 16.3 hr^{-1}, Q_t = 600 mL/min (%vol N_2 = 97.5, %vol C_2H_4 = 2.5%), m_{cat} = 63 mg.

Figure 6.19 presents similar trends to the observed in the previous graph showing conversion versus TOS (**Figure 6.18**). An initial drop of the activity for all materials is again evident, but this time it is more noticeable that deactivation is more pronounced in materials with higher Brønsted acidity. This initial decrease in catalytic activity could be attributed to the formation of Ni-alkyl complexes with long carbon chains. These reaction intermediates are unable to desorb, partially blocking the Ni^{2+} active centres[41]. A similar behaviour was previously reported by Moussa *et* al.[42], where the loss of activity was related to the adsorption of high molecular weight reaction intermediates on Ni^{2+} species in ion exchange positions, with strong Lewis acidity.

As the Si/Al ratio of the materials increases, a decrease in stationary TOF values (also the initial value at TOS = 0 min) is observed. It has been widely reported that Ni^{2+} species are catalytically effective for ethylene activation[72-77]. Numerous studies have emphasized the role of aluminium in the support structure in promoting this Ni^{2+} speciation. Indeed, the FTIR spectra of materials with higher Si/Al ratios reveal a tendency toward the formation of NiO, whereas materials with a greater concentration of acid sites display stronger indications of stabilizing Ni^{2+}. Thus, the activity trends observed and the FTIR-pyridine results evidences that the highest loss of Brønsted acid site density and the highest increase in Lewis acidity were observed for the most active sample (Ni-MFI15_ps), which is in agreement with the highest proportion of Ni^{2+} cations in ion exchange sites according to the low temperature CO-FTIR experiments. On the other hand, higher Si/Al ratios and smaller crystal sizes favoured the silanol grafted Ni^{2+} species, with weaker Lewis acidity. These Ni cations were described as the ones remaining active at longer TOS for the ethylene oligomerization reaction[41,42]. The presence of these cationic species grafted to the silanol groups could justify the milder deactivation of the materials, as the adsorbed species exhibit weaker interactions with the Lewis acid sites. This reduced interaction minimizes the degree of irreversible deactivation caused by the blockage of active sites.

Regarding the particle size, similar activities for the nanocrystalline MFI (Ni-nMFI30_ps) and the commercial-based Ni-MFI30_ps are observed, but the nanosized suffers slower deactivations, as expected from shorten the diffusional pathways. And finally, regarding the Ni incorporation methodology, the Ni-nMFI30_op is the material with the lowest activity due to the low proportion of Ni^{2+} species and the higher proportion of NiO

encapsulated nanoparticles, species reported as inactive for ethylene molecule activation[37].

Similar general trends are observed for the BEA type catalysts (see **Figure 6.18 B) and 6.19 B)**). Regarding the Beta nanocrystalline zeolites, the sample with the highest Al-content and Ni post-synthetically added showed the highest activity among the synthesized zeolites due to a higher amount of Ni stabilized as divalent cations. On the other hand, Ni-nBEA15_op sample was able to stabilize Ni species both as NiO nanoparticles and Ni^{2+} cations, despite possessing Ni added by one-pot synthesis, due to the high concentration of Al in the zeolite structure.

The catalytic activity of the synthesized catalysts with higher Si/Al ratios is aligned with the trend observed previously for MFI synthesized materials. Ni-nBEA30_ps shows the higher activity, explained by the proportion of Ni^{2+} species stabilized within the zeolite, than Ni-nBEA30_op, which exhibits lower activity, as the reduced Al content during synthesis favours the stabilization of Ni as NiO nanoparticles. The commercial sample, Ni-BEA11_ps, demonstrates a moderate activity between the nanocrystalline Beta sample with Si/Al ratios of 15 and 30. Although Ni-BEA11_ps possesses higher Lewis acidity (see **Table 6.5**), it also shows lower activity and slightly more pronounced initial deactivation, likely due to its larger particle size. These trends are consistent with previous studies on olefin oligomerization[58].

Regarding the product distribution obtained with the MFI type materials (see **Figure 6.20**), at longer times on stream (TOS > 120 min), butenes are the dominant products, with selectivities exceeding 75%, primarily due to ethylene dimerization. However, at initial TOS, when catalytic activity is

higher, other fractions such as C_3, C_5, C_6, and to a lesser extent, C_7, are also detected. The presence of products with odd carbon numbers suggests that, in addition to oligomerization occurring at the Ni^{2+} active sites, secondary reactions like cracking, isomerization, or further oligomerization of the primary products have also taken place, promoted by the Brønsted acid sites[78].

The formation of small isobutane fractions in the early stages of the reaction supports the contribution of carbocation-based mechanisms in the overall product distribution. The deactivation observed within the first 60 minutes of reaction, followed by the stabilization of the ethylene conversion at higher TOS, along with evolution of the product distribution (decrease in C_3 proportions and an increase in C_4 and C_6 fractions), suggests that the Brønsted acid sites, responsible for parallel isomerization and cracking reactions, deactivate much faster than the active Ni species. Among the MFI-type catalysts studied, Ni-nMFI30_op exhibits the lowest selectivity towards butenes and the highest towards C_{5+} products, likely due to its higher Brønsted acidity, which is preserved when Ni is incorporated via direct synthesis (see **Table 6.5**), despite having the lowest activity.

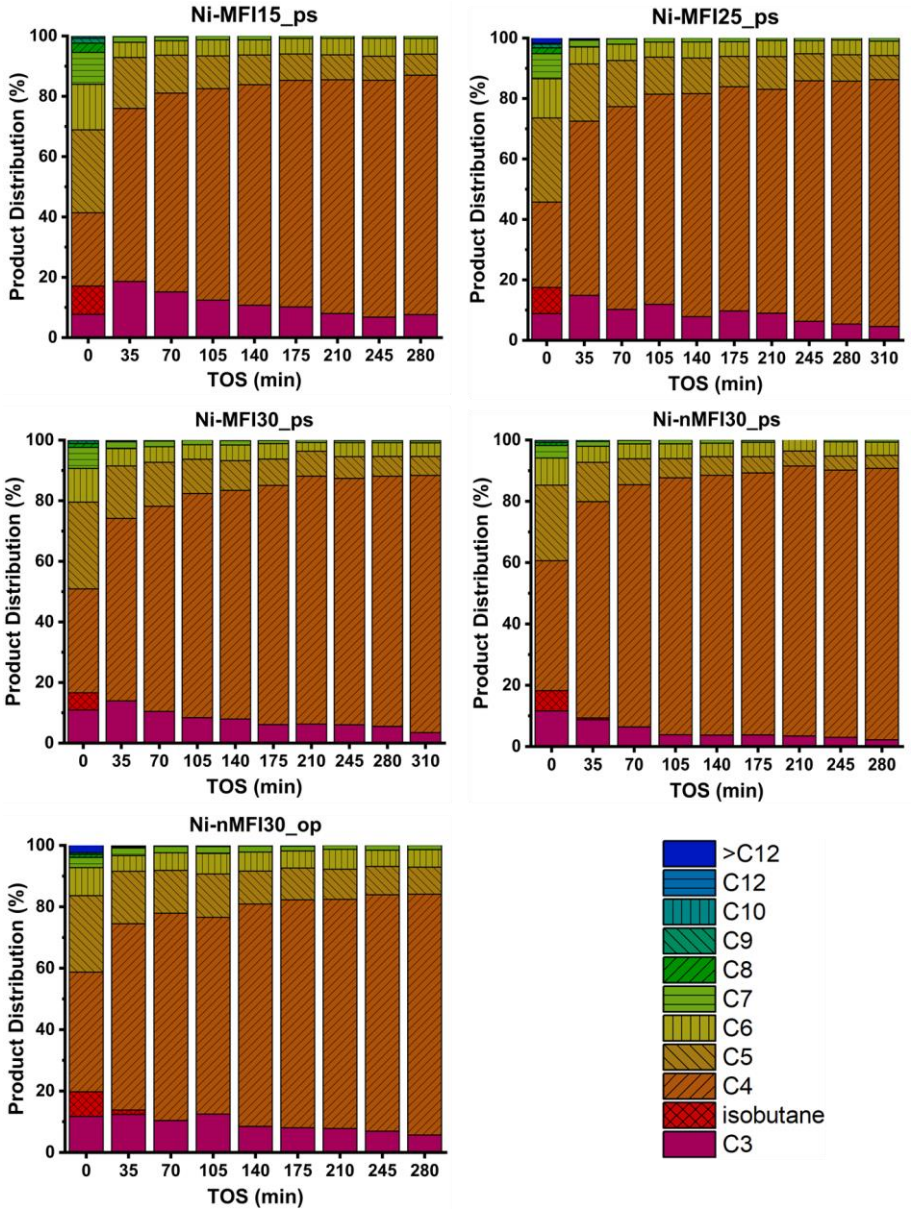

Figure 6.20. Product selectivities for Ni-containing nanosized MFI materials under near-ambient pressure. Reaction conditions: 180°C, 2.5 bar, WHSV = 16.3 hr^{-1}, Q_t = 600 mL/min (%vol N_2 = 97.5, %vol C_2H_4 = 2.5%), m_{cat} = 63 mg.

In the case of the overall product distribution obtained for the Beta-type catalysts (**Figure 6.21**), butenes remain as the predominant product. However, the selectivity toward butenes is notably higher compared to the MFI-type catalysts, over 90% once the reaction reaches steady-state for most of the samples. At short time on stream (TOS <36 min), minor fractions of C_3 and more noticeable fractions of C_5, C_6, and C_7 hydrocarbons were obtained. These odd carbon number distributions result from isomerisation/cracking reactions of heavier oligomers (>C_3), probably occurring at the channel intersections. Furthermore, isobutane formation is also observed at short TOS in higher proportions than in ZSM-5 catalysts, phenomena attributed to the greater hydrogen transfer capacity of the larger-pore Beta zeolites[58].

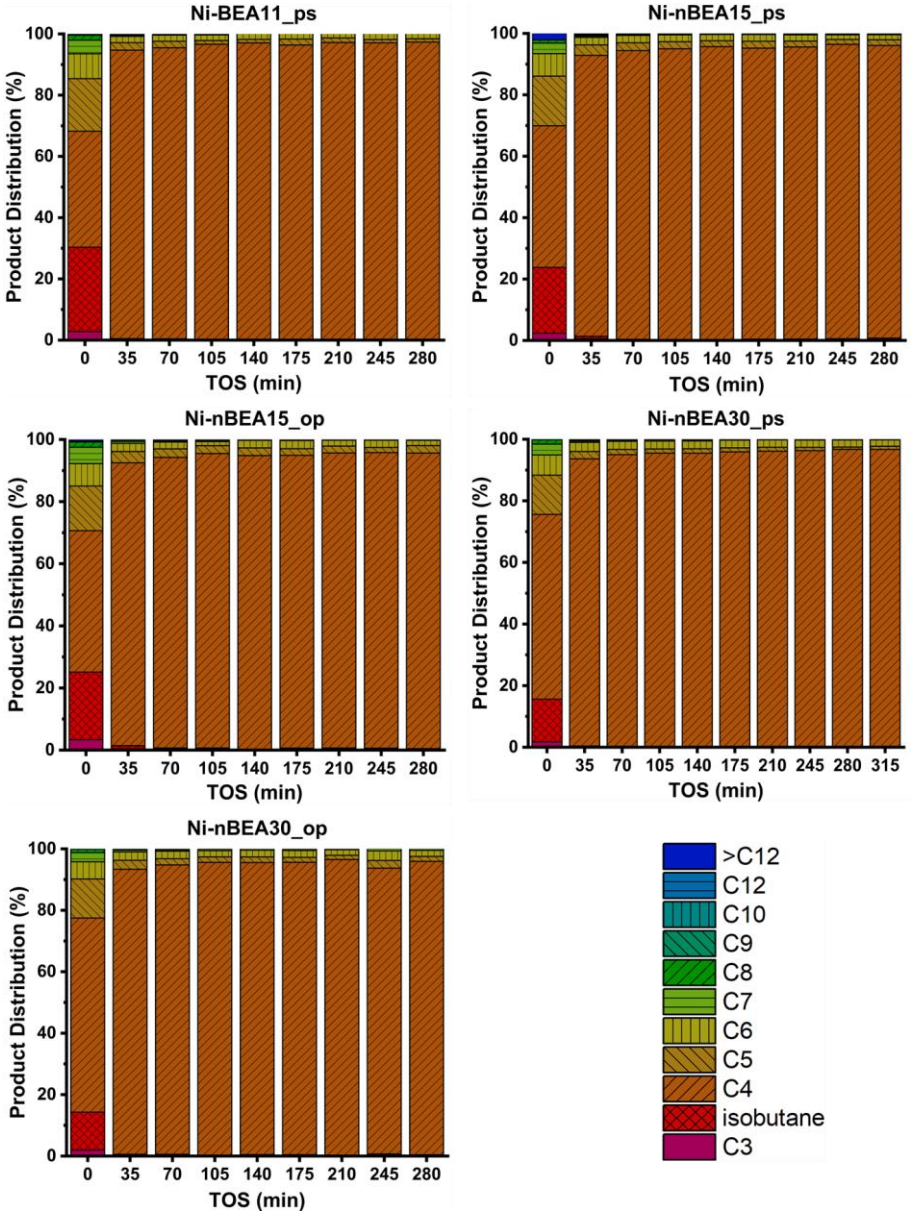

Figure 6.21. Product selectivities for Ni-containing nanosized BEA materials under near-ambient pressure. Reaction conditions: 180°C, 2.5 bar, WHSV = 16.3 hr^{-1}, Q_t = 600 mL/min (%vol N_2 = 97.5, %vol C_2H_4 = 2.5%), m_{cat} = 63 mg.

After examining the catalytic behaviour of the entire range of materials under near-ambient pressure conditions with low ethylene partial pressure and high space velocities, it can be concluded that all catalysts with Ni added post-synthetically exhibit superior catalytic performance compared to those with Ni encapsulated through one-pot synthesis. The post-synthetic incorporation of Ni enhances stabilization of the Ni species as divalent cations, particularly in materials with lower Si/Al ratios, a conclusion evidenced by the combination of various characterization techniques (*i.e.* "*in-situ*" IR experiments with different probe molecules, H_2-TPR, and STEM).

Interesting differences were observed when the catalytic tests were conducted under conditions more similar to those carried out in industry, characterized by remarkably higher pressures, high temperature, lower space velocities, and higher ethylene partial pressure in the reaction mixture. The initial conversions were substantially higher under these conditions. However, comparing with the study conducted at near-ambient pressure conditions, all materials experienced a much more severe deactivation (see **Figure 6.22**). With lower space velocity and a larger amount of catalyst used, the TOF values were expected to be significantly lower than those obtained under low-pressure conditions due to the high ethylene/Ni ratio employed in these catalytic tests (see **Figure 6.23**), in good agreement with findings reported in previous studies[42].

It is important to remark that the reaction carried out at high pressures and at high ethylene concentrations in the feed stream will lead to the formation of significantly larger oligomers. This effect has been reported previously[37] to be the factor that contributes to most of the drop of the catalysts activity. Under these conditions, it is expected that, in addition to the speciation of Ni

on the supports, other factors such as the particle size and the remanent Brønsted acidity will also impact the final catalytic behaviour of the bifunctional Ni-catalysts studied.

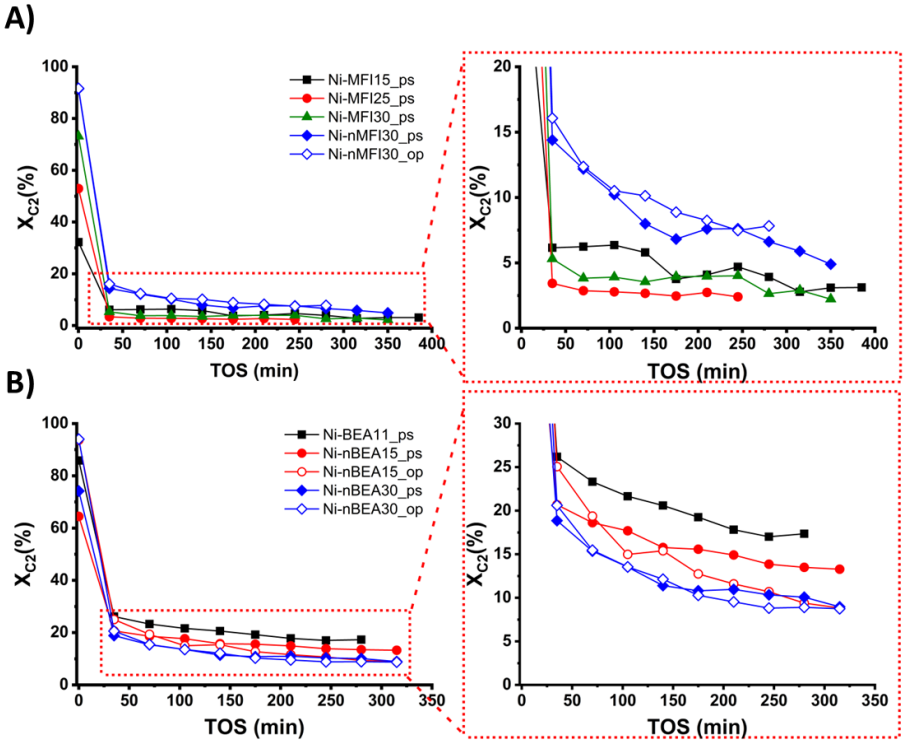

Figure 6.22. Reacted ethylene (mol) normalized by Ni content in Ni-containing **A)** MFI and **B)** BEA materials under high-pressure conditions. Reaction conditions: 200ºC, 35 bar, WHSV = 2.1 hr^{-1}, Q_t = 100 mL/min (%vol N_2 = 85, %vol C_2H_4 = 15%), m_{cat} = 500 mg.

In contrast to the activity curves gathered under low-pressure conditions, where the samples with the lowest Si/Al ratios exhibited the highest activity due to the role of aluminium in stabilizing Ni^{2+}, the behaviour at high pressure differs substantiality. Under low-pressure conditions, lower Al-containing samples showed reduced initial activity and deactivation rate, suggesting that factors like crystal size or diffusive properties were not relevant. However,

this trend has not been repeated in the high-pressure study. As shown in **Figure 6.22 A)**, during the catalytic evaluation of Ni-MFI catalyst under high pressure and ethylene concentration, the two nanocrystalline samples were the ones that demonstrate the highest initial activity and experienced the lowest deactivation degree, maintaining a more stable performance at high TOS as compared to the other MFI samples. In this case, it seems that the main factor improving the final catalytic behaviour is the crystal size, shortening the heavier intermediates pathway and delaying the catalyst deactivation.

To assess the influence of Ni species on the catalytic activity of the materials under these harsh conditions, stabilization curves were plotted using the TOF against the TOS.

Figure 6.23 presents the stabilization curves normalized by the Ni content of the materials, highlighting the differences in initial activity among the MFI samples (**Figure 6.22 A)**). The nanosized synthetized zeolites display the highest initial activity, indicating that the presence of Ni^{2+} species does not mitigate material deactivation. Notably, Ni-nMFI30_op demonstrates higher initial activity than all the commercial MFI zeolites (which have micronsized crystal particles). This suggests that, in reactions conducted under high pressure, high ethylene concentration and low space velocity, the most relevant factor determining the stability of the materials over time is the particle size.

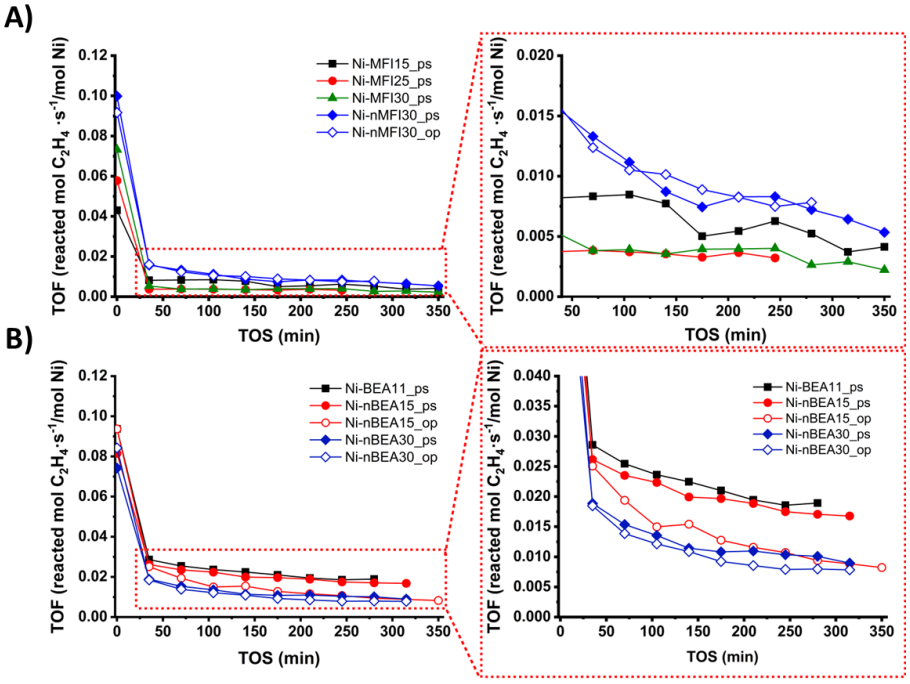

Figure 6.23. Reacted ethylene (mol) normalized by Ni content in Ni-containing **A)** MFI and **B)** BEA (B) materials under near-ambient pressure. Reaction conditions: 200ºC, 35 bar, WHSV = 2.1 hr^{-1}, Q_t = 100 mL/min (%vol N_2 = 85, %vol C_2H_4 = 15%), m_{cat} = 500 mg.

Regarding Beta zeolites, as all the materials exhibit nanometric crystals (ranging between 10-30 nm), higher activity is observed than for the MFI-based catalysts values (see **Figures 6.22 B)** and **6.23 B)**). In this case, the impact of the Ni species is more noticeable, with Ni-nBEA15_ps showing the highest catalytic activity, followed by Ni-nBEA11_ps. This enhanced performance is attributed to their higher capability to stabilize the Ni species as Ni^{2+} cations, as the elevated Al concentration allows for better stabilization of the metallic species in their cationic form.

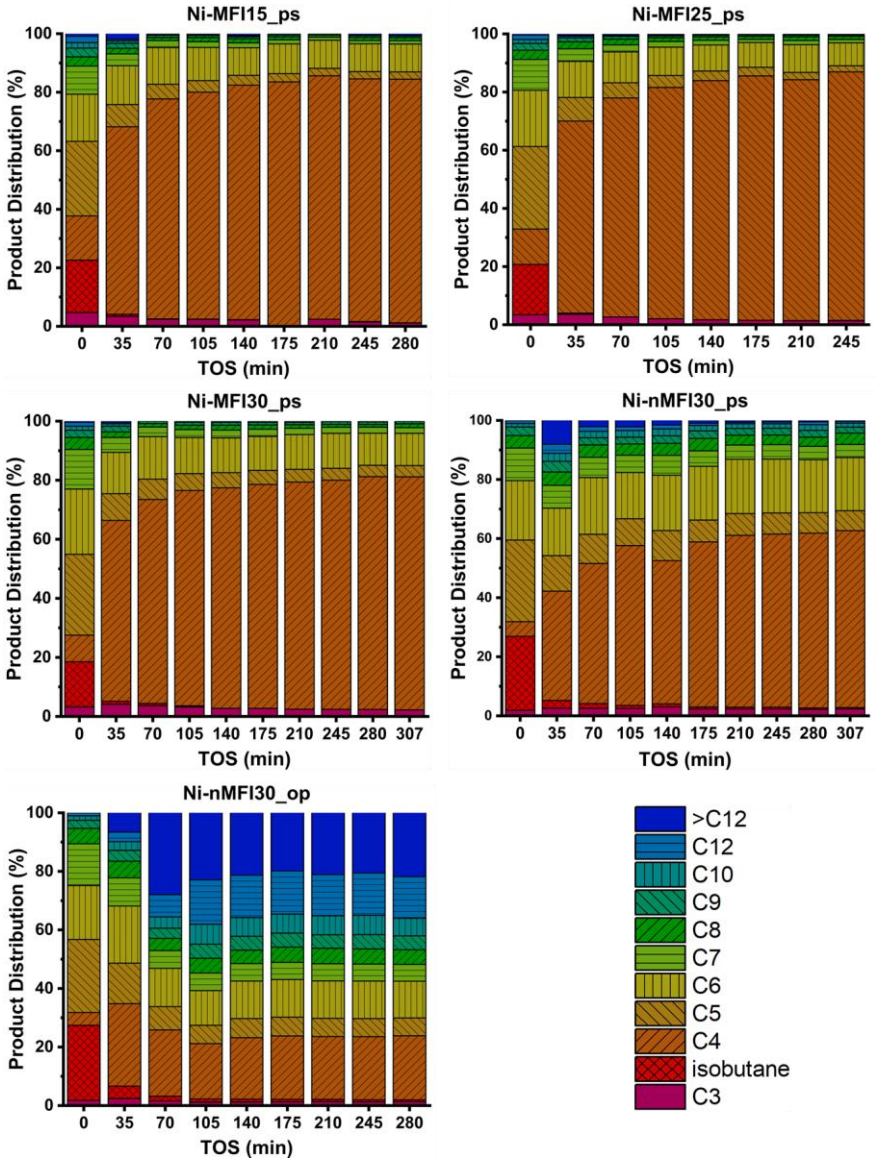

Figure 6.24. Product selectivities for Ni-containing nanosized MFI materials under high-pressure conditions. Reaction conditions: 200°C, 35 bar, WHSV = 2.1 hr^{-1}, Q_t = 100 mL/min (%vol N_2 = 85, %vol C_2H_4 = 15%), m_{cat} = 500 mg.

Figures 6.24 and **6.25** illustrate the product distributions for all MFI and Beta-type Ni-zeolites. Under these harsh reaction conditions, noticeable

differences in the overall product distribution appeared, compared to those obtained under near-atmospheric pressure. The results suggest that both the crystalline particle size and Ni speciation played a role in shaping the final hydrocarbon distribution.

For the commercial MFI samples, the product distribution remains similar to that obtained under lower pressure conditions, with products with 5 or more carbon atoms (C_5^+ > 60%) formed on the fresh catalysts at short TOS and butenes selectivity values approaching 70% at extended TOS. However, the higher ethylene concentration and high pressure promote consecutive ethylene oligomerization steps and the extension of side cracking reactions are reduced, resulting in the formation of trimers and tetramers (C_6 and C_8) and reducing the formation of C_5 hydrocarbons during the initial stages. In fact, the low selectivity to C3 hydrocarbons obtained under these conditions suggest that the C_3 compounds participate in the formation of the large oligomers.

In the case of nanosized MFI samples, their higher selectivity towards the formation of heavier hydrocarbons (C_5^+), as compared to their micronsized Ni-catalysts with similar Si/Al ratios has to be remarked. This is attributed to the enhanced diffusive properties of theses catalysts resulting from shortening the diffusional path lengths, facilitating the elution of heavy oligomers from the zeolite porous channels (see **Figure 6.24**). Notably, the catalyst where Ni was incorporated through one-pot synthesis, retaining higher Brønsted acid density than its post-synthetically Ni-added counterpart, extends the oligomerization products range, resulting in a increased formation of C_{12}^+ hydrocarbons at prolonged TOS (see **Figure 6.24**).

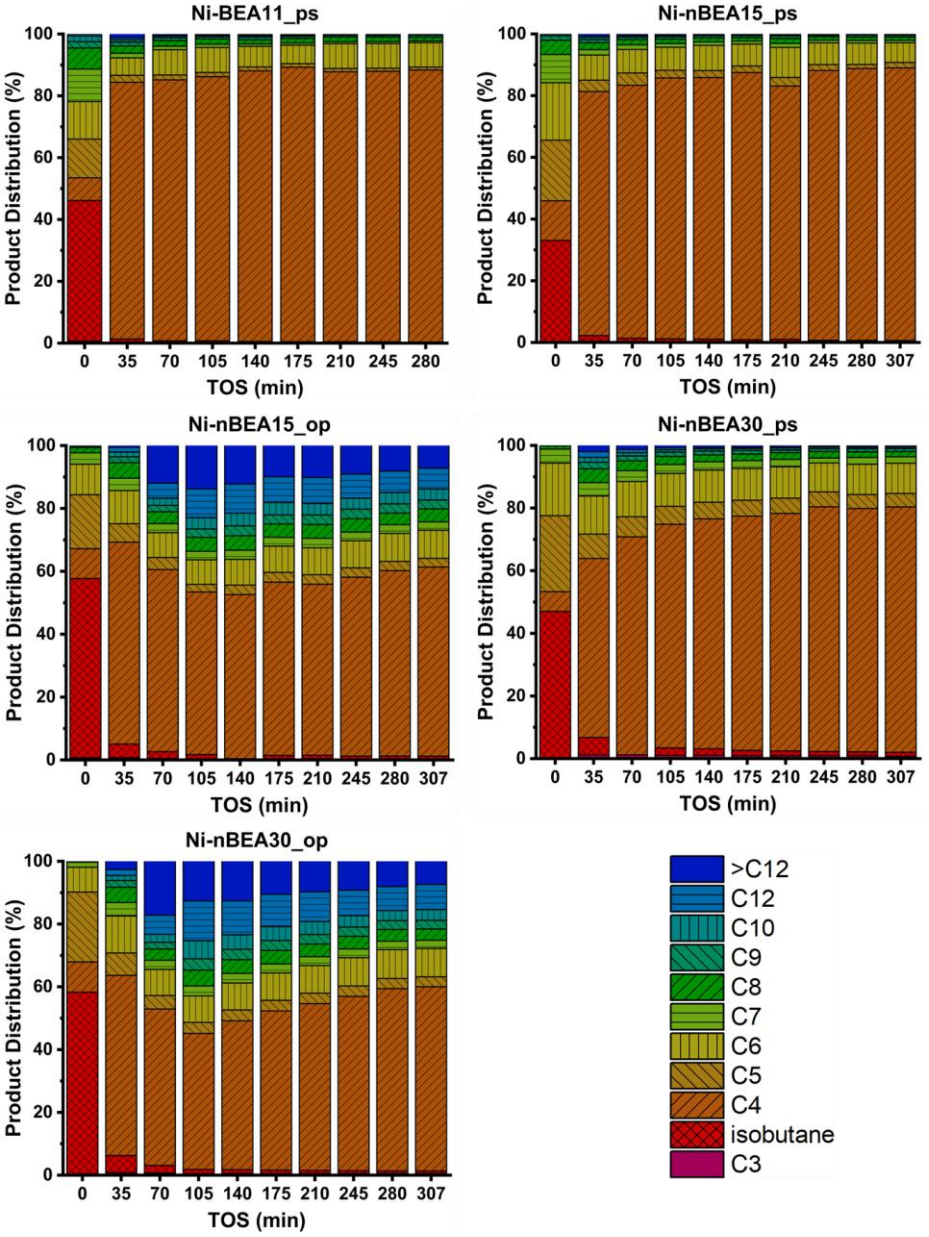

Figure 6.25. Product selectivities for Ni-containing nanosized BEA materials under high-pressure conditions. Reaction conditions: 200°C, 35 bar, WHSV = 2.1 hr^{-1}, Q_t = 100 mL/min (%vol N_2 = 85, %vol C_2H_4 = 15%), m_{cat} = 500 mg.

The differences observed in the product distributions for the Ni-Beta catalysts are even larger when comparing the catalytic results obtained under the two reaction conditions.

Under near-ambient pressure, specifically in those materials where the Ni was incorporated via post-synthetically impregnation, the product selectivity was predominantly favoured towards the formation of butenes (>90%). However, under high-pressure conditions, and once the reaction surpassed the initial stages of the reaction (TOS > 36 min), the selectivity evolved towards the formation of oligomers with a higher carbon number (see **Figure 6.25**). For materials where Ni was added via one-pot synthesis, the same trend was observed for the Ni-nBEA15_op and Ni-nBEA30_op samples compared to Ni-nMFI30_op sample. The higher density of Brønsted acid sites (see **Table 6.5**) enhanced oligomerisation steps, increasing the proportion of C_{12} and C_{12}^{+} hydrocarbons significantly, more than those obtained with their counterparts where Ni was introduced post-synthetically. These findings suggest that, similarly to the nanoMFI catalysts, the catalytic behaviour under high-pressure conditions, with elevated ethylene concentration and low space velocity, is more influenced by crystal size and Brønsted acid density than by Ni speciation.

Under more severe reaction conditions, bimolecular processes like hydrogen transfer are more favoured compared to milder conditions, leading to a higher fraction of isobutane in the early stages of the reaction. It was observed in both conditions that MFI-type catalysts are less selective for isobutane formation than Beta-type catalysts. Among the Beta catalysts, materials with Ni encapsulated via one-pot synthesis exhibit higher selectivity for isobutane production, attributed to their higher Brønsted acid sites

density. After 1 hour of TOS, the isobutane fraction stabilises at below 5%, probably as result of having some of these Brønsted acid sites blocked by the alkyl-complexes.

It can be concluded that the rational synthesis of Ni-containing zeolites, in which factors such as zeolite topology, crystal size, final density of Brønsted acid centres, and Ni speciation can be controlled through the synthesis conditions and the method of Ni incorporation (either via post-synthesis or encapsulation), enables the improvement of both the initial catalytic performance and the catalyst lifetime. This approach also increases the selectivity toward olefins with molecular weights in the liquid fuel range (C_5^+) when operating under conditions similar to those used in industry.

Under mild conditions (low ethylene concentration, ambient pressure, and low space velocities), crystal size plays a minimal role since there are only a few oligomerization steps that produce light oligomers (C_4-C_6). However, when reaction is carried out under industrial conditions (high pressure, high ethylene concentration, and low space velocity), crystal size becomes a critical factor in the catalyst stability enhancement.

Diffusive properties were improved through the synthesis of nanometric MFI and BEA zeolites, and the study allowed to corroborate that the final Ni speciation in the material was entirely dependent on the incorporation method employed, for both structures, and for two Si/Al ratio, as demonstrated in the case of Ni-nBEA.

For all conditions that have been studied, higher initial activities for ethylene transformation were obtained in those samples where Ni was added post-synthetically, as this method allowed the stabilization of Ni species primarily

as Ni^{2+} within the different structures. Additionally, the method of Ni incorporation also controlled the Brønsted acid site density in the materials, with higher density levels achieved when Ni was added via direct synthesis.

This physico-chemical property directly affected both the catalyst deactivation rate and the final product distribution under high-pressure conditions. It favoured the formation of C_5^+ fractions when Ni was incorporated post-synthetically, while C_{12}^+ fractions were observed in samples that maintained acidity through direct encapsulation of Ni.

6.4. CONCLUSIONS

A wide set of Ni-containing catalyst was rationally prepared, varying crystalline structures, crystal sizes, Si/Al ratios, and incorporating the Ni species by different methods. Different complementary characterization techniques revealed that the post-synthetic impregnation procedure favours the formation of Ni^{2+} species at ion exchange sites, particularly in materials with higher Al content, enhancing Ni incorporation. In contrast, the one-pot synthesis approach leads to the formation of encapsulated NiO nanoparticles within the zeolite pores. The catalytic performance of these materials for ethylene oligomerization was then evaluated under two distinct reaction conditions.

On the one hand, under mild conditions (near atmospheric pressure, low ethylene concentration, and high space velocity) it was observed that crystal size and improved diffusion properties did not influence the catalytic activity. Materials with Ni post-synthetically incorporated showed higher activity compared to those with Ni added via one-pot synthesis. This is attributed to the stabilization of Ni as Ni^{2+}, particularly in high-Al-content materials, species

that are the most active towards ethylene activation and subsequent dimerization.

Secondly, under harsher conditions, more similar to the industrial conditions (high pressure, elevated ethylene concentrations, and low space velocity) a large number of oligomerization steps are favoured, producing heavier hydrocarbons and leading to a faster catalyst deactivation. In this scenario, crystal size and good diffusive properties became critical, with the nanosized zeolites demonstrating greater stability than commercial zeolites with larger crystal sizes. Moreover, under these severe conditions, the method of Ni incorporation influenced both catalytic activity and product selectivity. While post-synthetically incorporated Ni^{2+} cations remained being the species most active, the direct synthesis of NiO nanoclusters allowed to preserve higher Brønsted acid sites density, influencing significantly the product distribution.

The results obtained from this chapter have been published in "Journal of Catalysis" in the work entitled "Design of bi-functional Ni-zeolites for ethylene oligomerization: Controlling Ni speciation and zeolite properties by one-pot and post-synthetic Ni incorporation", which DOI is: https://doi.org/10.1016/j.jcat.2023.07.010.

6.5. REFERENCES

(1) Lamichhane, P.; Pourali, N.; Scott, L.; Tran, N. N.; Lin, L.; Gelonch, M. E.; Rebrov, E. V.; Hessel, V. Critical Review: 'Green' Ethylene Production through Emerging Technologies, with a Focus on Plasma Catalysis. Renew. Sustain. Energy Rev. B 2024, 189, 1–18. https://doi.org/10.1016/j.rser.2023.114044.

(2) Zhao, Z.; Jiang, J.; Wang, F. An Economic Analysis of Twenty Light Olefin Production Pathways. J. Energy Chem. 2021, 56, 193–202. https://doi.org/10.1016/J.JECHEM.2020.04.021.

(3) Boulamanti, A.; Moya, J. A. Production Costs of the Chemical Industry in the EU and Other Countries: Ammonia, Methanol and Light Olefins. Renew. Sustain. Energy Rev. 2017, 68, 1205–1212. https://doi.org/10.1016/J.RSER.2016.02.021.

(4) Tian, P.; Wei, Y.; Ye, M.; Liu, Z. Methanol to Olefins (MTO): From Fundamentals to Commercialization. ACS Catal. 2015, 5 (3), 1922–1938. https://doi.org/10.1021/acscatal.5b00007.

(5) Khanmohammadi, M.; Amani, S.; Bagheri Garmarudi, A.; Niaei, A. Methanol-to-Propylene Process: Perspective of the Most Important Catalysts and Their Behavior. Chinese J. Catal. 2016, 37 (3), 325–339. https://doi.org/10.1016/S1872-2067(15)61031-2.

(6) Chakraborty, J. P.; Singh, S.; Maity, S. K. Advances in the Conversion of Methanol to Gasoline. In Hydrocarbon Biorefinery: Sustainable Processing of Biomass for Hydrocarbon Biofuels; Elsevier, 2021; pp 177–200. https://doi.org/10.1016/B978-0-12-823306-1.00008-X.

(7) ResearchAndMarkets.com. Global Ethylene Industry Report 2024-2030 Featuring SINOPEC, E. I. du Pont De Nemours and Co, Exxon Mobil, LyondellBasell Industries, Royal Dutch Shell, and SABIC. Finance Yahoo! https://finance.yahoo.com/news/global-ethylene-industry-report-2024-091700936.html.

(8) Leonzio, G.; Chachuat, B.; Shah, N. Towards Ethylene Production from Carbon Dioxide: Economic and Global Warming Potential Assessment. Sustain. Prod. Consum. 2023, 43, 124–139. https://doi.org/10.1016/j.spc.2023.10.015.

(9) Zacharopoulou, V.; Lemonidou, A. A. Olefins from Biomass Intermediates: A Review. Catalysts 2017, 8 (1), 2. https://doi.org/10.3390/CATAL8010002.

(10) Corma, A.; Iborra, S. Oligomerization of Alkenes. Microporous. Mesoporous S. Cat. 2006, 4, 125–140. https://doi.org/10.1002/0470094214.CH6.

(11) Alonso-Fariñas, B.; Gallego-Schmid, A.; Haro, P.; Azapagic, A. Environmental Assessment of Thermo-Chemical Processes for Bio-Ethylene Production in Comparison with Bio-Chemical and Fossil-Based Ethylene. J. Clean. Prod. 2018, 202, 817–829. https://doi.org/10.1016/J.JCLEPRO.2018.08.147.

(12) Nicholas, C. P. Applications of Light Olefin Oligomerization to the Production of Fuels and Chemicals. Appl. Catal. 2017, 543, 82–97. https://doi.org/10.1016/J.APCATA.2017.06.011.

(13) Martínez, C.; Corma, A. Inorganic Molecular Sieves: Preparation, Modification and Industrial Application in Catalytic Processes. Coord. Chem. Rev. 2011, 255 (13–14), 1558–1580. https://doi.org/10.1016/J.CCR.2011.03.014.

(14) Vermeiren, W.; Gilson, J. P. Impact of Zeolites on the Petroleum and Petrochemical Industry. Top. Catal. 2009, 52 (9), 1131–1161. https://doi.org/10.1007/S11244-009-9271-8.

(15) Sydora, O. L. Selective Ethylene Oligomerization. Organometallics 2019, 38 (5), 997–1010. https://doi.org/10.1021/acs.organomet.8b00799.

(16) Keim, W.; Ziegler, K.; Wilke, G.; Keim, W. Oligomerization of Ethylene to α-Olefins: Discovery and Development of the Shell Higher Olefin Process (SHOP). Angew. Chem. Int. Ed. 2013, 52 (48), 12492–12496. https://doi.org/10.1002/ANIE.201305308.

(17) Borges, P.; Pinto, R. R.; Lemos, M. A. N. D. A.; Lemos, F.; Védrine, J. C.; Derouane, E. G.; Ribeiro, F. R. Light Olefin Transformation over ZSM-5 Zeolites: A Kinetic Model for Olefin Consumption. Appl Catal A Gen 2007, 324 (1–2), 20–29. https://doi.org/10.1016/J.APCATA.2007.02.051.

(18) Bellussi, G.; Mizia, F.; Calemma, V.; Pollesel, P.; Millini, R. Oligomerization of Olefins from Light Cracking Naphtha over Zeolite-Based Catalyst for the Production of High Quality Diesel Fuel. Microporous. Mesoporous. Mater. 2012, 164, 127–134. https://doi.org/10.1016/J.MICROMESO.2012.07.020.

(19) Corma, A.; Martínez, C.; Doskocil, E. Designing MFI-Based Catalysts with Improved Catalyst Life for C3=andC5= Oligomerization to High-Quality Liquid Fuels. J. Catal. 2013, 300, 183–196. https://doi.org/10.1016/J.JCAT.2012.12.029.

(20) Mlinar, A. N.; Zimmerman, P. M.; Celik, F. E.; Head-Gordon, M.; Bell, A. T. Effects of Brønsted-Acid Site Proximity on the Oligomerization of

Propene in H-MFI. J. Catal. 2012, 288, 65–73. https://doi.org/10.1016/J.JCAT.2012.01.002.

(21) Martens, J. A.; Ravishankar, R.; Mishin, I. E.; Jacobs, P. A. Tailored Alkene Oligomerization with H-ZSM-57 Zeolite**. Angew. Chem. Int. Ed 2000, 39 (23). https://doi.org/10.1002/1521-3773(20001201)39:23.

(22) Martínez-Franco, R.; Paris, C.; Martínez-Armero, M. E.; Martínez, C.; Moliner, M.; Corma, A. High-Silica Nanocrystalline Beta Zeolites: Efficient Synthesis and Catalytic Application. Chem. Sci. 2015, 7 (1), 102–108. https://doi.org/10.1039/C5SC03019F.

(23) Díaz-Rey, M. R.; Paris, C.; Martínez-Franco, R.; Moliner, M.; Martínez, C.; Corma, A. Efficient Oligomerization of Pentene into Liquid Fuels on Nanocrystalline Beta Zeolites. ACS Catal. 2017, 7 (9), 6170–6178. https://doi.org/10.1021/ACSCATAL.7B00817.

(24) Xu, Z.; Chada, J. P.; Xu, L.; Zhao, D.; Rosenfeld, D. C.; Rogers, J. L.; Hermans, I.; Mavrikakis, M.; Huber, G. W. Ethylene Dimerization and Oligomerization to 1-Butene and Higher Olefins with Chromium-Promoted Cobalt on Carbon Catalyst. ACS Catal. 2018, 8 (3), 2488–2497. https://doi.org/10.1021/ACSCATAL.7B03205.

(25) Jan, O.; Song, K.; Dichiara, A.; Resende, F. L. P. Ethylene Oligomerization over Ni-Hβ Heterogeneous Catalysts. Ind. Eng. Chem. Res. 2018, 57 (31), 10241–10250. https://doi.org/10.1021/acs.iecr.8b01902.

(26) Koninckx, E.; Mendes, P. S. F.; Thybaut, J. W.; Broadbelt, L. J. Ethylene Oligomerization on Nickel Catalysts on a Solid Acid Support: From New

Mechanistic Insights to Tunable Bifunctionality. Appl. Catal. A. Elsevier B.V. August 25, 2021. https://doi.org/10.1016/j.apcata.2021.118296.

(27) Ehrmaier, A.; Peitz, S.; Sanchez-Sanchez, M.; Bermejo-Deval, R.; Lercher, J. On the Role of Co-Cations in Nickel Exchanged LTA Zeolite for Butene Dimerization. Microporous. Mesoporous. Mater. 2019, 284, 241–246. https://doi.org/10.1016/j.micromeso.2019.03.047.

(28) Yashima, T.; Ushida, Y.; Ebisawa, M.; Hara, N. Polymerization of Ethylene over Transition-Metal Exchanged Y Zeolites. J. Cat 1975, 36, 320–326. https://doi.org/10.1016/0021-9517(75)90042-1.

(29) Schmidt, F. K.; Belykh, L. B.; Gomboogiin, M.; Titova, Y. Y. Formation and Nature of Catalysts Based on Nickel(0) Phosphine Complexes Active in Lower Alkene Dimerization and Oligomerization. Kinet. Catal. 2010, 51 (2), 235–243. https://doi.org/10.1134/S0023158410020114.

(30) Hartmann, M.; Kevan, L. Dependence of Ethene Dimerization Activity and Selectivity on Ni I in Ion-Exchange vs. Framework Sites in SAPO-5 and SAPO-11 Materials. J. Chem. Soc, Faraday Trans. 1996, 92 (8), 1429–1434. https://doi.org/10.1039/FT9969201429.

(31) Choo, H.; Prakash, A. M.; Park, S. K.; Kevan, L. Electron Spin Resonance and Electron Spin Echo Modulation Studies on the Formation and Adsorbate Interactions of Ni(I) in Synthetic Clinoptilolite. J. Phys. Chem. B 1999, 103 (30), 6193–6199. https://doi.org/10.1021/JP990324D.

(32) Choo, H.; Hong, S. B.; Kevan, L. Comparative ESR Studies on the Reductibility and Adsorbate Interactions of Paramagnetic Ni(I) in Synthetic

Ferrierite and Mordenite. J. Phys. Chem. B 2001, 105 (10), 1995–2002. https://doi.org/10.1021/JP0036341.

(33) Elev, I. V.; Shelimov, B. N.; Kazansky, V. B. The Role of Ni+ Ions in the Activity of NiCaY Zeolite Catalysts for Ethylene Dimerization. J. Catal 1984, 89 (2), 470–477. https://doi.org/10.1016/0021-9517(84)90323-3.

(34) Prakash, A. M.; Kevan, L. Formation of Monovalent Nickel in NiNa-MCM-22 Zeolite and Its Interaction with Various Inorganic and Organic Adsorbates: Electron Spin Resonance Studies. J. Phys. Chem. 1996, 100 (50), 19587–19594. https://doi.org/10.1021/JP962321W.

(35) Bonneviot, L.; Olivier, D.; Che, M. Dimerization of Olefins with Nickel-Surface Complexes in X-Type Zeolite or on Silica. J. Mol. Catal. 1983, 21 (1–3), 415–430. https://doi.org/10.1016/0304-5102(93)80138-K.

(36) Wendt, G.; Finster, J.; Schöllner, R.; Siegel, H. Structural and Catalytic Properties of NiO-Al2O3/SiO2 Catalysts for the Dimerization and Isomerization of Olefins. Stud. Surf. Sci. 1981, 7 (PB), 978–992. https://doi.org/10.1016/S0167-2991(08)64708-4.

(37) Finiels, A.; Fajula, F.; Hulea, V. Nickel-Based Solid Catalysts for Ethylene Oligomerization-a Review. Cat. Sci. Technol. Royal Society of Chemistry 2014, pp 2412–2426. https://doi.org/10.1039/c4cy00305e.

(38) Brogaard, R. Y.; Olsbye, U. Ethene Oligomerization in Ni-Containing Zeolites: Theoretical Discrimination of Reaction Mechanisms. ACS Catal. 2016, 6 (2), 1205–1214. https://doi.org/10.1021/ACSCATAL.5B01957.

(39) Mohamed, H. O.; Velisoju, V. K.; Hita, I.; Abed, O.; Parsapur, R. K.; Zambrano, N.; Hassine, M. Ben; Morlanes, N.; Emwas, A. H.; Huang, K. W.;

Castaño, P. Highly Productive Framework Bounded Ni2+ on Hierarchical Zeolite for Ethylene Oligomerization. J. Chem. Eng 2023, 475, 146077. https://doi.org/10.1016/J.CEJ.2023.146077.

(40) Joshi, R.; Zhang, G.; Miller, J. T.; Gounder, R. Evidence for the Coordination-Insertion Mechanism of Ethene Dimerization at Nickel Cations Exchanged onto Beta Molecular Sieves. ACS Catal. 2018, 8 (12), 11407–11422. https://doi.org/10.1021/acscatal.8b03202.

(41) Moussa, S.; Concepción, P.; Arribas, M. A.; Martínez, A. The Nature of Active Ni Sites and the Role of Al Species in the Oligomerization of Ethylene on Mesoporous Ni-Al-MCM-41 Catalysts. Appl. Catal. A 2020, 608. https://doi.org/10.1016/j.apcata.2020.117831.

(42) Moussa, S.; Concepción, P.; Arribas, M. A.; Martínez, A. Nature of Active Nickel Sites and Initiation Mechanism for Ethylene Oligomerization on Heterogeneous Ni-Beta Catalysts. ACS Catal 2018, 8 (5), 3903–3912. https://doi.org/10.1021/acscatal.7b03970.

(43) Brückner, A.; Bentrup, U.; Zanthoff, H.; Maschmeyer, D. The Role of Different Ni Sites in Supported Nickel Catalysts for Butene Dimerization under Industry-like Conditions. J. Catal. 2009, 266 (1), 120–128. https://doi.org/10.1016/j.jcat.2009.05.021.

(44) Tanaka, M.; Itadani, A.; Kuroda, Y.; Iwamoto, M. Effect of Pore Size and Nickel Content of Ni-MCM-41 on Catalytic Activity for Ethene Dimerization and Local Structures of Nickel Ions. J. Phys. Chem. C 2012, 116 (9), 5664–5672. https://doi.org/10.1021/JP2103066.

(45) Ikeda, K.; Kawamura, Y.; Yamamoto, T.; Iwamoto, M. Effectiveness of the Template-Ion Exchange Method for Appearance of Catalytic Activity of Ni–MCM-41 for the Ethene to Propene Reaction. Catal. Commun. 2008, 9 (1), 106–110. https://doi.org/10.1016/J.CATCOM.2007.05.032.

(46) Caulkins, R.; Joshi, R.; Gounder, R.; Ribeiro, F. H. Effects of Ethene Pressure on the Deactivation of Ni-Zeolites During Ethene Oligomerization at Sub-Ambient Temperatures. ChemCatChem 2022, 14 (1). https://doi.org/10.1002/cctc.202101478.

(47) Zăvoianu, R.; Nenu, C.; Angelescu, E. Ni(2,2'-Bipyridine)2Cl2 Encapsulated in Y Zeolite New Catalyst for Ethylene Dimerization. Catal. Commun. 2005, 6 (6), 415–420. https://doi.org/10.1016/j.catcom.2005.03.007.

(48) Mignoni, M. L.; de Souza, M. O.; Pergher, S. B. C.; de Souza, R. F.; Bernardo-Gusmão, K. Nickel Oligomerization Catalysts Heterogenized on Zeolites Obtained Using Ionic Liquids as Templates. Appl. Catal. A. Gen. 2010, 374 (1–2), 26–30. https://doi.org/10.1016/j.apcata.2009.11.017.

(49) Yang, Y.; Lyu, Y.; Zhao, L.; Zhan, W.; Fan, L.; Li, F.; Liu, X. Ligand Assistance via Solid-State Coordination for Promoting Nickel Dispersion over the Ni/Beta Hydroisomerization Catalyst. Fuel 2022, 318. https://doi.org/10.1016/j.fuel.2022.123568.

(50) Nicola, B. P.; Lopes, C. W.; Marini, C.; Rossetto, E.; Pergher, S. B. C.; Bernardo-Gusmão, K. Ni-β-Diimine Complex Heterogenized in Delaminated ITQ-2 Zeolite as Catalytic Precursor for Ethylene Oligomerization. Catal. Today 2021, 381, 192–199. https://doi.org/10.1016/j.cattod.2020.07.019.

(51) Ismaila, A.; Chen, H.; Fan, X. Nickel Encapsulated in Silicalite-1 Zeolite Catalysts for Steam Reforming of Glycerol (SRG) towards Renewable Hydrogen Production. Fuel Process. Technol. 2022, 233. https://doi.org/10.1016/j.fuproc.2022.107306.

(52) Li, Y.; Du, T.; Chen, C.; Jia, H.; Sun, J.; Fang, X.; Wang, Y.; Na, H. Copper Nanoparticles Encapsulated in Zeolite 13X for Highly Selective Hydrogenation of CO2 to Methanol. J. Environ. Chem. Eng 2024, 12 (2), 111856. https://doi.org/10.1016/J.JECE.2023.111856.

(53) Xing, C.; Shen, W.; Yang, G.; Yang, R.; Lu, P.; Sun, J.; Yoneyama, Y.; Tsubaki, N. Completed Encapsulation of Cobalt Particles in Mesoporous H-ZSM-5 Zeolite Catalyst for Direct Synthesis of Middle Isoparaffin from Syngas. Catal. Commun 2014, 55, 53–56. https://doi.org/10.1016/J.CATCOM.2014.06.018.

(54) Saxena, A.; Joshi, R.; Seemakurthi, R. R.; Koninckx, E.; Broadbelt, L. J.; Greeley, J.; Gounder, R. Effect of Nickel Active Site Density on the Deactivation of Ni-Beta Zeolite Catalysts during Ethene Dimerization. ACS Eng. Au 2022, 2 (1), 12–16. https://doi.org/10.1021/acsengineeringau.1c00014.

(55) Moon, S.; Chae, H. J.; Park, M. B. Oligomerization of Light Olefins over ZSM-5 and Beta Zeolite Catalysts by Modifying Textural Properties. Appl. Catal. A 2018, 553, 15–23. https://doi.org/10.1016/j.apcata.2018.01.015.

(56) Gallego, E. M.; Paris, C.; Díaz-Rey, M. R.; Martínez-Armero, M. E.; Martínez-Triguero, J.; Martínez, C.; Moliner, M.; Corma, A. Simple Organic Structure Directing Agents for Synthesizing Nanocrystalline Zeolites. Chem. Sci. 2017, 8 (12), 8138–8149. https://doi.org/10.1039/C7SC02858J.

(57) Joshi, R.; Saxena, A.; Gounder, R. Mechanistic Insights into Alkene Chain Growth Reactions Catalyzed by Nickel Active Sites on Ordered Microporous and Mesoporous Supports. Catal. Sci. Technol. 2020, 10 (21), 7101–7123. https://doi.org/10.1039/D0CY01186J.

(58) Díaz-Rey, M. R.; Paris, C.; Martínez-Franco, R.; Moliner, M.; Martínez, C.; Corma, A. Efficient Oligomerization of Pentene into Liquid Fuels on Nanocrystalline Beta Zeolites. ACS Catal. 2017, 7 (9), 6170–6178. https://doi.org/10.1021/ACSCATAL.7B00817.

(59) Martínez-Franco, R.; Paris, C.; Martínez-Armero, M. E.; Martínez, C.; Moliner, M.; Corma, A. High-Silica Nanocrystalline Beta Zeolites: Efficient Synthesis and Catalytic Application. Chem. Sci. 2015, 7 (1), 102–108. https://doi.org/10.1039/C5SC03019F.

(60) Vázquez, M. I.; Corma, A.; Fornés, V. Characterization of NiO Supported on Zeolite Y, by Pyridine Adsorption. Zeolites 1986, 6 (4), 271–274. https://doi.org/10.1016/0144-2449(86)90080-1.

(61) Martínez, A.; Arribas, M. A.; Concepción, P.; Moussa, S. New Bifunctional Ni–H-Beta Catalysts for the Heterogeneous Oligomerization of Ethylene. Appl. Catal. A. 2013, 467, 509–518. https://doi.org/10.1016/J.APCATA.2013.08.021.

(62) Ganjkhanlou, Y.; Groppo, E.; Bordiga, S.; Volkova, M. A.; Berlier, G. Incorporation of Ni into HZSM-5 Zeolites: Effects of Zeolite Morphology and Incorporation Procedure. Microporous. Mesoporous. Mater. 2016, 229, 76–82. https://doi.org/10.1016/j.micromeso.2016.04.002.

(63) Moussa, S.; Arribas, M. A.; Concepción, P.; Martínez, A. Heterogeneous Oligomerization of Ethylene to Liquids on Bifunctional Ni-Based Catalysts: The Influence of Support Properties on Nickel Speciation and Catalytic Performance. Catal. Today 2016, 277, 78–88. https://doi.org/10.1016/j.cattod.2015.11.032.

(64) Hadjiivanov, K.; Knözinger, H.; Mihaylov, M. FTIR Study of CO Adsorption on Ni-ZSM-5. J. Phys. Chem. B 2002, 106 (10), 2618–2624. https://doi.org/10.1021/jp0132782.

(65) Penkova, A.; Dzwigaj, S.; Kefirov, W. R.; Hadjiivanov, K.; Che, M. Effect of the Preparation Method on the State of Nickel Ions in BEA Zeolites. A Study by Fourier Transform Infrared Spectroscopy of Adsorbed CO and NO, Temperature-Programmed Reduction, and X-Ray Diffraction. J. Phys. Chem. C 2007, 111 (24), 8623–8631. https://doi.org/10.1021/JP071927P/ASSET/IMAGES/LARGE/JP071927PF00012.JPEG.

(66) Aleksandrov, H. A.; Zdravkova, V. R.; Mihaylov, M. Y.; Petkov, P. S.; Vayssilov, G. N.; Hadjiivanov, K. I. Precise Identification of the Infrared Bands of the Polycarbonyl Complexes on Ni-MOR Zeolite by 12C 16O- 13C 18O Coadsorption and Computational Modeling. J. Physl Chem. C 2012, 116 (43), 22823–22831. https://doi.org/10.1021/jp304972u.

(67) Zecchina, A.; Bordiga, S.; Spoto, G.; Marchese, L.; Petrini, G.; Leofanti, G.; Padovan, M. Silicalite Characterization. 1. Structure, Adsorptive Capacity, and IR Spectroscopy of the Framework and Hydroxyl Modes. J. Phys. Chem. 1992, 96 (12), 4985–4990. https://doi.org/10.1021/J100191A047.

(68) Braschi, I.; Gatti, G.; Bisio, C.; Berlier, G.; Sacchetto, V.; Cossi, M.; Marchese, L. The Role of Silanols in the Interactions between Methyl Tert - Butyl Ether and High-Silica Faujasite y: An Infrared Spectroscopy and Computational Model Study. J. Phys. Chem. C 2012, 116 (12), 6943–6952. https://doi.org/10.1021/JP210605T.

(69) Mlinar, A. N.; Baur, G. B.; Bong, G. G.; Getsoian, A.; Bell, A. T. Propene Oligomerization over Ni-Exchanged Na-X Zeolites. J. Catal. 2012, 296, 156–164. https://doi.org/10.1016/J.JCAT.2012.09.010.

(70) Baran, R.; Śrębowata, A.; Kamińska, I. I.; Łomot, D.; Dzwigaj, S. Catalytic Activity of HAlBEA and NixHAlBEA Zeolites in Hydrogen-Assisted Dehydrochlorination of 1,2-Dichloroethane into Vinyl Chloride Monomer. Microporous. Mesoporous. Mater. 2013, 180, 209–218. https://doi.org/10.1016/J.MICROMESO.2013.06.037.

(71) Wang, L.; Chen, T.; Zhang, J.; Jiao, Y.; Wang, J.; Zhu, Q.; Li, X. High Catalytic Activity and Stability Quasi Homogeneous Alkali Metal Promoted Ni/SiO2 Aerogel Catalysts for Catalytic Cracking of n-Decane. Fuel 2020, 268, 117384. https://doi.org/10.1016/J.FUEL.2020.117384.

(72) Joshi, R.; Zhang, G.; Miller, J. T.; Gounder, R. Evidence for the Coordination-Insertion Mechanism of Ethene Dimerization at Nickel Cations Exchanged onto Beta Molecular Sieves. ACS Catal. 2018, 8 (12), 11407–11422. https://doi.org/10.1021/ACSCATAL.8B03202.

(73) Lacarriere, A.; Robin, J.; Świerczyński, D.; Finiels, A.; Fajula, F.; Luck, F.; Hulea, V. Distillate-Range Products from Non-Oil-Based Sources by Catalytic Cascade Reactions. ChemSusChem 2012, 5 (9), 1787–1792. https://doi.org/10.1002/CSSC.201200092.

(74) Henry, R.; Komurcu, M.; Ganjkhanlou, Y.; Brogaard, R. Y.; Lu, L.; Jens, K. J.; Berlier, G.; Olsbye, U. Ethene Oligomerization on Nickel Microporous and Mesoporous-Supported Catalysts: Investigation of the Active Sites. Catal. Today 2018, 299, 154–163. https://doi.org/10.1016/J.CATTOD.2017.04.029.

(75) Li, W.; Zhou, C.; Li, W.; Ge, L.; Yu, G.; Qiu, M.; Chen, X. Tuning the Ni Site Location of Bifunctional Ni-Based Catalysts for Improving the Performance in Ethylene Oligomerization. New J. Chem. 2022, 46 (19), 9461–9469. https://doi.org/10.1039/D2NJ01527G.

(76) Meloni, M.; Runnebaum, R. C. Tuning Supported Ni Catalysts by Varying Zeolite Beta Heteroatom Composition: Effects on Ethylene Adsorption and Dimerization Catalysis. Cat. Sci. Technol. 2021, 11 (10), 3393–3401. https://doi.org/10.1039/D1CY00308A.

(77) Ehrmaier, A.; Liu, Y.; Peitz, S.; Jentys, A.; Chin, Y. H. C.; Sanchez-Sanchez, M.; Bermejo-Deval, R.; Lercher, J. Dimerization of Linear Butenes on Zeolite-Supported Ni 2+. ACS Catal. 2019, 9 (1), 315–324. https://doi.org/10.1021/ACSCATAL.8B03095.

(78) Sarazen, M. L.; Doskocil, E.; Iglesia, E. Effects of Void Environment and Acid Strength on Alkene Oligomerization Selectivity. ACS Catal. 2016, 6 (10), 7059–7070. https://doi.org/10.1021/ACSCATAL.6B02128.

CHAPTER 7:
CONCLUSIONS

This doctoral thesis has introduced various innovative methodologies for synthesizing zeolitic materials, enabling precise control over their crystalline structure and particle size, as well as their textural and physicochemical properties. Furthermore, these methodologies have facilitated the selective positioning of homogeneously distributed metallic active centres within all zeolite crystalline particles. Due to these features, the synthesized materials show promising prospects for application as heterogeneous catalysts in chemical processes of significant industrial relevance.

Each chapter comprehensively compiles the conclusions drawn from a thorough and critical analysis of the results obtained along the research. Below, the most significant conclusions derived from this PhD thesis are outlined.

- **Resolving Complex K-PtSn Interactions in PtSn@K-MFI Catalysts for alkane dehydrogenation.**

In Chapter 4, three-dimensional medium-pore zeolites with MFI crystalline structure were synthesized in their purely siliceous form (S-1), incorporating Pt nanoclusters as active centres and varying atomic compositions of K^+ cations and Sn species. By optimizing the atomic balance within the synthesis gel, the interaction between the active sites and the alloying species was enhanced, thereby maximizing catalytic activity and stability in the non-oxidative dehydrogenation of propane, an industrially relevant reaction.

Increasing Sn content in the absence of K^+ resulted in a deficiency of PtSn alloys and a non-homogeneous distribution of these species within the zeolitic matrix, promoting the sintering of metal centres during catalytic use. Conversely, an excess of K^+ and Sn beyond the stoichiometric assimilable

threshold led to the precipitation of Sn silicate impurities, which sequestered catalytically active species and reduced PtSn interactions. This, in turn, diminished catalytic activity and reduced resistance to sintering upon reuse.

Optimal catalyst compositions, characterized by K^+ levels close to the maximum stoichiometric uptake (~0.7 wt% K) and intermediate Sn concentrations (~1 wt% Sn), facilitated the homogeneous dispersion and stabilization of PtSn bimetallic centres. This resulted in superior catalytic performance, exhibiting higher activity and selectivity towards the propylene formation at extended time-on-stream (TOS), and possessing enhanced resistance to sintering across multiple regeneration cycles.

These findings underscore the critical importance of atomic-scale catalyst design during synthesis and crystallization to satisfy the rigorous demands of modern industrial processes. Such an approach extends catalyst lifetime and enhances process sustainability by reducing deactivation and improving overall efficiency.

- **One-pot encapsulated metal zeolite with controlled zeolite particle sizes: from nano to submicron zeolite particles**

In the second chapter of this doctoral thesis, three-dimensional medium-pore zeolites with MFI structure were synthesized in their purely siliceous form (S-1). These materials exhibit different zeolite crystalline particle sizes and incorporate Pd nanoparticle-based active centres. The objective of this study was to investigate the impact of the catalysts´ diffusive properties on their activity and final selectivity in the semi-hydrogenation of phenylacetylene. Precise control of the diffusive properties of the S-1

supports was achieved by modulating the final crystalline particle size through the rational adjustment of the crystallization temperature.

A decrease in crystalline particle size resulted in enhanced catalytic activity and improved selectivity towards the semi-hydrogenation of phenylacetylene to styrene, as the smaller particles facilitated the rapid release of product molecules.

Additionally, ultrafast hydrothermal synthesis methodology was successfully employed to develop hydrophobic crystalline coatings of controlled thickness, regulated by the degree of hydration of the synthesis gel. This innovative approach provided an effective strategy for enhancing the stabilization of metal nanoparticles.

- **Design of bifunctional Ni-zeolites for ethylene oligomerization. Controlling Nickel speciation and zeolite properties through one-pot synthesis and post-synthetic Nickel incorporation.**

In the final chapter of this PhD thesis, nanocrystalline zeolites of both MFI and BEA crystalline structure, with varied physicochemical properties, were synthesized employing specific OSDAs. These properties were tailored by adjusting the Si/Al ratio in the synthesis gel and utilizing a specific method for incorporating Ni. This approach enabled the precise control over crystalline particle size and the strategic positioning of active centres at the atomic scale, optimizing the diffusive properties for the light olefin oligomerization reaction. The synthesized materials were compared to commercially available zeolites, where Ni incorporation was achieved through post-synthetic procedures.

The method used for Ni incorporation significantly impacts the final state of the material. Post-synthetic incorporation promotes the formation of Ni^{2+} centres, whereas direct synthesis leads to the formation of both Ni^{2+} cations and homogeneously dispersed NiO nanoparticles (with a higher concentration of Ni^{2+} at lower Si/Al ratios).

The chemical state of the Ni active centres is critical in the low-pressure ethylene oligomerization reaction. Ni^{2+} centres are the active species, maintaining stable catalytic activity over long reaction times in materials with higher Ni^{2+} content, which is grafted to zeolite silanol groups. Under these conditions, the particle size and topology of the material do not significantly influence the activity, with all catalysts showing a product distribution predominantly between C_4 and C_8. The variations in activity can be attributed to the differing Ni^{2+} concentrations in the materials.

Under near-industrial conditions, the importance of optimizing diffusive properties through the combined effects of topology and particle size reduction becomes relevant. While Ni^{2+} centres are responsible for activating the double bonds of the ethylene molecules, the formation of higher molecular weight hydrocarbons ($>C_{12}$) on the Brønsted acid sites cause a faster decline in catalyst activity. Nanocrystalline BEA-type catalysts (large pore) and nanocrystalline MFI-type catalysts (medium pore) exhibit the highest stability over time, as they enable efficient diffusion of higher molecular weight products before channel blockage by deposition of coke precursors, aided by the influence of reduced crystal size.

.

ANEX I: Table of Figure

ANEX II: Table of Tables

ANEX III: Scientific Production

Research Papers:

1. **Martínez Gómez-Aldaraví, Adrián**; Millán, Reisel; Millet, Isabel; Alós, Aroa; Vidal-Moya, Alejandro; Meller, Randall J.; Martínez, Cristina; Corma, Avelino; Boronat, Mercedes; Serna, Pedro; Moliner, Manuel. Resolving Complex K–Pt–Sn Interactions in PtSn@K-MFI Catalysts for Alkane Dehydrogenation. J. Am. Chem. Soc. 2025, 147, 15, 12833–12844. https://doi.org/10.1021/jacs.5c01536

2. **Martínez Gómez-Aldaraví, Adrián**; Paris, Cecilia; Moliner, Manuel; Martínez, Cristina. Design of bi-functional Ni-zeolites for ethylene oligomerization: Controlling Ni speciation and zeolite properties by one-pot and post-synthetic Ni incorporation. J. Catal. 2023, 426, 140–152. https://doi.org/10.1016/j.jcat.2023.07.010